AN INVESTIGATION OF THE COMPOUND NUCLEI ^{7}Li AND ^{7}Be

Thesis by

Robert John Spiger

In Partial Fulfillment of the Requirements

For the Degree of

Doctor of Philosophy

California Institute of Technology

Pasadena, California

1967

(Submitted October 27, 1966)

ACKNOWLEDGMENTS

It is a pleasure to acknowledge the generous assistance of the faculty, staff and students of the Kellogg Radiation Laboratory during the course of this work. Particularly appreciated was the assistance and guidance of my advisor, Professor Thomas A. Tombrello, who suggested the problem and was a constant source of help, advice and encouragement in both the experimental and theoretical portions of the work.

Credit for much of the design of the apparatus for the $t + \alpha$ experiment goes to Mr. Vic Ehrgott. Also appreciated are the efforts of Mr. George Fastle, Mr. Don Woshnak and Mr. Harold Larson who constructed many pieces of this equipment.

Assistance in performing the experiments was received from Mr. Andrew D. Bacher, who also introduced the author to many of the experimental techniques, and from Mr. M. Dwarakanath who constructed our current integrator.

Many weeks of tedious data reduction were avoided through the use of a data display program developed by Mr. Michael Mahon. His efforts and the help of Mrs. Barbara Zimmerman in computer programming are greatly appreciated. To Mr. Reagan Moore, Mr. Martin Cooper and Mr. George Fox go credit for the many months of work spent helping me to plot and analyze the data.

To my wife, Pearl, goes much of the credit for preliminary typing and encouragement in the preparation of this thesis. The many others who have assisted in this work may be assured that their help is appreciated even though they remain unnamed.

ABSTRACT

The differential elastic scattering cross section has been measured for the scattering of ^{3}He from ^{4}He and the scattering of ^{4}He from tritium. Incident particle energies of 5 to 18 MeV and 4 to 18 MeV, respectively, were used. Gas targets were used and solid state silicon detectors were employed to detect the scattered particles. Data were also obtained for the reactions ^{4}He(^{3}He, p)^{6}Li, ^{4}He(^{3}He, p^1)^{6}Li*, ^{3}H(α, n)^{6}Li and ^{3}H(α, n^1)^{6}Li*. Levels are seen at 4.65, 6.64, 7.47 and 9.7 MeV in ^{7}Li and at 4.57, 6.73, 7.21 and 9.3 MeV in ^{7}Be. A phase shift analysis suggests assignments of $\frac{7^-}{2}$ and $\frac{5^-}{2}$ for the two lower levels in ^{7}Li, confirms the $\frac{5^-}{2}$ assignment of the 7.47 level and suggests a $\frac{7^-}{2}$ assignment for the new level at 9.7 MeV. Similarly in ^{7}Be, the assignment of $\frac{7^-}{2}$ and $\frac{5^-}{2}$ for the lower two levels is reconfirmed and an assignment of $\frac{7^-}{2}$ is suggested for the new level at 9.3 MeV. The reduced widths for α and nucleon emission were determined by fitting the phase shifts near each level with a single and/or double level formula from the R-matrix formalism of Lane and Thomas (1958). The results of the analysis are discussed and compared with predictions of some recent nuclear model calculations.

v

TABLE OF CONTENTS

I. INTRODUCTION

In the past few years, several experimental studies of the excited states of the compound nuclei ^{7}Li and ^{7}Be have been made. The work to be described was designed to complement and extend the range of these studies. The tandem Van de Graaff accelerator was used to produce ^{4}He and ^{3}He beams at energies exceeding 18 MeV. These energies allowed the compound nuclei to be investigated over a fairly large energy range.

The entrance channels employed in this investigation were $t + \alpha$ for ^{7}Li and ^{3}He $+ ^4$He for ^{7}Be. From an experimental point of view these entrance channels have the advantage of allowing the use of a gas target. This provided a target of uniform thickness for which the data obtained could easily be given an absolute normalization. The theoretical analysis was also made simpler by the fact that both entrance channels were cases of the scattering of a spin $\frac{1}{2}$ particle from a spin 0 particle. In particular, the phase shift analysis to determine spins and parities of the various levels was considerably simplified.

The entrance channels used lead to several reactions. For ^{7}Li, the reactions ^{3}H$(\alpha, \alpha)^3$H, ^{3}H$(\alpha, n)^6$Li and ^{3}H$(\alpha, n_1)^6$Li* were investigated. For ^{7}Be the analogous reactions ^{4}He$(^3$He, ^{3}He$)^4$He, ^{4}He$(^3$He, p$)^6$Li and ^{4}He$(^3$He, p$_1)^6$Li* were studied. An analysis of the data obtained made it possible to compare α-widths and nucleon widths of various levels with predictions of nuclear models (for example, the calculations of Barker, (1966)). Several levels predicted by these calculations were investigated.

The experimental details of this work and the data obtained are discussed in Part II. The data are listed in the tables and shown

in the figures. In Part III, the theoretical analysis of the data is discussed. A phase shift analysis and R-matrix fitting are used to determine the level parameters. These are then compared with the predictions of nuclear models in Part IV.

Additional experimental details and a discussion of the computer programs which were used are contained in several appendices.

II. EXPERIMENTAL DISCUSSION

A. The Elastic Scattering $^3H(\alpha, \alpha)^3H$

(1) Apparatus

(a) The Chamber, Vacuum System and Safety Devices

The $^3H(\alpha, \alpha)^3H$ elastic scattering experiment was done with a gaseous target of $^3H_2$. The problems involved in protecting the laboratory from contamination by this radioactive gas required the use of more elaborate safety precautions than were convenient with the available gas scattering chambers. To utilize the tritium target, a complete new beam tube and target station were added in the target room of the C. I. T. -ONR Tandem Van de Graaff accelerator.

The scattering chamber was constructed of a cylindrical steel pipe with top and bottom of aluminum. The walls were 1.9 cm. thick and the inner diameter of the chamber was 27.9 cm. The top and bottom formed 0-ring seals with the walls. The chamber was provided with four ports set at 90° intervals around the chamber walls. A diagram of the chamber is shown in Figure 1.

The beam enters through a collimator formed by a series of tantalum discs pierced with holes 1.5 or 2.0 mm. in diameter. These serve to collimate the beam and provide resistance to the passage of gas from the chamber in the event of a leak in the gas cell. The opposite port leads to the Faraday cup used to catch the beam after passage through the target. The port opposite that containing the gas cell assembly leads to the main pumping station. It is also fitted with an ionization gauge which is used to monitor

chamber pressure during the course of a run. The path to the pumping station is closed by a two inch butterfly valve when tritium is in the gas cell.

The gas cell assembly is mounted on a brass flange and inserted into the fourth port. The flange is drilled to provide a vacuum passage to the gas handling system and has a threaded recess to attach the gas manifold.

Upstream from the beam collimator is a small charcoal trap followed by a second group of tantalum discs, which further increase the resistance to gas flow from the chamber. A bypass connects this trap to the main pumping system through a Circle-Seal valve. Upstream from the second set of discs is an electrically operated safety valve which can shut the main pumping station and beam tube off from the chamber.

In operation with tritium in the gas cell, the following procedure is used. The small charcoal trap and a large trap in the bottom of the chamber are cooled with liquid nitrogen. The bypass valves are closed. This leaves open only the small passage through which the beam enters. The large charcoal trap then provides internal pumping of the chamber. If a leak from the gas cell develops, the rise in chamber pressure will be detected by the ionization gauge and the electric safety valve will be automatically shut. Most of the escaped gas will be pumped by the large charcoal trap in the chamber and most of that escaping through the beam collimator will be pumped by the small charcoal trap. These traps may then be sealed off under vacuum, detached from the station and disposed of. The large charcoal trap will normally hold the closed chamber at a pressure of about $5 \cdot 10^{-6}$ mm. of Hg.

(b) The Gas Handling System and Gas Cell

The gas handling system and gas cell were constructed of hydrogen-free material, where possible, in order to minimize the contamination of the tritium target gas by ordinary hydrogen. A schematic diagram of this system is shown in Figure 2.

The gas cell is 4.45 cm. in diameter and 1.9 cm. high. It is constructed of brass and has nickel foil windows. The foils are sealed to the brass with Carter's Epoxy. The beam entrance foil is 8125 Å thick. The three foils for the exit of beam and scattered particles are approximately 13,000 Å thick. They are arranged so that all laboratory angles from 12° to 90° can be reached by the counter collimators (see Figure 1). The cell is soldered to a hollow tube connected to the flange at the chamber port. This supports the cell and provides an entrance for the gas.

The manifold is a brass block which screws into the threaded recess on the flange. The manifold has five interconnected outlets. One leads to the gas cell and another leads to a Wallace and Tiernan differential pressure gauge (0 - 50 mm. of Hg) by means of a length of 3.2 mm. copper tubing. The other three outlets are fitted with all metal Nupro bellows valves (model B-4H). One valve leads to a gas bottle which allows testing of the foils or the use of another target gas. The second valve connects to the vacuum passage through the flange and provides for pumping out the gas cell, the manifold and the vacuum chamber surrounding the tritium reservoir. The third valve is connected to the tritium reservoir. All the passages were kept as small as possible to maximize the pressure obtainable with our limited amount of tritium. The joints in the system were sealed with Teflon tape or soldered.

The tritium reservoir is shown in Figure 3. To facilitate handling and storage, the tritium gas is stored in the reservoir in the form of uranium tritide. The gas is evolved into the cell by heating the uranium and is pumped from the cell by the cool uranium when the run is over (see Appendix C). The construction material is stainless steel with joints being silver soldered or sealed with Teflon. A nichrome wire coil is used to heat the uranium in the reservoir.

(c) Collimation and Particle Detection

Before performing the experiment, the chamber was optically aligned with the beam tube using a Brunson telescope. A bellows and support behind the Faraday cup are provided to keep the forces on the chamber in equilibrium when the system is under vacuum.

The collimation slits for the particle detectors and the gas cell were also aligned in this manner. The zero positions were reproducible to about 3 minutes of arc. The slits were mounted in aluminum blocks which were suspended from two ground stainless steel tubes 1.27 cm. in diameter. The rods were press fitted into two concentric hubs which pass through the top of the chamber. This allowed the two collimators to be positioned independently. The positions were read with protractors on the top of the chamber lid. Nylon-tipped set screws hold the aluminum blocks in place on the rods and the slits in place in the blocks.

The slits are made of brass and are approximately 1.0 mm. thick. The front slit is defined in width and the rear slit in both width and height. The center slit is a wider anti-scattering slit designed to prevent particles scattered from slit edges and walls

from reaching the detectors. The dimensions of the slits and their spacing in the chamber are given in Table 1 (see also Figure 1 and Appendix B).

The detectors were surface-barrier and Li-drifted silicon solid-state detectors. They were mounted in brass cans to shield them from electrical noise. The cans were held in place directly behind the slits in lucite blocks suspended from the stainless steel rods. Detector leads from one collimator were fed through the hollow rod and led out through the hub at the center of the chamber. The leads from the other collimator were led out near the side of the chamber top. A further discussion of the detectors and electronics is contained in Appendix A.

(2) Procedure

On a typical run the following procedure was used. Liquid nitrogen was used to cool the charcoal traps until they were cold enough to pump the chamber unaided. During this time the electronics were set up and checked. The beam was brought to a viewer just in front of the chamber. The valves to the diffusion pump were then closed and the safety valve in the beam line was coupled to the ion gauge. The tritium reservoir was opened to the rest of the chamber and the accumulated ^{3}He was pumped off by briefly opening the main bypass valve. This valve was then shut as was the Nupro valve connecting the manifold to the chamber vacuum. Tritium gas was then evolved from the uranium by passing current through the nichrome wire coil on the reservoir. When the desired tritium pressure (about 40 mm. of Hg) was reached the reservoir was shut off from the manifold and allowed to cool. The safety valve in the beam line was opened and the beam was focused on target.

Data were then taken in the form of excitation curves at
a number of laboratory angles. A separate spectrum was taken for
each energy and angle on a 400-channel Radiation Instrument
Development Laboratories multi-channel analyzer. For each
spectrum the time for the run, the analyzer live time, the actual
time of day and the nominal beam energy were recorded. The
temperature and pressure in the gas cell were also recorded at
frequent intervals. Energy steps of 50, 100, or 250 keV were taken,
depending on the rate of variation of the cross section. The integrator
was calibrated at several times during the day.

Data were also taken in the same general manner in 500
keV steps for the elastic scattering $^1H(\alpha, \alpha)^1H$. These data provided
a calibration to determine the hydrogen contamination in our tritium
target gas.

The beam was obtained from the ONR-CIT tandem
accelerator. For beam energies between 4.0 and 13.25 MeV the
standard doubly charged $^4He^{++}$ beam was used. For higher energies,
a negative ^4He beam was extracted from the negative ion source.
This beam was stripped to a double positive charge at the center
terminal of the tandem and energies up to 18.25 MeV were obtained.
Typical beam currents on target were 200 nano Amps for the standard
beam and 5 - 15 nano Amps for the high energy beam.

(3) Results

A typical spectrum from the 400-channel analyzer is
shown in Figure 6. The α group is seen at channel 293, the triton
group at channel 122 and the proton contaminant group at channel 80.
The small group at channel 358 is composed of α particles scattered
from the walls and foils of the gas cell. This is also the source of

the low, continuous background in the spectrum. The shoulder at channel 40 marks the point at which the separation of charge one from charge two takes effect (see Appendix A).

The data obtained were reduced to differential cross sections (see Appendix B). Excitation curves at 17 center-of-mass angles from 39° to 146° were obtained in the region of 4 to 13 MeV. These data are tabulated in Table 3 and are shown in Figures 9 - 17. The open circles are the data points. The solid lines are fits to the data from the phase shift analysis, which will be discussed in Part III.

These data show clearly three resonances. The lowest is the resonance near 5 MeV corresponding to the level at 4.63 MeV excitation energy in ^{7}Li. The broad resonance near 9.5 MeV corresponds to the $\frac{5^-}{2}$ level at 6.6 MeV excitation in ^{7}Li. Note that the $\frac{5^-}{2}$ 7.47 MeV level also appears in these curves as the weakly excited dispersion curve near 11.5 MeV. This is of interest since the corresponding level in ^{7}Be is not seen in the elastic scattering ^{4}He(^{3}He, ^{3}He)^{4}He (Tombrello, 1963).

In the range from 13 to 18 MeV excitation curves were taken at 8 center-of-mass angles from 54° to 135°. These show a resonance near 16.8 MeV corresponding to an excitation of 9.7 MeV in ^{7}Li (see Figures 18 - 21). These data are tabulated in Table 4.

Figures 22 - 27 show angular distributions generated from these data. Once again, the solid line gives the phase shift analysis fit to the data. The angular distributions are shown at positions below, at and above each resonance energy.

A discussion of the experimental errors in the data is contained in Appendix D and the errors are tabulated in Table 5.

B. The Reaction ^{3}H$(\alpha, n)^6$Li

(1) Apparatus

This experiment was done at 0° using a solid target of zirconium tritide on a .025 cm. thick platinum backing. The target contained about $2 \cdot 10^{18}$ atoms of tritium per square centimeter in the form of a disc 2.54 cm. in diameter. This was placed in the center of a vertical quartz tube of approximately 3.75 cm. diameter. The target was oriented so that it was normal to the beam. A bias of 300 volts was used on the target for integration purposes. The tube was in the form of a T and was connected to the beam tube by its horizontal portion. A pressure of $5 \cdot 10^{-7}$ mm. of Hg was maintained at the target.

The beam current was integrated with an Eldorado Model CI-110 current integrator. A charge of 18.0 micro Coulombs was collected for each run. The neutrons were detected by a "long counter" placed very close to the quartz tube. This geometry was used so that all the neutrons in the cone about 0° would be intercepted by the detector. Pulses from the counter were amplified with a Hamner amplifier and counted in an Eldorado scalar. A bias was set on the scalar so that only pulses higher than those induced by gamma rays were counted.

(2) Procedure

The actual data for this reaction as well as for the reaction ^{3}H$(\alpha, n^1)^6$Li* were obtained by T. A. Tombrello. The neutron yield was taken at energy intervals of 40 keV except near threshold where steps of approximately 10 keV were taken. The beam energy, length of time of the run and number of counts on the scalar were recorded for each run.

(3) Results

The results are tabulated in Table 6 and are shown in Figure 28. These data show an s-wave behavior near threshold, but the overall behavior is dominated by the effect of the $\frac{5^-}{2}$ level at 7.47 MeV in ^{7}Li. These data were not used in the analysis, but do show good agreement with the data which were used.

C. The Reaction $^3H(\alpha, n^1)^6Li^*$

(1) Apparatus

The objective in this experiment was to obtain the total reaction cross section at beam energies between 12 and 18 MeV. Below 12.4 MeV, data were available from the inverse reaction $^6Li(n, \alpha)^3H$ (Schwarz, 1965). Once again the negative helium beam from the ion source of the tandem was used.

The target was a disc cut from the previously mentioned zirconium tritide target. Its diameter was approximately 0.95 cm. Figure 30 shows a schematic diagram of the target assembly and detector. The target is held at the back of a cylindrical aluminum target chamber by a liner of coiled tantalum sheet. The target chamber slips onto a metal tube and seals with an O-ring. The metal tube is fitted to a lucite plate at the end of the beam tube. This provides the insulation necessary for beam integration. For integration, a wire is attached to the aluminum chamber and a 45-Volt bias is used between the chamber and integrator. The same Eldorado integrator is used.

The detection apparatus consisted of two parts. The first part was a large paraffin cylinder designed to thermalize the neutrons.

The forward end was drilled to receive the target chamber so that a maximum number of neutrons from the target would be thermalized. The diameter of the cylinder was approximately 30 cm. and its length 41 cm. At the rear of the cylinder and on the axis, a hole was drilled to receive the second component. This was an Ne 402 phosphor mounted on a phototube. A standard Kellogg preamp was used with the phototube. The wax block was insulated from the target chamber by wrapping the chamber with Teflon tape.

(2) Procedure

An Eldorado scalar was used to count the pulses from the phototube. The pulse-height spectrum was a continuum and a bias was set at an arbitrary point in this spectrum. The scalar then counted pulses higher than the bias. Charge integrations of 2.7 μ Coulombs were taken. Runs were taken with beam energies from 11.0 to 18.0 MeV. Steps of 50 keV were used in the region of the resonance near 11.5 MeV. Near the 16.8 MeV resonance 100 keV steps were used, with 250 keV steps being used elsewhere. Runs were taken with the detector at the rear of the block and also with the detector on the side and near the front of the cylinder (see Figure 30). The side position was placed so that neutrons from this reaction could not reach the phosphor directly. Thus the neutrons from the reaction $^3H(\alpha, n)^6Li$ are emphasized here if all the neutrons are not thermalized.

(3) Results

The number of counts on the scalar were recorded at each energy. Figure 31 shows the data recorded and reduced to

cross sections for the configuration with the phosphor at the back of the cylinder. The reduction was carried out in the following way. As was mentioned before, the cross section from 11.0 to 12.4 MeV was obtained from the inverse reaction. The neutron threshold for $^3H(\alpha, n_1)^6Li^*$ is approximately 16.3 MeV. Our data were normalized to the inverse reaction data (see Figure 29) in the 11.0 to 12.4 MeV region. The shape and normalization were consistent to about 5%. This normalization was then used to convert our data to cross sections at the higher energies.

To obtain the $^3H(\alpha, n_1)^6Li^*$ cross sections a smooth background, representing the ground state neutron contribution, was subtracted from the data. The remainder was attributed to the contribution of the $^3H(\alpha, n_1)^6Li^*$ reaction.

The method of reduction assumes a neutron detection efficiency which is constant over the range 11 to 18 MeV. Using this normalization for the first excited state neutrons is quite reasonable since they have approximately the same energy range as the ground state neutrons from 11.0 to 12.4 MeV. The problem lies in the normalization of the ground state neutrons at the higher energies. The difference in the excitation curves, obtained with the two phosphor positions, shows that this normalization is possibly quite inaccurate. As a result, the accuracy of the total reaction cross section above 16.0 MeV is probably no better than ± 30%. The behavior of the ground state neutrons does seem to be smooth in this region, however, and thus, when separated from the background, the contribution from the first excited state neutrons may be expected to have somewhat better accuracy.

D. The Elastic Scattering $^4\text{He}(^3\text{He}, ^3\text{He})^4\text{He}$

(1) Apparatus

(a) Chamber

In this experiment, a ^4He gas target was contained in the gas scattering chamber described by Bacher (1967). To provide better angular resolution the slits in the moving counter telescope were replaced by a similar set with approximately one-half the width (see Table 1 for slit parameters). Beam collimation, charge collection, and the pumping system were not changed except for the addition of a liquid nitrogen trapped diffusion pump on the Faraday cup.

(b) Electronics

As in the $T(\alpha, \alpha)T$ experiment, a two-counter $\frac{dE}{dx}$, E telescope was used to detect the scattered particles. The same charge integrator was also used (see Appendix A).

(c) Target and Beam Below 14.8 MeV

In the range of ^3He bombarding energies between 4.6 and 14.8 MeV the neutral beam injector was used with the CIT tandem to produce a doubly charged ^3He beam. Beams of approximately 200 n A. were obtained on target. The beam entrance was sealed with a $1000\,\overset{\text{o}}{\text{A}}$ Nickel foil and the entire chamber was filled with ^4He gas. A pressure of approximately 13 cm. of oil on the oil manometer was maintained.

(d) Target and Beam from 14.8 to 18.0 MeV

In this range of bombarding energies we were no longer able to attain the desired energy using neutral beam injection. Here, the negative ion source was used to produce a beam of negative ^{3}He ions. These were then stripped to doubly charged positive ions at the center terminal of the tandem. This produced a doubly charged beam with three times the terminal voltage. After focusing, magnetic analysis and collimation, beams of 5 - 15 nano Amps. were obtained on target. Beams of this current range used with the low energy target configuration greatly increase the length of time needed to take the desired data. Therefore, the 1000 $\overset{o}{A}$ nickel foil was removed and the ^{4}He target gas was contained in a small gas cell at the center of the chamber. The cell (see Figure 32) was inserted through the top of the chamber and was fitted with connections to a gas handling system and to a Wallace and Tiernan differential pressure gauge (0 - 800 mm. of Hg.). The thicker foil windows on the gas cell enabled us to use a target pressure of 15 cm. of Hg. The scattered particle exit window was of 1/6 mil Mylar and the beam entrance and exit windows were of 6250 $\overset{o}{A}$ nickel foils. Temperature was monitored by a thermometer which was in contact with the gas cell.

(2) Procedure

The general experimental procedures employed to gather the data are as follows. If the entire chamber is to be filled with ^{4}He, the chamber is sealed off, filled with the target gas and the outgassed charcoal trap is cooled with liquid nitrogen. If the gas cell is to be used, it is filled with target gas and the diffusion pump continues to pump on most of the chamber. Suppression and bias voltages are

applied to the Faraday cup and the electronics are checked for noise as the detectors are biased. The integrator is calibrated and the beam is maximized in the Faraday cup by magnetic focusing and deflection. The discriminators are then adjusted to give proper particle separation using the $\frac{dE}{dx}$ counter signal and a pulser. The gains of the electronics for each counter are equalized.

Spectra are then taken at each angle desired for a given energy. The live time of the analyzer, the clock time for the run and the time of day are recorded for each run. The temperature and pressure of the target gas are recorded at frequent intervals. At the end of the day the integrator is recalibrated to check on possible drifts.

(3) Results

A typical spectrum is shown in Figure 33. The first 200 channels contain a proton group from the reaction channel $^4\text{He}(^3\text{He, p})^6\text{Li}$ in channel 84, a proton group from $^4\text{He}(^3\text{He, p}^1)^6\text{Li}*$, in channel 38, and a broad deuteron group from $^4\text{He}(^3\text{He, d})^5\text{Li}$ below channel 45. The ^3He and ^4He groups are seen in the second 200 channels at channels 351 and 330. At forward angles the ^3He yield is much larger than the α yield while they are of more nearly equal size at the mid-range angles. The yields tend, in general, to drop off slowly with energy. The data reduction is discussed in Appendix B. The main portion of the data consists of angular distributions at ^3He bombarding energies from 4.6 to 18.0 MeV. ^3He and recoil ^4He groups give elastic scattering information at 14 center-of-mass angles below 14.8 MeV and at 10 center-of-mass angles from 14.8 to 18.0 MeV.

The data are presented as excitation curves with angular distributions shown below, at and above each resonance (see Figures 34 - 45). The numerical values of the differential cross sections are tabulated in Table 8. The figures show the data points as open circles. The solid lines are the fits obtained with the phase shift analysis. They will be discussed later. The elastic scattering data clearly show the known $\frac{7^-}{2}$ and $\frac{5^-}{2}$ levels found at excitation energies in ^{7}Be of 4.55 and 6.51 MeV, respectively. The $\frac{5^-}{2}$ level at 7.19 MeV in ^{7}Be is not seen in the elastic scattering data. It is seen, however, in the ^{4}He(^{3}He, p)^{6}Li data (see Figure 46). The broad resonance in the elastic scattering data at 13.25 MeV lab energy is a new level corresponding to an excitation energy of approximately 9.3 MeV in ^{7}Be. It is also clearly seen in the ^{4}He(^{3}He, p^1)^{6}Li* data (see Figure 50). The $\frac{3^-}{2}$ level seen by Harrison (1966), at 9.9 MeV in ^{7}Be is not seen in our data. Experimental errors in the data are presented in Appendix D and Table 11.

E. The Reaction ^{4}He(^{3}He, p)^{6}Li

(1) Apparatus

The apparatus used in this experiment was the same as that used for the elastic scattering.

(2) Procedure

The procedure was essentially the same as that used for the elastic scattering measurements. Below 14.8 MeV, the only changes were the use of 30 cm. of pressure on the oil manometer and the taking of data at more laboratory angles and at closer energies. Above 14.8 MeV, data were taken at the same time as

for the elastic scattering. Here too, more laboratory angles were covered.

(3) Results

The data obtained are tabulated in Table 10. Data were obtained at 5 laboratory angles for most energies; these data form excitation curves. At several energies, more laboratory angles were used. These additional data allowed the formation of angular distributions. The data were reduced in the same manner as the elastic scattering data (see Appendix B).

Two of the excitation curves are shown in Figure 46. They clearly show the resonance (near 9.5 MeV) due to the 7.19 MeV level in ^{7}Be. The 45° curve shows a weaker effect near the 9.3 MeV level in ^{7}Be. In this curve, the blackened circles are data taken with the low energy configuration. The open circles are data taken with the high energy gas cell. (In all figures for this reaction and the reaction $^4\text{He}(^3\text{He}, p_1)^6\text{Li*}$ the lines shown serve only to connect the points.) Figure 47 and part of Figure 48 show angular distributions of the ground state protons. Experimental errors are discussed in Appendix D and shown in Table 11.

F. The Reaction $^4\text{He}(^3\text{He}, p_1)^6\text{Li*}$

(1) Apparatus

The apparatus used in this experiment was the same as that used in the elastic scattering.

(2) Procedure

The data were taken at the same time and in the same manner as the ^{4}He(^{3}He, p)^{6}Li data.

(3) Results

The data obtained are tabulated in Table 10. Angular distributions of the first excited state protons are shown in part of Figure 48 and in Figure 49. Figure 50 shows two of the excitation curves obtained. Both show the effect of the 9.3 MeV level in ^{7}Be and they are similar to each other in shape. Experimental errors are discussed in Appendix D and shown in Table 11.

III. THEORETICAL ANALYSIS OF THE DATA

A. Introduction

The experimental data obtained in this work combined with data from other sources (to be discussed later) give a considerable amount of information on the compound nuclei ^{7}Be and ^{7}Li over a wide energy range. This analysis is primarily concerned with the two-body properties of the nuclear levels involving the following open channels: ^{4}He + ^{3}He, ^{6}Li + p, and ^{6}Li* + p[1] for ^{7}Be and ^{4}He + ^{3}H, ^{6}Li + n, and ^{6}Li* + n[1] for ^{7}Li.

The analysis is divided into two parts. In the first, the elastic scattering and reaction data for each compound nucleus are subjected to a phase shift analysis which separates the influence of the various partial waves in the scattering. This then determines the ℓ and J values pertinent to each of the levels seen.

In the second part, the R-matrix formalism described by Lane and Thomas (1958) is employed to express the nuclear phase shifts in terms of parameters such as the reduced widths for the open channels, excitation energies, and nuclear radii. The phase shifts derived from the first part are then fitted with these expressions. This determines a best value of these parameters for each level. These parameters may then be compared with predictions of nuclear models for these nuclei.

B. The Phase Shift Analysis

(1) Method

The first step in the analysis of the reduced data was the phase shift analysis of both the ^{7}Li and ^{7}Be results. Both cases

represent scattering of a spin 1/2 from a spin 0 particle. This greatly simplifies the analysis by allowing only one ℓ-value for a given value of the total angular momentum and the parity. The formula for the differential elastic scattering cross section is given as (Critchfield, 1949):

$$\frac{d\sigma(\theta)}{d\Omega} = |f_c|^2 + |f_i|^2 \tag{1}$$

where

$$f_c(\theta) = \frac{-\eta}{2k} \csc^2\left(\frac{\theta}{2}\right) \exp\left[i\eta \ln \csc^2\left(\frac{\theta}{2}\right)\right]$$

$$+ \frac{1}{k} \sum_{\ell=0}^{\infty} e^{2i\alpha_\ell} P_\ell(\cos\theta) \left[(\ell+1)e^{i\delta_\ell^+} \sin\delta_\ell^+ + \ell e^{i\delta_\ell^-} \sin\delta_\ell^-\right]$$

and

$$f_i(\theta) = \frac{1}{k} \sum_{\ell=1}^{\infty} e^{2i\alpha_\ell} \sin\theta \frac{dP_\ell(\cos\theta)}{d(\cos\theta)} \left[e^{i\delta_\ell^-} \sin\delta_\ell^- - e^{i\delta_\ell^+} \sin\delta_\ell^+\right]$$

In these expressions:

θ ≡ the center-of-mass scattering angle,

k ≡ the wave number,

η ≡ $Z_1 Z_2 e^2 / \hbar v$,

v ≡ the relative velocity of the two particles,

$\delta_\ell^\pm = \delta_{J\pi} = \delta_J^\pi$ ≡ the phase shift for $j = \ell \pm 1/2$, $\pi = (-1)^\ell$

α_ℓ ≡ $\sigma_\ell - \sigma_0$ where σ_ℓ is the Coulomb phase shift, and

Z_1 and Z_2 are the charges of the bombarding particle and the target nucleus.

The spin polarization of the scattered particles is given by:

$$\bar{P}(\theta) = \frac{-2\text{Im}\,(f_c f_i^*)}{|f_c|^2 + |f_i|^2}$$ in the direction of $(\bar{k}_{in} \times \bar{k}_{out})$ where $\bar{k}_{in}$ and

$\bar{k}_{out}$ are unit vectors in the direction of the incident and scattered beams.

In both ^{7}Be and ^{7}Li the treatment of the reaction channels involving ^{6}Li + a nucleon must be considered. This can be done by allowing the phase shifts to become complex. We have:

$$e^{2i\delta} \to \cos^2 X e^{2i\delta},$$

then $e^{i\delta} \sin\delta \to \cos^2 X e^{i\delta} \sin\delta + i\left(\frac{1 - \cos^2 X}{2}\right)$, and the total

reaction cross section is given by:

$$\sigma_R = \frac{\pi}{k^2} \sum_{\ell=0}^{\infty} [(2\ell + 1) - (\ell + 1)(\cos^4 X_\ell^+) - \ell \cos^4 X_\ell^-] \qquad (2)$$

In our analysis, the real and imaginary part of the phase shifts from $\ell = 0$ to $\ell = 4$ were allowed to vary. This gives a total of 18 parameters, although these were not all varied at one time. The data were grouped into angular distributions at the various energies of the excitation curves. A program was written to fit the data of each angular distribution with a set of phase shifts from equation (1) (see Appendix E) by minimizing the quantity

$$\chi^2 = \frac{1}{N_\theta} \sum_{i=1}^{N_\theta} \left(\frac{\frac{d\sigma}{d\Omega}(\theta_i)_{exp} - \frac{d\sigma}{d\Omega}(\theta_i)_{calc}}{V(\theta_i)} \right)^2$$

Here N_θ is the number of data points in the angular distribution and $V(\theta_i)$ is the experimental error associated with each point.

No states of $l = 4$ have been found in ^{7}Li or ^{7}Be; therefore, these phase shifts were not varied during the analysis. Upon completion of the analysis with phase shifts through $l = 3$, the $l = 4$ phase shifts were allowed to vary. Their variation from 0° was very small ($\pm 2^\circ$), and we therefore felt justified in not considering them further.

(2) The Analysis of the ^{7}Be Data

The phase shift analysis of ^{4}He(^{3}He, ^{3}He)^{4}He has been done from 2.5 to 5.7 MeV bombarding energy by Barnard (1964) and from 5.75 to 12.0 MeV by Tombrello and Parker (1963). Because the splitting of the p-waves of Tombrello and Parker differs in sign from those of Barnard, we obtained data and performed the analysis over both these lower regions. The results could then be accurately extrapolated into the region above 12.0 MeV as trial phase shifts.

Below the first proton threshold at 7.0 MeV all values of $X_{J\pi}$ were held to zero and the real parts of the s, p, d, and f wave phase shifts were allowed to vary. The initial values of the phase shifts were determined from Barnard's data. The general procedure was to then use the computer program to search for a set of phase shifts for which only one would be resonant at the anomaly in the elastic scattering data. The selection of the $f_{7/2}^-$ phase shift was quickly accomplished, both by supplying trial phase shifts

with a step in $\delta_{7/2}^{-}$ and by letting the program generate phase shifts at an energy using the phase shifts at the next lower energy as starting values. Several orders of phase shift variation were tried with essentially the same result. The p and s wave phases were the most sensitive to the order of variation. Changing the order caused changes of $\pm 5^{O}$ in the s and p waves. The phase shifts finally selected were those for which the variation with energy was smooth and the χ^2's were low.

Above 7 MeV bombarding energy the reaction channel $^4\mathrm{He}(^3\mathrm{He}, p)^6\mathrm{Li}$ is open. Data on the inverse reaction $^6\mathrm{Li}(p, ^3\mathrm{He})^4\mathrm{He}$ were available and we used that of McCray (1962) and Marion (1956) to calculate the values of $X_{J\pi}$ from the total reaction cross section. The analysis of McCray attributes the cross section to a $\frac{5^{-}}{2}$ resonance and an s-wave background. We found that the background was too large to be accounted for by only the s-wave phase shift. Therefore, we set $X_{1/2}^{+} = X_{3/2}^{+}$ and used the sum of both terms for the non-resonant part of the reaction cross section. This choice gave slightly better fits but essentially the same phase shifts as were obtained by using $X_{1/2}^{+}$ and $X_{3/2}^{-}$.

With the values of $X_{J\pi}$ fixed, the real phase shifts were then varied. The initial values were obtained by extrapolation from the lower region. The s, p, d, and f waves were varied and the appropriate resonant phase shift proved to be $\delta_{5/2}^{-}$. As in the work of Tombrello and Parker, the state at 7.18 MeV excitation energy was not seen in the elastic scattering data or in the values found for the real part of the phase shift. Once again, several orders of variation of the phase shifts were tried. The f-wave phase shifts were stable to $\pm 2^{O}$ and the s and p wave phase shifts to $\pm 5^{O}$ under the different variations. The solutions with good χ^2's also provided good energy continuity.

Above 11 MeV both the $^4\text{He}(^3\text{He}, \text{p})^6\text{Li}$ and the $^4\text{He}(^3\text{He}, \text{p}^1)^6\text{Li}^*$ channels are open. Our data on the first channel were used in conjunction with Marion's to calculate values of $X_{5/2}^-$, $X_{3/2}^+$, and $X_{1/2}^+$ from 11 to 18 MeV. Data on the second reaction channel were limited to what we had obtained. These data were used to form angular distributions at several energies near the resonance. Smooth curves were then drawn through the data points. Our data extended only to 120° in the center-of-mass system; hence we were required to extrapolate the data to 180° and to 0° to obtain total cross sections from these angular distributions. This was done by assuming symmetry about 90° and by smoothly extending the curve to 0°. The resulting curves were then numerically integrated to obtain the total cross section. These values(and the fact that the excitation curves for first excited state protons all had a similar shape) were then used to generate the total reaction cross section as a function of the energy. An estimate was then made separating the curve into a resonant portion and a non-resonant background. The resulting resonance was too large to attribute to any one resonant $X_{J\pi}$ except $X_{7/2}^-$. The background was attributed to $X_{3/2}^-$ because of the proximity of the state at 9. 8 MeV excitation energy seen by Harrison (1966). Using these values of $X_{J\pi}$ it was found that only a resonant $f_{7/2}^-$ phase shift would provide a fit low in χ^2 and continuous in energy. The features of the various phase shifts will be discussed in section (4).

(3) The Analysis of the ^7Li Data

The target in these experiments was the lighter particle. This required a higher bombarding energy to observe the same resonances. In the region of 3. 6 to 11 MeV bombarding energy,

there are no open reaction channels. This allowed us to set all the $X_{J\pi} = 0$ in this region. As trial phase shifts, we started with values from the ^{7}Be analysis taken below the first $\frac{7}{2}^-$ resonance. We then allowed the s, p, d, and f wave phase shifts to vary and used the values obtained at a given energy as trial values for the next energy. The program selected $\delta_{7/2}^-$ as the resonant phase shift for the lowest level. It also selected $\delta_{5/2}^-$ as the resonant phase shift for the broad second level. Several orders of variation of all the phase shifts were used to obtain smoothness in the phase shifts and low values of χ^2.

In the range from 10 to 11 MeV, some difficulty was encountered in obtaining good energy continuity in the $p_{1/2}$ and $f_{7/2}$ phase shifts. The $p_{3/2}$ and $f_{5/2}$ phase shifts were quite stable when different orders of variation were tried. These latter two phase shifts were finally fixed at their preferred values in this region and the other phase shifts were varied until a reasonably smooth set of phase shifts was obtained. Values of χ^2 were about 25% larger, in general, when the smooth set was used instead of a highly discontinuous set (i. e., jumps up to 30° in 250 keV for the $p_{1/2}$ phase shift).

The range of bombarding energies from 11 to 13 MeV was of particular interest. In analogy with the ^{7}Be data, we did not expect to see the 7.47 MeV level (corresponding to the 7.18 MeV level in ^{7}Be) in the elastic scattering. However, the effect of this level is apparent in the data as a small dispersion shape in the excitation curves.

The reaction channel ^{3}H(α, n)^{6}Li is open in this region. The inverse reaction has been investigated by Schwarz (1965), and his data (see Figure 29 and Table 7) were converted to our system

and used to generate values of $X_{J\pi}$. His analysis indicated that the main effect was due to the $\frac{5^-}{2}$ resonance, with the nonresonant background being due to s-wave scattering of channel spin 1/2. It was found that we could account for all of the background by the $X_{1/2}^+$ parameter. Therefore, we did not use the $X_{3/2}^+$ parameter as was done in ^{7}Be. Using the values obtained for $X_{1/2}^+$ and $X_{5/2}^-$, and extrapolating the real phase shifts from lower energy, we used the program to see if $\delta_{5/2}^-$ would indicate a resonance behavior. No fit was obtained if we insisted on a step-type behavior such as is seen in the two lower resonances. It was found that a dispersion curve in the $\frac{5^-}{2}$ phase shift gave the best fit. This result was similar to the high energy $\frac{7^-}{2}$ resonance in ^{7}Be. Attempts to fit the resonance with other phase shifts (such as $\delta_{7/2}^-$) did not succeed.

The presence of the resonance in ^{7}Be near 13.5 MeV indicated that an analogous effect might be observed in ^{7}Li. Because the high energy beam was used, not as many data points were taken at each energy. All of the excitation curves indicated a more pronounced effect than was seen in ^{7}Be, however.

Data on ^{3}H(α, n^1)^{6}Li*, other than our own, were not available. These data were decomposed into a smooth background and a resonance peak. From 13.5 to 18.7 MeV the data of Murray and Schmitt (1959) on the reaction ^{6}Li(n, α)^{3}H were used to determine values of $X_{1/2}^+$ and $X_{3/2}^+$. The background in this region was too large to be accounted for by $X_{1/2}^+$ alone. The resonance peak which we separated from our ^{3}H(α, n^1)^{6}Li* data was of such magnitude that it could only be accounted for by $X_{7/2}^-$. This was the same result as for ^{7}Be. The background ^{3}H(α, n^1)^{6}Li* contribution was attributed to the $X_{3/2}^-$ term.

Using these values of $X_{J\pi}$, the real phase shifts were varied. Below the second neutron threshold, the resulting phase shifts were continuous with the lower results. At 12.8 and 13.1 MeV bombarding energy, separate angular distributions were obtained using the high energy beam and the low energy beam, respectively. Their separate analyses gave similar results, even though somewhat different values of the background $X_{J\pi}$ were used for each.

Above threshold, the resonant real phase shift was found to be $\delta_{7/2}^{-}$, as in the ^{7}Be case. However, it was not possible to obtain a good fit and maintain smooth behavior with energy of the supposedly non-resonant phase shifts. A variation of the $X_{J\pi}$ was tried to accomplish this, but without success. The final values obtained for the phase shifts were a compromise between the best fit and the smoothest phase shifts, with good fit being the major consideration.

(4) Discussion of the Phase Shifts and Polarizations

The phase shifts for ^{4}He(^{3}He, ^{3}He)^{4}He are listed in Table 13 and shown in Figures 52 - 54. Phase shifts for ^{3}H(α, α)^{3}H are listed in Table 12 and shown in Figures 56 - 58. In both cases the various symbols represent values obtained from the phase shift program and the lines show fits to these data using the R-matrix formalism.

S-wave Phase Shifts

The s-wave phase shifts appear in Figures 52 and 56. The dashed lines are calculated hard sphere phase shifts for radii

2.8 Fermis (^{3}He + α) and 2.6 Fermis (t + α). There is a tendency in both cases for the phase shifts at higher energies to lie somewhat above the calculated curve. This effect has been noted previously in ^{4}He(^{3}He, ^{3}He)^{4}He by Barnard (1964) and by Tombrello and Parker (1963). McCray (1962) suggested a $\frac{1}{2}^+$ level which might account for this behavior. Such a level has not been seen in this work, however. The choices of $X_{J\pi}$ for the representation of the reaction cross section do have an effect and may account for the discrepancy.

<div align="center">P-wave Phase Shifts</div>

The $\frac{1}{2}^-$ phase shifts are shown in Figures 52 and 56. The $\frac{3}{2}^-$ phase shifts appear in Figures 53 and 57. With the exception of the f-wave phase shifts, these were the most difficult to determine. In the case of ^{4}He(^{3}He, ^{3}He)^{4}He opposite splittings of the p-wave phase shifts were found by Barnard and by Tombrello and Parker. We therefore wished to investigate the sign of the splitting and to determine if there was a point at which the splitting reversed in sign. Both signs of the splitting were tried and that with $\delta_{3/2}^- > \delta_{1/2}^-$ was preferred in both ^{3}H(α, α)^{3}H and ^{4}He(^{3}He, ^{3}He)^{4}He. This result for ^{7}Be is in agreement with that of Barnard.

From the values in the tables, it is seen that these phase shifts have a very slight splitting at some energies. An example occurs near 11.5 MeV bombarding energy for ^{4}He(^{3}He, ^{3}He)^{4}He. Solutions with the opposite splitting were carefully investigated near these points and were found to be poorer than the solutions used.

Above 16 MeV bombarding energy in ^{3}H(α, α)^{3}H, all the phase shifts, and the p-waves in particular are somewhat discontinuous with energy. This is an effect of the suggested $\frac{7}{2}^-$ level and probably reflects our lack of knowledge of the proper values of

$X_{J\pi}$ used to represent the reaction cross section. The general fluctuations of the p-waves elsewhere in both $^3H(\alpha, \alpha)^3H$ and $^4He(^3He, ^3He)^4He$ are probably due in part to the fact that they and the f-waves are the only negative parity terms used in the analysis. Thus the p-waves probably absorb a fair amount of any inaccuracies in the data which would tend to make the f-wave behavior less smooth.

D-wave Phase Shifts

There are no d-wave levels in this energy range. The d-wave phase shifts were allowed to vary, but remained small over the total energy range in both cases. They are shown in Figures 52 and 53 for $^4He(^3He, ^3He)^4He$ and in Figures 56 and 57 for $^3H(\alpha, \alpha)^3H$. Both the $\frac{5}{2}^+$ and $\frac{3}{2}^+$ phase shifts tend to remain near zero rather than decreasing at higher energy as for a hard sphere phase shift. The points which depart from a smooth line for these phase shifts occur near resonances and are still relatively small. These excursions probably are the result of inaccuracies in the data near the resonances.

F-wave Phase Shifts

The f-wave phase shifts for $^4He(^3He, ^3He)^4He$ appear in Figure 54 while these for $^3H(\alpha, \alpha)^3H$ are shown in Figure 58. The most obvious features are the sharp steps in the $\frac{7}{2}^-$ phase shifts. These show the second excited states in ^7Be and ^7Li, thus indicating a $\frac{7}{2}^-$ assignment for this level in ^7Li.

The broad step in the $\frac{5}{2}^-$ phase shifts indicates an assignment of $\frac{5}{2}^-$ for the level at 6.6 MeV in ^7Li and reconfirms the $\frac{5}{2}^-$ assignment of Tombrello and Parker (1963) for this level in ^7Be.

The upper $\frac{5}{2}^{-}$ level was not seen in the ^{4}He(^{3}He, ^{3}He)^{4}He real phase shifts. It is seen in the parameter $X_{5/2}^{-}$, however. This result is not surprising since this level is also not seen in the elastic scattering data. Tombrello and Parker (1963) were also unable to see its effect in the elastic scattering. Note that this level does appear as a dispersion shape curve in $\delta_{5/2}^{-}$ and as a peak in $X_{5/2}^{-}$ for ^{3}H(α, α)^{3}H. A similar behavior is seen in the elastic scattering.

The dispersion curve shape appears in the $\frac{7}{2}^{-}$ phase shift for the level at 13.5 MeV bombarding energy in ^{4}He(^{3}He, ^{3}He)^{4}He and for the level at 16.8 MeV bombarding energy for ^{3}H(α, α)^{3}H. The level in ^{7}Be is much broader than that in ^{7}Li. The $\frac{5}{2}^{-}$ phase shift is fairly smooth through the region of this resonance for ^{7}Be; however, in ^{7}Li it varies by about 30° from a smooth curve. This effect persisted in the phase shift analysis, despite efforts to eliminate it by adjusting other δ's or the $X_{J\pi}$'s. We have therefore concluded that it is probably due to our poor reaction data in this region. Another possibility is the presence of a nearby $\frac{3}{2}^{-}$ state analogous to that seen by Harrison (1966) in ^{7}Be. We have, however, no conclusive evidence on this possibility.

G-wave Phase Shifts

No levels of $\ell = 4$ have been found in either ^{7}Be or ^{7}Li. We did not vary these phase shifts during the analysis. At the conclusion of the analysis, we allowed them to vary and found that they remained small ($\leq \pm 2^{\circ}$). Consequently, we felt justified in having neglected them in the analysis.

The polarizations for the ^{3}He's and tritons were calculated from the derived phase shifts. The results are shown in

Figure 55 for ^{4}He(^{3}He, ^{3}He)^{4}He and in Figure 59 for ^{3}H(α, α)^{3}H. Polarization contours are shown vs. center-of-mass angle and bombarding energy. The effects of the lower $\frac{7^-}{2}$ and $\frac{5^-}{2}$ levels are seen in both figures. As in the elastic scattering the effect of the higher $\frac{5^-}{2}$ level is not seen in the ^{3}He polarizations while it is for the triton polarizations. The higher $\frac{7^-}{2}$ level is seen in both figures although it has a weaker effect for the ^{3}He's than the tritons. This agrees with the relative effects in the elastic scattering reactions.

Of particular interest are the long regions of high negative polarization near 90^0. These may be of use in polarization experiments as sources or analyzers of polarized particles.

C. Extraction of Level Parameters Using R-Matrix Theory

(1) Method

The elastic scattering and reaction cross sections for two particle interactions have been treated by Lane and Thomas (1958). This formalism connects the observed cross section for a reaction or elastic scattering with a set of internal wave functions of the compound nucleus.

Our phase shift analysis of the data provides the spins and parities of the states we have investigated in ^{7}Li and ^{7}Be. This knowledge and the Lane and Thomas formalism are used to determine excitation energies and some reduced widths for these states.

We will use the following definitions (from Lane and Thomas):

σ_{cc^1} ≡ the cross section for formation of a particle pair c^1 from the scattering of the particle pair c. The symbol c denotes all information concerning the quantum states of the two particles, their spins, channel spin and relative angular momentum.

U_{cc^1} ≡ the collision matrix for this interaction. $\sigma_{cc^1} \, \alpha \, |U_{cc^1}|^2$. U_{cc^1} is unitary and symmetric.

r_c ≡ the distance between centers of a particle pair c.

a_c ≡ the effective interaction distance between the centers of a particle pair c. For $r_c > a_c$ only Coulomb forces are active.

E_c ≡ the center-of-mass energy of motion of the particle pair c.

M_c ≡ the reduced mass of a particle pair c.

k_c ≡ the relative wave number of the particle pair c. Also given as $(2M_c|E_c|/\hbar^2)^{1/2}$.

v_c ≡ the relative velocity of the two particles.

η_c ≡ a Coulomb parameter given as $Z_{1c}Z_{2c}e^2/\hbar v_c$ where Z_{1c} and Z_{2c} are the two charges (in units of electronic charge) of the particles.

σ_c ≡ the Coulomb phase shift.

$$\rho_c \equiv k_c r_c$$

Our analysis is concerned with two levels (at most) of the same spin and parity. We also consider an elastic channel and a reaction channel. Wave functions external to the nuclear surface are taken as the Coulomb wave functions. The following notations will apply:

$I_{e\ell}$ ≡ the incoming Coulomb wave in the elastic channel for angular momentum ℓ.

$O_{e\ell}$ ≡ the outgoing Coulomb wave in the elastic channel for angular momentum ℓ.

$I_{r\ell}$ ≡ the incoming Coulomb wave in the reaction channel for angular momentum ℓ.

$O_{r\ell}$ ≡ the outgoing Coulomb wave in the reaction channel for angular momentum ℓ.

x_c ≡ the coefficient of the outgoing wave for a given channel.

y_c ≡ the coefficient of the incoming wave for a given channel.

The collision matrix U is then defined by:

$$x_{c1} = -\sum_c U_{c1 c} y_c$$

The R-matrix for our case has 4 components and is defined as:

$$
\underline{R} \equiv \begin{pmatrix} R_{ee} & R_{er} \\ R_{re} & R_{rr} \end{pmatrix} = \begin{bmatrix} \dfrac{\gamma_{1e}^{2}}{E_1 - E} + \dfrac{\gamma_{2e}^{2}}{E_2 - E} \; , & \dfrac{\gamma_{1e}\gamma_{1r}}{E_1 - E} + \dfrac{\gamma_{2e}\gamma_{2r}}{E_2 - E} \\[3mm] \dfrac{\gamma_{1e}\gamma_{1r}}{E_1 - E} + \dfrac{\gamma_{2e}\gamma_{2r}}{E_2 - E} \; , & \dfrac{\gamma_{1r}^{2}}{E_1 - E} + \dfrac{\gamma_{2r}^{2}}{E_2 - E} \end{bmatrix}
$$

Here r and e refer to the reaction and elastic channels. E_1 and E_2 are eigenenergies of the internal wave functions. E is the excitation energy of the nucleus. The γ's are the reduced width amplitudes of the levels. For example, γ_{1e}^{2} is the elastic reduced width of level 1. Note that $R_{er} = R_{re}$. The general form of the R-matrix considers all the eigenenergies of the internal wave functions and has the form

$$
R_{cc1} = \sum_{\lambda} \frac{\gamma_{\lambda c1}\, \gamma_{\lambda c}}{E_\lambda - E} \; ,
$$

but we are only concerned with two levels in our analysis. We now obtain from Lane and Thomas the general relation relating the R-matrix to the collision matrix. We have:

$$
V_r = R_{re}\,(D_e - B_e V_e) + R_{rr}\,(D_r - B_r V_r) \tag{1}
$$

$$
V_e = R_{ee}\,(D_e - B_e V_e) + R_{er}\,(D_r - B_r V_r) \tag{2}
$$

where
$$
V_c \equiv \left(\frac{\hbar^2}{2}\right)^{1/2} \left(\rho_c^{-1/2}\, O_{c\ell}\, x_c + \rho_c^{-1/2}\, I_{c\ell}\, y_c\right)
$$

and
$$
D_c \equiv \left(\frac{\hbar^2}{2}\right)^{1/2} \left(\rho_c^{1/2}\, O'_{c\ell}\, x_c + \rho_c^{+1/2}\, I'_{c\ell}\, y_c\right)
$$

The primes indicate differentiation with respect to ρ_c. B_e and B_r are boundary values (taken as real in this work) for the elastic and reaction channels and are proportional to the logarithmic derivative of the internal wave functions at the nuclear radius a_c.

Using the relation of the x's and y's to the collision matrix and the fact that $y_r = 0$ in our experiments, we can solve equations (1) and (2) for U_{ee}. We employ the following definitions:

$$L_c \equiv \left(\frac{\rho_c O'_{c\ell}}{O_{c\ell}}\right)_{r_c = a_c} = S_{c\ell} + iP_{c\ell} \text{ where } S_{c\ell} \text{ is the}$$

shift function and $P_{c\ell}$ is the penetration factor

$$\Omega_{c\ell} = \left(\frac{I_{c\ell}}{O_{c\ell}}\right)_{r_c = a_c}$$

The solution then becomes:

$$U_{ee} = \Omega^2_{e\ell}\left[\frac{(1 - R_{rr}[L_r - B_r])(1 - R_{ee}[L_e^* - B_e]) - R_{re}^2(L_e^* - B_e)(L_r - B_r)}{(1 - R_{rr}[L_r - B_r])(1 - R_{ee}[L_e - B_e]) - R_{re}^2(L_e - B_e)(L_r - B_r)}\right] = \frac{z}{w}$$

Now $\Omega^2_{e\ell} = e^{2i(\omega_{e\ell} - \varphi_{e\ell})}$ where $\omega_{e\ell}$ gives the Coulomb phase shift and $\varphi_{e\ell}$ gives the hard sphere phase shift. In our phase shift analysis we have separated the Coulomb phase shift. Therefore, we define $\Omega^2_{e\ell o} \equiv e^{-2i\varphi_{e\ell}}$ and $U_{eeo} \equiv \frac{\Omega^2_{e\ell o}}{\Omega^2_{e\ell}} U_{ee} = \cos^2 X_\ell e^{2i\delta_\ell}$,

where δ_ℓ and X_ℓ are real. These definitions then give:

$$\delta_\ell = -\varphi_{e\ell} + \arctan\left(\frac{\text{Im}(zw^*)}{\text{Re}(zw^*)}\right) \tag{3}$$

$$X_\ell = \arccos \left(|U_{eeo}|^{1/2} \right)$$

We thus wish to compare δ_ℓ and X_ℓ with the $\delta_{J\pi}$ and $X_{J\pi}$ from the phase shift analysis.

The relations are for a two-level problem with two open channels. If we take the limiting case of one channel (elastic) and one level, then only R_{ee} remains. R_{ee} is then given by $\gamma_e^2/(E_\lambda - E)$. The relation for U_{eeo} is then:

$$U_{eeo} = e^{-2i\varphi_{e\ell}} \left[\frac{1 - R_{ee}(L_e^* - B_e)}{1 - R_{ee}(L_e - B_e)} \right]$$

$$= e^{-2i\varphi_{e\ell}} \left[\frac{(1 - R_{ee}(L_e^* - B_e))^2}{|1 - R_{ee}(L_e - B_e)|} \right]$$

and

$$\delta_\ell = -\varphi_{e\ell} + \arctan \left[\frac{-R_{ee}[Im(L_e^*)]}{1 - R_{ee}[Re(L_e^*)] + R_{ee}B_e} \right]$$

$$= -\varphi_{e\ell} + \arctan \left[\frac{\gamma_e^2 P_{e\ell}}{E_\lambda - E - \gamma_e^2(S_{e\ell} - B_e)} \right]$$

$$= -\varphi_{e\ell} + \arctan \left[\frac{\gamma_e^2 P_{e\ell}}{E_\lambda + \Delta_\lambda - E} \right] \text{ where } \Delta_\lambda = -\gamma_e^2(S_{e\ell} - B_e)$$

(4)

A fit of phase shifts to this single level formula can be approached as a linear least-squares fitting problem using γ_e^2 and E_λ as variable parameters. This will be done in our analysis for the second and third excited states of ^{7}Li and ^{7}Be. The other levels are treated as double levels or as single levels with an open reaction channel.

(2) Extraction of the ^{7}Be Level Parameters

The second excited state of ^{7}Be ($\frac{7}{2}^-$) is well below the
threshold for ^{4}He(^{3}He, p)^{6}Li. Because of this, the single level
formula (with only an elastic scattering channel open) was used to
fit the $\frac{7}{2}^-$ phase shift near this level. As was mentioned before,
the problem can be approached as a linear-least squares fit for a
given radius. Several values of radius were tried and 4.0 Fermis
was chosen as a suitable value. Good fits were also obtained for
higher values of radius, but 4.0 Fermis was more consistent with
results for the other levels fitted in ^{7}Be. For lower radii, the
values of the eigenenergy and reduced width change very rapidly and
fall outside reasonable limits. The values obtained are shown in
Table 14 and the fits are shown in Figure 54.

The two $\frac{5}{2}^-$ levels forming the third and fourth excited
states in ^{7}Be have previously been analyzed as single levels because
of the small reaction width of the $^2F_{5/2}$ level and the small elastic
width of the $^4P_{5/2}$ level. In our analysis we used the single level
formula to fit the lower level and obtain an elastic reduced width and
eigenenergy. We then used the reduced widths as given in Ajzenberg
and Lauritsen (1965) for trial values for the higher state. The para-
meters obtained for the lower state from the single level formula and
the trial parameters for the upper state were then used in the double
level formula for both an elastic and reaction channel. The trial
parameters were found to give a good fit to the data. Variations
of the eigenenergy or reduced width for the lower state produced
poorer fits. Once again 4.0 Fermis was used as a radius for both
states and both channels. Other radii were tried but the fits were
not as good. With the eigenenergies and reduced widths fairly well

determined, the reaction width for the lower level was varied from the assumed value of 0.0. The values obtained for the various parameters are shown in Table 14 and the fits are shown in Figure 54.

The boundary values used in the fitting (B_e and B_r) were set equal to $-\ell$ (the relative angular momentum of the two particles for each channel). This is a choice which is often used in the literature. Another common choice is to choose values which make the level shift zero at the resonance energy. For a single level, with or without a reaction channel, the two choices will give the same fit by simply adjusting the eigenenergy. For the double level formula, this is no longer the case. For the two $\frac{5^-}{2}$ levels in ^{7}Be, it was found that the boundary value in the reaction channel still did not affect γ_e, using a radius of 4.0 Fermis. However, to obtain a good fit when the elastic channel boundary value was changed from $-\ell$, it was necessary to change the elastic reduced width of the upper level. For example, the use of the zero level shift boundary value required γ_e to be approximately 2.4 times as large as for the $-\ell$ case. The lower level was not appreciably affected. Some choices of boundary value and the best value of γ_e are shown in Figure 60. The central region of B_e in this figure indicates no fit for γ_e up to 0.5. No fit appeared likely for values as high as 0.6 in this region.

In the other computations involving these two levels, we raised the elastic width of the upper level until we could see it in the elastic phase shift. This sets an upper limit of $\gamma_e^2 = .09$ for the elastic width of the upper level.

The $\frac{7^-}{2}$ level at 9.3 MeV in ^{7}Be was first analyzed as a single level with a reaction channel and elastic channel open. A base line was determined from the $\frac{7^-}{2}$ phase shifts below resonance. This corresponded to 0° in the analysis. The reduced widths for elastic

scattering and for the reaction leading to $^6Li^* + p^1$ were varied as was the eigenenergy of the state. A best fit was obtained for several radii and 4.0 Fermis was again found to give the best results. Changing the boundary condition resulted only in a change in the best eigenenergy. The values obtained for the various parameters are shown in Table 14 and the fits are shown in Figure 54.

As a final step, we attempted to fit the two $\frac{7^-}{2}$ levels with the double-level formula. To obtain a similar fit, it was necessary to reduce the reaction width of the top level and increase the elastic width. Unfortunately, the phase shifts above the lower level drop off much like hard sphere phase shifts. At the energy of the upper level they were too low to give fits as good as the single level fits obtained previously.

(3) Extraction of the ^7Li Level Parameters

The extraction of the parameters for ^7Li was carried out in essentially the same manner as for ^7Be. The second excited state ($\frac{7^-}{2}$) is below the $^3H(\alpha,n)^6Li$ threshold and was treated as a single channel single level problem. Again, a best fit to the $\frac{7^-}{2}$ phase shift (for a given radius) was obtained. Here too, 4.0 Fermis was chosen as a suitable radius. The values of excitation energy and reduced width for this level are shown in Table 14 and the fit to the $\frac{7^-}{2}$ phase shift is shown in Figure 58.

The two $\frac{5^-}{2}$ levels forming the third and fourth excited states of ^7Li were analyzed as a double level. A single-level analysis of the broad lower level gave an eigenenergy and reduced elastic width. These and values of the reduced widths for the upper level (from Ajzenberg and Lauritsen, (1965)) were used as trial values in the double-level formula. From these starting values best

values of eigenenergies and reduced widths were found. Changing
the elastic reduced width and eigenenergy of the lower level produced
poorer fits. The radius chosen was again 4.0 Fermis. A variation
of the reaction width of the lower level was also tried. The values
obtained are shown in Table 14 and the fits to the $\frac{5^-}{2}$ phase shifts
are shown in Figure 58. The reduced α-width is in good agreement
with that obtained in the analysis of the $^6Li(n, \alpha)^3H$ data by Schwarz,
(1965). However, his nucleon width is ~30% higher than ours.

The boundary values used in the fitting were again taken
as $-\ell$. A variation of the reaction channel boundary value changed
only the eigenenergy as in the ^7Be case. A change in the elastic
channel boundary value required both an eigenenergy change and a
change in the value of the elastic reduced width for the upper level.
Some cases are shown in Figure 61. The behavior for central values
of B_e is similar to that for ^7Be.

As in the ^7Be case, the $\frac{7^-}{2}$ level near 9.7 MeV in ^7Li
was fitted using a single level with both an elastic and reaction channel.
It was difficult to determine from the phase shift analysis whether this
level was best represented by a dispersion-shape or step-shape in the
phase shift curve. Slightly better results were obtained with a dis-
persion-shape in the phase shift analysis, but the R-matrix formalism
gave a better fit using a step-shape. Once again 4.0 Fermis was
obtained as the best radius. The fit is shown in Figure 58 and the
values of the reduced widths are shown in Table 14. The vertical
dashed line shows the point in energy above which 180° has been
subtracted from the calculated phase shifts to compare them with
the values obtained in the phase shift analysis.

(4) Discussion of the Derived Level Parameters

The fitting of the s-wave phase shifts by hard sphere scattering phase shifts has been discussed in Part III B(4).

An attempt was made to determine the reduced widths of the ground state and first excited state in ^{7}Li and ^{7}Be by fitting the p-wave phase shifts. Reasonable fits were obtained at most radii used, but the values of the resonance parameters were not reasonable. Many of the reduced widths were negative and none predicted the proper location for the positions of the levels.

There are no known d-wave levels in the two nuclei and the d-wave phase shifts remain small and inactive in the analysis. Therefore, no attempt was made to fit these phase shifts with the R-matrix formalism.

Good fits to the second excited state ($\frac{7}{2}^-$) of both ^{7}Be and ^{7}Li were obtained with the single-level, single-channel R-matrix formalism. The reduced widths agree quite well between the nuclei. In addition, the use of the same radius as that used by Barnard (1964) (4.4 Fermis) yields a reduced width in agreement with his results to within the expected errors. The reduced widths for the states tend to increase fairly rapidly as the radius is decreased from 4.4 Fermis.

The elastic reduced widths of the lower $\frac{5}{2}^-$ level in both nuclei were also obtained using the single-channel, single-level formalism. Good fits were obtained except for the regions on the upper edge of the lower $\frac{5}{2}^-$ levels. Here the phase shifts calculated from the R-matrix formalism lie below those obtained from the phase shift analysis. This difficulty was not (as was previously hoped) resolved by analyzing the two $\frac{5}{2}^-$ levels in each nucleus with the two-channel, two-level R-matrix formalism. The nucleon

reduced widths of the lower $\frac{5^-}{2}$ levels were determined from the double-level formula and were quite small in both cases. The errors for these reduced width amplitudes are quite large, but the fits to the phase shifts indicate that they have a negative sign in both ^{7}Li and ^{7}Be. The agreement of the reduced widths of the lower $\frac{5^-}{2}$ levels between the nuclei is very good. However, for ^{7}Be the reduced width obtained for this level is considerably larger than the value obtained by Tombrello and Parker (1963), even when the difference in radii is considered. This difference may be a result of the difference of sign in the p-wave splitting between the two analyses.

The analysis of the $^4P_{5/2}$ levels was done with the double-channel, double-level formula in both nuclei. Good fits were obtained for ^{7}Be using values in agreement with those found in Ajzenberg, Lauritsen (1965). The fits obtained for ^{7}Li were a compromise between a good fit to the elastic phase shift and a good fit to the $X_{5/2}^-$ parameter. The values obtained are in agreement with those given in Ajzenberg, Lauritsen (1965). There is also good agreement between the two nuclei.

The level at 9.3 MeV in ^{7}Be ($\frac{7^-}{2}$) was analyzed as a two-channel, single-level problem. The fits are least accurate on the high side of the resonance. This may well be a result of the possible errors in the reaction data used to fix the values of $X_{7/2}^-$ for this level. The reduced width for ^{6}Li* + p^1 is seen to be much larger than that for ^{3}He + α. This feature is also apparent in the scattering data itself.

The decay of this level appears to proceed almost entirely by ^{6}Li* + p^1 as opposed to the channel ^{6}Li + p. Recent work by Christensen and Cocke (1966) has shown the presence of a

small f-wave admixture in the configuration of the 2.43 MeV state in ^{9}Be. The decay of the 9.3 MeV level in ^{7}Be also offers an opportunity to determine such an f-wave admixture. The predominant mode is ^{7}Be (9.3)→^{6}Li (2.184, 3+) + p by a p-wave decay. The decay of this level to ^{6}Li (g.s.) + p requires the ^{6}Li and p to be in a relative f-state of angular momentum. Thus the ratio of the reduced widths for these two channels is a measure of the relative f-wave admixture in the level. A small amount of yield in the ground state protons was attributable to the decay of the 9.3 MeV level. The effect was seen at three angles. These data were used to form angular distributions from which the total cross section was crudely determined. The ratio of $\gamma^2_{g.s.}/\gamma^2_{1st\ ex.} = \gamma^2_{f-wave}/\gamma^2_{p-wave}$ was determined by the relation $\sigma_{g.s.} P_1/\sigma_{1st\ ex.} P_3 = \gamma^2_{g.s.}/\gamma^2_{1st\ ex.}$ which applies at the resonance energy. P_ℓ gives the penetration factor for each decay. The value obtained for the ratio of reduced widths was $(16\ ^{+5}_{-10})\%$. The high errors reflect the small size of the effect and the small amount of data available. This figure represents a value of $(1.3\ ^{+0.4}_{-0.8})$ MeV for the ground state reduced width.

The upper $\frac{7}{2}^-$ level in ^{7}Li was treated in the same manner as the corresponding level in ^{7}Be. Although the phase shift analysis was not as satisfactory, the values of reduced widths agree fairly well between the two levels. From our data, it was not possible to obtain an estimate of the f-wave admixture in this level.

The fits to the phase shifts were found to be consistently best for a radius of 4.0 Fermis. For the first $\frac{7}{2}^-$ and first $\frac{5}{2}^-$ in both nuclei, a higher choice of radius gave a similar fit and required a smaller reduced width. For the $^4P_{5/2}$ levels, a larger radius

(4.4 Fermi) produced a poorer fit. For example, the parameters $X_{5/2}^-$ calculated for this level in ^{7}Be were too high below the level and too low above to fit the experimental parameters. The best results for the higher $\frac{7^-}{2}$ levels also required a radius of 4.0 Fermis.

The behavior of the reduced width as a function of boundary value was of considerable interest. Figures 60 and 61 show the value of the elastic reduced width amplitude (γ_e) as a function of the elastic boundary value B_e. The value of γ_e is that which best fits the phase shifts for that value of B_e. The regions of B_e near -1.6 are where the boundary value results in zero level shift. Note the region of very high γ_e between this region and B_e = -3.0 or $-\ell$. We used B_e = $-\ell$ in extracting the reduced widths.

The effect is similar in both nuclei and only occurs where the double-channel, double-level program is used. For a radius of 4.0 Fermis, changing the value of the inelastic boundary value had the effect of changing only the eigenenergies. At other radii (such as 4.4 Fermis) the inelastic boundary value also had a similar effect on the best value of γ_e.

IV. COMPARISON WITH NUCLEAR MODELS

A. Introduction

The development of more sophisticated nuclear models and the extension of experimental knowledge of nuclei have a reciprocal effect upon one another. The purpose of the model calculations is first to attempt to fit known experimental data with a number of parameters pertinent to the particular model. With these parameters determined, other quantities of interest may be calculated. These quantities can be compared with experiment or used to predict future experimental findings. Predictions of this sort then provide an incentive for the experimentalist to measure the quantities and thereby prove or disprove the model's predictions. These measurements provide, in turn, a basis for yet more complex models.

Our part in this process has been the determination of the excitation energies and reduced widths discussed previously and shown in Table 14. We now wish to compare (qualitatively, at least) these measurements with the predictions of some of the more recent nuclear models.

There are two major reasons for the qualitative nature of these comparisons. The first concerns the way in which the models are developed. It is customary to use, as a starting set of wave functions, those appropriate to a central potential such as an infinite depth harmonic oscillator potential well. The result is a series of bound levels. It has been pointed out that for low-lying levels of a nucleus, the difference between a finite and infinite depth makes only a small difference in the levels and wave functions. However, in our case, the models are used to predict properties

of the nucleus far above the threshold for two-particle breakup. It does not seem unreasonable that the predictions of the models in this region should differ quantitatively from the experimental values. In fact, the degree of qualitative agreement is surprisingly good.

The second reason for the qualitative comparison lies in the fact that the reduced widths for the various levels have not yet been calculated from the wave functions for the various configurations. The following discussion will compare our results with those of the cluster model, the rotational model and the shell model.

B. Model Comparisons

(1) The Cluster Model

Several calculations have been made in an attempt to treat ^{7}Li and ^{7}Be as two clusters of nucleons such as an α particle and a triton (Tang, 1961). A variational procedure is used with trial wave functions to determine an upper bound to the energies of various levels. The wave functions consist of an internal wave function for each cluster and a wave function describing the relative motion of the clusters. The potential used is a finite depth central potential taken between each pair of particles. In the paper mentioned above a spin-orbit potential is also considered. The calculations were done for the ^{2}P and ^{2}F levels in ^{7}Be and ^{7}Li which should be well represented by the α + mass 3 cluster scheme. The calculated energy levels agree fairly well with the first and second excited states. The ^{2}F$_{5/2}$ level is predicted at a lower level than is found experimentally (as is the case in most of the model calculations) although it had not been identified at the time of these calculations. In a later paper (Khanna, 1961), a ^{6}Li + n cluster calculation is made and an

approximate number is obtained for the position of the $^4P_{5/2}$ level. At the same time, it is shown that a positive parity level near 6. 5 MeV in ^{7}Li is unlikely.

The cluster model calculations are of interest for several reasons. They show that the grouping of the nucleons into these clusters is a reasonable approach to the problem. The number of parameters which are varied to obtain the energy levels is smaller than in the usual shell model calculations. Also an attempt is made to use two-body central forces (derived from nucleon-nucleon scattering) between individual particles instead of placing the p-shell nucleons in a common potential well.

There are also some disadvantages. The calculations are mainly limited to the lowest levels of ^{7}Li and ^{7}Be and are rather approximate in that a spin-orbit potential is not used in part of the work. Because of this and an approximate choice for some of the trial wave functions, the higher energy levels tend to disagree with the experimental values. In addition, the wave functions are suitable for bound states and hence do not provide information on the particle scattering. It would be interesting to have these calculations done for the continuum energy range allowing several configurations such as ^{6}Li + nucleon, ^{6}Li* + nucleon and α + mass 3.

(2) The Rotational Model

Consideration has also been given to the rotational model as a description for the light nuclei. In particular, Chesterfield and Spicer (1962) have made calculations for ^{7}Li (and ^{7}Be) using this model. The model calculates the energy for a number of configurations using a Nilsson model potential. These energies are calculated as functions of a deformation parameter ϵ which is a measure

of the non-sphericity of the harmonic oscillator well used in the potential. The energy minimum for each configuration is used to determine the best value of ϵ.

Each configuration is then used as a basis state for the formation of a rotational band. If the energy of a basis configuration is given by E_K^0 then the energy of the other levels of the band is given by:

$$E(I) = E_K^0 + A[I(I+1) + \delta_{K, 1/2}\, a(-1)^{I+1/2}(I+1/2)]$$

where $A = \hbar^2/2I_i$ (I_i is the nuclear moment of inertia), I is the total angular momentum of the nucleus, and a is a decoupling parameter defined by Nilsson (1955). K is the projection of I on the body z-axis. A is chosen to give a best fit to the data. Of the six bands considered in these calculations, three are of positive parity. Since no positive parity levels were found in this work, we will not consider them further. The band based on the $\frac{1}{2}^-$ level at .48 MeV seems to represent the ground state and first three excited states quite well. The second band based on a $\frac{3}{2}^-$ level at 5.62 MeV predicts the $^4P_{5/2}$ level and has a $\frac{7}{2}^-$ level near an energy appropriate to the position of the $^4D_{7/2}$ level. The $\frac{3}{2}^-$ state forming the basis for this band does not appear to exist and is thought to be a spurious representation of the ground state. The third band is based on a $\frac{1}{2}^-$ level which also has not been observed. A $\frac{3}{2}^-$ level in this band could represent the level seen by Harrison (1966) at 9.8 MeV in ^7Be. The other members of this band have not been identified. The calculated levels which fit our current level scheme are shown in Figure 62b.

This model reproduces the lowest five levels in ^7Li and ^7Be quite well (with the exception of the $\frac{3}{2}^-$ basis of the second band).

It also gives good agreement with experiment for the ground state electromagnetic moments, the de-excitation of the first excited state and the decay of ^{7}Be. The use of this model to calculate the f-wave nucleon decay of the $^4D_{7/2}$ level gives values of $\gamma^2_{f\text{-wave}}/\gamma^2_{p\text{-wave}}$ from .06 to .22 for values of ϵ from 0.4 to 0.8, respectively. The energy minimum for the band occurs at $\epsilon = 0.4$. The calculations are relatively uncomplicated and it is interesting to see them produce such satisfactory results.

The model has, of course, the problem of trying to represent a continuum situation with bound state wave functions. Thus the scattering of particles has not been considered, nor have reduced widths for various configurations for the levels been calculated. The basis states of the second and third bands are also a problem since they do not appear to exist. However, it appears that these levels can be eliminated from the predictions without changing the remainder of the calculations.

(3) The Shell Model

Most of the calculations for ^{7}Li and ^{7}Be have made use of the shell model. The model normally considers negative (normal) parity levels formed by a $(1s)^4(1p)^3$ configuration. Several surveys of the light nuclei (including ^{7}Be and ^{7}Li) have been made using the shell model (Inglis, 1953, Kurath, 1956). The most recent calculations are those of Barker (1966). We shall be primarily concerned with these calculations. The wave functions used are those of an infinite depth harmonic oscillator potential well.

The L-S coupling limit is used in forming the total wave function of the three 1p shell nucleons. A residual potential between each pair of p- shell nucleons is then assumed. The potential

contains a spin-orbit term, as well as space, spin, and charge exchange operators. The energy levels are then calculated and a best fit to the data is obtained by varying the parameters available. This determination of the various parameters then allows predictions of level positions and configurations to be made at higher energy.

The energy levels obtained by Barker are in good qualitative agreement with the schemes found by the earlier investigators mentioned at the beginning of the section. Data at higher energies have enabled him to extend his predictions with more accuracy than was possible before. These predictions for the energy level schemes for ^{7}Be and ^{7}Li are shown in Figure 62c. Also shown in Figure 62 are the rotational model predictions and the experimental results. The first four excited states of ^{7}Li and ^{7}Be show agreement in energy and configuration with experimental observations. We have identified our highest level with his $\frac{7^-}{2}$ level which consists mainly of the $^4D_{7/2}$ configuration. Our relative nucleon and α widths for this level are in good qualitative agreement with the predicted configuration. The energy level predicted for the $^4D_{7/2}$ level also fits our experimental data. The calculation predicts a $\frac{3^-}{2}$ level below the $\frac{7^-}{2}$ level, whereas the data on ^{7}Be from our work and that of Harrison (1966) show the $\frac{3^-}{2}$ level at a higher energy than the $\frac{7^-}{2}$ level.

The model calculations predict $\frac{1^-}{2}$, $T = \frac{1}{2}$ and $\frac{3^-}{2}$, $T = \frac{3}{2}$ for the 7th and 8th excited states. The $\frac{1^-}{2}$, $T = \frac{1}{2}$ level has not been seen, but the $\frac{3^-}{2}$, $T = \frac{3}{2}$ level of Harrison's work is in agreement with the predictions.

The predictions of this nuclear model appear to be quite good even though the problem is not considered in the continuum. Since the only configuration considered is $(1s)^4(1p)^3$, the problem of the occurrence or non-occurrence of the positive parity levels does

not come up. The ground state magnetic moment, log ft values for the ^{7}Be decay and the lifetime of the first excited state are also calculated and agree with the experimental values. Quantities such as the quadrupole moments depend sensitively on configuration mixing and since this was not considered, the calculated values do not give a good fit to the experimental values.

The models discussed all make fairly good predictions for the lower levels. It is to be expected that the more recent shell model calculations of Barker will give better high energy agreement. This results from a greater abundance of experimental data and also from a larger number of fitting parameters than were used in the rotational model. None of the models, however, has attempted to describe the various particle scattering processes. A description of this sort would certainly be of great interest.

V. CONCLUSIONS

The previous section has shown the good qualitative agreement between the predictions of nuclear models and the results of this work. It is also worthwhile to point out the high degree of agreement between the experimental results for the two nuclei. This is especially evident in the reduced widths for the various levels. The two $\frac{5}{2}^-$ levels show excellent agreement between the two nuclei and the agreement for the two $\frac{7}{2}^-$ levels is also quite good. It is particularly nice to see the close agreement as to the structure of the nucleus for these levels (that is, the relative widths for nucleon versus α emission). One would expect this sort of agreement in mirror nuclei and it is gratifying to see it verified experimentally.

The agreement of the non-resonant phase shifts between the two nuclei is also very good. The p-wave phase shifts in particular show the same sign for the splitting and the same energy behavior in both nuclei. In our work, however, we were unable to account for the behavior of the p-waves in terms of the influence of the ground and first excited states in ^{7}Li and ^{7}Be. Whether this behavior can be explained by high energy p-wave levels remains open to question.

The existence of positive parity states in the range of this work has been a question for some time. For example, a paper by Lane (1960) uses configurations $(1s)^4 (1p)^2 2s$, $(1s)^4 (1p)^2 1d$ and $(1s)^3 (1p)^4$ to predict many low-lying, positive parity levels. On the experimental side, the $^2F_{5/2}$ level in ^{7}Be was thought to be a $\frac{3}{2}^+$ level in some of the earlier work (e. g. , see Marion (1957)).

Earlier experiments on ^{7}Be (Barnard, 1964), (Tombrello, 1963) as well as this work have found no evidence for a positive parity level within the energy range investigated.

The work which has been described examines a large energy range for both ^{7}Li and ^{7}Be. While good agreement between the two nuclei and with the nuclear shell model has been shown, there are still several experimental and theoretical problems of interest.

In the R-matrix analysis, the calculated phase shifts have a general tendency to lie below those obtained from the data on the high energy side of a resonance. It does not appear that one can account for this by errors in the phase shift analysis since the effect has the same sign for all the resonances.

The behavior of the reduced widths as a function of the boundary value in the R-matrix analysis is also a matter of some concern (see Figures 59 and 60). These results indicate that in the double-level analysis, it is possible to fit the data with a range of γ_e's which vary by a factor greater than five. Although this problem did not occur for the single-level analyses, it is still rather disturbing and should be investigated further. Fortunately, most analyses of data are done using single-level formulas and are therefore safe from this trouble.

The subject of an f-wave admixture in the predominantly p-wave decay of the $^4D_{7/2}$ level in ^{7}Be is another matter of considerable interest. A better determination of the f-wave decay width for this level in both ^{7}Be and ^{7}Li is needed and will be attempted in the near future.

In analogy with the work of Harrison (1966), it would be of interest to investigate ^{7}Li using ^{6}Li + n as an entrance channel.

Plans are currently being made to conduct an investigation of this sort.

In general, one can say that our work on ^{7}Be and ^{7}Li has been quite rewarding, due to both the knowledge we have gained about the nuclei from our investigations and to the number of interesting side-tracks which it has suggested for future exploration.

APPENDIX A ELECTRONICS

(1) Beam Current Integration

The method of beam current integration was essentially the same in both experiments. Electric and magnetic suppression were used on a Faraday cup (see Figure 1) which collected the beam after passage through the gas target. The magnet was annular in form and the field was in the plane of the ring so that electrons from the chamber would be deflected and not allowed to reach the Faraday cup. Electric suppression was supplied by a 300 V. battery on the ^{3}H$(\alpha, \alpha)^3$H experiment and by a 300 V. bias supply in the ^{4}He$(^3$He, ^{3}He$)^4$He experiment.

The collected charge was fed through a BNC cable to an integrator of the type described by E. J. Rogers (1963) at Brookhaven. Our integrator was constructed by M. Dwarakanath. It was used in our experiments because of its high accuracy in measuring small currents. The error indicated by our calibrations was less than 0.5%. Calibration was accomplished by carefully measuring the voltage across a precision resistor through which current was fed to the integrator. A current was used which approximated the beam current to avoid inaccuracies due to leakage.

Basically, the integrator works in the following manner. The input current is applied to a Miller integrator circuit which produces an output from -0.0 to -10.0 Volts. When this negative output voltage exceeds -1.5 V., an amplitude discriminator gates a charge pump which delivers negative charge pulses of a precise magnitude to the integrator until the output falls below -1.5 V. The circuit is designed so that one charge pulse raises the integrator

output by 1 V. Hence the integrator output voltage will lie between -0.5 and -1.5 V. at the completion of an integration.

The charge pump delivers charge pulses at a 500 cps rate determined by a continuously running multivibrator. An external scalar then simply counts the number of charge pulses delivered by the charge pump, thus determining the total integrated charge. In our work, integrations of 5000 to 10,000 charge pulses were used to minimize inaccuracies due to neglecting a fraction of a pulse.

(2) Particle Detection and Charge Separation

In both experiments it was necessary to separate the charge 1 hydrogen isotopes from the charge 2 helium isotopes. To accomplish this a counter telescope was used. The telescope consisted of a thin (ΔE) counter and a thick (E) counter sandwiched together. The schematic diagram in Figure 5 shows the electronics configuration used in both experiments.

The ΔE counter was a thin, silicon surface-barrier transmission detector. Detectors used were 26μ or 39μ in thickness. The energy loss in the thin ΔE counter is roughly proportional to Z^2/v^2 where Z is the charge of the particle and v is its velocity. For particles of the same energy passing through the ΔE detector, the charge 1 particles will lose less energy than those of charge 2. A bias level was set in the spectrum from the ΔE counter to make the desired separation.

The E counter was a silicon surface-barrier or lithium-drifted detector of sufficient thickness to stop the particles. Detectors used ranged from 300μ to 3mm in thickness. The pulses from the counters were amplified by Tennelec preamplifiers

and then fed into a summing amplifier to obtain a total energy pulse. The signal from the ΔE preamplifier was split for use in the charge separation. A bias level "b" was set in this spectrum. If the pulse from this counter was greater than "b", then the particle was charge 2 and the sum of the pulses E and ΔE was routed to the second 200 channels of the 400-channel Radiation Instrument Development Laboratories multi-channel analyzer. If the pulse was less than "b", then the particle was charge 1 and the sum of the pulses was routed to the first 200 channels. In this way a separate spectrum is obtained for each charge.

The method works quite well down to the point where particles of both charges have the same energy and the charge 1 particles lose all their energy in the ΔE counter (about 1. 5 MeV for protons). This technique was especially valuable in the $^3H(\alpha, \alpha)^3H$ experiment where the tritons and α's were often very close in energy.

APPENDIX B DATA REDUCTION

Data obtained in the two elastic scattering experiments were very similar in form. The raw data consisted of spectra from the 400-channel analyzer. Figure 6 shows a typical spectrum for the ^{3}H$(\alpha, \alpha)^3$H experiment and Figure 33 shows a typical spectrum for the ^{4}He$(^3$He, ^{3}He$)^4$He experiment. For each of these spectra data on length of time required for the integration (clock time), length of live time on the 400-channel analyzer and the time of day were taken. The gas temperature and pressure were also noted at intervals of one half to one hour.

The next step was to obtain the yield of particles (Y) in each group by integrating the peaks observed in the spectra. A great amount of time was saved in this process by the use of a computer program written by Mr. Michael Mahon. The program uses the Burrough's 220 computer to display the spectra from the analyzer on a cathode ray tube. In Figure 7(a) we see a photograph of such a display. The data may be displayed on any desired vertical or horizontal scale. In particular, a logarithmic vertical scale was often used. In Figure 7(b), we see the use of a light pen to draw in a background under a peak. Figure 7(c) shows the spectrum after the peak has been integrated between two points flagged by the light pen and the background subtracted. The channel numbers of the horizontal integration limits are shown as well as the counts in each of these channels. Figure 7(d) shows the values of the total counts between the two channels; the counts in the background and the difference between the two. This process can be continued for all the groups in the spectrum allowing one to extract yields for all the groups in about one to two minutes per spectrum. The quantities

displayed on the screen are also printed out on tape by the computer.

The yields (Y) for each group are then converted to differential cross sections in the center-of-mass system by the relation

$$\frac{d\sigma(\theta_{cm})}{d\Omega} = \frac{Y(\frac{CT}{LT})(\frac{P_o}{P})(\frac{T}{T_o})(\frac{CM}{LAB})\sin\theta_{Lab}}{Q_m\,G_o\,N_o}$$

where: $\frac{d\sigma}{d\Omega}$ is the differential cross section in the center-of-mass system.

Y = the yield of counts in a group on a spectrum.

$\frac{CT}{LT}$ = the ratio of actual integration time (clock time) to the live time on the analyzer.

$\frac{P_o}{P}$ = the ratio of standard pressure 76.0 cm. of Hg to the gas pressure used in the target.

$\frac{T}{T_o}$ = the ratio of the target temperature to standard temperature (273.18°K.).

$\frac{CM}{LAB}$ = the ratio of the center-of-mass cross section to the laboratory cross section.

θ_{Lab} = the laboratory scattering angle.

θ_{cm} = the center-of-mass scattering angle.

Q_m = the number of incident particles.

N_o = the number of target nuclei per cubic centimeter at T_o and P_o.

G_o = A_r w/Rh where A_r is the area of the rear slit in the collimator, R is the distance from target center to the rear slit, h is the distance from front to rear slit, and w is the width of the front slit. This is essentially the target thickness at 90° in the laboratory multiplied by the solid angle subtended by the slit system.

This form for $G_o/\sin\theta_{Lab}$ is a first order approximation. A discussion of higher order terms is contained in the thesis by L. Senhouse (1964) and in articles by Breit, Thaxton and Eisenbud (1939) and by Silverstein (1959). See Figure 8 for a schematic of the geometry for G_o.

The following is a sample calculation for $\dfrac{d\sigma}{d\Omega}$ at E_{Lab} = 7.953 MeV, θ_{Lab} = 31.6° θ_{cm} = 54.7° in the $^4He(^3He, ^3He)^4He$ experiment.

$$\frac{d\sigma(54.7^\circ)}{d\Omega} = \frac{(5833)\ (\frac{1.82}{1.81})\ (\frac{76.0}{.8558})\ (\frac{297.1}{273.18})\ (.3774)(.52399)}{Q_m\ (4.842 \cdot 10^{-4})\ (2.687 \cdot 10^{19})}$$

$$= \frac{8.6144 \cdot 10^{-2}}{Q_m}$$

$$Q_m = T\ \frac{V}{R}\ \frac{1}{Q_p}$$

$$Q_m = \frac{14300}{60} \cdot \frac{1.3551}{15.121 \cdot 10^6} \cdot \frac{1}{(1.602 \cdot 10^{-19} \cdot 2.0)} = 9.035 \cdot 10^{13}$$

Where T is the time in seconds to complete an integration using a current determined by a voltage V across a resistance R. Q_p is the charge per beam particle in Coulombs. Thus

$$\frac{d\sigma(54.7^{\circ})}{d\Omega} = \frac{8.614 \cdot 10^{-12}}{6.666 \cdot 10^{13}} = 129.1 \cdot 10^{-27} \frac{cm^2}{sr} = 129.1 \frac{mb}{sr}$$

Calculations on the $^3H(\alpha, \alpha)^3H$ experiment are essentially the same. The only additional complication was in determining what fraction of the target gas was actually tritium, since the normal hydrogen contamination was of the order of 27%. To make this determination we made calibration runs using the reaction $^1H(\alpha, \alpha)^1H$ at 0.5 MeV steps at the same angles as the $^3H(\alpha, \alpha)^3H$ data. The values of $\frac{d\sigma}{d\Omega}$ were computed as above. The proton groups in the $^3H(\alpha, \alpha)^3H$ data were then used to determine the same $\frac{d\sigma}{d\Omega}$ assuming that all the tritium was hydrogen. The ratio of these two $\frac{d\sigma}{d\Omega}$'s was then used as a measure of the hydrogen fraction in the tritium gas.

Data on $^4He(^3He, p)^6Li$ was also reduced in the same manner as that on $^4He(^3He, ^3He)^4He$.

Corrections were applied to the nominal beam energies to correct for the energy loss in gas cell foils and target gas. These values were calculated from the stopping cross sections of Demirlioglu (1962) using our data on pressure and foil thickness. In the case of the $^3H(\alpha, \alpha)^3H$ data the beam entrance foil was found to be considerably thicker (approximately 30%) than its nominal thickness. The thickness used in the energy corrections was determined by forcing the positions of the narrow $\frac{7^-}{2}$ resonance near 5 MeV and the narrow $\frac{5^-}{2}$ resonance near 11.5 MeV to agree with the known positions of these levels in ^7Li. Values of the corrections for the several experimental configurations are shown in Table 2.

APPENDIX C

TRITIUM TARGET PREPARATION

Tritium, the mass 3 isotope of hydrogen, decays by β^- emission to ^{3}He. The end point energy of this decay is approximately 18 keV. An 18 keV electron is stopped in the windows of most of the common radiation monitoring devices. For this reason, special precautions and monitoring devices are used with tritium. As an isotope of hydrogen, this gas readily exchanges with any hydrogen in a material to which it may be exposed. We have attempted to minimize this exchange by using hydrogen-free materials in our gas handling systems.

Tritium was obtained in 2 cc STP lots (5 curies of radioactivity) from Oak Ridge. It arrives in a small glass vial and may or may not be mixed with a helium carrier (see Figure 4). To avoid dangerous leaks of tritium into the vacuum system or atmosphere we store it in our apparatus in the form of uranium tritide. At room temperature, properly prepared uranium acts as a good pump for hydrogen isotopes. The reservoir was constructed of stainless steel and silver soldered at the joints. A schematic diagram is shown in Figure 3. Electrical feed-throughs carry current to the nichrome wire coil which is used to heat the uranium tritide and evolve the tritium gas. Asbestos cloth electrically insulates the wires from the tube, and an outer cloth layer directs more heat to the tube. Glass wool keeps the uranium chips in the heated portion of the reservoir.

Uranium chips are cut from a rod on a lathe and cleaned with acetone. They are then deoxidized in a 30% solution of warm nitric acid, placed in the reservoir and heated to approximately

600° C with the heating coil while being pumped on with a liquid nitrogen trapped diffusion pump. When the uranium is thoroughly outgassed, it is cooled in a hydrogen atmosphere approximately 40 psi.). Reheating and cooling in this atmosphere is repeated several times, until approximately 40 atmospheric cubic centimeters are absorbed and evolved with each cooling and heating. Heating and cooling in H_2 causes the metal to powder and become porous, thus giving it a high effective surface area. Once this has been accomplished, the uranium is heated and pumped on while being agitated for approximately one day to evolve all the H_2 so as to avoid contaminating the tritium.

The prepared reservoir and gas vial are placed in a transfer manifold and the system is checked with a helium leak detector. A schematic of the transfer manifold is shown in Figure 4. The reservoir is opened to the manifold and leak checked. The manifold is then closed off from the leak detector and the internal pressure is monitored with a Hasting's vacuum gauge. Nuts holding the sylphon in an expanded position are backed off and the sylphon compresses. This allows the brass plunger to move in and break the neck on the vial. The tritium is quickly absorbed by the uranium in the reservoir. The valve to the reservoir is then shut off and the reservoir and valve removed from the manifold. The whole operation is carried out in the hot laboratory under a hood. An open ended ionization chamber (sniffer) is used to monitor the tritium level in the area. The tritium reservoir is then put in place on the chamber gas handling system.

APPENDIX D EXPERIMENTAL ERRORS

(1) Types of Errors

Errors in both the ^{3}H(α, α)^{3}H and ^{4}He(^{3}He, ^{3}He)^{4}He experiments were of two forms. Systematic errors are those involving inaccuracies in quantities related to the chambers and electronics. These errors are independent of the energy of the scattered particles. The second group of errors consist of relative errors such as those involved in subtracting background and statistics of counts in peaks. These errors are highly energy and angle dependent.

(2) Systematic Errors

(a) Target Particles

The error in the number of target particles per cubic centimeter depends on the accuracy of the pressure and temperature readings and on the partial pressure of the target gas. In the ^{4}He(^{3}He, ^{3}He)^{4}He experiment the target gas was not contaminated with other gases; however, in the ^{3}H(α, α)^{3}H experiment the hydrogen contamination of the tritium rose to approximately 27%. The estimated error in the target particle density from this cause is 3%. The error in determining the temperature and pressure on both experiments is estimated at less than .5% with the exception of the high energy ^{4}He(^{3}He, ^{3}He)^{4}He experiment where it is less than 1%.

(b) Incident Particles

The error in the charge collection is less than .5% as determined by integrator calibrations.

(c) Detector Geometry

The error due to approximating the differential cross section expression by the use of G_0 is estimated at less than .1% using the calculations of Senhouse (1964). The errors in the measurement of the quantities involved in $G_0 = \frac{A_r w}{Rh}$ give errors of less than .5% for $^4He(^3He, {}^3He)^4He$ and less than .25% for $^3H(\alpha, \alpha)^3H$. The only angular dependent parameter in the list of systematic errors is $\sin \theta_{Lab} \left(\frac{C.M.}{Lab} \right)$. The error in both experiments for θ_{Lab} is estimated at .1°. This leads to a maximum error in $\sin \theta_{Lab} \left(\frac{C.M.}{Lab} \right)$ of less than .8%.

(d) Resultant Systematic Errors

The resultant systematic error is then less than 3.2% for $^3H(\alpha, \alpha)^3H$ and less than 1.1% for $^4He(^3He, {}^3He)^4He$ below 14.8 MeV. For the high energy $^4He(^3He, {}^3He)^4He$ data, it is less than 1.5%.

(3) Relative Errors

(a) Sources of Relative Errors

The relative errors are those involving the differences between the individual spectra and the judgement of the experimenter in reducing the data. They arise primarily through the background subtractions and the statistics of the peaks.

(b) Relative Errors in the $^3H(\alpha, \alpha)^3H$ Experiment

In the $^3H(\alpha, \alpha)^3H$ experiment, these difficulties appeared in several ways. At the lower energies, the background of particles

scattered from the walls and foils of the gas cell became far larger than the group of particles we were trying to separate from it. This resulted in a poor background subtraction with the relative inconsistency between neighboring points being quite high. The effect is most pronounced at low energies and/or at forward angles, where the Rutherford cross section is greatest.

The error in the setting of the laboratory angle is significant only at forward angles where $\partial(\frac{d\sigma}{d\Omega})/\partial\theta$ is large. Maximum errors due to the term $\Delta\theta(\partial(\frac{d\sigma}{d\Omega})/\partial\theta)$ are approximately 1.5%. Over most of the angles and energies this error is less than 0.5%.

At the backward laboratory angles (mid-range center-of-mass angles) the recoil triton groups were quite difficult to distinguish clearly from the recoil proton contamination groups. This tended to provide poor background subtraction in this region, especially at the lower energies.

The statistics of the counts in the groups begin to become relatively important at some of the low points in the excitation curves. All four of these sources of relative error are combined for each center-of-mass angle in Table 5.

(c) Relative Errors in the $^4\mathrm{He}(^3\mathrm{He},\,^3\mathrm{He})^4\mathrm{He}$, $^4\mathrm{He}(^3\mathrm{He},\,p)^6\mathrm{Li}$ and $^4\mathrm{He}(^3\mathrm{He},\,p^1)^6\mathrm{Li}^*$ Experiments

The background in these experiments was, in general, less than on the $^3\mathrm{H}(\alpha,\,\alpha)^3\mathrm{H}$ experiment. This results from the lower target pressures and thinner foils used for the low energy data. At the most forward angles the $^3\mathrm{He}$'s are somewhat difficult to separate from the α particles in the spectra. The proton groups at the more

backward angles suffer from a lack of statistics and difficulties in separating the charge 1 particles from charge 2 at low energies. These errors are tabulated in Table 11.

(4) Beam Energy

The nominal energy of the beam from the tandem accelerator is accurate to approximately 20 keV. For the ^{3}He + α work below 14.8 MeV, this number is a fair estimate of the total beam energy inaccuracy. For the ^{3}He + α work at higher energies, the width of the resonances did not allow us to determine whether there was an inaccuracy in the nominal thickness of the entrance foil to the gas cell.

For the ^{3}H + α work, the entrance foil thickness for the gas cell was determined by positioning the low $\frac{7}{2}^-$ level and the $^4P_{5/2}$ levels as near as possible to their known energies. The discrepancy in indicated foil thicknesses was about 50 keV. It seems reasonable to take 25 keV as a probable error due to the foil. This gives a total r. m. s. error of 32 keV.

APPENDIX E COMPUTER PROGRAMS

(1) Phase Shift Analysis Program

A Fortran IV program for the IBM 7094 was written to fit the elastic scattering data with the phase parameters of equation (1) (page 21). The fit was obtained by seeking a minimum value of χ^2 where

$$\chi^2 \equiv \sum_{i=1}^{N_\theta} \left(\frac{\frac{d\sigma}{d\Omega}(\theta_i)_{exp} - \frac{d\sigma}{d\Omega}(\theta_i)_{calc.}}{V(\theta_i)} \right)^2 \frac{1}{N_\theta}$$

The program is divided into a main program and a subroutine. The function of the subroutine is to calculate the differential cross sections, polarizations, and χ^2 for an input set of phase shifts. The basic normal operation of the main program is as follows.

(a) Several data cards are read telling the program how many different energies, angles, and variations of phase shifts it is dealing with.

(b) The laboratory energy, charges, masses involved in the scattering, trial phase shifts, experimental cross sections, center-of-mass angles and estimated errors in cross sections are read in.

(c) From this information the required Legendre functions are generated and the Rutherford scattering amplitude is calculated.

(d) The main program then calls the subroutine which uses the trial phase shifts to calculate $\frac{d\sigma}{d\Omega}$, polarizations, and χ^2.

(e) The gradient of χ^2 with respect to those phase shifts being varied is then calculated, and a step in phase shifts is taken towards smaller χ^2 along this gradient vector. If the resulting values of $\frac{d\sigma}{d\Omega}$ do give a lower χ^2, the same procedure is repeated until a minimum is reached.

(f) The cross sections, polarizations, and χ^2 are then printed out and the program proceeds to the next energy. A listing is given at the end of this appendix (IBFTC DEL and IBFTC BEL).

The following list defines or gives the equivalent of non-obvious parameters used in the phase shift program.

KONG   -   an integer giving the total number of angular distributions being analyzed.

KING   -   an integer code telling the program how it is to obtain trial phase shifts for an angular distribution.

NUM   -   an integer giving the number of code word cards to be considered.

E   -   laboratory energy in MeV of incident particle.

ZI, ZT   -   charges of incident and target particles.

AI, AT   -   masses of incident and target particles in atomic mass units.

NDEL   - the number of phase shifts being considered.

MUT   - a meaningless parameter to allow program expansion.

NTH   - the number of points in the angular distribution.

DELT(I) - for I = 1-9, these are $\delta_{1/2}{}^{+}$, $\delta_{3/2}{}^{-}$, $\delta_{1/2}{}^{-}$, $\delta_{5/2}{}^{+}$, $\delta_{3/2}{}^{+}$, $\delta_{7/2}{}^{-}$, $\delta_{5/2}{}^{-}$, $\delta_{9/2}{}^{+}$, and $\delta_{7/2}{}^{+}$ in that order. For I = 10-18, DELT(I) gives the corresponding values of $X_{J\pi}$.

T(I)   - these are the values of the center-of-mass angles.

S(I)   - these are the experimental values of $d\sigma(\theta_i)/d\Omega$.

D(I)   - these are the percentage errors in $d\sigma(\theta_i)/d\Omega$.

FINC(I) - these are step sizes to be taken along the gradient of χ^2.

CAY   - k.

CHI   - χ^2.

SIGR   - the total reaction cross section σ_R.

SIG(I) - the calculated values of $d\sigma(\theta_i)/d\Omega$.

POL(I) - the polarization values for θ_i.

(2)   Below the reaction thresholds the $\ell = 3$ phase shifts obtained were fitted using a single level R-matrix expression. (See equation (4), page 37.) A simple program was written to perform a least-squares fit to the phase shifts at a number of different energies. If the interaction radius is held constant, the problem can be expressed as a simple linear least-squares fit. This program uses the sub-routine COOL to calculate the Coulomb functions and desired

combinations thereof, and then employs a standard least squares-fitting program to obtain the best values for the reduced width and eigenenergy at a given radius. A listing is given at the end of this appendix (IBFTC SIN).

(3)   The data above the reaction thresholds was fitted with the more complicated two-channel R-matrix formalism (equations (3), page 36). A program was written to calculate the values of the phase shifts given the reduced widths, eigenenergies, boundary values, and interaction radii. A listing is given at the end of this appendix (IBFTC RMA).

```
$IBFTC DEL      DECK
C       PHASE SHIFT ANALYSIS OF SPIN HALF PLUS SPIN ZERO
      ODIMENSION DELT(18),T(75),V(75),S(75),FINC(3),ICW(18,43),DEL(18),
      1POL(75),POL1(75),POL2(75),POL3(75),POL4(75),POLS(75),POLS1(75),
      2POLS2(75),POLS3(75),POLS4(75),RR(75),RI(75),DELTA(18),A(18),
      3SIG(75)        , D(75)
       DIMENSION  APLOT(95),SHIFT(80,18),ENERG(80)
      OCOMMON DELTA,DEL,DELT,T,V,S,FINC,SIG,CHI,POL,SIGR,POL1,POL2,
      1POL3,POL4,POLS,POLS1,POLS2,POLS3,POLS4,CAY,RR,RI,CA1,CA2,CA3,CA4,
      2SA1,SA2,SA3,SA4,ICW,NUM,NTH
       DATA   APLOT/ 95*1H /,STAR/1H*/,BLANK/1H /
       READ(5,57)  KONG
       JIT  =  1
       READ(5,40)KING,NUM
   40 FORMAT(2I5)
       IF (NUM) 4,4,2
    2 READ (5,105) ((ICW(I,J),I=1,18),J=1,NUM)
    4 READ(5,103)(T(I),V(I),S(I),I=1,35)
    1 READ (5,101) E,ZI,ZT,AI,AT,NDEL,MUT,JTH
      NTH  = JTH + 35
  101 FORMAT (F10.3,2F5.2,2F10.3/3I5)
   57 FORMAT(I5)
       IF (KING)58,58,59
   58 CONTINUE
       READ (5,102)(DELT(I),I=1,18)
  102 FORMAT(9F6.1/9F6.1)
   59 CONTINUE
       DO 1002 I=1,18
 1002 DEL(I)=DELT(I)/57.29578
       READ(5,103)(T(I),V(I),S(I),I=36 ,NTH)
  103 FORMAT(F10.2,F10.3,F10.5)
   56 CONTINUE
       READ (5,104)(FINC(I),I=1,3)
  104 FORMAT (3F5.2)
  105 FORMAT (18I4)
    3 ASP =SQRT(E/AI)
       CAY =0.06917*AI*AT*ASP/(AI+AT)
       ETA =0.15767*ZI*ZT/ASP
       BAY=ETA/(2.0*CAY)
       ALFA0=0.0
       ALFA1=ATAN(ETA)
       ALFA2=ALFA1+ATAN(ETA/2.0)
       ALFA3=ALFA2+ATAN(ETA/3.0)
       ALFA4=ALFA3+ATAN(ETA/4.0)
       CA1= COS(ALFA1*2.0)
       CA2= COS(ALFA2*2.0)
       CA3= COS(ALFA3*2.0)
       CA4= COS(ALFA4*2.0)
       SA1= SIN(ALFA1*2.0)
       SA2= SIN(ALFA2*2.0)
       SA3= SIN(ALFA3*2.0)
```

```
      SA4= SIN(ALFA4*2.0)
      DO 21 I=1,NTH
      RAD =T(I)/57.29578
      POL1(I) =COS(RAD)
      POL2(I) =0.5*(3.0*(POL1(I)**2) -1.0)
      POL3(I) = 0.5*(5.0*( POL1(I)**3) -3.0*POL1(I))
      POL4(I) =0.125*(35.0*(POL1(I)**4) -30.0*(POL1(I)**2)+3.0)
      POLS(I) =SIN(RAD)
      POLS1(I) =SIN(RAD)
      POLS2(I) = 3.0*POLS(I)*POL1(I)
      POLS3(I)=  7.5*POLS(I)*(POL1(I)**2) -1.5*POLS(I)
      POLS4(I)=  0.125*(140.0*POLS(I)*(POL1(I)**3)-60.0*POLS(I)*POL1(I))
      BIN=SIN(RAD/2.0)
      BAN =1.0/(BIN**2)
      BUN = ALOG(BAN)
      RR(I) = -BAY*BAN*COS(ETA*BUN)
   21 RI(I) =-BAY*BAN*SIN(ETA*BUN)
      CALL SNAG(-1,-1)
      IF (NUM) 15,15,6
    6 DO 14 IKE =1,NUM
      DO 13 JACK =1,3
  165 OCHI=CHI
      DO 7 I=1,18
    7 DELTA(I) =DEL(I)
      SUMP =0.0
      DO 9 K=1,18
      IF (ICW(K,IKE))9,9,8
    8 DEL(K) =DEL(K) +0.05/57.29578
      CALL SNAG(-1,K)
      A(K) =(OCHI-CHI)/0.05
      SUMP=SUMP +A(K)**2
      DEL(K) =DEL(K) -0.05/57.29578
    9 CONTINUE
      SUMPR=SQRT(SUMP)
      DO 11 K=1,18
      IF (ICW(K,IKE))11,11,10
   10 DEL(K) =DEL(K) + FINC(JACK)*A(K)/SUMPR
   11 CONTINUE
      CALL SNAG (-1,-1)
      IF (CHI -OCHI) 165,12,12
   12 DO 125 K=1,18
  125 DEL(K) =DELTA(K)
      CALL SNAG (1,-1)
   13 CONTINUE
   14 CONTINUE
      DO 1001 I=1,18
 1001 DELT(I) =DEL(I)*57.29578
   15 WRITE(6,111)
  111 FORMAT(30H1SPIGER, PHASE SHIFT ANALYSIS )
      WRITE(6,106)E
  106 FORMAT(//1X,F6.3//)
```

```
      WRITE (6,107)AI,ZI,AT,ZT
107 FORMAT(1X,F6.3,5X,F4.1,5X,F6.3,5X,F4.1//)
      DO  54 I=1,18
      WRITE (6,108)  DELT(I)
108 FORMAT (  3X,F8.3        )
      SHIFT(JIT,I)=  DELT(I)
      ENERG(JIT)  =  E
 54 CONTINUE
      WRITE (6,109) CHI, SIGR
109 FORMAT(//1X,E15.8//4X,F8.3//)
      WRITE(6,110) (T(I), V(I),S(I),SIG(I),POL(I),I=1,NTH)
110 FORMAT(1X,F6.2,5X,F5.2,5X,F9.3,5X,F9.3,5X,F9.6)
      PUNCH  102,  (DELT(I),I= 1,18)
      IF (KONG  -  JIT   ) 53,53,55
 55 CONTINUE
      JIT =JIT  +  1
      GO TO 1
 53 DO 52    I=1,18
      WRITE (6,45)
 45 FORMAT(17H1 DELTA VS E PLOT)
      DO 51 K=1,KONG
      APLOT(1)  = STAR
      IF( SHIFT(K,I))          42,43,43
 42 SHIFT(K,I)  =  SHIFT(K,I)    +  180.
 43 IPLOT  =SHIFT(K,I)*(.5)    +  1.
      APLOT(IPLOT)  = STAR
      WRITE (6,46)ENERG(K), SHIFT(K,I),      APLOT
 46 FORMAT(2X,F6.3,4X,F7.3,95A1//)
 51 APLOT(IPLOT)  =BLANK
 52 CONTINUE
      END
```

```
$IBFTC BEL        DECK
      SUBROUTINE SNAG (IT, JAG)
      ODIMENSION DELT(18),T(75),V(75),S(75),FINC(3),ICW(18,43),DEL(18),
     1POL(75),POL1(75),POL2(75),POL3(75),POL4(75),POLS(75),POLS1(75),
     2POLS2(75),POLS3(75),POLS4(75),RR(75),RI(75),DELTA(18),A(18),
     3SIG(75)       ,  D(75)
      OCOMMON DELTA,DEL,DELT,T,V,S,FINC,SIG,CHI,POL,SIGR,POL1,POL2,
     1POL3,POL4,POLS,POLS1,POLS2,POLS3,POLS4,CAY,RR,RI,CA1,CA2,CA3,CA4,
     2SA1,SA2,SA3,SA4,ICW,NUM,NTH
 1000 CONTINUE
      IF (JAG) 202,202,60
   60OGO TO (201,231,261,291,321,351,381,411,441,471,501,531,561,591,
     1621,651,681,711), JAG
  201 SSCO=SCO
      SSSO=SSO
  202 SSO=(SIN(DEL(1))**2)
      SCO=COS(DEL(1))*SIN(DEL(1))
      IF (JAG) 232,232,61
  203 SCO=SSCO
      SSO=SSSO
      GO TO 999
  231 SSC1=SC1
      SSS1=SS1
  232 SC1=(SA1*COS(DEL(2))+CA1*SIN(DEL(2)))*SIN(DEL(2))
      SS1=(CA1*COS(DEL(2))-SA1*SIN(DEL(2)))*SIN(DEL(2))
      IF (JAG) 262,262,61
  233 SC1=SSC1
      SS1=SSS1
      GO TO 999
  261 SSC2=SC2
      SSS2=SS2
  262 SC2=(SA1*COS(DEL(3))+CA1*SIN(DEL(3)))*SIN(DEL(3))
      SS2=(CA1*COS(DEL(3))-SA1*SIN(DEL(3)))*SIN(DEL(3))
      IF (JAG) 292,292,61
  263 SC2=SSC2
      SS2=SSS2
      GO TO 999
  291 SSC3=SC3
      SSS3=SS3
  292 SC3=(SA2*COS(DEL(4))+CA2*SIN(DEL(4)))*SIN(DEL(4))
      SS3=(CA2*COS(DEL(4))-SA2*SIN(DEL(4)))*SIN(DEL(4))
      IF (JAG) 322,322,61
  293 SC3=SSC3
      SS3=SSS3
      GO TO 999
  321 SSC4=SC4
      SSS4=SS4
  322 SC4=(SA2*COS(DEL(5))+CA2*SIN(DEL(5)))*SIN(DEL(5))
      SS4=(CA2*COS(DEL(5))-SA2*SIN(DEL(5)))*SIN(DEL(5))
      IF (JAG)352,352,61
  323 SC4=SSC4
      SS4=SSS4
```

```
          GO TO 999
351 SSC5=SC5
    SSS5=SS5
352 SC5=(SA3*COS(DEL(6))+CA3*SIN(DEL(6)))*SIN(DEL(6))
    SS5=(CA3*COS(DEL(6))-SA3*SIN(DEL(6)))*SIN(DEL(6))
    IF (JAG)   382,382,61
353 SC5=SSC5
    SS5=SSS5
    GO TO 999
381 SSC6=SC6
    SSS6=SS6
382 SC6=(SA3*COS(DEL(7))+CA3*SIN(DEL(7)))*SIN(DEL(7))
    SS6=(CA3*COS(DEL(7))-SA3*SIN(DEL(7)))*SIN(DEL(7))
    IF (JAG)   412,412,61
383 SC6=SSC6
    SS6=SSS6
    GO TO 999
411 SSC7=SC7
    SSS7=SS7
412 SC7=(SA4*COS(DEL(8))+CA4*SIN(DEL(8)))*SIN(DEL(8))
    SS7=(CA4*COS(DEL(8))-SA4*SIN(DEL(8)))*SIN(DEL(8))
    IF (JAG)   442,442,61
413 SC7=SSC7
    GO TO 999
441 SSC8=SC8
    SSS8=SS8
442 SC8=(SA4*COS(DEL(9))+CA4*SIN(DEL(9)))*SIN(DEL(9))
    SS8=(CA4*COS(DEL(9))-SA4*SIN(DEL(9)))*SIN(DEL(9))
    IF (JAG)    472,472,61
443 SC8=SSC8
    SS8=SSS8
    GO TO 999
471 SFIT0=FIT0
472 FIT0=(COS(DEL(10)))**2
    IF (JAG)    502,502,61
473 FIT0=SFIT0
    GO TO 999
501 SFIT1= FIT1
    SFIS1= FIS1
    SFIC1= FIC1
502 FIT1=(COS(DEL(11)))**2
    FIS1= FIT1*SA1
    FIC1= FIT1*CA1
    IF (JAG)    532,532,61
503 FIT1= SFIT1
    FIS1= SFIS1
    FIC1=SFIC1
    GO TO 999
531 SFIT2= FIT2
    SFIS2= FIS2
    SFIC2= FIC2
```

```
532 FIT2=(COS(DEL(12)))**2
    FIS2= FIT2*SA1
    FIC2= FIT2*CA1
    IF (JAG)    562,562,61
533 FIT2= SFIT2
    FIS2= SFIS2
    FIC2=SFIC2
    GO TO 999
561 SFIT3= FIT3
    SFIS3= FIS3
    SFIC3= FIC3
562 FIT3=(COS(DEL(13)))**2
    FIS3= FIT3*SA2
    FIC3= FIT3*CA2
    IF (JAG)    592,592,61
563 FIT3= SFIT3
    FIS3= SFIS3
    FIC3=SFIC3
    GO TO 999
591 SFIT4= FIT4
    SFIS4= FIS4
    SFIC4= FIC4
592 FIT4=(COS(DEL(14)))**2
    FIS4= FIT4*SA2
    FIC4= FIT4*CA2
    IF (JAG)    622,622,61
593 FIT4= SFIT4
    FIS4= SFIS4
    FIC4=SFIC4
    GO TO 999
621 SFIT5= FIT5
    SFIS5= FIS5
    SFIC5= FIC5
622 FIT5=(COS(DEL(15)))**2
    FIS5= FIT5*SA3
    FIC5= FIT5*CA3
    IF (JAG)    652,652,61
623 FIT5= SFIT5
    FIS5= SFIS5
    FIC5=SFIC5
    GO TO 999
651 SFIT6= FIT6
    SFIS6= FIS6
    SFIC6= FIC6
652 FIT6=(COS(DEL(16)))**2
    FIS6= FIT6*SA3
    FIC6= FIT6*CA3
    IF (JAG)    682,682,61
653 FIT6= SFIT6
    FIS6= SFIS6
```

```
      FIC6=SFIC6
      GO TO 999
  681 SFIT7= FIT7
      SFIS7= FIS7
      SFIC7= FIC7
  682 FIT7=(COS(DEL(17)))**2
      FIS7= FIT7*SA4
      FIC7=' FIT7*CA4
      IF (JAG)    712,712,61
  683 FIT7= SFIT7
      FIS7= SFIS7
      FIC7=SFIC7
      GO TO 999
  711 SFIT8= FIT8
      SFIS8= FIS8
      SFIC8= FIC8
  712 FIT8=(COS(DEL(18)))**2
      FIS8= FIT8*SA4
      FIC8= FIT8*CA4
      GO TO 61
  713 FIT8= SFIT8
      FIS8= SFIS8
      FIC8=SFIC8
      GO TO 999
   61 CHI = 0.0
      DO 998 I=1,NTH
      OFCOR= RR(I)+ ((FIT0*SC0)+ POL1(I)*(2.0*SS1*FIT1+ FIS1
     1-1.5*SA1 + 0.5*FIS2+FIT2*SS2) +(POL2(I))*(3.0*SS3*FIT3+1.5*FIS3
     2-2.5*SA2+ FIS4 +2.0*SS4*FIT4)+(POL3(I))*(4.0*SS5*FIT5+2.0*FIS5
     3-3.5*SA3 +1.5*FIS6+3.0*SS6*FIT6) + POL4(I)*(5.0*SS7*FIT7+2.5*FIS7
     4-4.5*SA4 +2.0*FIS8+4.0*SS8*FIT8))/CAY
      OFCOI=RI(I) +((FIT0*SS0+.5*(1.0-FIT0))+POL1(I)*(2.0*SC1*FIT1-FIC1
     1+1.5*CA1-0.5*FIC2+ SC2*FIT2) +POL2(I)*(3.0*SC3*FIT3 -1.5*FIC3
     2+2.5*CA2- FIC4 +2.0*SC4*FIT4) + POL3(I)*(4.0*SC5*FIT5 -2.0*FIC5
     3+3.5*CA3 -1.5*FIC6 +3.0*SC6*FIT6)+POL4(I)*(5.0*SC7*FIT7 -2.5*FIC7
     4+4.5*CA4 -2.0*FIC8 +4.0*SC8*FIT8))/CAY
      OFINR=(1.0/CAY)*(POLS1(I)*(SS2*FIT2 +0.5*FIS2 -0.5*FIS1
     1-SS1*FIT1) +POLS2(I)*(SS4*FIT4+.5*FIS4-0.5*FIS3-SS3*FIT3)
     2+POLS3(I)*(SS6*FIT6+0.5*FIS6-0.5*FIS5-SS5*FIT5)
     3+POLS4(I)*(SS8*FIT8+0.5*FIS8-0.5*FIS7-SS7*FIT7))
      OFINI=(1.0/CAY)*(POLS1(I)*(SC2*FIT2-0.5*FIC2+0.5*FIC1 -SC1*FIT1)
     1+POLS2(I)*(SC4*FIT4-0.5*FIC4+0.5*FIC3 -SC3*FIT3)
     2+POLS3(I)*(SC6*FIT6-0.5*FIC6+0.5*FIC5-SC5*FIT5)
     3+POLS4(I)*(SC8*FIT8-0.5*FIC8+0.5*FIC7-SC7*FIT7))
      SIG(I)=FCOR**2+FCOI**2+FINR**2+FINI**2
      GLOP = NTH
      CHI = CHI +(((S(I)-SIG(I))/(       V(I)))**2)/GLOP
      IF(NUM) 777,777,345
  345 IF (IT) 998,998,777
  777 POL(I) =-2.0*(FCOI*FINR -FCOR*FINI)/SIG(I)
      OSIGR    =(3.14159/(CAY*CAY))*((1.0-FIT0*FIT0)+(3.0-2.0*FIT1*FIT1
```

```
      1-FIT2*FIT2)+(5.0-3.0*FIT3*FIT3-2.0*FIT4*FIT4)+(7.0-4.0*FIT5*FIT5
     2-3.0*FIT6*FIT6)+(9.0-5.0*FIT7*FIT7-4.0*FIT8*FIT8))
 998 CONTINUE
 456 IF(JAG) 999,999,234
 2340GO TO (203,233,263,293,323,353,383,413,443,473,503,533,563,593,
     1623,653,683,713),JAG
 999 CONTINUE
     RETURN
     END
```

```
$IBFTC SIN     DECK
C     SINGLE LEVEL RESONANCE PARAMETERIZATION OF PHASE SHIFT
C     PROGRAM BY SPIGER
C     PROGRAM PERFORMS LEAST SQUARES FIT TO DATA
C     COULOMB WAVE PROGRAM COOL REQUIRED
      DOUBLE PRECISION  BET,ALP,ALPINV
         COMMON/ARR/C,D
      COMMON F, FP, G, GP, PHI, AS, P, S, SL, CP
      COMMON/LSQ/ X,CHI2, SIG,R, ITEST,IA,IALP,IALINV,ICOE,ICAL
      DIMENSION  CHUNK(100)
     ODIMENSION   ERR(100),DEL(100),DELPHI(100),B(100),        CALCU(100)
     1,FSR(100),CALCUD(100),H(100)
      DIMENSION X(100)
      DIMENSION A(100,25),Z(100),ERROR(100),WT(100),ALP(25,25),BET(25)
      DIMENSION ALPINV(25,25),COE(25),DELCO (25),CAL(100),DELCAL(100)
     ODIMENSION T(4),E(100),DELT(100) ,FS(100), FGSQ(100),
     1PEN(100),SH(100),SANDL(100),COF(100),DELTAR(100),DELTA(100),
     2    DIF(100),SHIFT(100)              ,ECM(100)
      DIMENSION C(90),D(90)
      EXTERNAL   ARRAY
      READ(5,1001) ND
 1001 FORMAT (I5)
      READ (5,101) ZI, ZT, AI, AT, L
  101 FORMAT (2F5.1,2F10.6/I5)
      IA=5
      IALP=5
      IALINV=5
      ICOE=5
      ICAL=5
  889 FORMAT (F10.4)
      DO 1  I=1,99
    1 X(I) =I
      WRITE(6,207)
  207  FORMAT(1H1)
      DO  199 I = 1, ND
      READ (5,888) E(I), DELT(I), ERR(I)
  199 CONTINUE
   17 READ (5,889) RD
      DO 200 I = 1, ND
  888 FORMAT(2F7.3,F7.3)
      ASP = SQRT(E(I)/AI)
      ETA     =    0.15767*ZI*ZT/ASP
      CAY=0.06917*AI*AT*ASP/(AI + AT)
      RO = (CAY  )*3.162278*RD
      ECM(I) = E(I)*(AT/(AI+AT))
      CALL COOL(ETA,RO,L)
      FS(I) = PHI
      FGSQ(I) = AS
      PEN(I) = P
      SH(I) = S
      SANDL(I) = SL
```

```
      COr(I) = CP
      DEL(I)  = DELT(I)/57.29578
      DELPHI(I) =DEL(I)  + FS(I)
      B(I) =1./TAN (DELPHI(I))
      FAT  = 1./(TAN(DELPHI(I) + ERR(I))   )
      CAT  = 1./(TAN(DELPHI(I) - ERR(I))   )
      ERROR(I) = ABS (FAT - CAT)
      C(I) =1./PEN(I)
      D(I)  = -ECM(I)/PEN(I)
      H(I) = (-SANDL(I))/PEN(I)
      Z(I) = B(I)   -   H(I)
        WRITE(6,209)ETA,RO,CAY
  209  FORMAT(1H 3E15.5)
        WRITE(6,210)FS(I),PEN(I),C(I),D(I),Z(I),H(I),B(I)
  210  FORMAT(1H 7E15.5)
  200 CONTINUE
      WT(1)   =   100.
    0 CALL LSTSQR(A,Z,ND,2,ERROR,WT,ALP,BET,ALPINV,COE,DELCO ,CAL,
    1 DELCAL,ARRAY)
      GAMSQ =1./COE(2)
      ELAM =GAMSQ*COE(1)
      DO 205 I=1,ND
      CALCU(I) = ATAN (1./(CAL(I)+H(I)))-FS(I)
      FSR(I) =  FS(I)*57.29578
      IF(CALCU(I)) 31,32,32
   31 CALCU(I) =CALCU(I) + 3.14159
   32 CONTINUE
      CALCUD(I) = CALCU(I)*57.29578
      WRITE(6,1000) E(I),ECM(I),DELT(I),CALCUD(I),FSR(I)
10000FORMAT(7H ELAB= F7.3,4X,5HECM= F7.3,4X,6HDEXP= F7.3,4X6HDCAL= F7.
   13,4X,6HHDSP= F7.3)
  205 CONTINUE
      WRITE (6,1002) ELAM,GAMSQ, RD, CHI2
10020FORMAT(7H ELAM= E14.7,5X,7HGAMSQ= E14.7,5X,8HRADIUS= E14.7,5X,6HCH
   1I2= E14.7)
      GO TO 17
      END
```

```
$IBFTC RMA      DECK
C      PROGRAM TO FIT A DOUBLE LEVEL PHASE SHIFT BY A 2 LEVEL R-MATRIX
C      THEORY. PROGRAMMER - SPIGER. PROGRAM REQUIRES COOL.
       COMMON F,FP,G,GP,PHI,AS,P,S,SL,CP
       REAL  KYEC    ,KYE
       OCOMPLEX        EL,ELSTAR,ELR,ELRSTR,OMEGAE,OMEGAR, FEE,FER,X,Y,U,
      1V,W,Z ,GUNK
       ODIMENSION E1SUB(50),E2SUB(50),GAM1E(50),GAM1R(50),GAM2E(50),
      1GAM2R(50)
       ODIMENSION EL(50),ELSTAR(50),ELR(50),ELRSTR(50),OMEGAE(50),
      1OMEGAR(50),FEE(50),UEE(50),X(50),Y(50),V(50),W(50),GUNK(50),
      2KYEC(50),DELTAC(50),E(50),EEX(50),DELTA(50),KYE(50),ICW(50),
      3DELTAR(50),DELTRC(50),FER(50)
       DIMENSION CAYE(50),ETAIN(50), ROIN(50), SCE(50),PENE(50),EN(50)
       DIMENSION ASPR(50), CAYR(50),ETAOUT(50),ROOUT(50),SCR(50),PENR(50)
       DIMENSION ASPE(50)
       READ (5,100) ZI,ZT,AI,AT,ZIO,ZTO,AIO,ATO
 100 FORMAT (2F5.2,2F10.5,2F5.2,2F10.5)
       OREAD (5,101) LIN,LOUT,BE,BR,RIN,ROUT,E1,E2,GAMEL1,GAMEL2,GAMR1,
      1GAMR2,NE,KING,QR,ED
 101 FORMAT (2I5/2F6.3/2F6.3/2F6.3/4F6.3/I5/I5/2F7.4)
       IF(KING)17,17,2
   2 READ (5,102) (ICW(I),I=1,10)
  17 CONTINUE
 102 FORMAT (10I4)
       WRITE(6,200)ZI,ZT,AI,AT
 200 FORMAT(5X,3HZI=F5.2,4X,3HZT=F5.2,4X,3HAI=F7.3,4X,3HAT=F7.3/)
       WRITE(6,201)ZIO,ZTO,AIO,ATO
 201 FORMAT(4X,4HZIO=F5.2,3X,4HZTO=F5.2,3X,4HAIO=F7.3,3X,4HATO=F7.3/)
       OWRITE(6,202)LIN,LOUT,BE,BR,RIN,ROUT,E1,E2,GAMEL1,GAMEL2,GAMR1,
      1GAMR2,QR,ED
2020FORMAT(5X,4HLIN=I5,4X,5HLOUT=I5/5X,3HBE=F6.3,4X,3HBR=F6.3/5X,4HRIN
      1=F6.3,4X,5HROUT=F6.3/5X,3HE1=F6.3,4X,3HE2=F6.3/5X,7HGAMEL1=F6.3,
      24X,7HGAMEL2=F6.3,4X,6HGAMR1=F6.3,4X,6HGAMR2=F6.3/5X,3HQR=F6.3,
      34X,3HED=F6.3)
   1 DO 3 I=1,NE
       READ (5,103) E(I),DELTA(I),KYE(I)
 103 FORMAT(3F10.4)
       DELTAR(I) = DELTA(I)/57.29578
       ASPE(I)=SQRT(E(I)/AI)
       CAYE(I) =0.06917*AI*AT*ASPE(I)/(AI + AT)
       ETAIN(I) =0.15767*ZI*ZT/ASPE(I)
       ROIN(I)  = CAYE(I)*RIN*3.162278
       CALL COOL (ETAIN(I),ROIN(I),LIN)
       SCE(I) = S
       PENE(I) = P
       EL(I) =CMPLX(SCE(I),PENE(I))
       ELSTAR(I)  = CONJG(EL(I))
      .FEE(I) =CMPLX(0.0,PHI)
       EN(I) = (E(I)*(AT/(AI +AT))-QR)/(ATO/(ATO +AIO))
       ASPR(I) = SQRT(ABS(EN(I)))/AIO
```

```
      CAYR(I)  = 0.06917*AIO*ATO*ASPR(I)/(AIO +ATO)
      ETAOUT(I) = 0.15767*ZIO*ZTO/ASPR(I)
      ROOUT(I) = CAYR(I)*ROUT*3.162278
      WRITE (6,304)  ETAOUT(I),ROOUT(I),LOUT
      IF (ZIO)  40,40,41
   41 IF  (EN(I)) 18,19,19
   18 PENR(I) =0.0
      PHI  =0.0
      FLOUT  = LOUT
      CSEE = SQRT((FLOUT+0.5)**2+2.*ROOUT(I)*ETAOUT(I)+ROOUT(I)**2)
      SCR(I)=-CSEE+0.5*(ROOUT(I)*ETAOUT(I)+(FLOUT+0.5)**2)/(CSEE*CSEE)
      GO TO 20
  304 FORMAT(2E15.8,I20)
   40 IF (EN(I))39,38,38
   39 PENR(I) = 0.0
      SCR(I) =-(1.0+ROOUT(I)+ROOUT(I)**2.0)/(1.0+ROOUT(I))
      GO TO 20
   38 PENR(I) = (ROOUT(I) **3.0)/(1.0+ROOUT(I)**2.0   )
      SCR(I) = -(1.0/(1.0+ROOUT(I)**2.0))
      GO TO   20
   19 CALL COOL(ETAOUT(I),ROOUT(I),LOUT)
      WRITE(6,303) S,P
  303 FORMAT(2E15.8)
      SCR(I)  = S
      PENR(I) = P
   20 ELR(I) =CMPLX(SCR(I),PENR(I))
      ELRSTR(I) = CONJG(ELR(I))
      FER(I)  =CMPLX(0.0,PHI)
      EEX(I)  = E(I)*(AT/(AI +AT)) +ED
      WRITE(6,203)E(I),DELTA(I),KYE(I),EL(I),ELSTAR(I),FEE(I)
 2030FORMAT(5X,5HE(I)=F7.3,4X,9HDELTA(I)=F7.3,4X,7HKYE(I)=F7.3/5X,6HEL(
     1I)=E15.8,4X,E15.8,4X,10HELSTAR(I)=E15.8,4X,E15.8/5X,7HFEE(I)=E15.8
     2,4X,E15.8)
      WRITE(6,204)EN(I),ELR(I),ELRSTR(I),FER(I),EEX(I)
 2040FORMAT(5X,6HEN(I)=F7.3/5X,7HELR(I)=E15.8,4X,E15.8,4X,10HELRSTR(I)=
     1E15.8,4X,E15.8/5X,7HFER(I)=E15.8,4X,E15.8/5X,7HEEX(I)=F7.3)
    3 CONTINUE
      READ(5,1202)   NE1,NE2,NGE1,NGE2,NGR1,NGR2
 1202 FORMAT(I5/I5/I5/I5/I5/I5)
      READ(5,1201)(E1SUB(I),I=1,NE1)
      READ(5,1201)(E2SUB(I),I=1,NE2)
      READ(5,1201)(GAM1E(I),I=1,NGE1)
      READ(5,1201)(GAM2E(I),I=1,NGE2)
      READ(5,1201)(GAM1R(I),I=1,NGR1)
      READ(5,1201)(GAM2R(I),I=1,NGR2   )
 1201 FORMAT(F6.3)
      DO 1300 IK=1,NE1
     ·E1=E1SUB(IK)
      DO 1301 J=1,NE2
      E2=E2SUB(J)
      DO 1302  K=1,NGE1
```

```
      GAMEL1=GAM1E(K)
      DO 1303  L=1,NGR1
      GAMR1=GAM1R(L)
      DO 1304   M=1,NGE2
      GAMEL2=GAM2E(M)
      DO 1305 N=1,NGR2
      GAMR2=GAM2R(N)
      WRITE(6,1505)E1,E2,GAMEL1,GAMEL2,GAMR1,GAMR2
15050FORMAT(5X,3HE1=F7.3,4X,3HE2=F7.3,4X,7HGAMEL1=F7.3,4X,7HGAMEL2=F7.3
     1 ,4X,6HGAMR1=F7.3,4X,6HGAMR2=F7.3)
      WRITE(6,1401)
14010FORMAT(3X,4HE(I),8X,8HDELTA(I),6X,9HDELTAC(I),5X,6HKYE(I),8X,
     17HKYEC(I),8X,3HREE,10X,3HRRE,10X,3HRRR)
      DO 4 I=1,NE
      REE= ((GAMEL1*GAMEL1)/(E1-EEX(I))) +(GAMEL2*GAMEL2/(E2-EEX(I)))
      RRE= (GAMEL1*GAMR1/(E1-EEX(I))) + (GAMEL2*GAMR2/(E2-EEX(I)))
      RRR=(GAMR1*GAMR1/(E1-EEX(I))) + (GAMR2*GAMR2/(E2-EEX(I)))
      X(I)=(1.0 - RRR*(ELR(I)-BR))
      Y(I)=(1.0 - REE*(ELSTAR(I) - BE))
      V(I) = EL(I) - BE
      W(I) = RRE*RRE*(ELR(I) - BR)
     OGUNK(I) = (X(I)*Y(I) - W(I)*CONJG(V(I)))/(X(I)*CONJG(Y(I)) - W(I)*
     1V(I))
      KYEC(I) =(ACOS(SQRT(CABS(GUNK(I)))))*57.29578
      HUNK = ATAN2 (AIMAG(GUNK(I)),REAL(GUNK(I)))
      IF (HUNK)34,35,35
   34 HUNK = HUNK +2.*3.14159
   35 CONTINUE
      DELTRC(I)   =-AIMAG(FEE(I))  + 0.5*HUNK
      DELTAC(I)        =57.29578*DELTRC(I)
      WRITE(6,1402)E(I),DELTA(I),DELTAC(I),KYE(I),KYEC(I), REE,RRE,RRR
 1402 FORMAT(F8.3,7X,F8.3,6X,F9.3,5X,E10.4,4X,E11.4,4X,3(E10.4,3X))
    4 CONTINUE
 1305 CONTINUE
 1304 CONTINUE
 1303 CONTINUE
 1302 CONTINUE
 1301 CONTINUE
 1300 CONTINUE
      END
```

REFERENCES

1. F. Ajzenberg-Selove and T. Lauritsen, Nucl. Phys. 78, 1 (1966).

2. A. D. Bacher, Ph. D. thesis, California Institute of Technology, in preparation (1967).

3. A. C. L. Barnard, C. M. Jones and G. C. Phillips, Nucl. Phys. 50, 629 (1964).

4. F. C. Barker, Nucl. Phys., to be published (1966).

5. G. Breit, H. M. Thaxton, and L. Eisenbud, Phys. Rev. 55, 1018 (1939).

6. C. M. Chesterfield and B. M. Spicer, Nucl. Phys. 41, 675 (1962).

7. P. R. Christensen and C. L. Cocke, Nucl. Phys., to be published (1966).

8. C. L. Critchfield and D. C. Dodder, Phys. Rev. 76, 602 (1949).

9. D. Demirlioglu and W. Whaling, unpublished, (1962).

10. W. D. Harrison, Ph. D. thesis, California Institute of Technology (1966).

11. D. R. Inglis, Rev. Mod. Phys. 25, 390 (1953).

12. F. C. Khanna, Y. C. Tang, and K. Wildermuth, Phys. Rev. 124, 515 (1961).

13. D. Kurath, Phys. Rev. 101, 216 (1956).

14. A. M. Lane and R. G. Thomas, Rev. Mod. Phys. 30, 257 (1958).

15. A. M. Lane, Rev. Mod. Phys. 32, 519 (1960).

16. J. B. Marion, G. Weber, and F. S. Mozer, Phys. Rev. 104, 1402 (1956).

17. J. B. Marion, Nucl. Phys. 4, 282 (1957).

18. J. A. McCray, Ph. D. thesis, California Institute of Technology (1962).

19. R. B. Murray and H. W. Schmitt, Phys. Rev. 115, 1707 (1959).

20. E. J. Rogers, Rev. Scientific Inst. 34, 660 (1963).

21. S. Schwarz, L. G. Strömberg and A. Bergström, Nucl. Phys. 63, 593 (1965).

22. L. S. Senhouse, Ph. D. thesis, California Institute of Technology (1964).

23. E. A. Silverstein, Nucl. Inst. and Meth. 4, 53 (1959).

24. Y. C. Tang, K. Wildermuth, and L. D. Pearlstein, Phys. Rev. 123, 548 (1961).

25. T. A. Tombrello and P. D. Parker, Phys. Rev. 130, 1112 (1963).

Table 1

Detection Geometry Parameters

This table lists the parameters pertinent to the solid angle subtended by the detectors and the target thickness seen by the detectors. Parameters are given for both the $^3H(\alpha, \alpha)^3H$ and $^4He(^3He, ^3He)^4He$ experiments. (Pages 7, 14, 61)

Table 1

Parameters on Slit Size and Positioning
Used to Calculate G_o

$$^3H(\alpha, \alpha)^3H \text{ Experiment}$$

Collimator 1: (Used to take data for $\theta_{Lab} \geq 55^o$)

Front Slit Width (w)	–	.1558 cm.
Rear Slit Width	–	.1577 cm.
Rear Slit Height	–	.7179 cm.
Rear Slit Area (A_r)	–	.1132 cm^2.
Distance from Front Slit to Rear Slit (h)	–	4.068 cm.
Distance from Center of Chamber to Rear Slit (R)	–	8.518 cm.
G_o	–	$5.090 \cdot 10^{-4}$ cm.

Collimator 2:

w	–	.1563 cm.
Rear Slit Width	–	.1559 cm.
Rear Slit Height	–	.7155 cm.
A_r	–	.1115 cm^2.
h	–	4.085 cm.
R	–	8.533 cm.
G_o	–	$5.000 \cdot 10^{-4}$ cm.

The half-angle seen by either collimator is 2.2^o.

Table 1 (cont.)

^{4}He(^{3}He, ^{3}He)^{4}He and ^{4}He(^{3}He, p)^{6}Li Experiments

w	-	.1533 cm.
Rear Slit Width	-	.1540 cm.
Rear Slit Height	-	.7157 cm.
A_r	-	.1102 cm^2.
h	-	4.074 cm.
R	-	8.567 cm.
G_o	-	$4.842 \cdot 10^{-4}$ cm.

The half-angle seen by this collimator is 2.2^O.

Table 2

Foil Energy Losses

This table shows the incident particle losses due to
passage of the beam through the various entrance foils to
the target gases. The nominal beam energies, energy losses
and corrected energies are shown for several values of nom-
inal beam energy. A smooth curve was drawn through these
points to obtain energy losses for other energies. (Page 62)

Table 2

Energy Loss of α Particles in Tritium Gas and
Entrance Foil (8125 $\overset{o}{A}$) for $^3H(\alpha,\alpha)^3H$ Experiment

Nominal Beam Energy (MeV)	Energy Loss (keV)	Corrected Beam Energy (MeV)
4.0	388	3.612
8.0	261	7.739
12.0	201	11.799
16.0	166	15.834
20.0	141	19.859

Energy Loss of ^{3}He Particles in Entrance Foil
(6250 $\overset{o}{A}$) and ^{4}He Gas of the High Energy Gas
Cell for the $^4He(^3He,^3He)^4He$ Experiment

7.5	208	7.292
9.0	184	8.816
10.5	165	10.335
12.0	151	11.849
13.5	136	13.364
15.0	128	14.872
16.5	121	16.379
18.0	111	17.889

Table 2 (cont.)

Energy Loss of ^{3}He Particles in Entrance Foil
(1000Å) and ^{4}He Gas of ^{4}He(^{3}He, p)^{6}Li Experiment

Nominal Beam Energy (MeV)	Energy Loss (keV)	Corrected Beam Energy (MeV)
6.0	102	5.898
9.0	74	8.926
12.0	57	11.943
15.0	49	14.951
18.0	43	17.957

Energy Loss of ^{3}He Particles in Entrance Foil
(1000Å) and ^{4}He Gas of ^{4}He(^{3}He, ^{3}He)^{4}He Experiment

6.0	58	5.942
9.0	43	8.957
12.0	34	11.966
15.0	29	14.971
18.0	26	17.974

Table 3

Data for the ^{3}H$(\alpha,\alpha)^3$H Experiment

This table shows the center-of-mass differential elastic cross sections (SIGMA), as a function of beam energy (LAB ENERGY). The energy range is from 4 to 13 MeV. The spaces marked by a series of asterisks are points for which data were not obtained. (Page 9)

TABLE 3

(TEXT 9 , FIGURE 9)
CENTER OF MASS ANGLE = 39.23

LAB ENERGY	SIGMA	LAB ENERGY	SIGMA
3.612	******	8.249	291.000
3.717	******	8.504	303.000
3.822	******	8.759	252.000
3.916	******	9.012	276.000
4.031	******	9.266	266.000
4.135	******	9.520	292.000
4.239	******	9.774	284.000
4.343	******	10.027	287.000
4.447	349.000	10.280	258.000
4.551	343.000	10.534	254.000
4.655	352.000	10.787	246.000
4.758	340.000	11.040	235.000
4.862	354.000	11.293	225.000
4.913	359.000	11.343	211.000
4.966	388.000	11.393	210.000
5.017	439.000	11.444	204.000
5.069	451.000	11.494	200.000
5.121	428.000	11.545	195.000
5.172	374.000	11.595	196.000
5.224	362.000	11.645	204.000
5.276	338.000	11.697	211.000
5.328	335.000	11.747	208.000
5.379	324.000	11.798	206.000
5.431	329.000	11.848	208.000
5.482	320.000	11.899	208.000
5.585	313.000	11.950	202.000
5.689	312.000	12.001	203.000
5.946	313.000	12.051	201.000
6.203	311.000	12.101	203.000
6.460	315.000	12.152	196.000
6.717	349.000	12.202	197.000
6.973	336.000	12.253	194.000
7.228	327.000	12.304	192.000
7.484	339.000	12.558	181.000
7.739	301.000	12.810	176.000
7.994	305.000	13.063	159.000

TABLE 3

(TEXT 9 , FIGURE 9)
CENTER OF MASS ANGLE =   46.99

LAB ENERGY	SIGMA	LAB ENERGY	SIGMA
3.612	*******	8.249	251.000
3.717	*******	8.5C4	248.000
3.822	*******	8.759	242.000
3.916	*******	9.012	233.000
4.031	*******	9.266	225.000
4.135	*******	9.520	205.000
4.239	*******	9.774	189.000
4.343	*******	10.027	171.000
4.447	333.000	10.280	164.000
4.551	338.000	10.534	151.000
4.655	340.000	10.787	144.000
4.758	325.000	11.040	134.000
4.862	329.000	11.293	154.000
4.913	346.000	11.343	156.000
4.966	334.000	11.393	156.000
5.017	320.000	11.444	154.000
5.069	261.000	11.494	153.000
5.121	224.000	11.545	155.000
5.172	211.000	11.595	153.000
5.224	226.000	11.645	148.000
5.276	227.000	11.697	132.000
5.328	233.000	11.747	142.000
5.379	233.000	11.798	144.000
5.431	248.000	11.848	144.000
5.482	240.000	11.899	145.000
5.585	257.000	11.950	144.000
5.689	258.000	12.001	141.000
5.946	264.000	12.051	*******
6.203	260.000	12.101	145.000
6.460	262.000	12.152	145.000
6.717	268.000	12.202	140.000
6.973	275.000	12.253	141.000
7.228	263.000	12.304	142.000
7.484	274.000	12.558	139.000
7.739	263.000	12.810	139.000
7.994	254.000	13.063	116.000

TABLE 3

(TEXT 9 , FIGURE 10)
CENTER OF MASS ANGLE = 54.73

LAB ENERGY	SIGMA	LAB ENERGY	SIGMA
3.612	144.000	8.249	155.000
3.717	165.000	8.504	160.000
3.822	175.000	8.759	137.000
3.916	154.000	9.012	132.000
4.031	178.000	9.266	104.000
4.135	188.000	9.520	84.100
4.239	184.000	9.774	60.300
4.343	188.000	10.027	53.300
4.447	193.000	10.280	57.100
4.551	214.000	10.534	57.400
4.655	214.000	10.787	65.300
4.758	220.000	11.040	75.000
4.862	233.000	11.293	79.200
4.913	229.000	11.343	81.200
4.966	212.000	11.393	83.400
5.017	165.000	11.444	88.000
5.069	77.300	11.494	90.400
5.121	57.500	11.545	92.000
5.172	84.500	11.595	86.600
5.224	107.000	11.645	71.800
5.276	122.000	11.697	68.700
5.328	139.000	11.747	68.600
5.379	142.000	11.798	70.500
5.431	147.000	11.848	74.000
5.482	146.000	11.899	73.300
5.585	162.000	11.950	76.000
5.689	173.000	12.001	74.000
5.946	170.000	12.051	74.500
6.203	159.000	12.101	75.700
6.460	166.000	12.152	78.300
6.717	185.000	12.202	79.900
6.973	164.000	12.253	76.900
7.228	183.000	12.304	80.400
7.484	164.000	12.558	83.600
7.739	175.000	12.810	81.500
7.994	157.000	13.063	83.200

TABLE 3

(TEXT 9 , FIGURE 10)
CENTER OF MASS ANGLE =   60.00

LAB ENERGY	SIGMA	LAB ENERGY	SIGMA
3.612	230.000	8.249	125.000
3.717	229.000	8.504	119.000
3.822	228.000	8.759	106.000
3.916	227.000	9.012	89.800
4.031	219.000	9.266	70.500
4.135	206.000	9.520	45.300
4.239	211.000	9.774	29.800
4.343	199.000	10.027	24.600
4.447	187.000	10.280	25.500
4.551	194.000	10.534	33.700
4.655	194.000	10.787	41.000
4.758	193.000	11.040	50.000
4.862	191.000	11.293	56.000
4.913	186.000	11.343	58.600
4.966	166.000	11.393	59.900
5.017	115.000	11.444	64.600
5.069	45.900	11.494	67.600
5.121	32.400	11.545	70.000
5.172	38.300	11.595	59.900
5.224	57.500	11.645	48.800
5.276	86.100	11.697	43.600
5.328	103.700	11.747	44.700
5.379	112.000	11.798	45.000
5.431	115.000	11.848	47.900
5.482	120.000	11.899	50.700
5.585	137.000	11.950	51.800
5.689	138.000	12.001	53.400
5.946	147.000	12.051	55.800
6.203	135.000	12.101	55.400
6.460	134.000	12.152	55.400
6.717	141.000	12.202	57.200
6.973	145.000	12.253	57.000
7.228	139.000	12.304	57.900
7.484	145.000	12.558	60.200
7.739	138.000	12.810	60.900
7.994	132.000	13.063	63.200

TABLE 3

(TEXT 9 , FIGURE 11)
CENTER OF MASS ANGLE = 63.43

LAB ENERGY	SIGMA	LAB ENERGY	SIGMA
3.612	149.000	8.249	120.000
3.717	164.000	8.504	107.000
3.822	165.000	8.759	97.600
3.916	154.000	9.012	77.100
4.031	157.000	9.266	53.700
4.135	163.000	9.520	33.700
4.239	155.000	9.774	18.800
4.343	160.000	10.027	15.200
4.447	155.000	10.280	17.600
4.551	155.000	10.534	26.200
4.655	166.000	10.787	34.000
4.758	186.000	11.040	43.900
4.862	178.000	11.293	51.500
4.913	171.000	11.343	55.200
4.966	142.000	11.393	56.700
5.017	94.100	11.444	60.100
5.069	27.600	11.494	63.500
5.121	10.100	11.545	61.100
5.172	25.200	11.595	49.400
5.224	47.800	11.645	38.500
5.276	69.800	11.697	37.400
5.328	79.600	11.747	38.800
5.379	90.700	11.798	40.300
5.431	101.000	11.848	42.500
5.482	100.000	11.899	47.700
5.585	110.000	11.950	46.000
5.689	116.000	12.001	47.000
5.946	126.000	12.051	48.200
6.203	132.000	12.101	48.400
6.460	*******	12.152	51.600
6.717	*******	12.202	51.600
6.973	*******	12.253	52.300
7.228	141.000	12.304	52.900
7.484	140.000	12.558	57.400
7.739	137.000	12.810	57.200
7.994	129.000	13.063	59.000

TABLE 3

(TEXT 9 , FIGURE 11)
CENTER OF MASS ANGLE = 64.97

LAB ENERGY	SIGMA	LAB ENERGY	SIGMA
3.612	122.000	8.249	100.000
3.717	143.000	8.504	97.100
3.822	146.000	8.759	80.700
3.916	149.000	9.012	61.900
4.031	144.000	9.266	44.300
4.135	132.000	9.520	27.200
4.239	141.000	9.774	14.200
4.343	150.000	10.027	12.600
4.447	148.000	10.280	14.600
4.551	152.000	10.534	21.700
4.655	149.000	10.787	27.300
4.758	153.000	11.040	34.000
4.862	152.000	11.293	39.900
4.913	151.000	11.343	40.500
4.966	126.000	11.393	42.800
5.017	72.900	11.444	44.500
5.069	23.500	11.494	47.000
5.121	10.600	11.545	46.800
5.172	33.000	11.595	38.100
5.224	49.200	11.645	29.400
5.276	65.300	11.697	26.700
5.328	75.900	11.747	28.500
5.379	81.200	11.798	30.400
5.431	90.800	11.848	31.800
5.482	90.100	11.899	33.000
5.585	103.000	11.950	34.700
5.689	105.000	12.001	35.300
5.946	112.000	12.051	36.300
6.203	112.000	12.101	37.800
6.460	115.000	12.152	37.900
6.717	112.000	12.202	37.600
6.973	113.000	12.253	39.200
7.228	114.000	12.304	39.300
7.484	108.000	12.558	40.900
7.739	106.000	12.810	42.300
7.994	103.000	13.063	43.800

TABLE 3

(TEXT 9 , FIGURE 12)
CENTER OF MASS ANGLE = 70.00

LAB ENERGY	SIGMA	LAB ENERGY	SIGMA
3.612	196.000	8.249	82.300
3.717	172.000	8.504	78.800
3.822	150.000	8.759	67.500
3.916	154.000	9.012	55.200
4.031	148.000	9.266	41.300
4.135	147.000	9.520	27.700
4.239	142.000	9.774	19.500
4.343	134.000	10.027	16.100
4.447	144.000	10.280	20.600
4.551	146.000	10.534	27.200
4.655	149.000	10.787	33.900
4.758	156.000	11.040	39.400
4.862	152.000	11.293	45.200
4.913	148.000	11.343	45.100
4.966	128.000	11.393	46.900
5.017	92.400	11.444	46.700
5.069	45.300	11.494	49.500
5.121	38.900	11.545	47.900
5.172	48.300	11.595	42.000
5.224	62.100	11.645	32.600
5.276	72.400	11.697	30.400
5.328	78.400	11.747	31.800
5.379	82.200	11.798	34.000
5.431	88.200	11.848	34.800
5.482	90.400	11.899	37.800
5.585	95.400	11.950	39.000
5.689	97.100	12.001	40.000
5.946	98.600	12.051	41.400
6.203	102.000	12.101	42.300
6.460	101.000	12.152	43.600
6.717	100.000	12.202	44.200
6.973	100.000	12.253	44.700
7.228	97.400	12.304	44.700
7.484	95.500	12.558	46.200
7.739	94.400	12.810	47.800
7.994	88.900	13.063	48.900

TABLE 3

(TEXT 9, FIGURE 12)
CENTER OF MASS ANGLE = 75.95

LAB ENERGY	SIGMA	LAB ENERGY	SIGMA
3.612	******	8.249	68.100
3.717	******	8.504	64.500
3.822	******	8.759	59.200
3.916	******	9.012	50.500
4.031	******	9.266	44.600
4.135	94.400	9.520	37.500
4.239	101.000	9.774	33.000
4.343	94.300	10.027	32.000
4.447	103.000	10.280	33.500
4.551	96.600	10.534	36.600
4.655	99.400	10.787	40.900
4.758	103.000	11.040	41.900
4.862	104.000	11.293	44.400
4.913	106.000	11.343	44.700
4.966	102.600	11.393	43.700
5.017	91.900	11.444	45.300
5.069	75.800	11.494	44.100
5.121	65.300	11.545	42.000
5.172	58.700	11.595	34.700
5.224	66.400	11.645	31.200
5.276	70.200	11.697	32.300
5.328	72.000	11.747	33.700
5.379	72.600	11.798	35.900
5.431	76.500	11.848	37.100
5.482	78.400	11.899	38.600
5.585	82.000	11.950	39.200
5.689	80.100	12.001	39.400
5.946	81.300	12.051	40.400
6.203	80.000	12.101	40.800
6.460	78.100	12.152	41.600
6.717	81.900	12.202	41.000
6.973	78.300	12.253	41.400
7.228	76.900	12.304	41.900
7.484	71.200	12.558	43.300
7.739	70.300	12.810	43.300
7.994	71.000	13.063	43.100

TABLE 3

(TEXT 9 , FIGURE 13)
CENTER OF MASS ANGLE = 84.75

LAB ENERGY	SIGMA	LAB ENERGY	SIGMA
3.612	******	8.249	60.700
3.717	******	8.504	61.200
3.822	******	8.759	64.700
3.916	******	9.012	67.000
4.031	******	9.266	69.700
4.135	******	9.520	72.300
4.239	55.800	9.774	72.600
4.343	57.200	10.027	70.600
4.447	61.000	10.280	64.700
4.551	60.900	10.534	64.700
4.655	60.300	10.787	60.300
4.758	64.400	11.040	56.600
4.862	69.400	11.293	51.400
4.913	77.200	11.343	50.300
4.966	87.600	11.393	48.200
5.017	112.000	11.444	45.800
5.069	124.000	11.494	42.600
5.121	119.000	11.545	38.500
5.172	95.300	11.595	35.900
5.224	81.300	11.645	39.900
5.276	77.000	11.697	44.900
5.328	72.700	11.747	46.300
5.379	71.700	11.798	46.800
5.431	67.400	11.848	47.900
5.482	65.100	11.899	47.700
5.585	64.500	11.950	47.400
5.689	61.900	12.001	47.300
5.946	62.400	12.051	47.600
6.203	61.300	12.101	46.200
6.460	60.500	12.152	46.900
6.717	61.100	12.202	46.300
6.973	59.800	12.253	46.500
7.228	59.400	12.304	45.000
7.484	58.900	12.558	44.400
7.739	59.400	12.810	43.500
7.994	59.500	13.063	42.000

TABLE 3

(TEXT 9 , FIGURE 13)
CENTER OF MASS ANGLE =   90.00

LAB ENERGY	SIGMA	LAB ENERGY	SIGMA
3.612	71.700	8.249	57.700
3.717	68.600	8.504	62.400
3.822	63.200	8.759	67.800
3.916	65.300	9.012	77.200
4.031	64.000	9.266	89.000
4.135	62.400	9.520	95.400
4.239	61.600	9.774	98.000
4.343	60.400	10.027	94.300
4.447	60.000	10.280	88.400
4.551	60.400	10.534	79.300
4.655	62.800	10.787	69.600
4.758	69.400	11.040	63.600
4.862	86.100	11.293	54.400
4.913	108.200	11.343	51.400
4.966	150.000	11.393	47.100
5.017	201.000	11.444	46.400
5.069	216.000	11.494	41.900
5.121	174.000	11.545	34.800
5.172	133.000	11.595	34.900
5.224	106.000	11.645	40.500
5.276	90.000	11.697	48.500
5.328	81.300	11.747	50.000
5.379	75.200	11.798	51.400
5.431	69.900	11.848	49.000
5.482	67.200	11.899	50.400
5.585	62.800	11.950	49.200
5.689	58.400	12.001	47.500
5.946	52.600	12.051	48.300
6.203	52.400	12.101	47.600
6.460	49.300	12.152	48.300
6.717	49.600	12.202	47.000
6.973	49.700	12.253	45.400
7.228	48.700	12.304	44.300
7.484	49.600	12.558	42.500
7.739	52.400	12.810	38.400
7.994	54.500	13.063	39.200

TABLE 3

(TEXT 9 , FIGURE 14)
CENTER OF MASS ANGLE = 95.63

LAB ENERGY	SIGMA	LAB ENERGY	SIGMA
3.612	******	8.249	47.800
3.717	******	8.504	54.500
3.822	******	8.759	65.300
3.916	******	9.012	74.700
4.031	******	9.266	85.500
4.135	******	9.520	95.300
4.239	******	9.774	95.300
4.343	******	10.027	91.900
4.447	******	10.280	80.100
4.551	******	10.534	75.500
4.655	******	10.787	66.400
4.758	******	11.040	57.000
4.862	******	11.293	47.900
4.913	******	11.343	45.500
4.966	******	11.393	42.400
5.017	******	11.444	39.300
5.069	******	11.494	35.400
5.121	******	11.545	30.200
5.172	******	11.595	29.200
5.224	******	11.645	37.800
5.276	63.400	11.697	43.900
5.328	49.900	11.747	45.800
5.379	48.100	11.798	47.200
5.431	44.600	11.848	46.300
5.482	42.800	11.899	45.800
5.585	41.400	11.950	44.400
5.689	37.300	12.001	43.500
5.946	36.400	12.051	42.600
6.203	35.700	12.101	42.100
6.460	34.700	12.152	41.100
6.717	33.000	12.202	40.600
6.973	31.600	12.253	39.900
7.228	35.600	12.304	32.900
7.484	37.200	12.558	34.400
7.739	40.200	12.810	36.200
7.994	42.700	13.063	39.400

TABLE 3

(TEXT 9 , FIGURE 14)
CENTER OF MASS ANGLE = 102.00

LAB ENERGY	SIGMA	LAB ENERGY	SIGMA
3.612	******	8.249	45.900
3.717	******	8.504	53.900
3.822	******	8.759	65.700
3.916	37.900	9.012	80.000
4.031	37.600	9.266	91.700
4.135	27.600	9.520	101.000
4.239	32.000	9.774	102.000
4.343	36.500	10.027	93.900
4.447	37.000	10.280	83.100
4.551	41.900	10.534	72.100
4.655	49.700	10.787	59.900
4.758	59.300	11.040	50.500
4.862	91.200	11.293	39.600
4.913	126.000	11.343	36.900
4.966	186.000	11.393	34.100
5.017	268.000	11.444	30.500
5.069	292.000	11.494	26.700
5.121	218.000	11.545	21.900
5.172	144.000	11.595	22.700
5.224	93.200	11.645	32.100
5.276	70.100	11.697	38.300
5.328	55.800	11.747	39.800
5.379	47.800	11.798	40.100
5.431	39.800	11.848	39.300
5.482	38.700	11.899	37.800
5.585	32.600	11.950	37.000
5.689	31.300	12.001	35.400
5.946	28.600	12.051	33.800
6.203	27.900	12.101	33.800
6.460	26.500	12.152	32.600
6.717	29.800	12.202	31.700
6.973	29.300	12.253	30.900
7.228	29.400	12.304	22.800
7.484	30.700	12.558	25.200
7.739	34.900	12.810	27.800
7.994	39.600	13.063	29.800

TABLE 3

(TEXT 9 , FIGURE 15)
CENTER OF MASS ANGLE = 109.87

LAB ENERGY	SIGMA	LAB ENERGY	SIGMA
3.612	8.300	8.249	43.700
3.717	12.100	8.504	52.100
3.822	15.700	8.759	63.300
3.916	19.200	9.012	74.500
4.031	22.800	9.266	84.800
4.135	27.700	9.520	90.600
4.239	29.800	9.774	88.200
4.343	35.300	10.027	79.600
4.447	39.800	10.280	65.700
4.551	44.900	10.534	55.000
4.655	54.700	10.787	44.400
4.758	73.100	11.040	34.600
4.862	111.000	11.293	24.400
4.913	154.000	11.343	22.400
4.966	220.000	11.393	19.600
5.017	297.000	11.444	16.600
5.069	301.000	11.494	13.300
5.121	216.000	11.545	12.400
5.172	126.500	11.595	16.500
5.224	78.000	11.645	24.300
5.276	53.400	11.697	26.900
5.328	39.600	11.747	26.000
5.379	31.600	11.798	25.100
5.431	26.400	11.848	23.900
5.482	23.400	11.899	22.900
5.585	20.600	11.950	21.700
5.689	18.500	12.001	21.700
5.946	17.700	12.051	20.500
6.203	18.600	12.101	19.500
6.460	19.700	12.152	19.000
6.717	20.800	12.202	18.300
6.973	21.900	12.253	17.600
7.228	24.400	12.304	17.100
7.484	27.100	12.558	14.500
7.739	31.500	12.810	13.200
7.994	35.900	13.063	11.600

TABLE 3

(TEXT 9 , FIGURE 15)
CENTER OF MASS ANGLE = 116.57

LAB ENERGY	SIGMA	LAB ENERGY	SIGMA
3.612	24.900	8.249	39.600
3.717	26.800	8.504	47.100
3.822	29.700	8.759	55.700
3.916	30.900	9.012	63.500
4.031	******	9.266	74.400
4.135	******	9.520	77.400
4.239	******	9.774	72.200
4.343	27.800	10.027	61.700
4.447	34.800	10.280	49.400
4.551	41.500	10.534	38.400
4.655	55.900	10.787	29.600
4.758	75.400	11.040	19.800
4.862	113.000	11.293	13.700
4.913	154.000	11.343	11.900
4.966	211.000	11.393	10.800
5.017	285.000	11.444	8.410
5.069	276.000	11.494	6.380
5.121	190.000	11.545	5.590
5.172	103.000	11.595	9.180
5.224	59.800	11.645	14.400
5.276	37.700	11.697	16.000
5.328	26.200	11.747	16.300
5.379	19.600	11.798	14.400
5.431	16.600	11.848	13.800
5.482	14.700	11.899	12.900
5.585	13.000	11.950	12.100
5.689	12.500	12.001	11.400
5.946	12.400	12.051	10.900
6.203	14.000	12.101	9.930
6.460	15.100	12.152	9.650
6.717	17.200	12.202	8.980
6.973	18.900	12.253	8.750
7.228	21.400	12.304	8.150
7.484	22.700	12.558	6.780
7.739	27.800	12.810	5.610
7.994	33.600	13.063	4.720

TABLE 3

(TEXT 9 , FIGURE 16)
CENTER OF MASS ANGLE = 125.27

LAB ENERGY	SIGMA	LAB ENERGY	SIGMA
3.612	8.500	8.249	44.000
3.717	12.200	8.504	54.900
3.822	21.800	8.759	63.200
3.916	24.200	9.012	68.100
4.031	25.500	9.266	74.800
4.135	25.100	9.520	76.600
4.239	29.700	9.774	69.900
4.343	31.700	10.027	58.600
4.447	33.700	10.280	45.300
4.551	38.700	10.534	33.400
4.655	45.500	10.787	24.800
4.758	60.500	11.040	18.200
4.862	93.600	11.293	11.600
4.913	129.000	11.343	10.100
4.966	176.000	11.393	8.800
5.017	227.000	11.444	7.100
5.069	207.000	11.494	5.900
5.121	129.000	11.545	5.500
5.172	67.300	11.595	7.900
5.224	38.400	11.645	12.800
5.276	24.600	11.697	14.400
5.328	17.100	11.747	14.300
5.379	13.500	11.798	13.300
5.431	10.800	11.848	12.400
5.482	10.000	11.899	11.700
5.585	10.000	11.950	11.100
5.689	10.000	12.001	10.000
5.946	11.500	12.051	9.800
6.203	13.300	12.101	9.300
6.460	15.400	12.152	9.000
6.717	18.100	12.202	8.400
6.973	20.300	12.253	8.400
7.228	24.100	12.304	8.100
7.484	28.100	12.558	6.800
7.739	32.400	12.810	6.100
7.994	36.900	13.063	5.500

TABLE 3

(TEXT 9 , FIGURE 16)
CENTER OF MASS ANGLE = 140.00

LAB ENERGY	SIGMA	LAB ENERGY	SIGMA
3.612	*******	8.249	66.500
3.717	*******	8.504	78.300
3.822	*******	8.759	91.600
3.916	*******	9.012	110.000
4.031	*******	9.266	129.000
4.135	*******	9.520	141.000
4.239	*******	9.774	147.000
4.343	*******	10.027	140.000
4.447	27.600	10.280	130.000
4.551	30.100	10.534	121.000
4.655	33.500	10.787	117.000
4.758	40.600	11.040	*******
4.862	62.900	11.293	73.600
4.913	86.700	11.343	65.200
4.966	129.100	11.393	64.100
5.017	195.000	11.444	59.300
5.069	224.000	11.494	54.300
5.121	185.000	11.545	48.400
5.172	129.000	11.595	49.600
5.224	93.800	11.645	60.700
5.276	72.700	11.697	69.400
5.328	59.100	11.747	73.900
5.379	51.900	11.798	73.200
5.431	46.400	11.848	71.600
5.482	43.800	11.899	71.600
5.585	39.100	11.950	70.800
5.689	36.200	12.001	68.600
5.946	33.600	12.051	*******
6.203	32.400	12.101	67.700
6.460	34.400	12.152	67.000
6.717	35.400	12.202	67.100
6.973	37.600	12.253	66.500
7.228	40.600	12.304	65.600
7.484	46.000	12.558	64.700
7.739	50.500	12.810	57.000
7.994	58.000	13.063	54.700

TABLE 3

(TEXT 9, FIGURE 17)
CENTER OF MASS ANGLE = 146.50

LAB ENERGY	SIGMA	LAB ENERGY	SIGMA
3.612	******	8.249	85.100
3.717	******	8.504	96.100
3.822	******	8.759	118.000
3.916	******	9.012	147.000
4.031	******	9.266	177.000
4.135	******	9.520	195.000
4.239	******	9.774	213.000
4.343	******	10.027	218.000
4.447	22.900	10.280	208.000
4.551	23.400	10.534	177.000
4.655	24.700	10.787	162.000
4.758	29.200	11.040	144.000
4.862	50.400	11.293	130.000
4.913	82.900	11.343	126.000
4.966	139.000	11.393	121.000
5.017	239.000	11.444	111.000
5.069	306.000	11.494	103.000
5.121	272.000	11.545	86.600
5.172	199.000	11.595	86.800
5.224	149.000	11.645	107.000
5.276	121.000	11.697	122.000
5.328	97.900	11.747	132.000
5.379	85.300	11.798	124.000
5.431	74.900	11.848	127.000
5.482	68.500	11.899	125.000
5.585	59.700	11.950	124.000
5.689	55.600	12.001	120.000
5.946	47.200	12.051	121.000
6.203	44.300	12.101	118.000
6.460	43.800	12.152	117.000
6.717	43.400	12.202	118.000
6.973	44.300	12.253	116.000
7.228	49.600	12.304	116.000
7.484	58.400	12.558	111.000
7.739	61.800	12.810	109.000
7.994	71.700	13.063	109.000

Table 4

Data for the ^{3}H(α, α)^{3}H Experiment

This table shows the center-of-mass differential elastic cross sections in the same manner as Table 3. The energy range is from 12.8 to 18 MeV. (Page 9)

TABLE 4

(TEXT 9 , FIGURE 18)
CENTER OF MASS ANGLE =   54.70

LAB ENERGY	SIGMA	LAB ENERGY	SIGMA
12.810	85.900	16.341	54.700
13.063	87.100	16.442	43.700
13.315	86.500	16.542	34.700
13.568	86.800	16.643	28.700
13.820	85.600	16.743	27.000
14.073	85.300	16.844	28.900
14.325	86.700	16.944	32.100
14.577	85.400	17.046	38.100
14.829	86.300	17.146	40.500
15.082	85.900	17.247	42.000
15.333	83.800	17.347	45.800
15.585	81.900	17.448	49.700
15.837	78.900	17.548	52.100
15.938	78.500	17.648	52.500
16.039	73.300	17.849	55.600
16.139	72.100	18.100	58.000
16.241	64.600	18.500	******

TABLE 4

(TEXT 9 , FIGURE 18)
CENTER OF MASS ANGLE = 63.40

LAB ENERGY	SIGMA	LAB ENERGY	SIGMA
12.810	54.700	16.341	18.000
13.063	55.100	16.442	11.000
13.315	56.800	16.542	6.570
13.568	57.400	16.643	6.090
13.820	50.800	16.743	8.910
14.073	57.000	16.844	13.700
14.325	56.100	16.944	18.500
14.577	54.300	17.046	23.100
14.829	54.800	17.146	28.300
15.082	50.100	17.247	31.000
15.333	52.100	17.347	33.600
15.585	47.800	17.448	37.300
15.837	43.400	17.548	39.400
15.938	39.400	17.648	39.300
16.039	35.700	17.849	42.400
16.139	31.300	18.100	44.600
16.241	25.000	18.500	*******

TABLE 4

(TEXT 9 , FIGURE 19)
CENTER OF MASS ANGLE = 77.00

LAB ENERGY	SIGMA	LAB ENERGY	SIGMA
12.810	46.400	16.341	25.400
13.063	45.400	16.442	21.700
13.315	46.000	16.542	19.300
13.568	43.700	16.643	18.000
13.820	44.200	16.743	17.300
14.073	42.800	16.844	16.900
14.325	43.200	16.944	18.900
14.577	41.700	17.046	19.700
14.829	41.500	17.146	21.800
15.082	39.900	17.247	23.200
15.333	39.400	17.347	23.900
15.585	36.600	17.448	24.700
15.837	34.900	17.548	25.800
15.938	32.600	17.648	26.200
16.039	31.000	17.849	27.100
16.139	30.700	18.100	27.200
16.241	28.500	18.500	*******

TABLE 4

(TEXT 9, FIGURE 19)
CENTER OF MASS ANGLE =   91.39

LAB ENERGY	SIGMA	LAB ENERGY	SIGMA
12.810	38.900	16.341	48.800
13.063	37.800	16.442	47.700
13.315	37.100	16.542	46.600
13.568	36.200	16.643	42.900
13.820	34.700	16.743	37.000
14.073	33.400	16.844	33.700
14.325	33.900	16.944	27.800
14.577	32.600	17.046	24.200
14.829	32.700	17.146	21.900
15.082	33.300	17.247	20.100
15.333	33.900	17.347	18.300
15.585	35.200	17.448	16.300
15.837	38.300	17.548	16.100
15.938	38.500	17.648	14.900
16.039	42.000	17.849	13.200
16.139	44.400	18.100	12.300
16.241	46.100	18.500	*******

TABLE 4

(TEXT 9 , FIGURE 20)
CENTER OF MASS ANGLE = 105.00

LAB ENERGY	SIGMA	LAB ENERGY	SIGMA
12.810	19.700	16.341	37.300
13.063	18.700	16.442	44.000
13.315	18.300	16.542	48.300
13.568	16.000	16.643	50.600
13.820	14.800	16.743	50.700
14.073	14.500	16.844	47.800
14.325	13.900	16.944	43.600
14.577	13.400	17.046	39.200
14.829	12.900	17.146	34.600
15.082	13.300	17.247	33.000
15.333	14.400	17.347	30.100
15.585	14.600	17.448	26.100
15.837	17.700	17.548	24.400
15.938	19.900	17.648	23.100
16.039	23.100	17.849	20.900
16.139	27.900	18.100	17.100
16.241	31.600	18.500	*******

TABLE 4

(TEXT 9, FIGURE 20)
CENTER OF MASS ANGLE = 115.80

LAB ENERGY	SIGMA	LAB ENERGY	SIGMA
12.810	5.860	16.341	16.300
13.063	5.070	16.442	22.400
13.315	4.160	16.542	28.000
13.568	4.120	16.643	32.600
13.820	3.470	16.743	35.600
14.073	3.120	16.844	35.500
14.325	2.570	16.944	33.000
14.577	2.680	17.046	31.500
14.829	2.480	17.146	28.900
15.082	2.290	17.247	26.100
15.333	2.680	17.347	23.300
15.585	3.130	17.448	22.800
15.837	4.250	17.548	21.700
15.938	5.500	17.648	20.600
16.039	6.530	17.849	17.600
16.139	9.310	18.100	16.300
16.241	11.630	18.500	*******

TABLE 4

(TEXT 9, FIGURE 21)
CENTER OF MASS ANGLE = 126.50

LAB ENERGY	SIGMA	LAB ENERGY	SIGMA
12.810	8.240	16.341	19.920
13.063	7.470	16.442	20.510
13.315	7.070	16.542	20.180
13.568	7.220	16.643	18.680
13.820	7.010	16.743	17.140
14.073	6.600	16.844	14.980
14.325	7.050	16.944	12.400
14.577	7.100	17.046	10.120
14.829	7.290	17.146	8.560
15.082	8.370	17.247	7.440
15.333	8.760	17.347	6.520
15.585	9.400	17.448	5.970
15.837	10.600	17.548	5.290
15.938	12.150	17.648	4.880
16.039	13.770	17.849	4.050
16.139	14.820	18.100	4.270
16.241	17.440	18.500	*******

TABLE 4

(TEXT 9 , FIGURE 21)
CENTER OF MASS ANGLE = 133.60

LAB ENERGY	SIGMA	LAB ENERGY	SIGMA
12.810	24.000	16.341	36.300
13.063	22.600	16.442	34.000
13.315	23.400	16.542	28.800
13.568	23.100	16.643	22.100
13.820	23.300	16.743	16.300
14.073	23.000	16.844	11.900
14.325	23.100	16.944	7.800
14.577	23.100	17.046	5.360
14.829	24.200	17.146	4.000
15.082	25.000	17.247	3.530
15.333	24.700	17.347	2.960
15.585	28.000	17.448	2.420
15.837	30.300	17.548	2.370
15.938	31.400	17.648	2.040
16.039	32.600	17.849	2.320
16.139	34.400	18.100	2.930
16.241	34.500	18.500	*******

Table 5

Experimental Errors in the ^{3}H(α, α)^{3}H Data

This table shows the systematic error and relative error at each center-of-mass angle. For some angles the relative error has been given separately for several different energy ranges. In general, the relative error tends to decrease with energy because of the lower backgrounds at higher energies. Statistics of the data are the major variation from this trend. (Pages 9, 65)

Table 5

Tabulation of Experimental Errors

$$^3\text{H}(\alpha, \alpha)^3\text{H} \; (3.6\text{-}13.1 \text{ MeV})$$
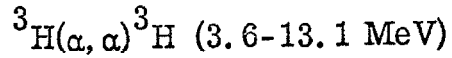
$^\theta\text{CM}$	Systematic Error (%)	Relative Error (%)	Energy Range (MeV)
39.23	3.2	6 - 12	3.6 - 10
		4 - 6	10 - 13
46.99		5 - 10	3.6 - 11
		3 - 5	11 - 13
54.73		8 - 15	3.6 - 8
		4 - 8	8 - 13
60.00		6 - 12	3.6 - 8
		4 - 6	8 - 13
63.43		6 - 10	3.6 - 9
		4 - 6	9 - 13
64.97		3 - 6	3.6 - 8
		1.5 - 3	8 - 13
70.00		5 - 8	3.6 - 8
		3 - 5	8 - 13
75.95		5 - 10	3.6 - 6
		2.5 - 5	6 - 8
		1 - 2.5	8 - 13
84.75		4 - 8	3.6 - 7
		2 - 4	7 - 11
		1 - 2	11 - 13
90.00		3 - 6	3.6 - 8
		1.5 - 3	8 - 13
95.63		6 - 10	5 - 7
		3 - 6	7 - 10
		1.5 - 3	10 - 13
102.00		1 - 2.5	3.6 - 13
109.87		1 - 2	3.6 - 13

Table 5 (cont.)

θ_{CM}	Systematic Error (%)	Relative Error (%)	Energy Range (MeV)
116.57	3.2	1.5 - 2	3.6 - 13
125.27		2 - 3	3.6 - 13
140.00		1 - 2	3.6 - 13
146.50		1 - 2	3.6 - 13

$^3H(\alpha, \alpha)^3H$ (13 - 18 MeV)

θ_{CM}	Systematic Error (%)	Relative Error (%)	Energy Range (MeV)
54.70	3.2	2	13 - 18
63.40		1.5 - 3.5	13 - 18
77.00		2 - 3	13 - 18
91.39		1.5 - 3	13 - 18
105.00		2 - 4	13 - 18
115.80		4 - 8	13 - 16.3
		2 - 4	16.3 - 18
126.50		2.5 - 4	13 - 18
133.60		2 - 4	13 - 17
		4 - 7	17 - 18

Table 6

Data for the Reaction ^{3}H$(\alpha, n)^6$Li

This table shows the data obtained using the zirconium tritide target. The number of counts obtained is shown for each beam energy. These data were not used directly in our analysis. (Page 11)

Table 6

Data on the Reaction $^3H(\alpha, n)^6Li$

Beam Energy	Counts		Beam Energy	Counts
11.000	2488		11.297	12546
11.040	2546		11.308	13070
11.042	2670		11.317	13824
11.052	2696		11.320	12920
11.062	2732		11.327	14342
11.071	2764		11.360	15140
11.080	2740		11.400	18176
11.090	2706		11.440	22840
11.099	2880		11.480	28394
11.108	2830		11.520	38676
11.118	2920		11.560	53812
11.120	2920		11.600	82448
11.127	2950		11.640	111590
11.137	2854		11.680	127678
11.146	2936		11.720	118468
11.155	3250		11.760	92702
11.160	3302		11.800	74016
11.165	3592		11.840	56516
11.174	3942		11.880	48124
11.183	4490		11.920	42262
11.193	5028		11.960	38102
11.200	5238		12.000	34504
11.202	5498		12.040	31942
11.212	6252		12.080	30472
11.221	7014		12.120	28632
11.230	7730		12.160	27546
11.240	8498		12.200	26468
11.250	9356		12.240	25822
11.259	9918		12.280	25026
11.269	10938		12.320	25218
11.278	11614		12.360	25020
11.280	10854		12.400	24514
11.287	12178			

Table 7

Data for the Reaction $^3H(\alpha, n)^6Li$

This table shows actual reaction cross sections obtained from the data of Schwarz, et al. (1965) on the inverse reaction. The cross sections and energies are shown for our system. The data above 12.5 MeV were obtained from those of Murray (1959). (Pages 26, 27)

Table 7

Data on ^{3}H$(\alpha, n)^6$Li Obtained from the Inverse Reaction
^{6}Li$(n, \alpha)^3$H (Schwarz, 1965, Murray, 1959)

Lab Energy	Total Reaction Cross Section
11.329	13.96
11.348	15.53
11.369	17.29
11.408	21.62
11.448	27.71
11.488	36.90
11.527	51.15
11.567	73.18
11.609	104.31
11.649	137.1
11.688	154.1
11.728	147.3
11.768	127.2
11.807	107.0
11.847	90.84
11.889	78.90
11.929	70.24
11.968	63.63
12.008	58.91
12.048	55.08
12.087	52.35
12.127	50.13
12.169	48.33
12.209	46.90
12.248	45.78
12.228	44.87
12.328	44.13
12.367	43.50
13.530	72.4
13.630	84.7
13.750	78.9
14.009	80.5
14.248	85.7
14.406	97.0
14.567	95.7
14.746	97.2
14.965	106.
15.205	105.

Table 7 (cont.)

Lab Energy	Total Reaction Cross Section
15.444	104.
15.903	110.
16.959	98.7
18.751	78.2

Table 8

Data for the Reaction $^3H(\alpha, n^1)^6Li^*$

This table shows the total reaction cross section for the two reactions $^3H(\alpha, n)^6Li$ and $^3H(\alpha, n^1)^6Li^*$ as a function of beam energy. The data below the $^3H(\alpha, n^1)^6Li^*$ threshold was due only to the $^3H(\alpha, n)^6Li$ reaction and provided a normalization of the cross sections and the means to separate the effect of the two reactions. (Page 12)

Table 8

Data on ^{3}H$(\alpha, n^1)^6$Li*

Lab Energy (MeV)	Total Reaction Cross Section (millibarns)
11.00	4.4
11.05	4.3
11.10	4.4
11.15	4.5
11.20	8.4
11.25	12.7
11.30	15.6
11.35	18.2
11.40	22.2
11.45	30.0
11.50	40.9
11.55	68.8
11.60	103.4
11.65	140.
11.70	156.
11.75	133.
11.80	102.
11.85	78.3
11.90	69.8
11.95	60.4
12.00	58.9
12.05	53.2
12.10	51.4
12.15	52.1
12.20	51.7
12.25	50.1
12.50	49.4
12.75	53.1
13.00	55.4
13.25	66.5
13.50	71.4
13.75	75.7
14.00	84.6
14.25	95.7
14.50	108.
14.75	113.

Table 8 (cont.)

Lab Energy (MeV)	Total Reaction Cross Section (millibarns)
15.00	116.
15.25	126.
15.5	128.
15.75	140.
16.00	141.
16.10	145.
16.20	152.
16.30	166.
16.40	199.
16.50	247.
16.60	294.
16.70	346.
16.80	365.
16.90	379.
17.00	377.
17.10	379.
17.20	376.
17.30	358.
17.40	366.
17.50	341.
17.60	338.
17.70	341.
17.80	327.
18.00	337.

Table 9

Data for the ^{4}He(^{3}He, ^{3}He)^{4}He Experiment

This table shows the center-of-mass differential elastic cross sections (SIGMA) as a function of beam energy (LAB ENERGY). The energy range is from 4.6 - 17.9 MeV. The spaces marked by a series of asterisks are points for which data were not obtained. (Page 17)

TABLE 9

(TEXT 17, FIGURE 34)
CENTER OF MASS ANGLE =   39.20

LAB ENERGY	SIGMA	LAB ENERGY	SIGMA
4.634	542.000	9.459	325.000
4.735	542.000	9.710	308.000
4.836	543.000	9.961	293.000
4.936	534.000	10.211	285.000
4.986	538.000	10.462	268.000
5.037	549.000	10.713	258.000
5.087	574.000	10.964	252.000
5.137	598.000	11.214	240.000
5.188	633.000	11.465	229.000
5.238	654.000	11.715	229.000
5.288	642.000	11.966	220.000
5.339	606.000	12.217	217.000
5.389	575.000	12.467	210.000
5.439	559.000	12.717	203.000
5.691	492.000	12.968	200.000
5.942	467.000	13.218	194.000
6.194	454.000	13.469	180.000
6.445	437.000	13.719	180.000
6.696	427.000	13.970	180.000
6.948	417.000	14.220	169.000
7.199	401.000	14.470	158.000
7.450	397.000	14.721	153.600
7.702	394.000	14.872	152.800
7.953	403.000	15.375	141.000
8.204	413.000	15.878	131.600
8.455	397.000	16.380	118.400
8.706	394.000	16.883	114.700
8.957	373.000	17.386	109.300
9.208	349.000	17.888	103.200

TABLE 9

(TEXT 17, FIGURE 34)
CENTER OF MASS ANGLE = 47.00

LAB ENERGY	SIGMA	LAB ENERGY	SIGMA
4.634	350.000	9.459	148.000
4.735	349.000	9.710	146.000
4.836	345.000	9.961	144.000
4.936	339.000	10.211	149.000
4.986	333.000	10.462	143.000
5.037	333.000	10.713	139.000
5.087	305.000	10.964	137.000
5.137	292.000	11.214	134.000
5.188	258.000	11.465	135.000
5.238	227.000	11.715	133.000
5.288	218.000	11.966	132.000
5.339	227.000	12.217	127.000
5.389	244.000	12.467	121.000
5.439	251.000	12.717	109.000
5.691	277.000	12.968	103.000
5.942	278.000	13.218	94.000
6.194	278.000	13.469	90.000
6.445	272.000	13.719	91.000
6.696	266.000	13.970	92.000
6.948	260.000	14.220	89.000
7.199	255.000	14.470	90.000
7.450	246.000	14.721	86.100
7.702	240.000	14.872	******
7.953	226.000	15.375	******
8.204	216.000	15.878	******
8.455	195.000	16.380	******
8.706	180.000	16.883	******
8.957	164.000	17.386	******
9.208	154.000	17.888	******

TABLE 9

(TEXT 17, FIGURE 35)
CENTER OF MASS ANGLE =   54.70

LAB ENERGY	SIGMA	LAB ENERGY	SIGMA
4.634	245.400	9.459	70.100
4.735	245.100	9.710	75.000
4.836	244.200	9.961	78.400
4.936	232.600	10.211	78.000
4.986	188.600	10.462	81.600
5.037	214.000	10.713	85.100
5.087	187.800	10.964	88.700
5.137	154.000	11.214	88.300
5.188	97.800	11.465	86.600
5.238	58.100	11.715	85.800
5.288	58.400	11.966	81.800
5.339	82.200	12.217	75.800
5.389	105.400	12.467	69.600
5.439	130.100	12.717	61.100
5.691	175.800	12.968	52.000
5.942	180.000	13.218	50.800
6.194	189.500	13.469	52.600
6.445	180.300	13.719	55.800
6.696	182.800	13.970	58.000
6.948	175.900	14.220	58.600
7.199	165.700	14.470	61.000
7.450	158.400	14.721	60.600
7.702	144.300	14.872	58.300
7.953	126.300	15.375	58.900
8.204	104.500	15.878	53.300
8.455	80.600	16.380	49.400
8.706	67.100	16.883	47.600
8.957	58.400	17.386	44.900
9.208	62.900	17.888	41.900

TABLE 9

(TEXT 17, FIGURE 35)
CENTER OF MASS ANGLE = 63.40

LAB ENERGY	SIGMA	LAB ENERGY	SIGMA
4.634	159.000	9.459	32.700
4.735	156.100	9.710	39.300
4.836	151.800	9.961	42.600
4.936	141.200	10.211	48.600
4.986	135.700	10.462	51.000
5.037	123.400	10.713	55.800
5.087	100.300	10.964	58.200
5.137	68.800	11.214	56.500
5.188	*******	11.465	56.100
5.238	4.200	11.715	54.100
5.288	10.900	11.966	51.700
5.339	33.900	12.217	44.100
5.389	57.200	12.467	38.300
5.439	73.600	12.717	31.600
5.691	107.300	12.968	39.500
5.942	120.400	13.218	30.400
6.194	121.300	13.469	34.900
6.445	118.200	13.719	40.000
6.696	115.400	13.970	42.200
6.948	105.900	14.220	44.900
7.199	104.000	14.470	45.800
7.450	90.400	14.721	48.100
7.702	75.700	14.872	46.800
7.953	58.900	15.375	47.200
8.204	37.900	15.878	46.300
8.455	20.700	16.380	43.500
8.706	12.600	16.883	42.000
8.957	14.600	17.386	41.300
9.208	23.400	17.888	38.600

TABLE 9

(TEXT 17, FIGURE 36)
CENTER OF MASS ANGLE = 70.10

LAB ENERGY	SIGMA	LAB ENERGY	SIGMA
4.634	112.200	9.459	31.700
4.735	111.200	9.710	34.800
4.836	103.100	9.961	38.700
4.936	98.300	10.211	42.600
4.986	90.400	10.462	46.500
5.037	81.400	10.713	47.900
5.087	70.500	10.964	49.100
5.137	51.100	11.214	47.900
5.188	29.800	11.465	46.000
5.238	20.400	11.715	45.100
5.288	32.000	11.966	41.600
5.339	46.100	12.217	34.800
5.389	60.700	12.467	30.200
5.439	70.300	12.717	24.700
5.691	90.000	12.968	24.700
5.942	93.100	13.218	25.600
6.194	88.800	13.469	30.300
6.445	88.800	13.719	32.100
6.696	85.500	13.970	34.900
6.948	78.300	14.220	38.300
7.199	71.200	14.470	41.300
7.450	65.100	14.721	40.600
7.702	54.400	14.872	39.400
7.953	39.300	15.375	40.100
8.204	26.300	15.878	39.600
8.455	16.900	16.380	39.200
8.706	12.400	16.883	37.400
8.957	18.000	17.386	37.400
9.208	25.000	17.888	36.300

TABLE 9

(TEXT 17, FIGURE 36)
CENTER OF MASS ANGLE = 77.00

LAB ENERGY	SIGMA	LAB ENERGY	SIGMA
4.634	80.600	9.459	40.400
4.735	77.100	9.710	40.000
4.836	73.800	9.961	42.700
4.936	71.300	10.211	44.100
4.986	68.500	10.462	43.300
5.037	66.400	10.713	43.300
5.087	62.200	10.964	43.300
5.137	56.000	11.214	42.500
5.188	57.200	11.465	39.500
5.238	60.100	11.715	38.800
5.288	68.500	11.966	36.400
5.339	75.100	12.217	34.300
5.389	78.800	12.467	29.400
5.439	79.600	12.717	26.900
5.691	79.400	12.968	24.300
5.942	76.600	13.218	23.400
6.194	71.800	13.469	25.600
6.445	66.300	13.719	26.700
6.696	65.300	13.970	28.200
6.948	63.100	14.220	30.100
7.199	60.400	14.470	29.900
7.450	54.500	14.721	28.700
7.702	46.700	14.872	28.000
7.953	41.900	15.375	28.700
8.204	37.900	15.878	28.600
8.455	33.200	16.380	27.400
8.706	33.400	16.883	27.600
8.957	35.200	17.386	26.600
9.208	40.000	17.888	26.400

TABLE 9

(TEXT 17, FIGURE 37)
CENTER OF MASS ANGLE =   80.00

LAB ENERGY	SIGMA	LAB ENERGY	SIGMA
4.634	66.600	9.459	45.100
4.735	65.400	9.710	44.200
4.836	61.900	9.961	45.100
4.936	62.000	10.211	44.800
4.986	60.700	10.462	45.200
5.037	62.700	10.713	43.000
5.087	62.100	10.964	44.500
5.137	69.000	11.214	40.900
5.188	77.500	11.465	37.500
5.238	85.400	11.715	37.800
5.288	89.900	11.966	35.300
5.339	92.300	12.217	33.500
5.389	86.400	12.467	31.900
5.439	82.500	12.717	26.900
5.691	75.000	12.968	23.700
5.942	71.800	13.218	*******
6.194	67.500	13.469	*******
6.445	65.800	13.719	*******
6.696	62.000	13.970	*******
6.948	59.400	14.220	*******
7.199	56.300	14.470	*******
7.450	54.000	14.721	*******
7.702	47.800	14.872	*******
7.953	46.600	15.375	*******
8.204	47.600	15.878	*******
8.455	46.200	16.380	*******
8.706	47.100	16.883	*******
8.957	47.100	17.386	*******
9.208	48.400	17.888	*******

TABLE 9

(TEXT 17, FIGURE 37)
CENTER OF MASS ANGLE = 85.26

LAB ENERGY	SIGMA	LAB ENERGY	SIGMA
4.634	55.100	9.459	48.600
4.735	51.900	9.710	46.700
4.836	55.400	9.961	46.600
4.936	57.500	10.211	46.300
4.986	56.600	10.462	44.200
5.037	64.400	10.713	40.800
5.087	70.400	10.964	38.300
5.137	84.100	11.214	36.400
5.188	105.000	11.465	36.900
5.238	118.800	11.715	35.700
5.288	114.400	11.966	33.400
5.339	109.400	12.217	30.900
5.389	96.500	12.467	30.000
5.439	88.900	12.717	27.800
5.691	70.400	12.968	24.000
5.942	61.800	13.218	21.500
6.194	58.300	13.469	20.000
6.445	56.100	13.719	18.400
6.696	52.600	13.970	16.900
6.948	52.400	14.220	15.800
7.199	51.000	14.470	16.300
7.450	49.900	14.721	17.100
7.702	52.700	14.872	*******
7.953	55.100	15.375	*******
8.204	57.500	15.878	*******
8.455	59.900	16.380	*******
8.706	61.100	16.883	*******
8.957	59.700	17.386	*******
9.208	52.900	17.888	*******

TABLE 9

(TEXT 17, FIGURE 38)
CENTER OF MASS ANGLE =   90.00

LAB ENERGY	SIGMA	LAB ENERGY	SIGMA
4.634	49.400	9.459	53.500
4.735	46.000	9.710	47.800
4.836	52.600	9.961	43.500
4.936	58.600	10.211	40.000
4.986	65.900	10.462	39.400
5.037	74.700	10.713	36.700
5.087	87.100	10.964	34.600
5.137	116.000	11.214	34.000
5.188	141.900	11.465	32.000
5.238	151.600	11.715	30.600
5.288	142.300	11.966	30.700
5.339	118.200	12.217	30.600
5.389	101.100	12.467	29.400
5.439	90.200	12.717	28.300
5.691	59.600	12.968	24.900
5.942	53.900	13.218	20.900
6.194	47.800	13.469	19.900
6.445	46.800	13.719	15.000
6.696	43.700	13.970	13.700
6.948	47.300	14.220	11.200
7.199	46.100	14.470	11.000
7.450	50.800	14.721	10.500
7.702	54.300	14.872	9.480
7.953	62.000	15.375	8.450
8.204	68.500	15.878	7.500
8.455	70.400	16.380	6.650
8.706	72.400	16.883	6.260
8.957	67.500	17.386	5.900
9.208	61.400	17.888	5.740

TABLE 9

(TEXT 17, FIGURE 38)
CENTER OF MASS ANGLE = 98.40

LAB ENERGY	SIGMA	LAB ENERGY	SIGMA
4.634	45.400	9.459	46.900
4.735	49.400	9.710	41.800
4.836	54.800	9.961	36.400
4.936	69.200	10.211	34.400
4.986	83.600	10.462	31.100
5.037	101.500	10.713	27.300
5.087	122.400	10.964	24.100
5.137	165.300	11.214	24.100
5.188	196.300	11.465	22.900
5.238	194.500	11.715	22.100
5.288	159.100	11.966	21.700
5.339	120.200	12.217	21.800
5.389	95.100	12.467	23.200
5.439	78.200	12.717	21.900
5.691	40.200	12.968	21.200
5.942	35.000	13.218	19.500
6.194	32.600	13.469	16.100
6.445	32.000	13.719	13.800
6.696	33.600	13.970	11.000
6.948	34.300	14.220	10.100
7.199	38.500	14.470	8.800
7.450	41.800	14.721	6.800
7.702	48.100	14.872	6.980
7.953	59.700	15.375	5.520
8.204	72.200	15.878	3.970
8.455	76.600	16.380	3.780
8.706	74.900	16.883	3.160
8.957	70.600	17.386	2.650
9.208	59.000	17.888	2.190

TABLE 9

(TEXT 17, FIGURE 39)
CENTER OF MASS ANGLE = 106.40

LAB ENERGY	SIGMA	LAB ENERGY	SIGMA
4.634	49.200	9.459	34.700
4.735	54.700	9.710	28.900
4.836	64.700	9.961	26.000
4.936	87.400	10.211	22.200
4.986	102.200	10.462	17.600
5.037	123.100	10.713	16.300
5.087	156.300	10.964	14.700
5.137	196.200	11.214	14.000
5.188	*******	11.465	12.500
5.238	204.700	11.715	10.700
5.288	156.100	11.966	11.600
5.339	105.000	12.217	12.200
5.389	74.000	12.467	13.600
5.439	55.700	12.717	14.600
5.691	23.000	12.968	15.800
5.942	17.300	13.218	16.900
6.194	17.800	13.469	15.500
6.445	20.600	13.719	14.600
6.696	23.000	13.970	12.500
6.948	23.900	14.220	10.700
7.199	28.400	14.470	10.200
7.450	36.300	14.721	8.600
7.702	42.300	14.872	8.740
7.953	50.600	15.375	8.000
8.204	60.500	15.878	7.030
8.455	64.900	16.380	6.810
8.706	66.700	16.883	6.500
8.957	56.200	17.386	5.920
9.208	45.700	17.888	5.460

TABLE 9

(TEXT 17, FIGURE 39)
CENTER OF MASS ANGLE = 116.80

LAB ENERGY	SIGMA	LAB ENERGY	SIGMA
4.634	51.000	9.459	17.200
4.735	58.200	9.710	13.500
4.836	71.900	9.961	11.200
4.936	92.400	10.211	8.700
4.986	100.800	10.462	7.000
5.037	130.500	10.713	5.600
5.087	160.700	10.964	4.500
5.137	186.700	11.214	3.600
5.188	203.800	11.465	3.200
5.238	179.100	11.715	2.800
5.288	125.500	11.966	2.300
5.339	76.300	12.217	2.600
5.389	44.000	12.467	3.200
5.439	29.400	12.717	4.900
5.691	7.700	12.968	6.900
5.942	8.300	13.218	7.600
6.194	12.000	13.469	8.300
6.445	13.400	13.719	9.000
6.696	17.300	13.970	9.800
6.948	19.800	14.220	9.800
7.199	24.100	14.470	9.300
7.450	28.100	14.721	9.500
7.702	32.600	14.872	8.780
7.953	39.100	15.375	8.840
8.204	45.000	15.878	8.630
8.455	48.000	16.380	8.510
8.706	46.800	16.883	8.230
8.957	35.200	17.386	9.050
9.208	26.600	17.888	8.340

TABLE 9

(TEXT 17, FIGURE 40)
CENTER OF MASS ANGLE = 125.20

LAB ENERGY	SIGMA	LAB ENERGY	SIGMA
4.634	46.800	9.459	18.900
4.735	52.500	9.710	14.500
4.836	62.400	9.961	12.600
4.936	79.400	10.211	10.400
4.986	92.400	10.462	8.200
5.037	111.400	10.713	8.000
5.087	129.900	10.964	7.700
5.137	154.400	11.214	7.200
5.188	165.200	11.465	6.900
5.238	145.800	11.715	7.900
5.288	98.000	11.966	7.400
5.339	61.300	12.217	6.500
5.389	39.900	12.467	6.400
5.439	26.000	12.717	5.300
5.691	11.300	12.968	4.200
5.942	13.000	13.218	4.200
6.194	16.600	13.469	4.100
6.445	20.600	13.719	3.800
6.696	20.900	13.970	3.900
6.948	26.800	14.220	4.900
7.199	30.200	14.470	5.300
7.450	35.400	14.721	4.400
7.702	39.500	14.872	*******
7.953	44.500	15.375	*******
8.204	50.600	15.878	*******
8.455	52.000	16.380	*******
8.706	47.100	16.883	*******
8.957	36.800	17.386	*******
9.208	27.300	17.888	*******

TABLE 9

(TEXT 17, FIGURE 40)
CENTER OF MASS ANGLE = 135.00

LAB ENERGY	SIGMA	LAB ENERGY	SIGMA
4.634	36.100	9.459	53.200
4.735	38.700	9.710	47.900
4.836	44.800	9.961	43.600
4.936	55.000	10.211	39.900
4.986	64.300	10.462	37.000
5.037	75.800	10.713	34.600
5.087	94.100	10.964	33.500
5.137	121.600	11.214	32.600
5.188	143.000	11.465	32.300
5.238	147.400	11.715	30.700
5.288	122.100	11.966	31.300
5.339	98.000	12.217	29.900
5.389	74.700	12.467	29.500
5.439	66.200	12.717	24.700
5.691	43.700	12.968	21.000
5.942	37.500	13.218	16.100
6.194	35.400	13.469	14.000
6.445	36.500	13.719	10.500
6.696	41.100	13.970	10.700
6.948	45.100	14.220	10.800
7.199	46.700	14.470	11.000
7.450	56.800	14.721	8.900
7.702	65.500	14.872	8.940
7.953	75.800	15.375	8.100
8.204	88.200	15.878	6.630
8.455	89.200	16.380	6.050
8.706	86.900	16.883	6.080
8.957	79.200	17.386	5.670
9.208	68.400	17.888	5.850

Table 10

Data for the ^{4}He(^{3}He, p)^{6}Li and ^{4}He(^{3}He, p^1)^{6}Li* Reactions

Table 10A shows the laboratory differential reaction cross sections for the reactions ^{4}He(^{3}He, p)^{6}Li (SIGMA0) and ^{4}He(^{3}He, p^1)^{6}Li* (SIGMA1) as a function of beam energy (LAB ENERGY) for each laboratory angle investigated. A row of asterisks indicates that the data for that point were not obtained even though the energy was above the required threshold. Table 10B and 10C show angular distributions of the ground state and first excited state protons. The cross sections are listed as a function of the center-of-mass angle. (Pages 18, 19)

TABLE 10

LABORATORY ANGLE = 15.00

LAB ENERGY	SIGMA0	SIGMA1
7.919	5.790	
8.171	8.740	
8.422	9.570	
8.523	10.400	
8.624	10.700	
8.725	10.800	
8.825	12.700	
8.926	12.300	
9.027	14.200	
9.127	15.900	
9.228	17.700	
9.328	20.900	
9.429	23.800	
9.530	27.400	
9.630	29.100	
9.731	30.400	
9.832	28.700	
9.932	27.900	
10.033	25.600	
10.133	22.800	
10.234	21.200	
10.335	17.500	
10.435	17.800	
10.686	15.900	
10.938	16.100	*******
11.189	12.100	*******
11.441	15.700	*******
11.692	12.300	9.670
11.943	11.400	13.800
12.194	10.100	20.100
12.445	9.540	25.900
12.696	7.610	31.900
12.946	6.770	36.700
13.197	6.440	35.500
13.448	5.740	32.500
13.698	5.200	36.300
13.949	4.890	45.900

TABLE 10

LABORATORY ANGLE = 20.00

LAB ENERGY	SIGMA0	SIGMA1
8.422	10.200	
9.731	29.200	
10.435	18.300	
10.938	16.500	*******
11.441	16.000	6.150
12.354	12.910	25.540
12.445	11.500	29.900
13.111	11.310	42.000
13.197	8.740	43.900
13.866	12.340	33.380
14.872	11.310	28.170

TABLE 10

LABORATORY ANGLE = 22.50

LAB ENERGY	SIGMA0	SIGMA1
7.805	5.570	
8.311	8.970	
8.817	12.410	
9.323	19.460	
9.829	28.170	
10.335	19.070	
10.840	16.920	
11.345	15.550	*******
11.850	15.050	11.960
12.102	15.050	23.180
12.354	14.490	29.580
12.607	13.940	41.660
12.859	13.890	60.120
13.111	13.290	49.400
13.363	13.850	65.890
13.614	13.700	52.170
13.866	13.270	36.330
14.118	13.580	31.970
14.369	13.240	28.670
14.872	12.680	34.340
15.375	12.480	33.650
15.878	12.060	33.020
16.380	12.110	29.840
16.883	12.410	29.640
17.386	11.230	32.260
17.888	10.140	30.280

TABLE 10

LABORATORY ANGLE = 25.00

LAB ENERGY	SIGMA0	SIGMA1
7.919	1.030	
8.171	7.510	
8.422	9.180	
8.523	9.740	
8.624	9.980	
8.725	10.800	
8.825	11.500	
8.926	12.300	
9.027	13.100	
9.127	14.100	
9.228	16.500	
9.328	18.500	
9.429	21.900	
9.530	25.200	
9.630	27.100	
9.731	27.300	
9.832	27.200	
9.932	25.200	
10.033	23.100	
10.133	21.700	
10.234	20.700	
10.335	18.700	
10.435	17.700	
10.686	17.100	
10.938	16.200	*******
11.189	15.200	*******
11.441	16.500	6.290
11.692	15.000	11.700
11.943	14.000	16.300
12.194	13.900	25.800
12.445	13.200	30.700
12.696	12.600	41.300
12.946	12.100	46.200
13.197	10.900	56.600
13.448	10.300	44.100
13.698	9.010	46.100

TABLE 10

LABORATORY ANGLE = 27.00

LAB ENERGY	SIGMA0	SIGMA1
12.354	14.370	27.100
13.111	14.670	45.890
13.866	13.870	37.340
14.872	13.510	32.920

TABLE 10

LABORATORY ANGLE = 30.0'0

LAB ENERGY	SIGMA0	SIGMA1
8.422	8.420	
9.731	24.200	
10.435	17.700	
10.938	15.900	******
11.441	17.000	5.560
12.445	14.900	33.400
13.197	12.800	56.300

TABLE **10**

LABORATORY ANGLE =   31.60

LAB ENERGY	SIGMA0	SIGMA1
7.805	5.070	
8.311	8.620	
8.817	10.910	
9.323	16.240	
9.829	23.430	
10.335	17.730	
10.840	15.480	
11.345	14.950	*******
11.850	14.850	12.800
12.102	15.770	23.880
12.354	15.860	33.180
12.607	16.530	45.430
12.859	14.950	50.870
13.111	15.680	52.100
13.363	15.130	42.370
13.614	15.680	46.840
13.866	14.450	42.670
14.118	14.570	40.230
14.369	13.990	34.710
14.872	14.000	32.020
15.375	13.310	28.120
15.878	12.440	25.820
16.380	13.040	24.560
16.883	12.230	23.790
17.386	10.740	22.750
17.888	9.890	18.130

TABLE 10

LABORATORY ANGLE =   35.00

LAB ENERGY	SIGMA0	SIGMA1
8.422	6.850	
9.731	22.000	
10.435	16.000	
10.938	14.600	******
11.441	16.000	******
12.445	16.300	34.400
13.197	15.100	56.700

TABLE 10

LABORATORY ANGLE = 36.80

LAB ENERGY	SIGMA0	SIGMA1
7.805	3.640	
8.311	7.450	
8.817	10.070	
9.323	14.820	
9.829	19.930	
10.335	15.870	
10.840	14.540	
11.345	15.590	*******
11.850	16.070	11.610
12.102	16.460	24.490
12.354	16.520	28.910
12.607	16.550	46.670
12.859	16.590	50.950
13.111	15.530	51.180
13.363	16.090	55.320
13.614	15.910	53.320
13.866	15.020	48.470
14.118	15.400	42.050
14.369	14.280	37.630
14.872	14.050	29.680
15.375	13.420	26.320
15.878	13.260	23.210
16.380	11.780	20.930
16.883	9.860	20.040
17.386	10.090	18.010
17.888	8.390	17.480

TABLE 10

LABORATORY ANGLE = 40.00

LAB ENERGY	SIGMA0	SIGMA1
8.422	1.980	
9.731	19.600	
10.435	14.400	
10.938	14.700	*******
11.441	16.000	*******
12.445	16.800	25.300
13.197	15.900	59.300

TABLE 10

LABORATORY ANGLE = 40.80

LAB ENERGY	SIGMA0	SIGMA1
7.805	******	
8.311	6.850	
8.817	9.700	
9.323	13.650	
9.829	18.710	
10.335	14.000	
10.840	13.870	
11.345	14.860	******
11.850	15.290	13.450
12.102	16.400	21.100
12.354	16.690	26.860
12.607	17.430	41.380
12.859	17.050	51.200
13.111	15.570	55.110
13.363	16.360	53.790
13.614	15.040	52.500
13.866	14.850	48.830
14.118	13.630	40.930
14.369	13.620	38.750
14.872	12.950	31.580
15.375	12.960	25.480
15.878	12.470	23.250
16.380	10.970	20.870
16.883	10.880	19.400
17.386	9.700	17.130
17.888	8.180	15.840

TABLE 10

LABORATORY ANGLE = 45.00

LAB ENERGY	SIGMAO	SIGMA1
7.805	*******	
8.311	*******	
8.523	0.540	
8.624	1.730	
8.725	3.920	
8.817	8.980	
8.825	6.480	
8.926	7.930	
9.027	9.390	
9.127	10.100	
9.228	11.600	
9.323	13.000	
9.328	13.300	
9.429	14.300	
9.530	16.300	
9.630	18.300	
9.731	17.000	
9.829	15.690	
9.832	16.300	
9.932	15.300	
10.033	15.100	
10.133	14.200	
10.234	14.100	
10.335	13.650	
10.435	12.600	
10.686	13.700	
10.840	14.400	
10.938	14.000	*******
11.189	14.300	*******

TABLE 10

LABORATORY ANGLE = 45.00

LAB ENERGY	SIGMA0	SIGMA1
11.345	14.080	******
11.441	15.600	******
11.692	14.300	******
11.850	14.980	7.570
11.943	14.300	14.100
12.102	14.380	16.390
12.194	15.600	17.300
12.354	15.100	23.890
12.445	16.600	30.200
12.607	16.570	39.830
12.696	15.600	43.200
12.859	16.990	51.110
12.946	15.000	52.400
13.111	15.270	56.650
13.197	14.600	49.900
13.363	15.360	54.880
13.448	14.100	54.200
13.614	14.090	48.390
13.698	13.900	50.300
13.866	14.070	46.940
14.118	12.730	42.540
14.369	12.130	36.870
14.872	11.970	30.410
15.375	11.390	25.960
15.878	11.130	21.330
16.380	10.680	21.040
16.883	9.160	17.520
17.386	8.110	16.260
17.888	7.780	14.570

TABLE 10

LABORATORY ANGLE =   50.00

LAB ENERGY	SIGMA0	SIGMA1
9.731	14.300	
10.435	11.900	
10.938	12.100	******
11.441	14.500	******
12.354	14.890	20.140
12.445	14.700	29.900
13.111	13.650	51.000
13.197	14.200	50.700
13.866	11.940	44.220
14.872	10.720	28.760

TABLE **10**

LABORATORY ANGLE = 55.00

LAB ENERGY	SIGMA0	SIGMA1
9.630	12.600	
9.731	12.700	
10.435	11.000	
10.938	11.700	******
11.441	13.600	******
12.354	******	******
12.445	13.100	23.600
13.111	12.160	50.210
13.197	11.900	47.100
14.872	8.930	27.760

TABLE 10

LABORATORY ANGLE =   60.00

LAB ENERGY	SIGMA0	SIGMA1
9.630	******	
9.731	10.100	
10.435	9.570	
10.938	10.400	******
11.441	11.600	******
12.354	******	******
12.445	11.400	18.900
13.111	10.630	59.400
13.197	10.900	39.800
14.872	7.740	26.060

TABLE 10

LABORATORY ANGLE = 65.00

LAB ENERGY	SIGMA0	SIGMA1
9.630	1.440	
9.731	2.390	
9.832	4.480	
9.932	6.150	
10.033	7.510	
10.133	8.700	
10.234	8.030	
10.335	8.600	
10.435	8.640	
10.686	9.330	
10.938	9.420	******
11.189	7.810	******
11.441	10.900	******
11.692	9.290	******
11.943	9.770	******
12.194	10.200	******
12.354	******	******
12.445	10.600	******
12.696	11.000	20.200
12.946	10.200	27.000
13.111	8.590	49.760
13.197	9.370	32.400
13.448	9.160	34.800
13.698	8.670	32.900
14.872	7.370	18.350

TABLE 10

LABORATORY ANGLE = 70.00

LAB ENERGY	SIGMA0	SIGMA1
10.435	7.700	
10.938	*******	*******
11.441	8.440	*******
12.445	9.020	*******
13.197	8.530	25.800

TABLE 10

LABORATORY ANGLE = 75.00

LAB ENERGY	SIGMA0	SIGMA1
10.435	7.180	
10.686	6.690	
10.938	******	******
11.441	7.200	******
12.445	6.910	******
13.197	7.350	******

TABLE 10

LABORATORY ANGLE = 80.00

LAB ENERGY	SIGMA0	SIGMA1
10.435	5.140	
10.938	******	******
11.441	6.660	******
12.445	6.500	******
13.197	6.860	******

TABLE 10

LABORATORY ANGLE = 85.00

LAB ENERGY	SIGMA0	SIGMA1
10.234	4.890	
10.335	5.610	
10.435	5.190	
11.189	5.680	******
11.441	6.350	******
11.692	5.630	******
11.943	5.290	******
12.194	6.170	******
12.445	6.320	******
12.696	5.860	******
12.946	6.100	******
13.197	5.560	******
13.448	5.750	9.620
13.698	4.390	11.300

TABLE **10**

LABORATORY ANGLE = 90.00

LAB ENERGY	SIGMA0	SIGMA1
12.445	5.160	******
12.696	5.440	******
13.197	4.690	******

TABLE 10B

GROUND STATE PROTONS

LAB ENERGY = 10.938

CENTER OF MASS ANGLE	CENTER OF MASS CROSS SECTION
23.9	6.50
31.8	6.82
39.6	6.89
47.3	7.02
55.0	6.73
62.5	7.13
69.9	7.19
77.2	6.64
84.2	6.92
91.1	6.68
97.7	6.63

TABLE 10B

GROUND STATE PROTONS

LAB ENERGY = 12.445

CENTER OF MASS ANGLE	CENTER OF MASS CROSS SECTION
23.0	4.13
30.6	5.09
38.2	6.01
45.7	7.01
53.0	7.99
60.3	8.63
67.4	9.00
74.4	8.46
81.2	8.07
87.9	7.57
94.3	7.64
100.5	7.10
106.4	5.98
112.1	6.22
117.5	6.72
122.7	6.13

TABLE 108

GROUND STATE PROTONS

LAB ENERGY = 13.197

CENTER OF MASS ANGLE	CENTER OF MASS CROSS SECTION
22.7	2.86
30.3	3.96
37.7	5.08
45.1	6.16
52.4	7.56
59.6	8.33
66.6	8.06
73.5	8.31
80.2	7.44
86.8	7.32
93.2	6.81
99.3	6.74
105.2	6.36
110.9	6.54
116.2	5.86
121.4	5.49

TABLE 10C

FIRST EXCITED STATE PROTONS

LAB ENERGY = 12.445

CENTER OF MASS ANGLE	CENTER OF MASS CROSS SECTION
30.0	6.69
40.0	7.94
50.1	8.45
60.1	9.62
70.1	10.50
80.1	8.24
90.1	10.70
100.2	11.60
110.2	10.30
120.2	9.43

TABLE 10C

FIRST EXCITED STATE PROTONS

LAB ENERGY = 13.197

CENTER OF MASS ANGLE	CENTER OF MASS CROSS SECTION
27.7	10.80
36.9	13.70
46.0	18.20
55.1	19.00
64.1	20.10
73.0	22.40
81.9	20.40
90.5	22.60
99.0	23.30
107.3	22.20
115.2	20.80
122.9	19.50

TABLE 10C

FIRST EXCITED STATE PROTONS

LAB ENERGY = 14.872

CENTER OF MASS ANGLE	CENTER OF MASS CROSS SECTION
33.6	10.47
37.7	12.95
45.2	12.81
52.7	12.97
61.1	12.67
67.5	14.14
74.0	14.39
81.7	14.67
89.2	15.42
96.5	15.94
103.4	12.49

Table 11

Experimental Errors

This table shows the experimental errors associated with the ^{3}He + α scattering. The first column shows the laboratory or center-of-mass angle in question. The second column gives the systematic error for the angle and the third column gives the relative errors. The reactions ^{4}He(^{3}He, ^{3}He)^{4}He, ^{4}He(^{3}He, p)^{6}Li and ^{4}He(^{3}He, p^1)^{6}Li* are considered. (Pages 17, 18, 19).

Table 11

Experimental Errors for the $^4\text{He}(^3\text{He},\,^3\text{He})^4\text{He}$,
$^4\text{He}(^3\text{He},\,p)^6\text{Li}$ and $^4\text{He}(^3\text{He},\,p^1)^6\text{Li*}$ Experiments

$$^4\text{He}(^3\text{He},\,^3\text{He})^4\text{He}$$
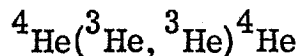
θ_{CM}	Systematic Error (%)	Relative Error (%)	Energy Range (MeV)
39.2	1.1	4 - 5	4.7 - 8.0
	1.1	1.5 - 4	8.0 - 14.7
47.0	1.1	2 - 4	4.7 - 8.0
	1.1	2 - 3.5	8.0 - 14.7
	1.5	2.5	15 - 18
54.7	1.1	2 - 3	4.7 - 8.0
	1.1	1.5 - 2	8.0 - 14.7
	1.5	2	15 - 18
63.4	1.1	1.5 - 2.5	4.7 - 5.25
	1.1	3 - 7	5.25 - 5.4
	1.1	2 - 2.5	5.5 - 8
	1.1	2.5 - 5	8 - 14.7
	1.5	1 - 2	15 - 18
70.1	1.1	2.5 - 5	4.7 - 8
	1.1	3 - 5	8 - 14.7
	1.5	1.5 - 2	15 - 18
77.0	1.1	2.5 - 3	4.7 - 8.0
	1.1	3.0 - 4.5	8 - 14.7
	1.5	1.5 - 2.5	15 - 18
80.0	1.1	2.5 - 3.5	4.7 - 8
	1.1	3.5 - 4.5	8 - 13
85.3	1.1	2.5 - 3.5	4.7 - 8
	1.1	3.5 - 5.5	8 - 14.7
90.0	1.1	2.5 - 3	4.7 - 8
	1.1	2.5 - 5.5	8 - 14.7
	1.5	2.5 - 3.5	15 - 18

178

Table 11 (cont.)

θ_{CM}	Systematic Error (%)	Relative Error (%)	Energy Range (MeV)
98.4	1.1	1.5 - 3	4.7 - 8
	1.1	2 - 4	8 - 13.25
	1.1	4 - 6	13.25 - 14.7
	1.5	3 - 5	15 - 18
106.4	1.1	1.5 - 3.5	4.7 - 8
	1.1	2.5 - 5	8 - 14.7
	1.5	2.5 - 3.5	15 - 18
116.8	1.1	1 - 2.5	4.7 - 5.5
	1.1	2.5 - 5	5.5 - 8
	1.1	2 - 5	8 - 10
	1.1	5 - 9	10 - 14.7
	1.5	2.5	15 - 18
125.2	1.1	1.5 - 3.5	4.7 - 8
	1.1	2 - 5	8 - 14.7
	1.5	2.5 - 3	15 - 18
135.0	1.1	1 - 2	4.7 - 8
	1.1	2 - 4	8 - 14.7

Table 11 (cont.)

$$^4\text{He}(^3\text{He}, \text{p})^6\text{Li}$$
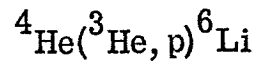
Laboratory Angle	Systematic Error %	Relative Error %
15	1.1	2.5 - 4.5
20	1.1	2.5 - 4.5
22.5	1.5	2 - 4
25	1.1	3 - 5
27	1.5	4
30	1.1	3 - 5
31.6	1.5	2.5 - 4.5
35	1.1	4 - 6
36.8	1.5	3.5 - 6
40	1.1	4 - 8
40.8	1.5	4 - 6
45	1.1	5 - 10 (8-13.8 MeV)
	1.5	4 - 6 (14-18 MeV)
50	1.1	5
55	1.1	5
60	1.1	6
65	1.1	6 - 12
70	1.1	7
75	1.1	7
80	1.1	7 - 12
85	1.1	7 - 9
90	1.1	8

Table 11 (cont.)

$$^4\text{He}(^3\text{He}, p^1)^6\text{Li}^*$$
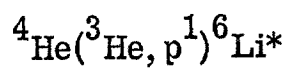
Laboratory Angle	Systematic Error %	Relative Error %
15	1.1	6 - 10
20	1.1	15
22.5	1.5	15
25	1.1	15
27		15
30	1.1	15
31.6		15
35	1.1	15
36.8		15
40	1.1	15
40.8		15
45	1.5	12
50	1.1	10
55	1.1	10
60	1.1	8
65	1.1	8
70	1.1	8
85	1.1	10

Table 12

$^3H(\alpha, \alpha)^3H$ Phase Shifts in Degrees

This table shows the phase shifts obtained from the $^3H + \alpha$ scattering data. The laboratory energy is shown in the first column (ELAB). The quality of the fit at that energy is indicated by χ^2 in the second column (CHI2). The number at the top of each of the next 7 columns gives the value of $J\pi$ for the phase shifts listed below. The letter 0 indicates the real phase shifts $\delta_{J\pi}$. The letter X indicates the parameters $X_{J\pi}$ used in the analysis. Tables 12A and 12C show the real phase shifts and $X_{J\pi}$'s obtained from data below 13.1 MeV. Tables 12B and 12D show the real phase shifts and $X_{J\pi}$'s obtained from data above 12.8 MeV (data obtained using negative ion injection). (Page 28)

TABLE 12A

LI7 PHASE SHIFTS

ELAB	CHI2	D1/2+	D3/2-	D1/2-	D5/2+	D3/2+	D7/2-	D5/2-
3.612	24.000	-34.15	158.27	148.56	-3.12	-14.84	-6.53	-4.77
3.717	12.400	-31.80	159.35	145.97	1.58	2.52	-1.20	-0.90
3.822	6.590	-35.15	160.71	148.71	0.73	8.27	1.98	-1.08
3.916	4.030	-35.00	164.15	154.44	4.80	9.49	4.00	-1.10
4.031	0.721	-35.00	162.00	150.00	4.45	5.66	7.58	-5.66
4.135	1.780	-36.00	163.15	153.44	4.33	1.73	6.00	-0.60
4.239	1.610	-37.00	163.15	151.15	0.50	1.20	7.00	-0.60
4.343	1.340	-38.00	163.15	150.15	3.22	-0.95	8.00	0.
4.447	0.773	-38.00	162.15	149.00	5.00	-4.00	11.20	-2.00
4.551	0.663	-39.00	162.15	145.71	0.70	-1.10	12.30	-0.90
4.655	0.883	-40.00	162.15	145.71	0.	-2.00	14.90	-0.40
4.758	0.943	-41.00	161.00	147.00	1.10	-1.90	20.00	0.50
4.862	0.878	-41.00	160.00	147.00	-1.80	-1.10	28.70	1.80
4.913	0.951	-42.00	158.85	147.00	-3.47	0.93	36.39	2.90
4.966	1.350	-42.00	158.85	149.29	-5.20	0.40	49.53	3.35
5.017	1.790	-42.00	161.15	151.73	-3.08	-3.51	69.20	2.90
5.069	1.940	-41.85	158.85	151.73	-0.26	-0.75	84.45	-17.22
5.121	3.060	-45.29	158.85	147.15	10.60	-0.20	121.60	-3.30
5.172	1.750	-44.15	157.85	146.15	7.61	0.18	137.94	-0.48
5.224	1.210	-44.00	157.85	145.00	4.43	-1.72	147.10	0.10
5.276	0.944	-44.00	159.00	143.85	3.86	-0.74	153.90	3.10
5.328	1.240	-45.15	159.00	142.85	2.00	-1.00	158.40	3.00
5.379	0.793	-46.15	158.00	141.71	0.80	-1.20	161.10	3.29
5.431	0.631	-46.15	156.85	140.56	2.40	0.	163.40	2.00
5.482	0.620	-46.15	156.85	140.71	1.30	-0.80	164.30	2.00
5.585	0.441	-47.15	156.85	138.42	1.97	1.53	167.80	2.78
5.689	0.522	-46.00	157.00	138.42	1.80	1.20	169.12	3.68
5.946	0.305	-48.00	156.00	136.27	1.50	1.27	171.19	4.14

TABLE 12A

LI7 PHASE SHIFTS

ELAB	CHI2	D1/2+	D3/2-	D1/2-	D5/2+	D3/2+	D7/2-	D5/2-
6.203	0.419	-47.85	156.00	135.27	1.10	2.00	172.71	6.02
6.460	0.443	-49.85	155.00	133.12	0.06	0.06	172.94	6.99
6.717	0.537	-50.85	154.00	129.83	-0.40	4.60	173.91	9.87
6.973	0.802	-51.85	153.00	131.12	-0.73	4.10	174.60	11.60
7.228	0.656	-52.85	153.15	130.12	1.00	5.60	175.09	14.22
7.484	0.897	-55.00	151.00	131.42	1.29	7.18	174.62	16.89
7.739	0.777	-56.00	150.00	133.85	1.48	10.99	175.08	21.14
7.994	0.720	-56.00	146.71	134.00	0.79	6.82	175.43	25.99
8.249	0.527	-58.15	144.56	136.44	0.83	8.11	175.19	30.83
8.504	0.309	-58.15	142.42	135.44	2.08	8.50	176.74	37.65
8.759	0.608	-58.00	142.56	136.73	2.40	6.30	176.85	45.07
9.012	0.750	-58.00	141.56	136.88	1.86	6.91	176.58	54.05
9.266	0.951	-59.15	140.56	137.02	1.20	1.30	178.86	64.18
9.520	0.787	-60.15	140.71	137.17	1.60	-0.20	179.70	76.22
9.774	1.162	-59.00	139.85	137.31	1.89	0.82	180.10	88.82
10.027	0.960	-60.00	139.30	132.00	3.23	4.22	182.70	99.40
10.280	1.300	-60.80	138.80	127.00	5.87	7.14	186.50	110.30
10.534	1.976	-61.60	138.30	122.00	8.85	12.35	188.10	116.90
10.787	1.686	-62.40	137.80	117.00	5.83	10.73	185.00	124.00
11.040	1.283	-63.30	137.30	113.67	6.02	9.70	181.88	133.30
11.293	0.654	-64.45	135.10	111.80	3.90	5.20	179.90	136.70
11.343	0.902	-64.49	135.10	111.90	3.10	3.20	180.30	138.60
11.393	0.807	-68.10	133.90	114.30	2.90	3.00	178.30	139.00
11.444	0.876	-69.19	133.90	114.40	3.30	1.20	179.20	142.00
11.494	0.959	-65.75	133.90	114.45	2.80	2.10	179.80	145.70
11.545	0.676	-66.29	133.90	115.55	2.39	1.20	177.45	147.80
11.595	1.115	-62.90	136.10	114.61	1.58	0.26	176.74	142.90
11.645	1.055	-61.75	135.00	108.85	2.73	0.13	179.03	131.00

TABLE 12A

LI7 PHASE SHIFTS

ELAB	CHI2	D1/2+	D3/2-	D1/2-	D5/2+	D3/2+	D7/2-	D5/2-
11.697	1.099	-60.61	135.00	107.65	3.94	2.11	182.97	127.30
11.747	0.871	-65.60	134.00	106.65	3.68	3.93	180.73	127.70
11.798	0.782	-69.05	134.00	107.85	2.10	0.40	181.50	130.00
11.848	0.625	-66.75	134.00	107.85	3.80	2.90	180.40	132.10
11.899	0.882	-70.75	134.05	106.80	2.40	1.80	180.10	132.90
11.950	0.706	-73.05	132.90	108.00	3.00	1.10	179.70	133.80
12.001	0.711	-68.45	134.00	108.00	2.10	1.40	180.20	135.70
12.051	0.841	-72.35	134.00	108.15	2.70	1.30	179.40	136.60
12.101	0.570	-73.50	132.90	108.10	1.70	0.10	179.60	136.60
12.152	0.867	-73.50	131.90	106.95	1.81	1.17	178.46	136.60
12.202	0.879	-75.14	131.90	108.15	3.20	1.20	179.30	137.70
12.253	0.777	-75.15	131.90	108.25	2.00	0.70	179.00	137.80
12.304	1.694	-79.79	133.00	110.55	1.51	1.55	175.55	138.85
12.558	1.250	-79.14	131.90	108.45	3.90	1.20	179.10	142.30
12.810	1.142	-74.99	129.75	108.55	3.61	0.47	179.16	142.30
13.063	2.006	-77.84	129.75	107.55	2.00	-1.40	181.30	144.60

TABLE 12B

L17 PHASE SHIFTS

ELAB	CHI2	D1/2+	D3/2-	D1/2-	D5/2+	D3/2+	D7/2-	D5/2-
12.810	0.680	-76.64	136.60	110.14	-2.50	-2.50	183.00	146.00
13.063	0.671	-77.71	136.89	109.17	-2.50	-2.50	183.00	147.00
13.315	0.678	-77.91	133.93	108.40	-2.50	-2.50	185.09	150.15
13.568	1.038	-81.01	134.01	108.54	-2.50	-2.50	185.44	150.98
13.820	1.013	-81.59	132.09	107.24	-2.50	-2.50	185.40	151.86
14.073	0.997	-83.50	130.23	105.88	-1.89	-3.47	184.63	152.08
14.325	0.727	-82.00	128.00	105.00	-2.50	-2.50	186.00	152.00
14.577	0.730	-83.62	126.63	103.27	-2.50	-2.50	185.45	153.00
14.829	1.110	-83.20	123.31	102.54	-2.50	-2.50	187.00	152.00
15.082	0.488	-85.00	122.00	102.00	-3.35	-1.73	187.60	151.03
15.333	0.229	-84.27	120.15	99.86	-3.39	-1.77	189.15	152.00
15.585	0.549	-89.04	119.98	100.51	-3.32	-1.70	190.00	151.00
15.837	0.379	-90.29	117.51	99.23	-1.83	-3.43	194.15	151.00
15.938	0.345	-90.21	118.46	100.99	-1.76	-3.37	197.15	151.00
16.039	0.573	-91.00	118.32	100.92	-0.79	-4.03	200.29	151.00
16.139	0.821	-88.05	116.36	100.06	-3.42	-6.69	207.12	149.46
16.241	1.359	-89.17	115.60	101.27	-2.89	-6.35	210.78	145.78
16.341	1.082	-90.15	112.68	103.43	-0.89	-7.98	220.01	147.75
16.442	1.751	-87.12	120.23	106.61	2.11	-0.35	214.78	130.20
16.542	2.541	-94.53	119.71	100.45	-1.21	-2.83	212.25	121.78
16.643	3.137	-92.30	123.23	97.70	-1.16	-2.78	213.15	121.68
16.743	1.413	-99.17	129.91	85.86	2.00	-1.50	193.75	115.48
16.844	6.788	-90.12	100.81	79.38	3.42	-0.36	105.62	142.87
16.944	3.939	-93.45	106.27	78.42	2.27	0.29	119.98	143.55
17.046	2.909	-95.10	108.38	76.99	1.98	3.77	133.38	144.19
17.146	1.034	-94.21	113.74	73.52	2.62	12.80	144.59	147.06
17.247	2.460	-100.10	115.11	75.57	1.25	1.64	144.06	148.02
17.347	3.501	-100.00	118.13	77.50	-0.10	0.78	145.96	149.67

TABLE 12B

LI7 PHASE SHIFTS

ELAB	CHI2	D1/2+	D3/2-	D1/2-	D5/2+	D3/2+	D7/2-	D5/2-
17.448	4.887	-99.01	120.54	79.84	-0.86	-1.86	148.31	149.45
17.548	4.448	-101.64	119.69	77.83	-1.46	-0.46	151.96	148.92
17.648	4.047	-104.01	121.72	81.73	0.23	1.88	149.25	150.13
17.849	4.487	-108.83	120.68	81.49	-0.16	1.62	152.71	149.35
18.100	2.819	-112.19	118.74	80.76	-0.25	0.53	153.77	150.01

TABLE 12C

LI7 PHASE SHIFTS

ELAB	CHI2	X1/2+	X3/2-	X1/2-	X5/2+	X3/2+	X7/2-	X5/2-
11.293	0.654	16.50	-0.	-0.	-0.	-0.	-0.	4.30
11.343	0.902	18.00	-0.	-0.	-0.	-0.	-0.	6.30
11.393	0.807	18.50	-0.	-0.	-0.	-0.	-0.	8.80
11.444	0.876	20.00	-0.	-0.	-0.	-0.	-0.	12.40
11.494	0.959	20.50	-0.	-0.	-0.	-0.	-0.	17.40
11.545	0.676	21.50	-0.	-0.	-0.	-0.	-0.	24.10
11.595	1.115	22.00	-0.	-0.	-0.	-0.	-0.	31.90
11.645	1.055	23.00	-0.	-0.	-0.	-0.	-0.	36.50
11.697	1.099	23.50	-0.	-0.	-0.	-0.	-0.	33.30
11.747	0.871	24.00	-0.	-0.	-0.	-0.	-0.	28.30
11.798	0.782	24.50	-0.	-0.	-0.	-0.	-0.	24.20
11.848	0.625	25.00	-0.	-0.	-0.	-0.	-0.	20.90
11.899	0.882	25.50	-0.	-0.	-0.	-0.	-0.	18.30
11.950	0.706	26.00	-0.	-0.	-0.	-0.	-0.	16.50
12.001	0.711	26.50	-0.	-0.	-0.	-0.	-0.	15.00
12.051	0.841	27.00	-0.	-0.	-0.	-0.	-0.	13.90
12.101	0.570	27.50	-0.	-0.	-0.	-0.	-0.	12.90
12.152	0.867	27.50	-0.	-0.	-0.	-0.	-0.	12.20
12.202	0.879	28.00	-0.	-0.	-0.	-0.	-0.	11.50
12.253	0.777	28.50	-0.	-0.	-0.	-0.	-0.	10.80
12.304	1.694	29.00	-0.	-0.	-0.	-0.	-0.	10.60
12.558	1.250	30.00	-0.	-0.	-0.	-0.	-0.	10.00
12.810	1.142	31.00	-0.	-0.	-0.	-0.	-0.	9.40
13.063	2.006	32.00	-0.	-0.	-0.	-0.	-0.	8.80

TABLE 12D

LI7 PHASE SHIFTS

ELAB	CHI2	X1/2+	X3/2-	X1/2-	X5/2+	X3/2+	X7/2-	X5/2-
12.810	0.680	22.50	-0.	-0.	-0.	22.50	-0.	5.00
13.063	0.671	24.50	-0.	-0.	-0.	24.50	-0.	-0.
13.315	0.673	26.50	-0.	-0.	-0.	26.50	-0.	-0.
13.568	1.038	28.00	-0.	-0.	-0.	28.00	-0.	-0.
13.820	1.013	29.50	-0.	-0.	-0.	29.50	-0.	-0.
14.073	0.997	31.50	-0.	-0.	-0.	31.50	-0.	-0.
14.325	0.727	32.50	-0.	-0.	-0.	32.50	-0.	-0.
14.577	0.730	34.00	-0.	-0.	-0.	34.00	-0.	-0.
14.829	1.110	35.50	-0.	-0.	-0.	35.50	-0.	-0.
15.082	0.488	36.50	-0.	-0.	-0.	36.50	-0.	-0.
15.333	0.229	37.50	-0.	-0.	-0.	37.50	-0.	-0.
15.585	0.549	38.00	-0.	-0.	-0.	38.00	-0.	-0.
15.837	0.379	39.00	-0.	-0.	-0.	39.00	-0.	-0.
15.938	0.345	39.00	-0.	-0.	-0.	39.00	-0.	-0.
16.039	0.573	39.50	-0.	-0.	-0.	39.50	-0.	-0.
16.139	0.821	39.00	5.50	-0.	-0.	39.00	-0.	-0.
16.241	1.359	39.50	9.50	-0.	-0.	39.50	6.50	-0.
16.341	1.082	39.50	13.00	-0.	-0.	39.50	14.50	-0.
16.442	1.751	39.50	15.00	-0.	-0.	39.50	24.00	-0.
16.542	2.541	39.50	17.50	-0.	-0.	39.50	33.00	-0.
16.643	3.137	39.50	20.00	-0.	-0.	39.50	43.00	-0.
16.743	1.413	39.50	21.00	-0.	-0.	39.50	49.50	-0.
16.844	6.788	39.50	23.00	-0.	-0.	39.50	50.50	-0.
16.944	3.939	39.00	25.00	-0.	-0.	39.00	51.00	-0.
17.046	2.909	39.00	26.50	-0.	-0.	39.00	49.50	-0.
17.146	1.034	39.00	27.50	-0.	-0.	39.00	47.00	-0.
17.247	2.460	39.00	29.00	-0.	-0.	39.00	44.50	-0.
17.347	3.501	38.50	30.50	-0.	-0.	38.50	41.50	-0.

TABLE 12D

LI7 PHASE SHIFTS

ELAB	CHI2	X1/2+	X3/2-	X1/2-	X5/2+	X3/2+	X7/2-	X5/2-
17.448	4.887	38.50	32.00	-0.	-0.	38.50	38.50	-0.
17.548	4.448	38.50	33.50	-0.	-0.	38.50	36.50	-0.
17.648	4.047	38.00	34.50	-0.	-0.	38.00	34.00	-0.
17.849	4.487	37.50	36.50	-0.	-0.	37.50	30.00	-0.
18.100	2.819	37.00	39.50	-0.	-0.	37.00	27.00	-0.

Table 13

^{4}He(^{3}He, ^{3}He)^{4}He Phase Shifts in Degrees

      This table shows the phase shifts obtained from the ^{3}He + ^{4}He scattering data. The laboratory energy is shown in the first column (ELAB). The quality of the fit at that energy is indicated by χ^2 in the second column (CHI2). The number at the top of each of the next 7 columns gives the value of Jπ for the phase shifts listed below. The letter D indicates the real phase shifts $\delta_{J\pi}$. The letter X indicates the parameters $X_{J\pi}$ used in the analysis. Table 13A shows the real phase shifts and Table 13B shows the parameter $X_{J\pi}$.
(Page 28)

TABLE 13A

BE7 PHASE SHIFTS

ELAB	CHI2	D1/2+	D3/2-	D1/2-	D5/2+	D3/2+	D7/2-	D5/2-
4.634	0.396	-37.40	151.10	142.80	-3.00	-2.00	10.29	4.33
4.735	0.490	-38.40	151.20	139.30	-3.50	-2.30	6.95	11.44
4.836	0.656	-39.40	148.30	141.10	-3.50	-1.80	16.99	5.20
4.936	0.250	-41.10	147.40	139.80	-2.30	-1.10	23.68	5.73
4.986	1.621	-41.00	148.70	140.50	-3.40	0.70	28.48	5.31
5.037	0.393	-42.10	146.70	138.60	-5.10	2.40	35.46	6.75
5.087	0.328	-43.35	146.02	136.55	-8.90	6.70	44.03	8.13
5.137	1.639	-41.93	149.21	138.33	-12.11	9.17	57.01	8.21
5.188	4.297	-44.15	151.15	143.05	-3.07	1.24	68.99	5.48
5.238	3.079	-44.07	149.26	139.85	-2.18	-3.43	89.07	11.64
5.288	1.313	-48.15	142.81	138.54	-0.12	-4.92	101.94	2.43
5.339	0.801	-44.23	143.06	137.40	-0.01	-4.08	117.26	4.06
5.389	0.840	-43.49	143.19	137.41	1.02	-1.06	128.90	5.20
5.439	0.761	-42.01	142.75	136.05	0.96	-0.34	135.41	5.57
5.691	0.636	-40.70	146.12	130.12	-3.18	-2.69	151.13	5.75
5.942	0.870	-50.10	144.83	133.86	-4.24	-2.01	162.91	8.10
6.194	0.987	-51.52	143.21	132.95	-4.95	-1.97	166.93	9.59
6.445	0.853	-52.55	141.82	131.97	-4.85	-1.82	167.97	11.41
6.696	0.657	-54.68	140.06	130.78	-5.49	-1.64	168.90	13.71
6.948	0.845	-56.78	139.11	129.59	-3.83	-2.23	169.10	16.51
7.199	0.880	-58.59	138.06	128.86	-4.28	-2.01	170.46	19.75
7.450	1.065	-60.66	135.59	128.68	-3.00	-2.00	170.65	26.36
7.702	0.682	-62.11	133.52	127.29	-3.05	-3.51	170.66	32.32
7.953	0.842	-63.29	131.26	126.61	-2.14	-7.38	171.74	41.98
8.204	0.693	-64.93	129.90	124.61	-0.21	-14.80	172.68	53.73
8.455	0.874	-68.67	132.52	126.42	0.25	-10.88	173.79	64.47
8.706	1.179	-71.40	134.30	126.60	-7.12	-3.46	173.30	75.00
8.957	0.615	-72.07	131.83	122.86	-5.16	-2.75	170.98	83.27

TABLE 13A

BE7 PHASE SHIFTS

ELAB	CHI2	D1/2+	D3/2-	D1/2-	D5/2+	D3/2+	D7/2-	D5/2-
9.208	0.610	-72.68	131.33	118.11	-3.00	-2.00	169.01	94.31
9.459	1.126	-73.51	130.33	115.99	-1.59	2.19	170.68	104.91
9.710	0.806	-73.39	129.57	114.59	-1.55	4.09	170.51	108.95
9.961	0.672	-73.66	130.47	112.61	-3.75	3.38	170.24	113.60
10.211	0.461	-70.62	126.32	114.89	-4.89	3.37	170.48	119.30
10.462	0.727	-72.80	124.66	117.38	-5.59	2.35	169.90	122.60
10.713	0.459	-73.74	122.96	116.04	-4.63	2.67	170.77	125.43
10.964	0.950	-76.20	120.22	116.35	-4.36	-0.35	170.76	127.35
11.214	0.744	-77.12	118.26	116.35	-2.88	-0.39	172.13	129.17
11.465	1.011	-78.46	116.66	115.62	-2.99	-1.46	172.64	130.14
11.715	2.070	-78.76	115.23	115.08	-3.90	-0.76	173.74	130.78
11.966	1.216	-79.31	114.53	113.14	-2.78	-1.41	176.75	130.94
12.217	1.274	-79.66	113.32	110.34	-1.77	-0.52	177.77	130.05
12.467	1.398	-80.20	110.80	107.37	-1.96	0.39	182.91	130.09
12.717	1.236	-79.90	107.71	103.56	-1.67	-0.76	190.14	133.64
12.968	4.342	-81.94	105.51	98.70	0.20	-2.34	192.54	139.89
13.218	1.262	-83.06	109.16	101.10	0.74	-1.95	185.64	140.11
13.469	1.091	-83.45	109.48	98.62	-0.54	-2.38	170.33	140.71
13.719	1.796	-84.39	110.36	98.93	1.82	-5.90	156.81	142.63
13.970	1.495	-85.81	109.17	99.25	1.35	-7.72	155.06	142.19
14.220	1.905	-86.85	109.59	98.25	-0.21	-3.59	153.97	143.49
14.470	1.130	-86.72	110.75	96.60	-0.97	-1.96	155.74	143.98
14.721	1.500	-87.33	114.02	97.54	-1.55	-2.28	154.58	145.80
14.872	0.359	-87.53	115.04	96.97	0.02	-1.69	154.95	147.39
15.375	0.634	-89.22	117.76	97.03	-0.51	-1.74	153.49	149.43
15.878	0.598	-90.45	121.42	100.81	-2.20	-1.39	149.60	148.79
16.380	0.317	-93.63	124.72	102.45	-1.68	-1.14	149.93	148.60
16.880	0.526	-96.71	126.47	102.79	-1.60	-1.73	149.60	149.58

TABLE 13A

BE7 PHASE SHIFTS

ELAB	CHI2	D1/2+	D3/2-	D1/2-	D5/2+	D3/2+	D7/2-	D5/2-
17.386	0.575	-98.60	127.06	103.76	-2.50	-2.50	149.10	148.21
17.888	0.831	-100.53	128.14	105.54	-2.50	-2.50	148.00	150.50

TABLE 13B

BE7 PHASE SHIFTS

ELAB	CHI2	X1/2+	X3/2-	X1/2-	X5/2+	X3/2+	X7/2-	X5/2-
7.450	1.065	6.00	0.	0.	0.	6.00	0.	0.50
7.702	0.682	9.00	0.	0.	0.	9.00	0.	1.00
7.953	0.842	11.00	0.	0.	0.	11.00	0.	1.50
8.204	0.693	12.50	0.	0.	0.	12.50	0.00	2.00
8.455	0.874	14.00	0.	0.	0.	14.00	0.	0.50
8.706	1.179	15.00	0.	0.	0.	15.00	0.	5.00
8.957	0.615	15.50	0.	0.	0.	15.50	0.	8.00
9.208	0.610	16.50	0.	0.	0.	16.50	0.	12.00
9.459	1.126	17.00	0.	0.	0.	17.00	0.	17.50
9.710	0.806	18.00	0.	0.	0.	18.00	0.	22.00
9.961	0.672	20.50	0.	0.	0.	20.50	0.	22.00
10.211	0.461	22.00	0.	0.	0.	22.00	0.00	8.00
10.462	0.727	23.50	0.	0.	0.	23.50	0.	15.50
10.713	0.459	25.50	0.	0.	0.	25.50	0.	13.00
10.964	0.950	27.00	0.	0.	0.	27.00	0.	11.50
11.214	0.744	28.50	0.	0.	0.	28.50	0.	9.50
11.465	1.011	29.50	5.00	0.	5.00	29.50	4.00	8.00
11.715	2.070	31.00	7.00	0.	7.00	31.00	8.50	5.50
11.966	1.216	32.00	9.50	0.	9.50	32.00	13.00	3.50
12.217	1.274	32.50	11.00	0.	11.00	32.50	19.50	0.
12.467	1.398	33.00	12.50	0.	12.50	33.00	28.50	0.
12.717	1.236	33.50	13.50	0.	13.50	33.50	43.00	0.
12.968	4.342	34.00	14.50	0.	14.50	34.00	57.00	0.
13.218	1.262	34.50	16.00	0.	16.00	34.50	63.50	0.
13.469	1.091	35.00	16.50	0.	16.50	35.00	63.00	0.
13.719	1.796	35.50	17.50	0.	17.50	35.50	59.50	0.
13.970	1.495	36.00	18.50	0.	18.50	36.00	54.00	0.
14.220	1.905	36.50	19.50	0.	19.50	36.50	48.50	0.

TABLE 13B

BE7 PHASE SHIFTS

ELAB	CHI2	X1/2+	X3/2-	X1/2-	X5/2+	X3/2+	X7/2-	X5/2-
14.470	1.130	37.00	20.00	0.	20.00	37.00	43.00	0.
14.721	1.500	37.50	21.00	0.	21.00	37.50	38.50	0.
14.872	0.359	37.50	21.50	0.	21.50	37.50	36.00	0.
15.375	0.634	38.00	22.50	0.	22.50	38.00	30.00	0.
15.878	0.598	38.00	23.50	0.	23.50	38.00	25.00	0.
16.380	0.317	38.00	24.00	0.	24.00	38.00	20.50	0.
16.883	0.526	38.50	24.50	0.	24.50	38.50	16.00	0.
17.386	0.575	38.50	25.50	0.	25.50	38.50	10.50	0.
17.888	0.831	38.50	26.00	0.	26.00	38.50	0.	0.

Table 14

Resonance Energies and Reduced Widths

This table shows the resonance energies and reduced widths obtained for ^{7}Li and ^{7}Be. A radius of 4.0 Fermis was used for the analysis of all the levels. The subscripts n_0 and p_0 refer to the decay of the level to ^{6}Li + nucleon. The subscripts n_1 and p_1 refer to the decay of the level to ^{6}Li* + nucleon. (Pages 40, 41)

Table 14

^{7}Li

State	J_π	γ^2_α (MeV)	θ^2_α	γ^2_{n0} (MeV)	θ^2_{n0}	γ^2_{n1} (MeV)	θ^2_{n1}	E_{res} (MeV)
$^2F_{7/2}$	$7/2^-$	1.3 ± 0.1	0.57 ± 0.04	–	–	–	–	4.65 ± 0.05
$^2F_{5/2}$	$5/2^-$	3.1 ± 0.3	1.36 ± 0.13	0.00 ± 0.01	0.000 ± 0.002	–	–	6.64 ± 0.10
$^4P_{5/2}$	$5/2^-$	0.024 ± 0.003	0.011 ± 0.001	1.2 ± 0.1	0.26 ± 0.02	–	–	7.47 ± 0.03
$^4D_{7/2}$	$7/2^-$	1.2 ± 0.5	0.53 ± 0.22	–	–	10.6 ± 3.0	2.3 ± 0.7	9.67 ± 0.10

$$\theta^2_c = \frac{\gamma^2_c}{\dfrac{3\hbar^2}{2\mu_c a^2_c}}$$

where a is the radius of interaction and μ is the reduced mass of the particle pair c.

Table 14 (cont.)

^{7}Be

State	J_π	γ^2_α (MeV)	θ^2_α	γ^2_{p0} (MeV)	θ^2_{p0}	γ^2_{p1} (MeV)	θ^2_{p1}	E_{res} (MeV)
$^2F_{7/2}$	$7/2^-$	1.6 ± 0.1	0.70 ± 0.04	–	–	–	–	4.57 ± 0.05
$^2F_{5/2}$	$5/2^-$	3.1 ± 0.3	1.36 ± 0.13	0.00 ± 0.01	0.000 ± 0.002	–	–	6.73 ± 0.10
$^4P_{5/2}$	$5/2^-$	0.023 ± 0.003	0.010 ± 0.001	1.2 ± 0.1	0.26 ± 0.02	–	–	7.21 ± 0.06
$^4D_{7/2}$	$7/2^-$	1.6 ± 0.6	0.70 ± 0.26	$1.3 \begin{smallmatrix} +0.4 \\ -0.8 \end{smallmatrix}$	$0.29 \begin{smallmatrix} +0.09 \\ -0.18 \end{smallmatrix}$	8.4 ± 2.5	$1.8 \pm .5$	9.27 ± 0.10

Figure 1

The Tritium Chamber

The tritium chamber is shown as seen from the top on a horizontal plane through the beam line. The numbered items are listed below.

(1) Blank off flange connecting to the force equalization bellows.
(2) Outer body of Faraday cup.
(3) Brass Faraday cup body.
(4) Tantalum liner.
(5) Teflon insulator.
(6) Electrical feed through.
(7) Suppression magnet.
(8) Lucite insulator.
(9) Tantalum aperture.
(10) Brass insert.
(11) Chamber body.
(12) Brass can for counters.
(13) Lucite can holders.
(14) Counter collimator.
(15) Gas cell windows.
(16) Brass counter collimator slits.
(17) To main pumping system.
(18) Gas cell body.
(19) Typical O-ring seal.
(20) Vacuum passage to gas handling system.
(21) Receptacle for gas manifold.
(22) Spacers for collimation disks.
(23) Tantalum collimation disks.
(24) Gas cell support.
(25) Beam collimator.
(26) To upstream pumping and second set of slits.

(Pages 3, 4)

STEEL
BRASS
ALUMINUM
LUCITE
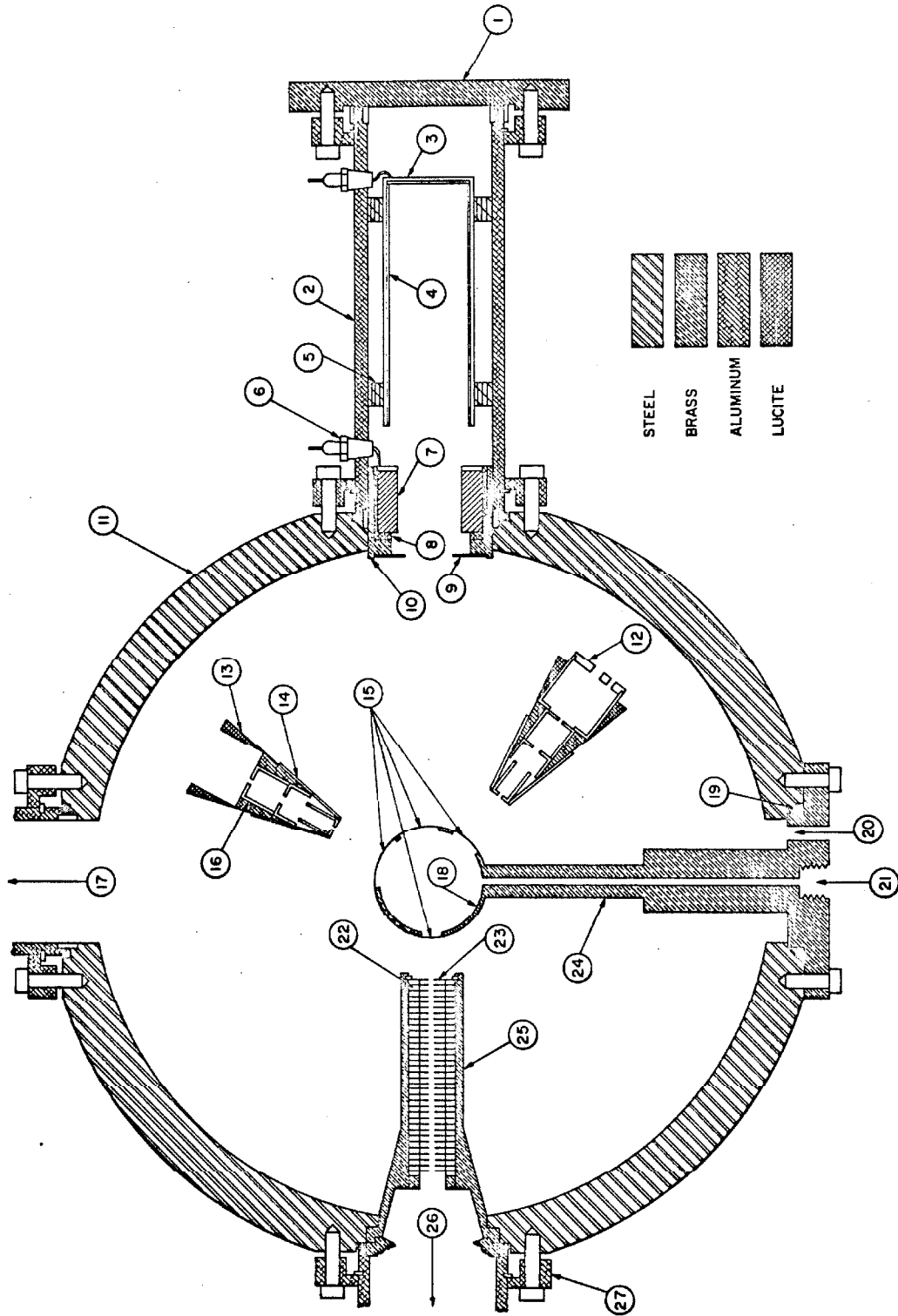
Figure 2

Gas Handling System

A schematic diagram of the gas handling system used in the $^3H(\alpha, \alpha)^3H$ experiment.   (Page 5)

SCHEMATIC DIAGRAM OF GAS
HANDLING SYSTEM FOR
T (a,a)T EXPERIMENT
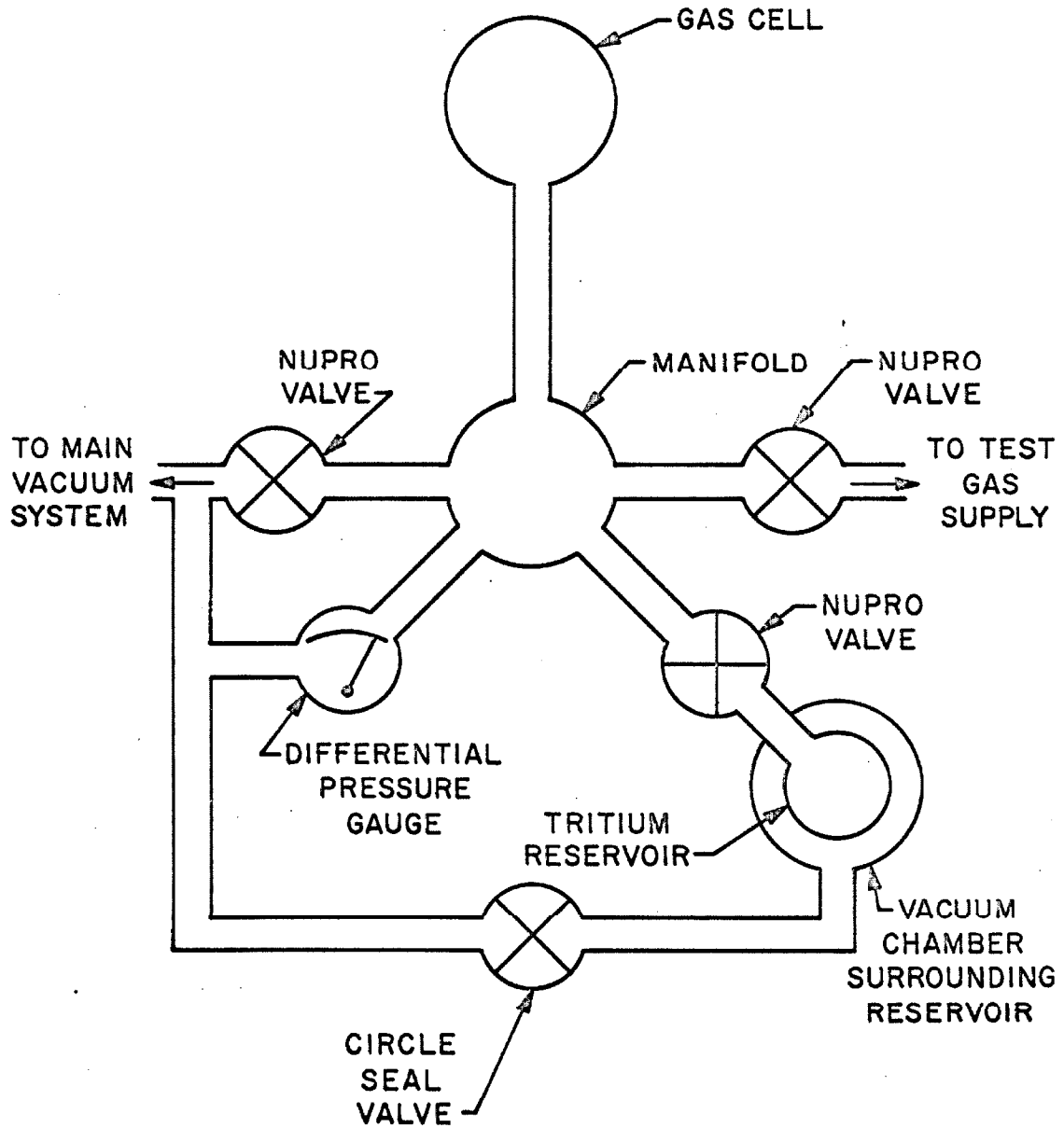
Figure 3

Tritium Reservoir

A schematic diagram of the reservoir used to store the tritium as uranium tritude. (Pages 6, 63)

204
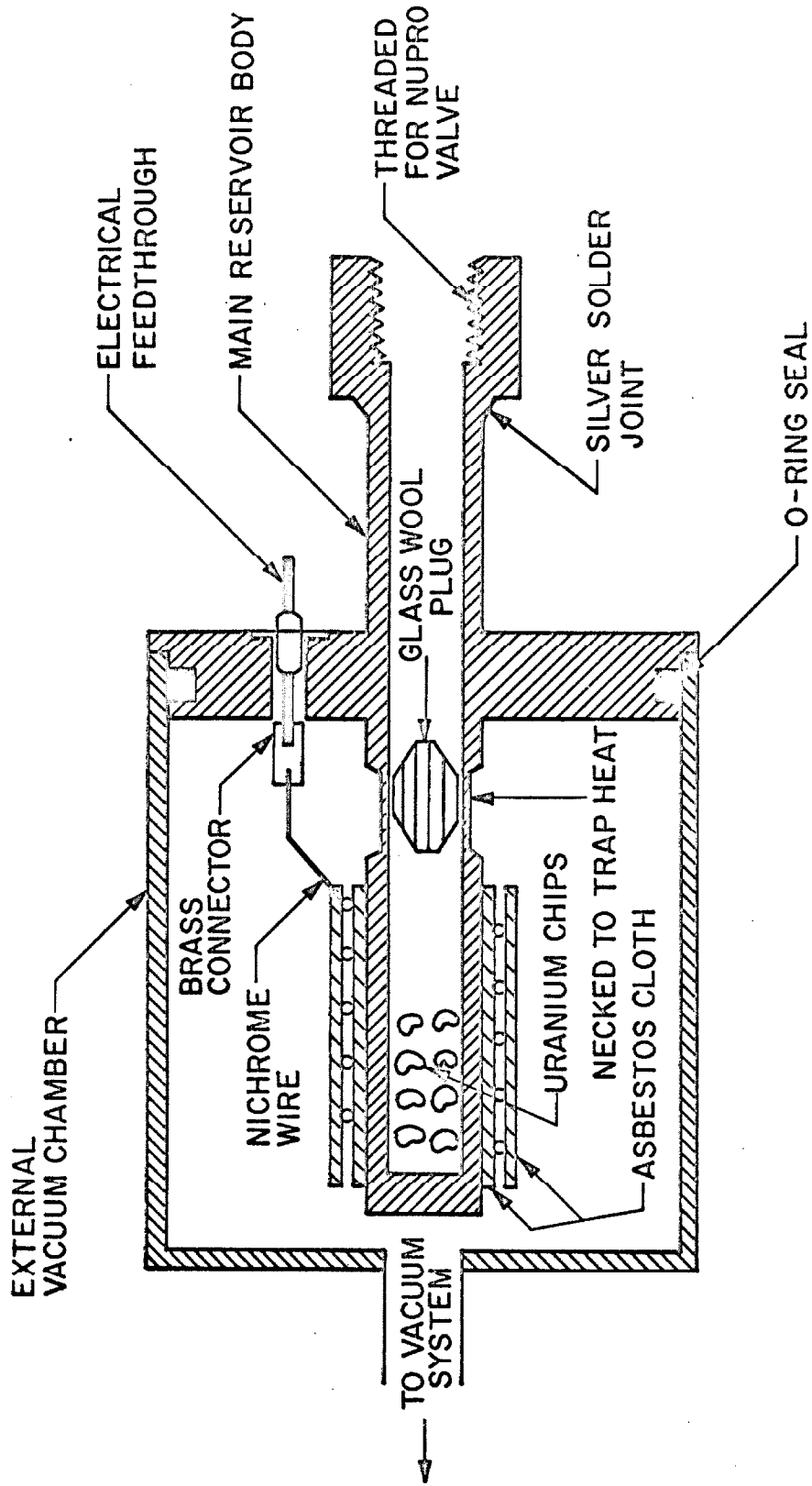
SCHEMATIC DIAGRAM OF TRITIUM RESERVOIR

ELECTRICAL
FEEDTHROUGH

MAIN RESERVOIR BODY

THREADED
FOR NUPRO
VALVE

SILVER SOLDER
JOINT

O-RING SEAL

GLASS WOOL
PLUG

EXTERNAL
VACUUM CHAMBER

BRASS
CONNECTOR

NICHROME
WIRE

URANIUM CHIPS

NECKED TO TRAP HEAT

ASBESTOS CLOTH

TO VACUUM
SYSTEM

Figure 4

Transfer Manifold

A schematic diagram of the manifold used to transfer the tritium gas from the glass shipping container to the reservoir. (Page 64)
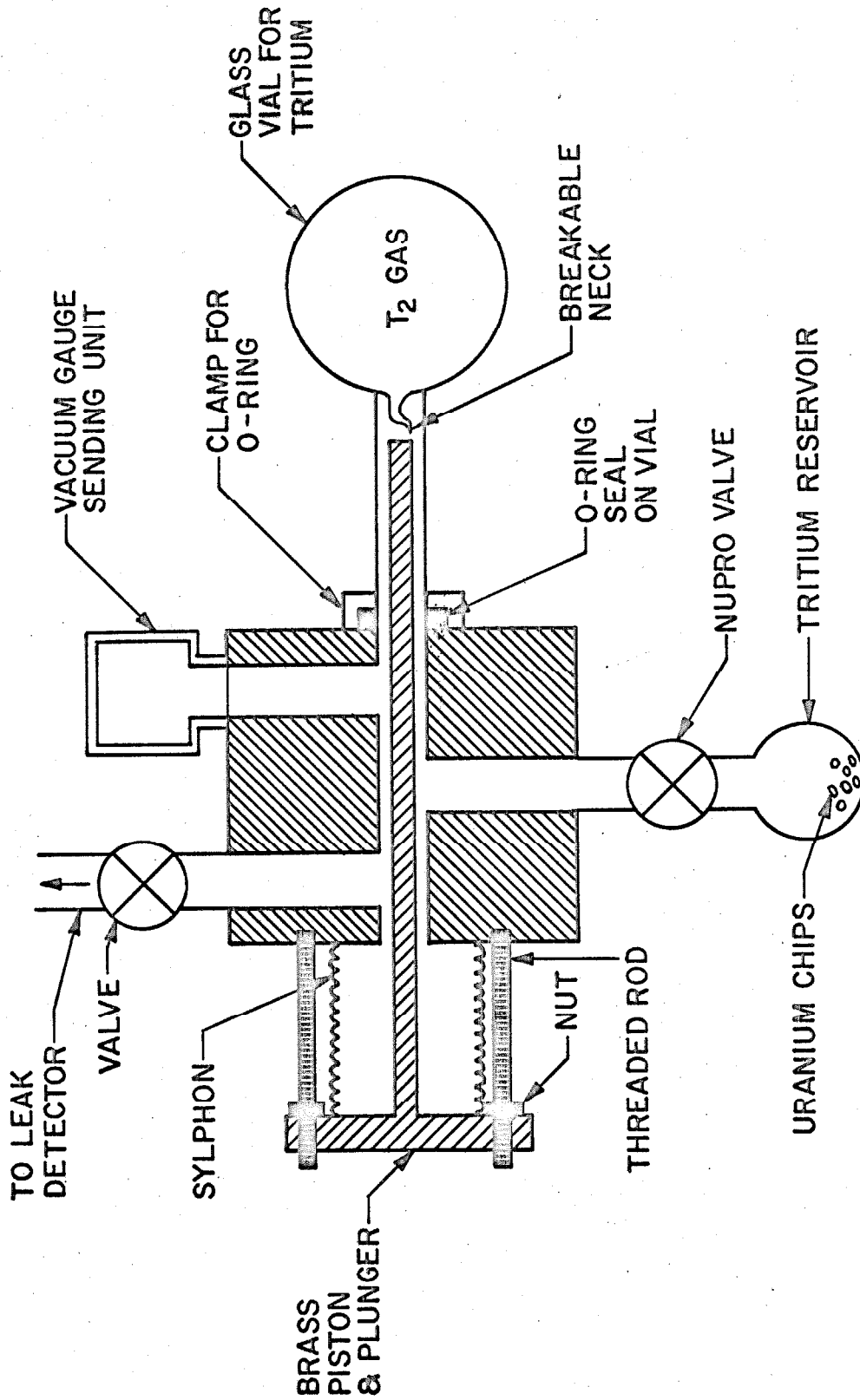
SCHEMATIC DIAGRAM OF TRITIUM TRANSFER MANIFOLD

Figure 5

Electronics

A schematic diagram of the electronics used with the $\frac{dE}{dx}$, E counter telescope. (Page 57)

SCHEMATIC DIAGRAM OF ELECTRONICS

ΔE COUNTER → [P.A.] → ΔE

E COUNTER → [P.A.] → E

SUMMING AMPLIFIER → E+ΔE

ΔE > b?

NO / YES

E+ΔE

1st 200 CHANNELS | 2nd 200 CHANNELS

400 CHANNEL
RIDL ANALYZER
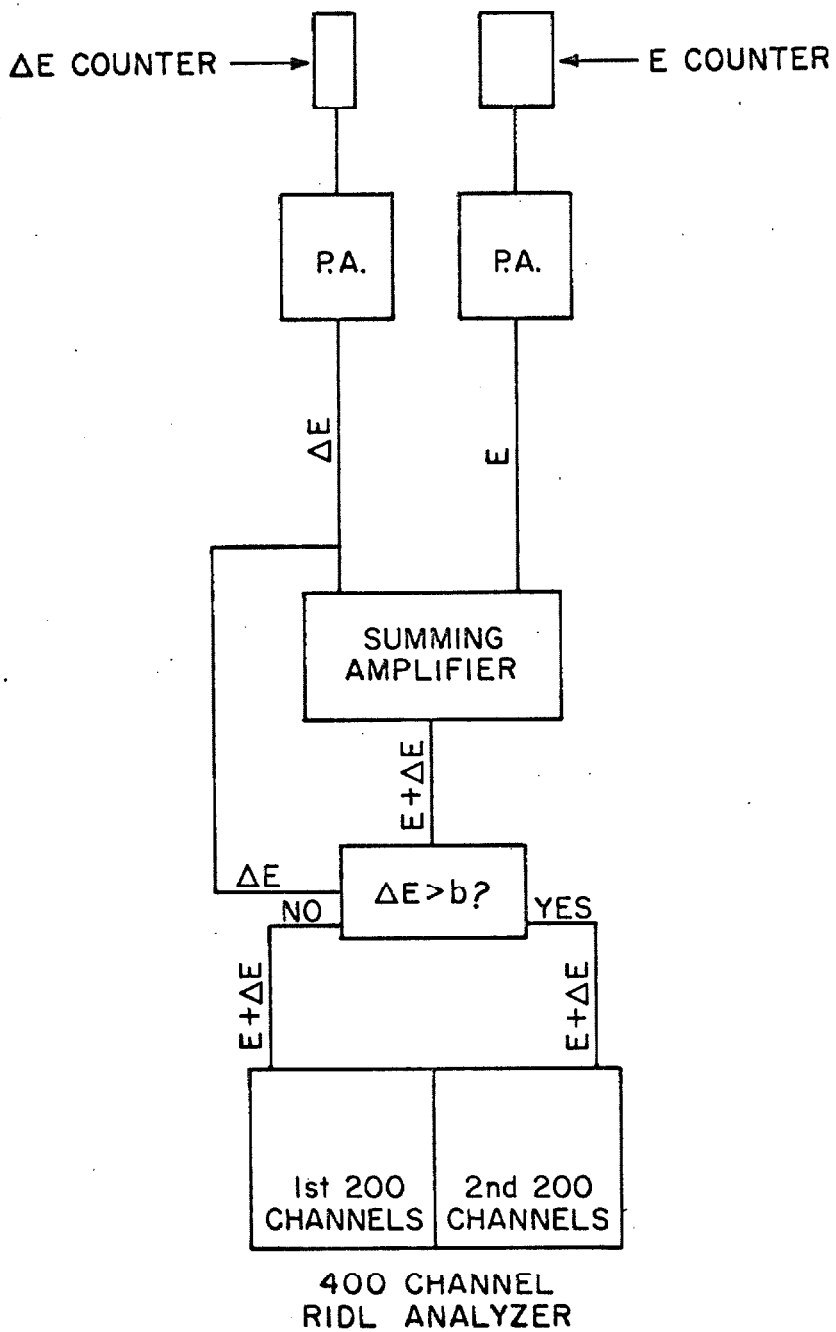
Figure 6

Typical Spectrum from the ^{3}H(α, α)^{3}H Experiment

A spectrum obtained using the $\frac{dE}{dx}$, E telescope and the 400-channel analyzer. The first 200 channels show charge 1 particles and the second 200 channels show charge 2 particles. (Page 8)

NUMBER OF COUNTS

CHANNEL NUMBER
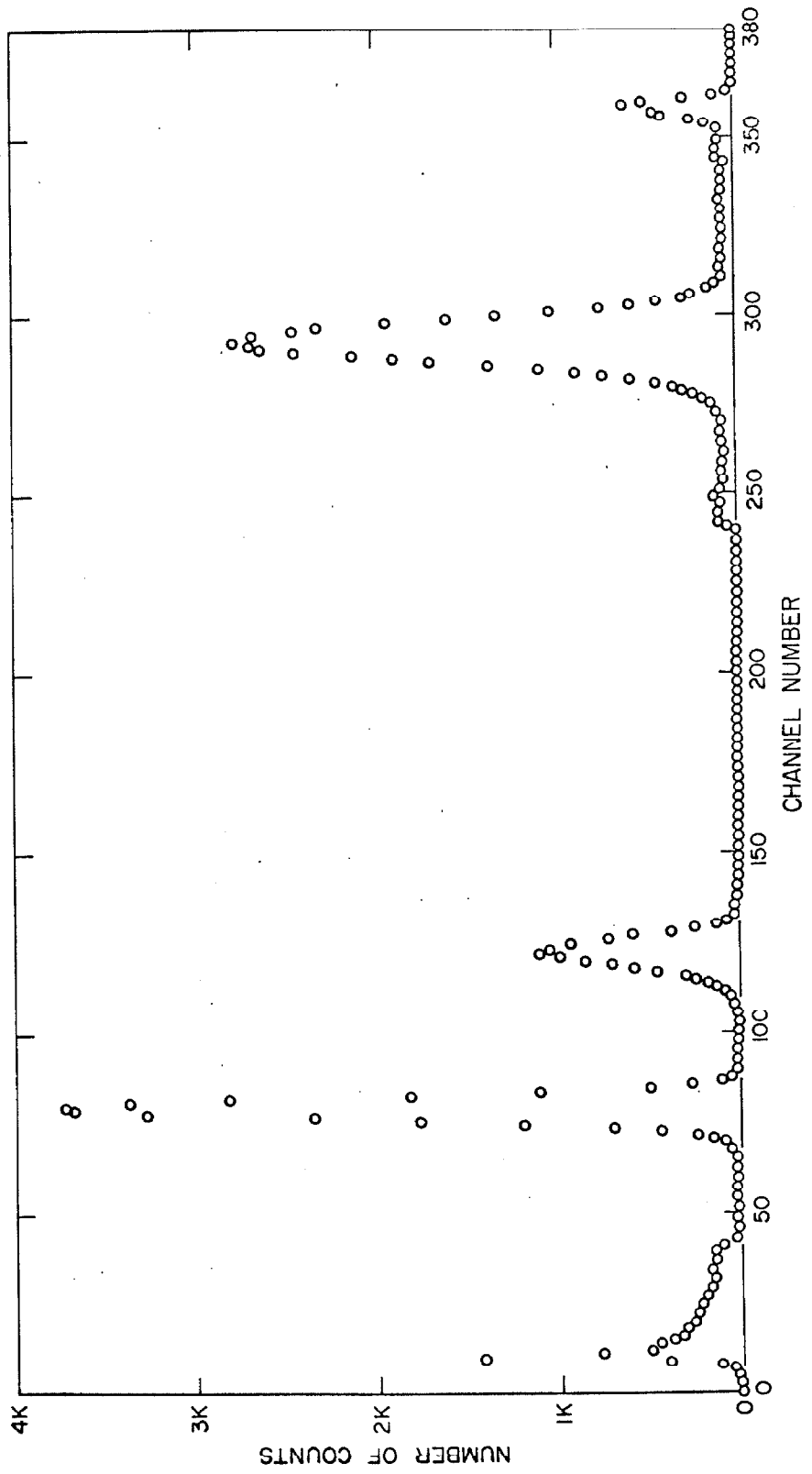
Figure 7

Data Reduction Display

This figure shows a sequence of photographs of the cathode ray tube used (with the Burroughs 220 computer) to display and partially reduce our data. (Page 59)
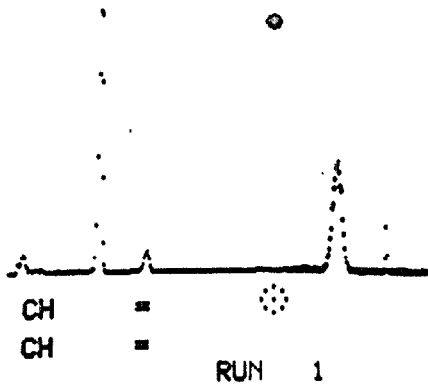
a
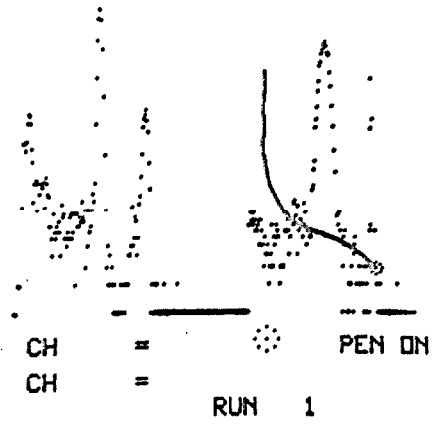
b
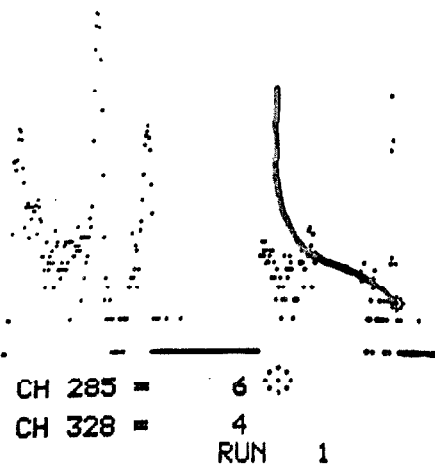
c
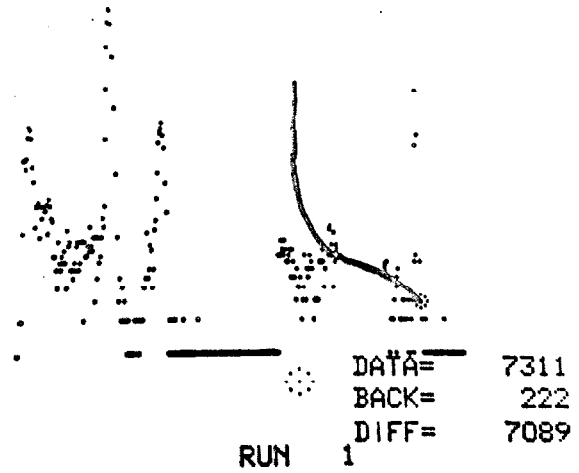
d

Figure 8

Slit Geometry

A schematic diagram showing the slit arrangement in the detector collimators and the relevant parameters for determining solid angle and target thickness.   (Page 61)

REAR SLIT

A_R

FRONT SLIT

w

h

R

θ_{Lab}

TARGET

BEAM LINE
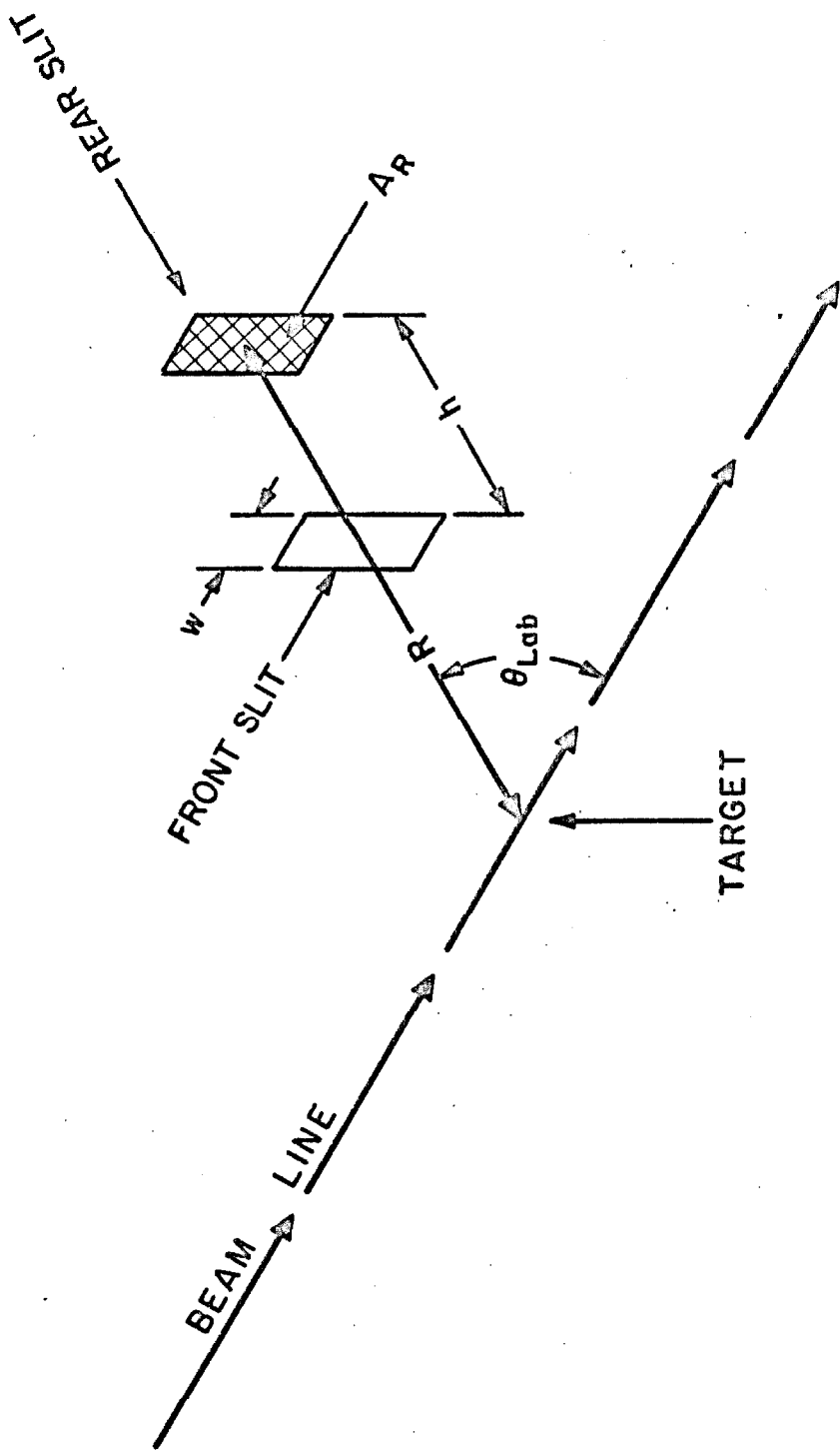
SCHEMATIC DIAGRAM OF DETECTOR
SLIT GEOMETRY

Figure 9

Excitation Curve from the ^{3}H(α, α)^{3}H Experiment

The open circles show the experimental points. The lines show fits to the data from the phase shift analysis. (Pages 9, 25)
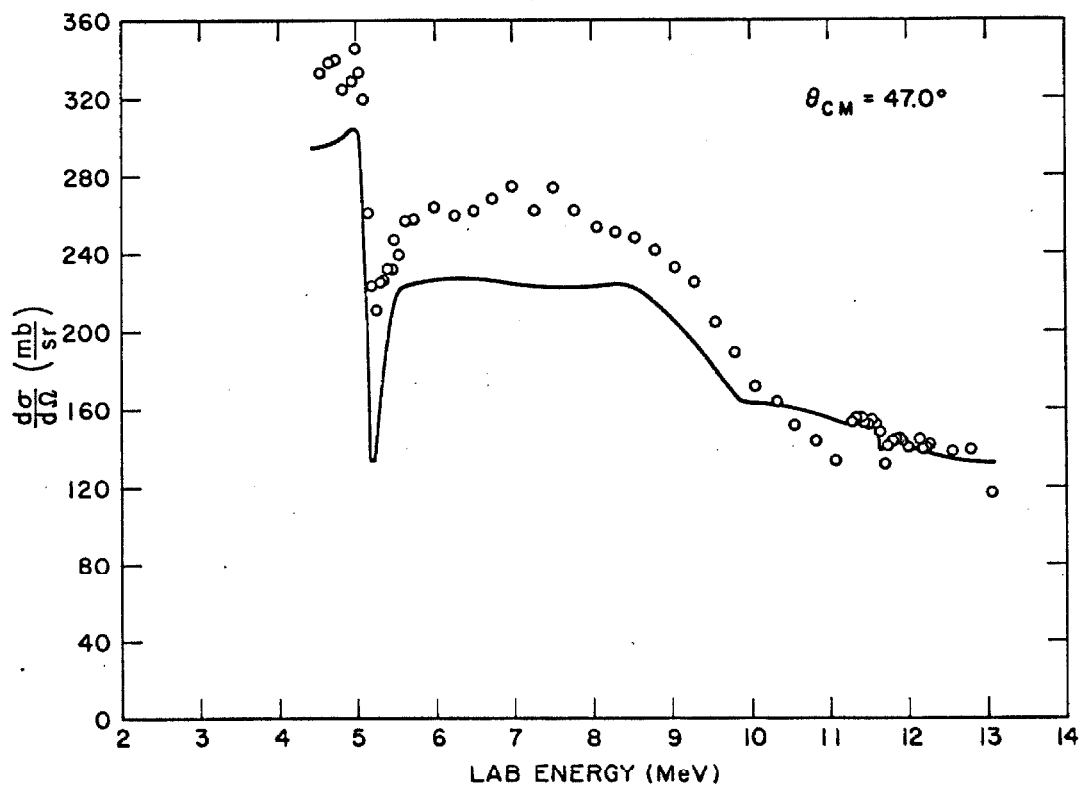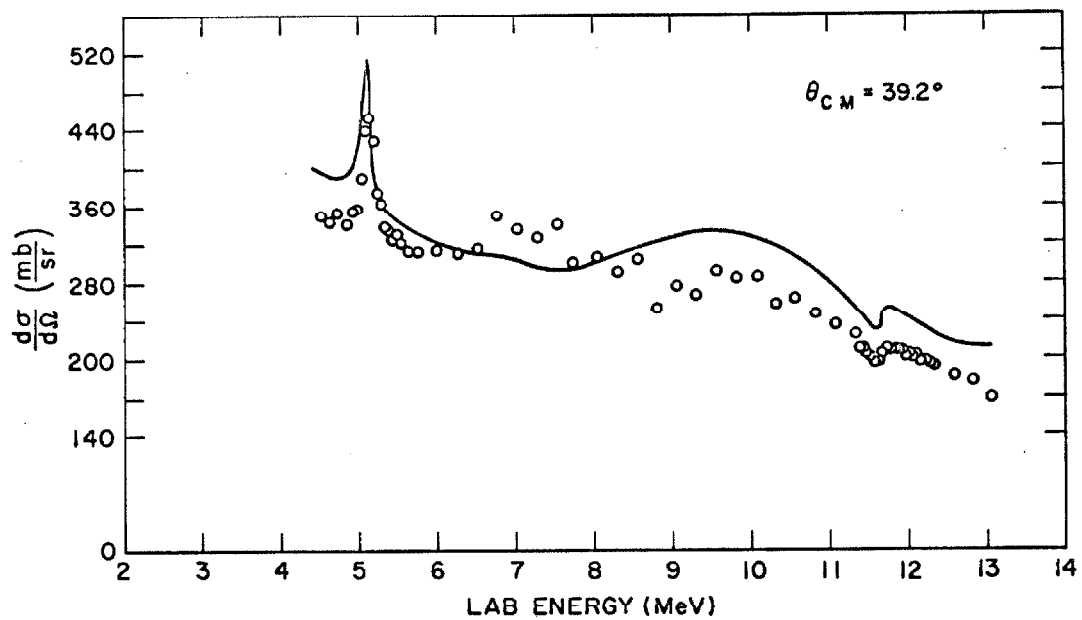
Figure 10

Excitation Curve from the ^{3}H(α, α)^{3}H Experiment

The open circles show the experimental points. The lines show fits to the data from the phase shift analysis. (Pages 9, 25)
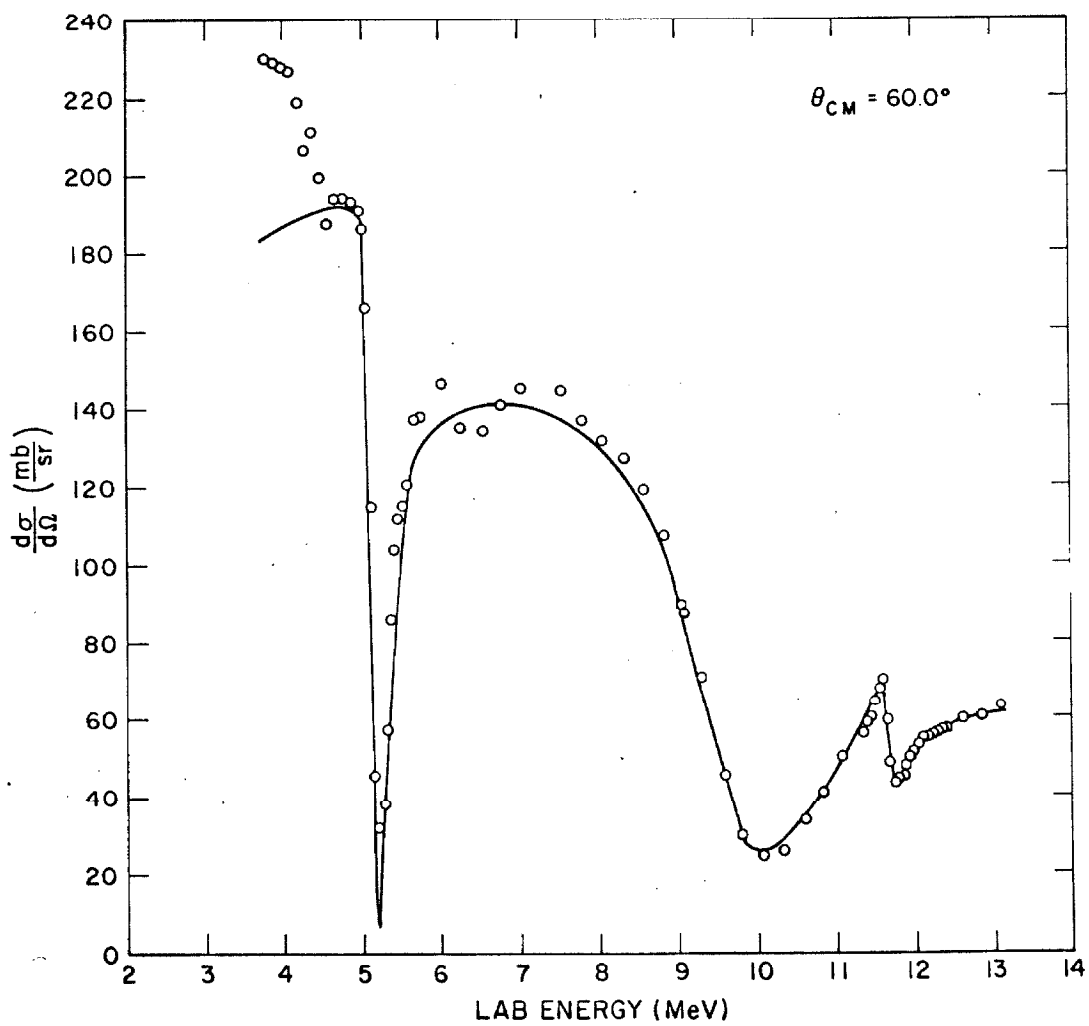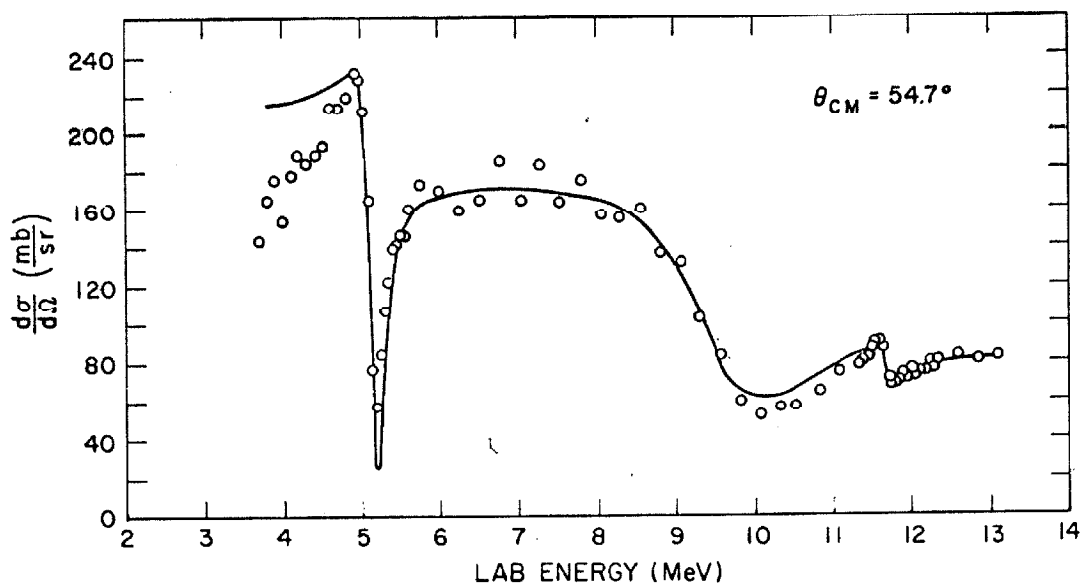
Figure 11

Excitation Curve from the ^{3}H$(\alpha, \alpha)^3$H Experiment

      The open circles show the experimental points. The lines show fits to the data from the phase shift analysis. (Pages 9, 25)

$\theta_{CM} = 63.4°$

$\theta_{CM} = 65.0°$
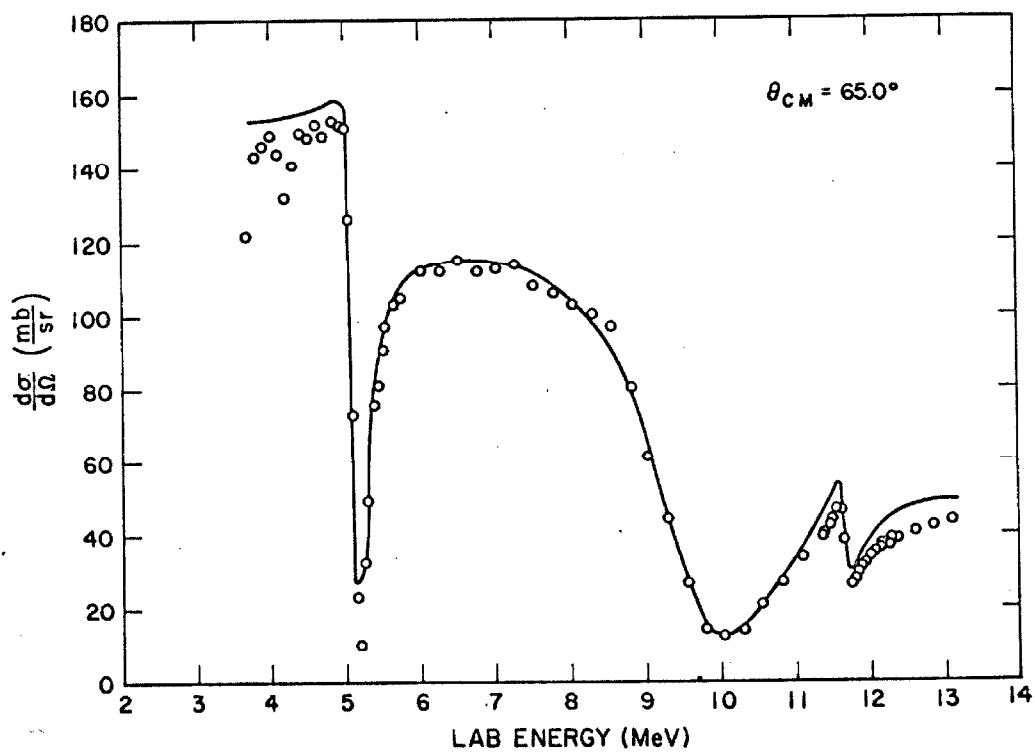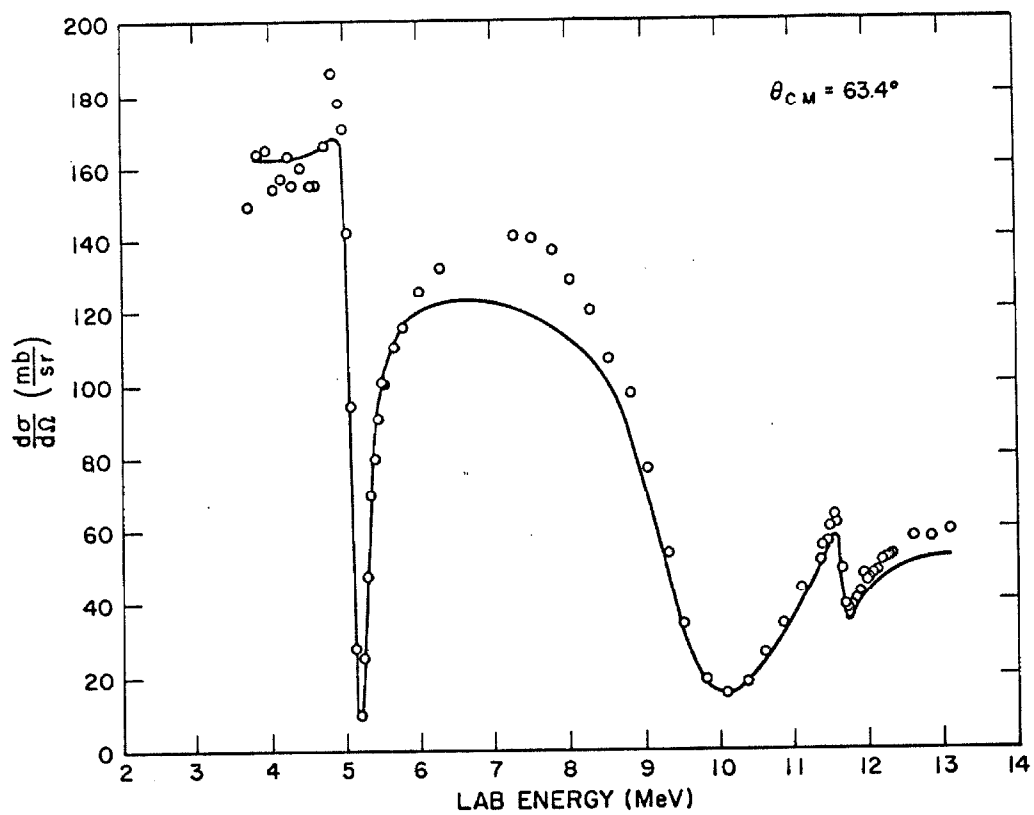
Figure 12

Excitation Curve from the ^{3}H(α, α)^{3}H Experiment

The open circles show the experimental points. The lines show fits to the data from the phase shift analysis. (Pages 9, 25)
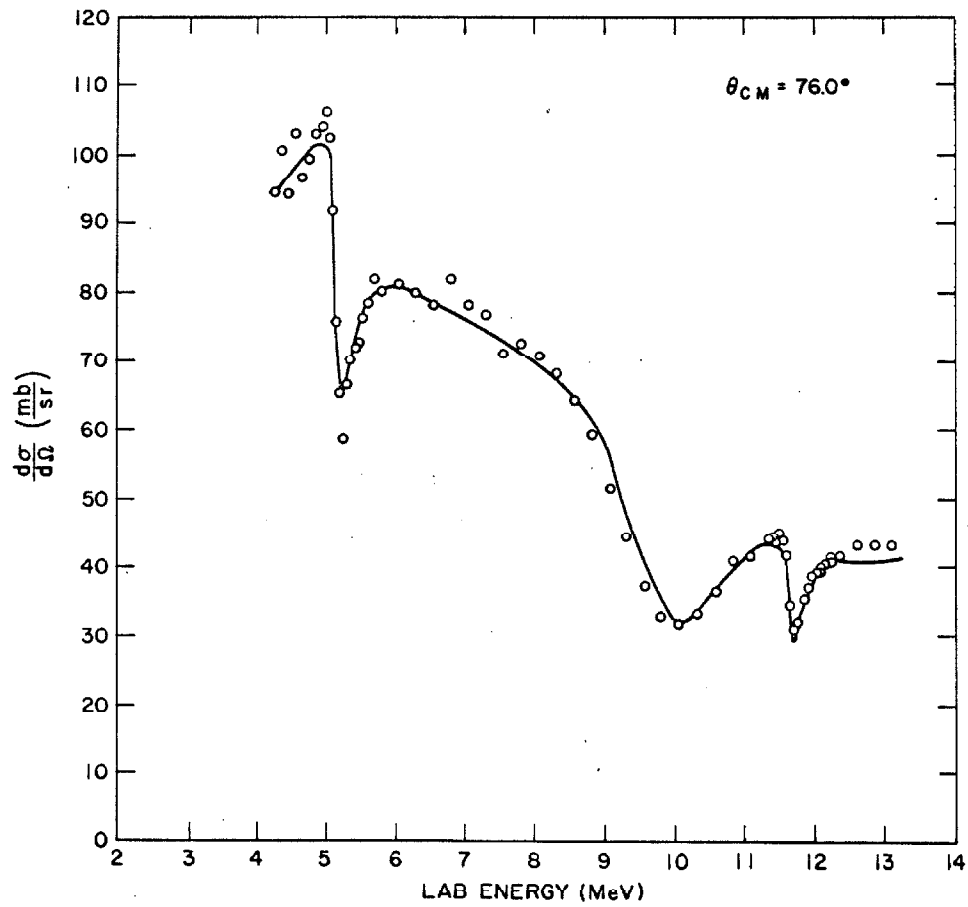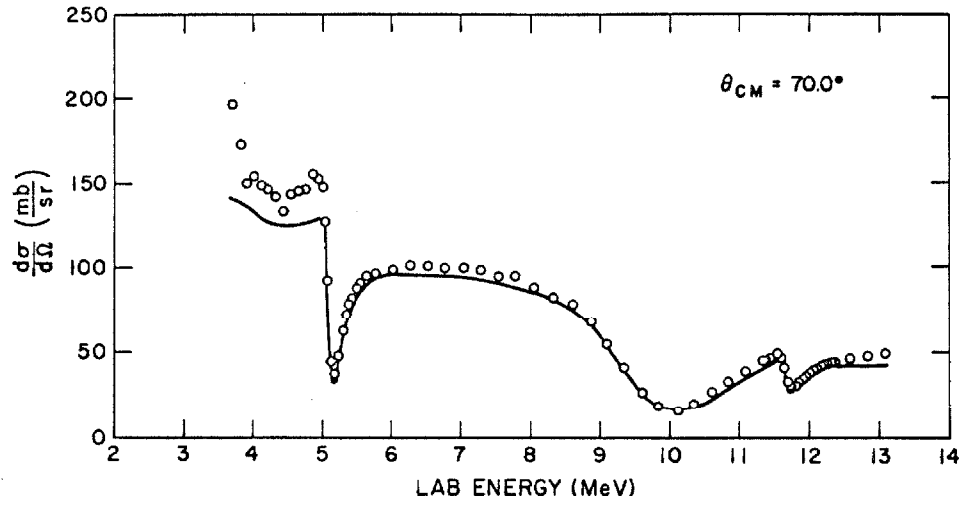
Figure 13

Excitation Curve from the ^{3}H$(\alpha, \alpha)^3$H Experiment

The open circles show the experimental points. The lines show fits to the data from the phase shift analysis. (Pages 9, 25)
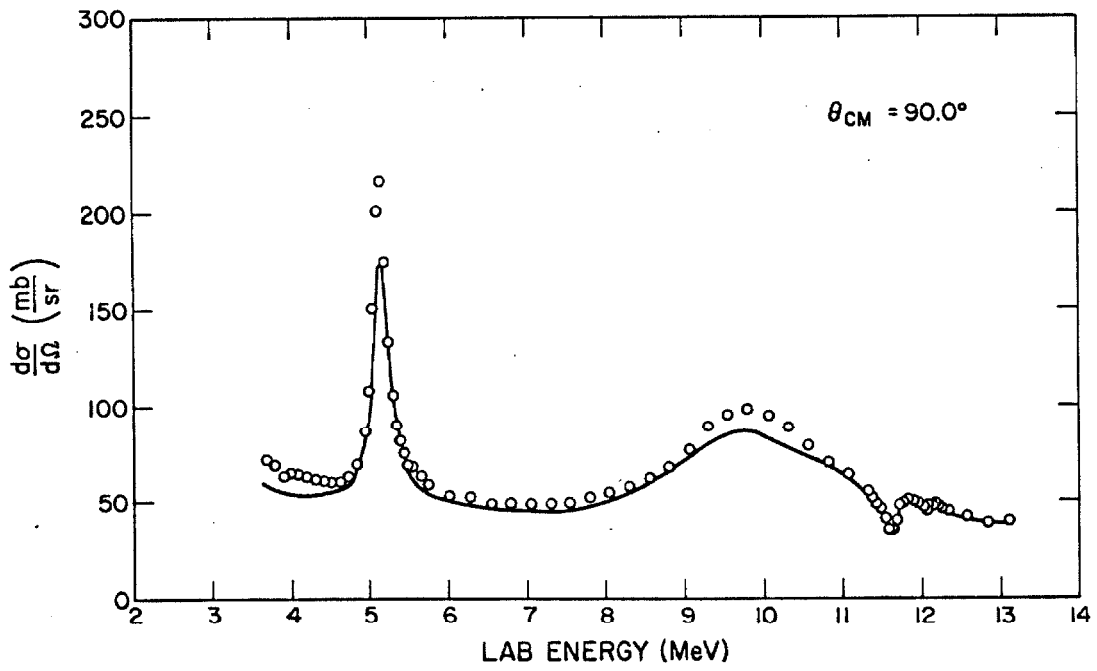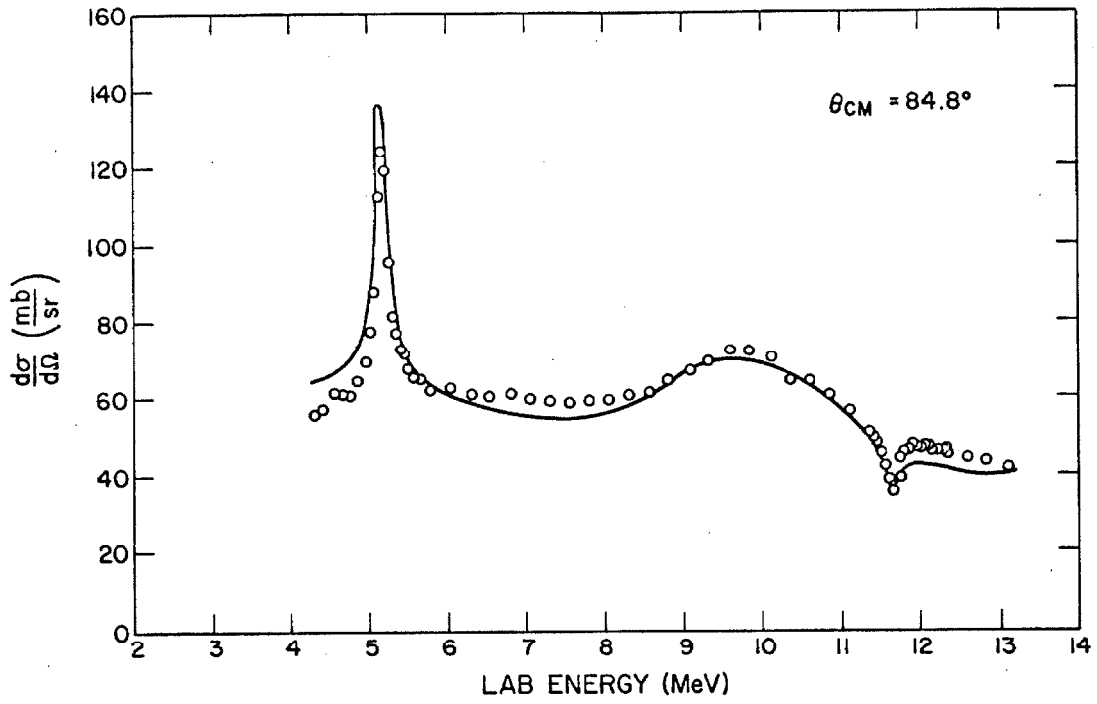
Figure 14

Excitation Curve from the ^{3}H$(\alpha, \alpha)^3$H Experiment

The open circles show the experimental points. The lines show fits to the data from the phase shift analysis. (Pages 9, 25)
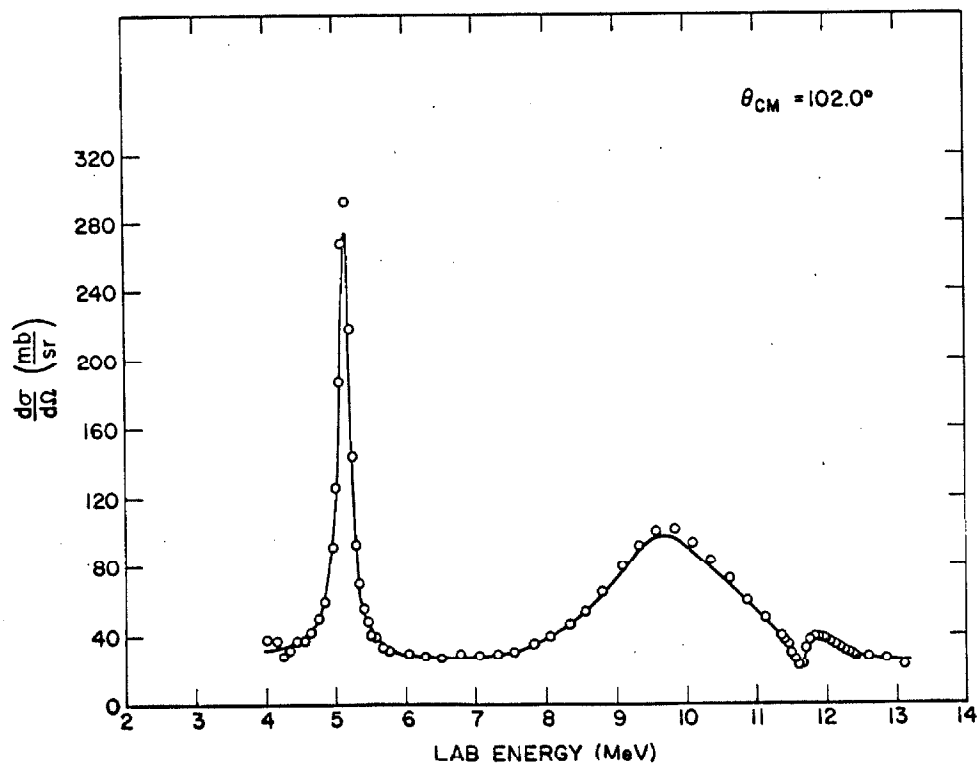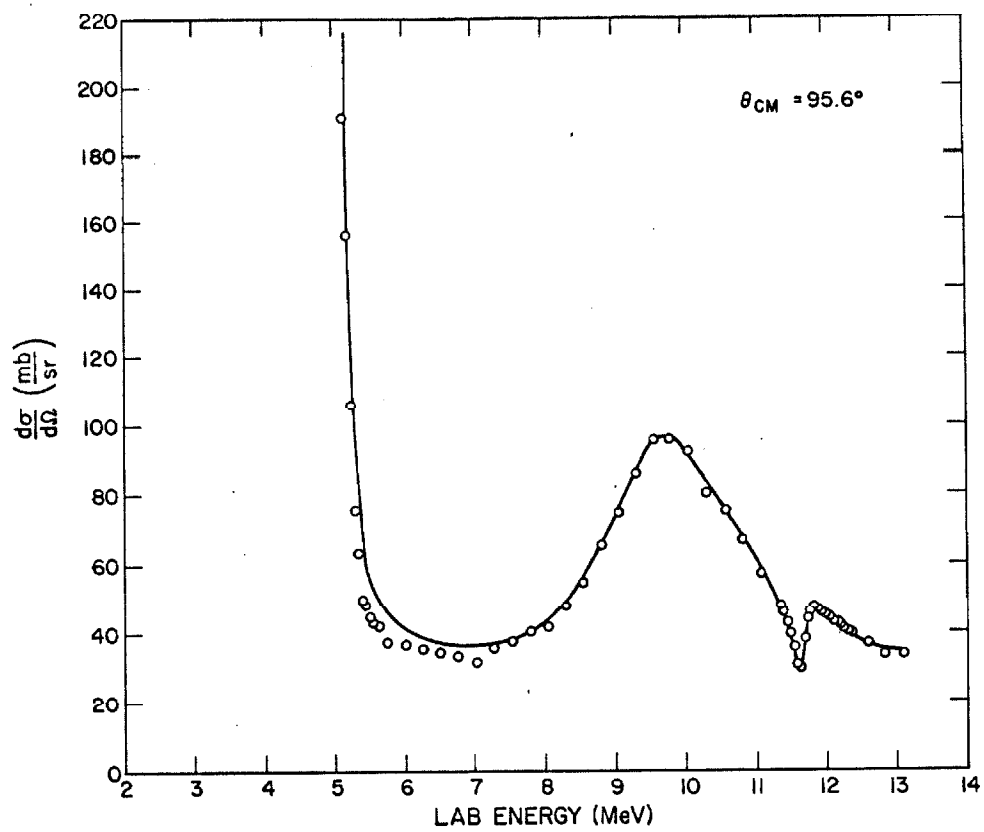
Figure 15

Excitation Curve from the ^{3}H$(\alpha, \alpha)^3$H Experiment

The open circles show the experimental points. The lines show fits to the data from the phase shift analysis. (Pages 9, 25)

$\theta_{CM} = 109.9°$

$\theta_{CM} = 116.6°$
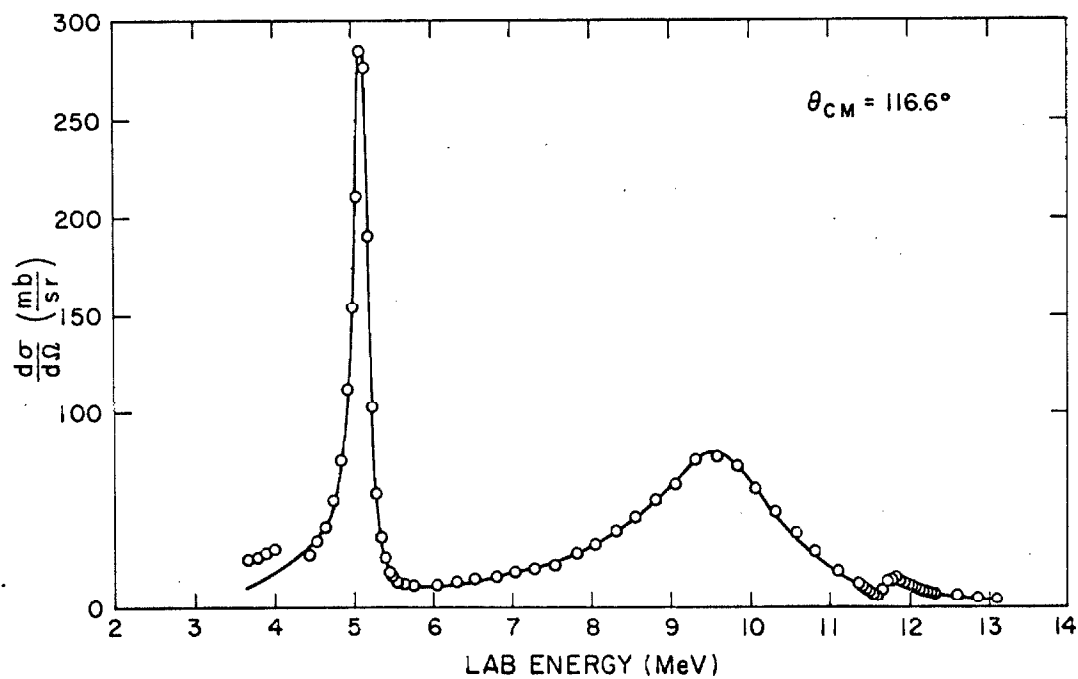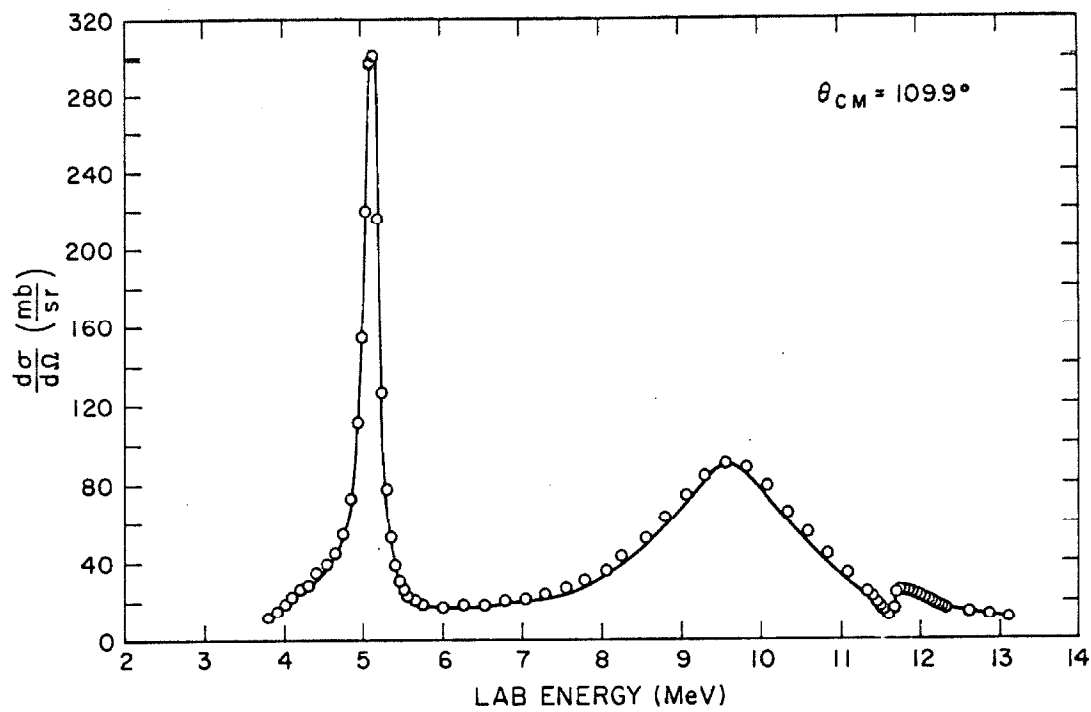
Figure 16

Excitation Curve from the ^{3}H(α, α)^{3}H Experiment

The open circles show the experimental points. The lines show fits to the data from the phase shift analysis. (Pages 9, 25)
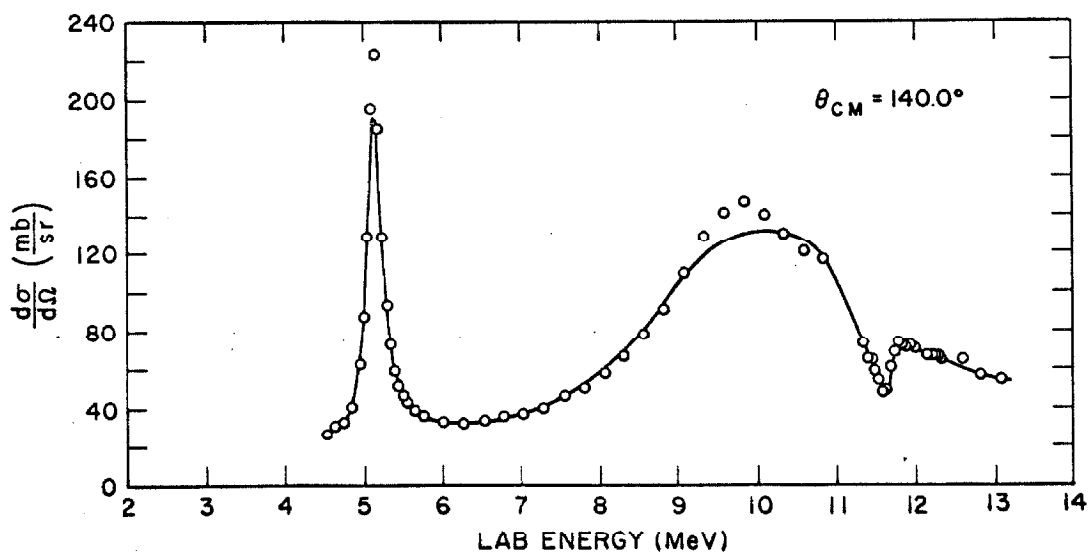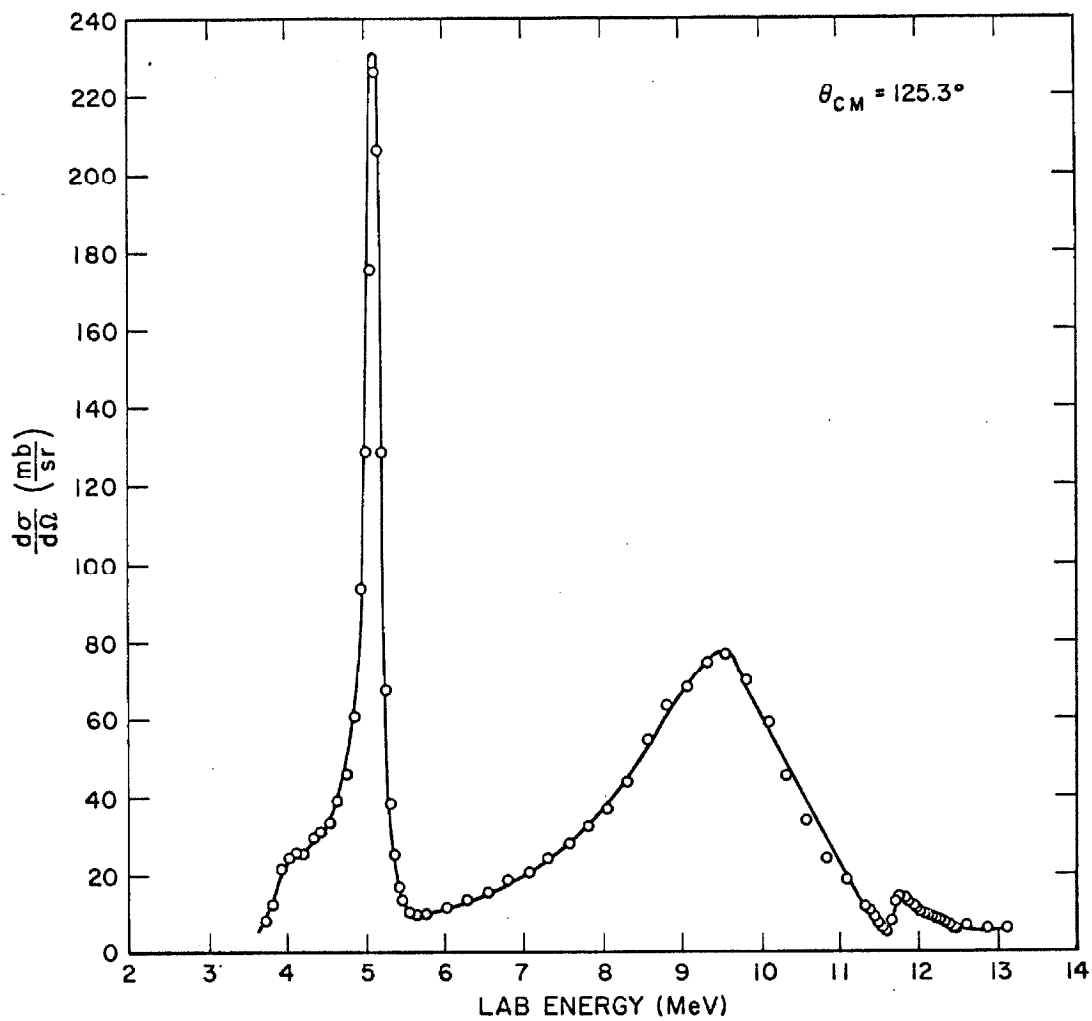
Figure 17

Excitation Curve from the ^{3}H(α, α)^{3}H Experiment

The open circles show the experimental points. The lines show fits to the data from the phase shift analysis. (Pages 9, 25)
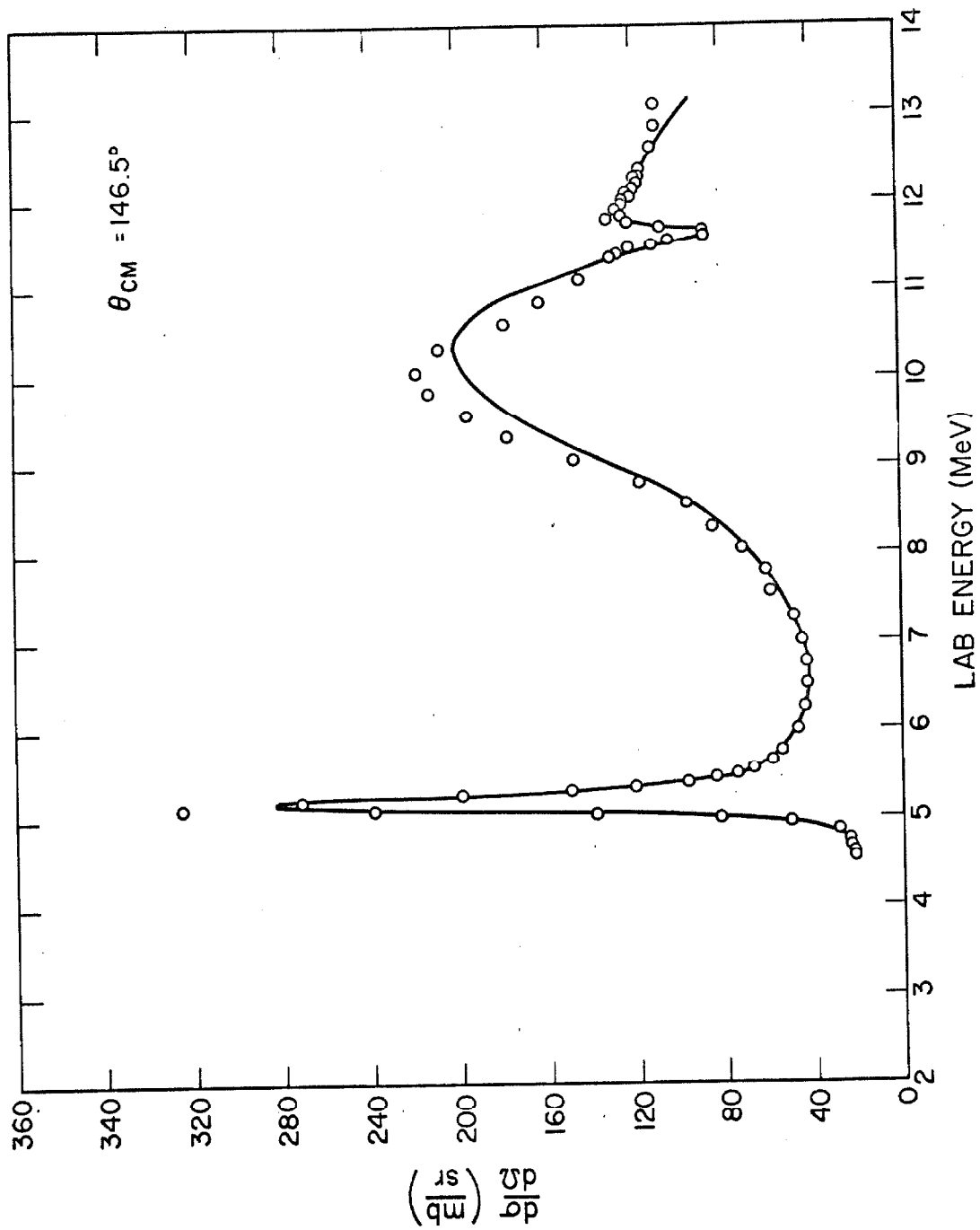
Figure 18

Excitation Curve from the ^{3}H(α, α)^{3}H Experiment

The open circles show the experimental points. The lines show fits to the data from the phase shift analysis. (Pages 9, 25)
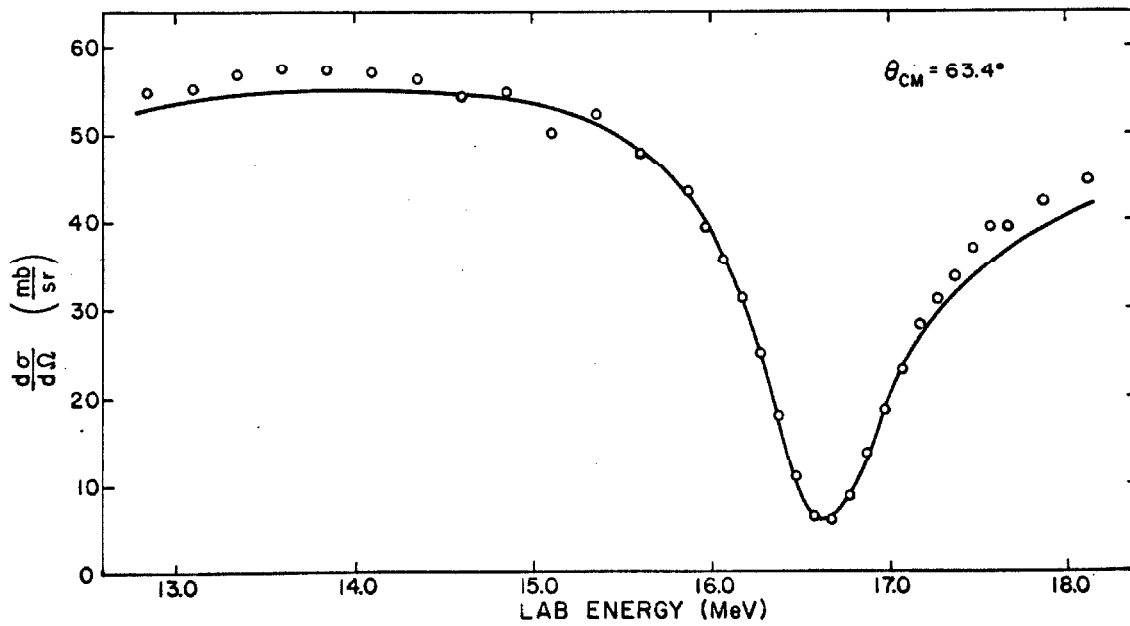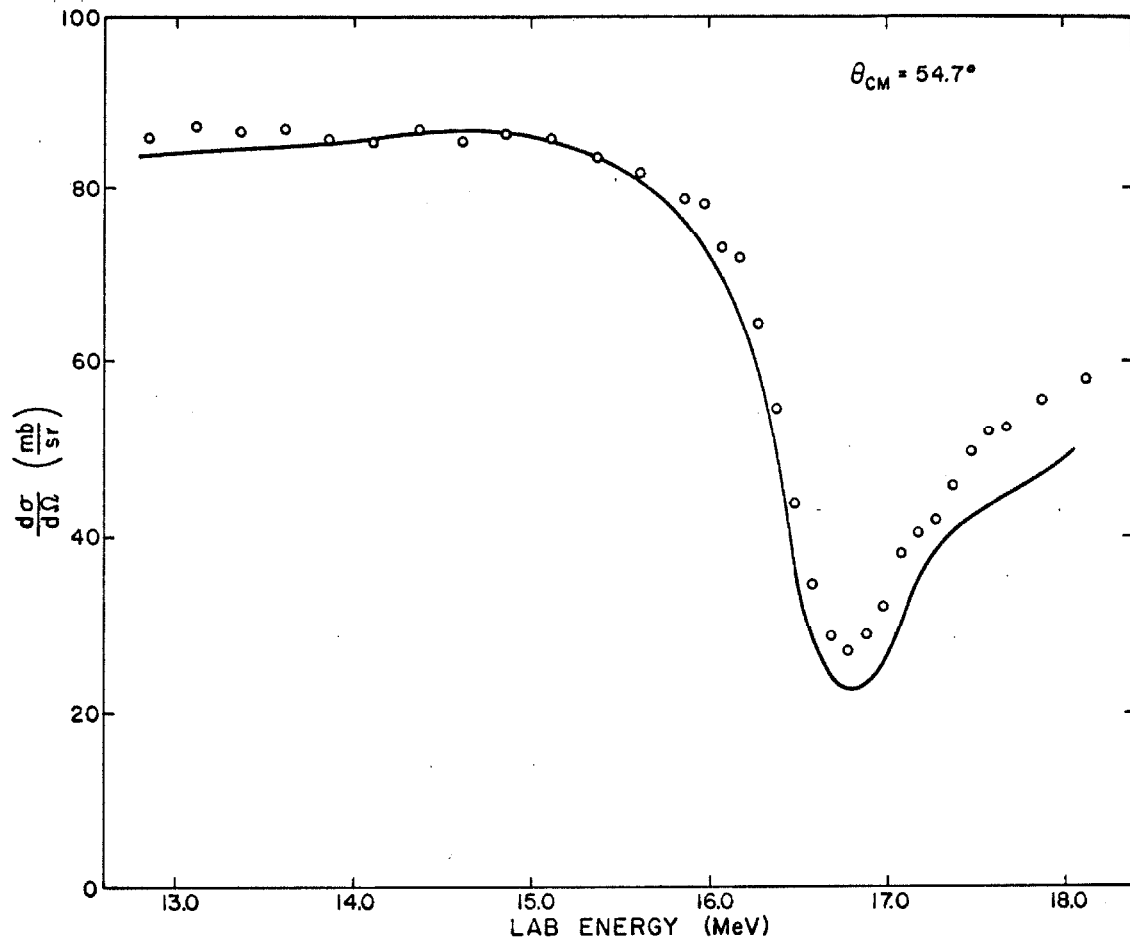
Figure 19

Excitation Curve from the ^{3}H(α, α)^{3}H Experiment

The open circles show the experimental points. The lines show fits to the data from the phase shift analysis. (Pages 9, 25)
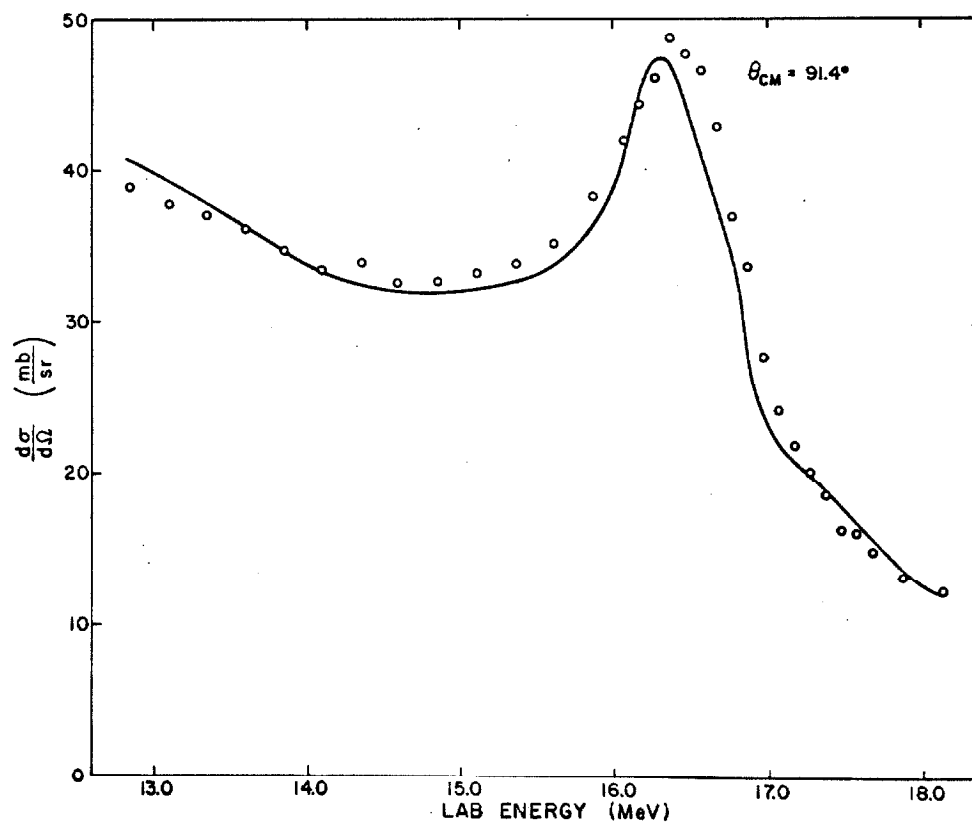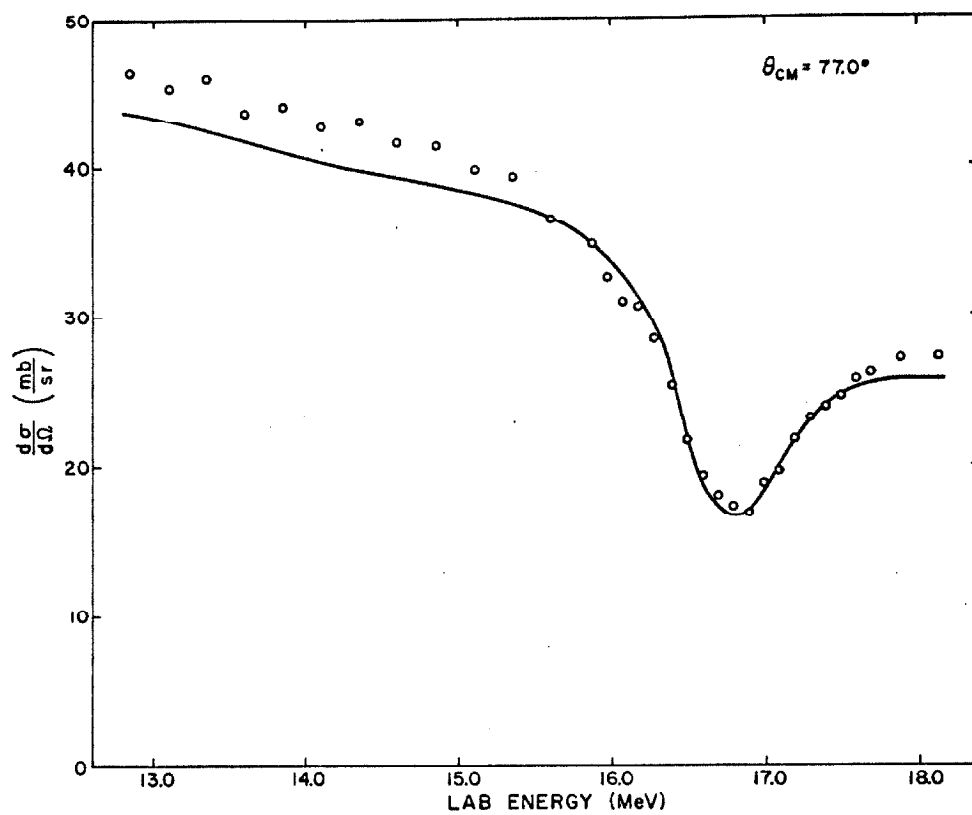
Figure 20

Excitation Curve from the ^{3}H(α, α)^{3}H Experiment

The open circles show the experimental points. The lines show fits to the data from the phase shift analysis. (Pages 9, 25)
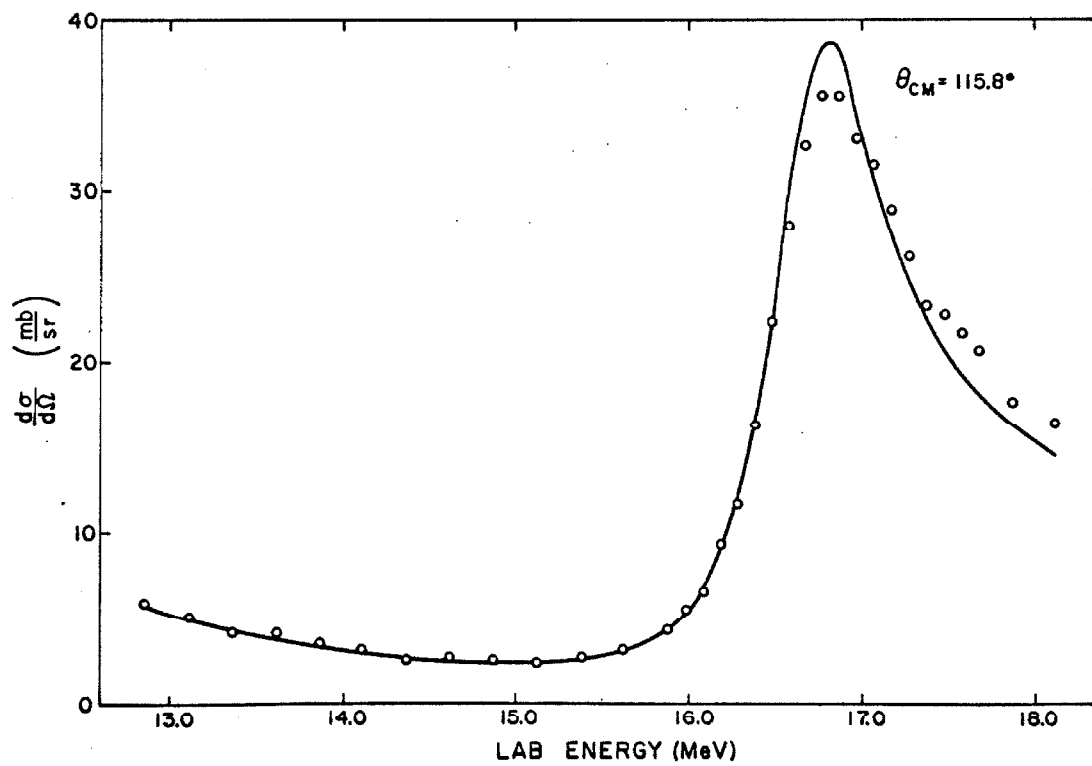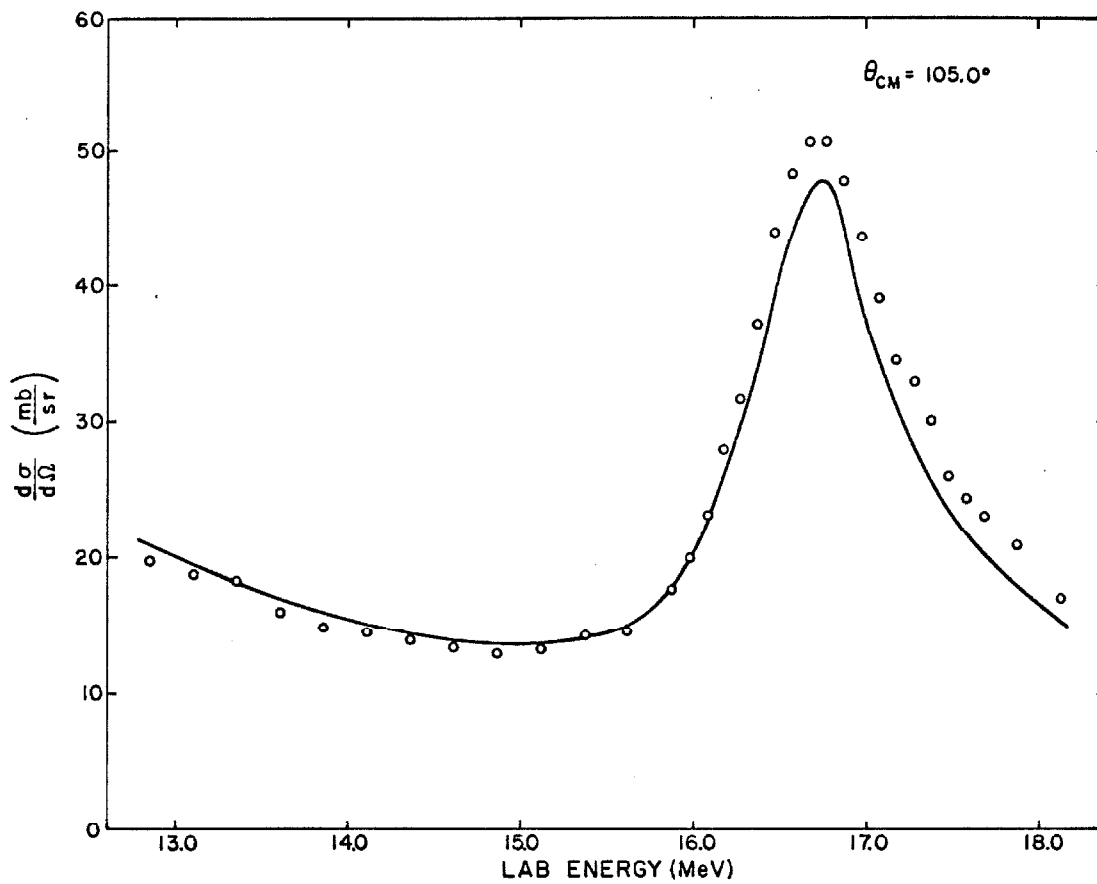
Figure 21

Excitation Curve from the $^3H(\alpha, \alpha)^3H$ Experiment

The open circles show the experimental points. The lines show fits to the data from the phase shift analysis. (Pages 9, 25)
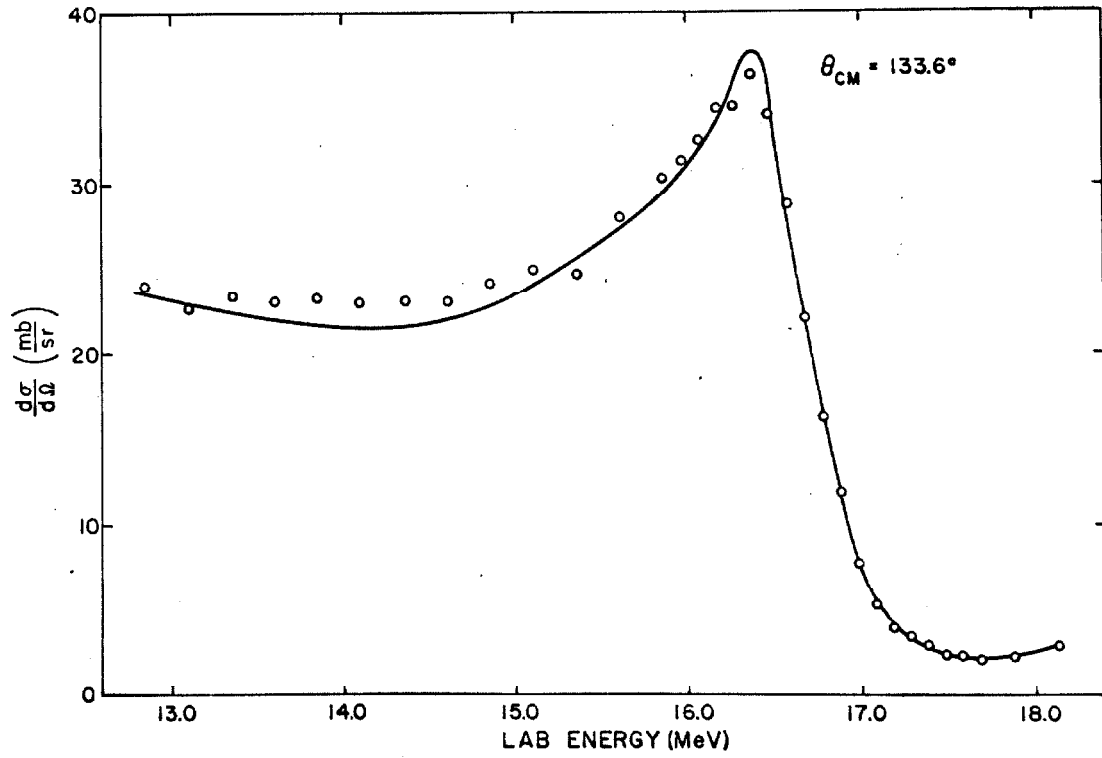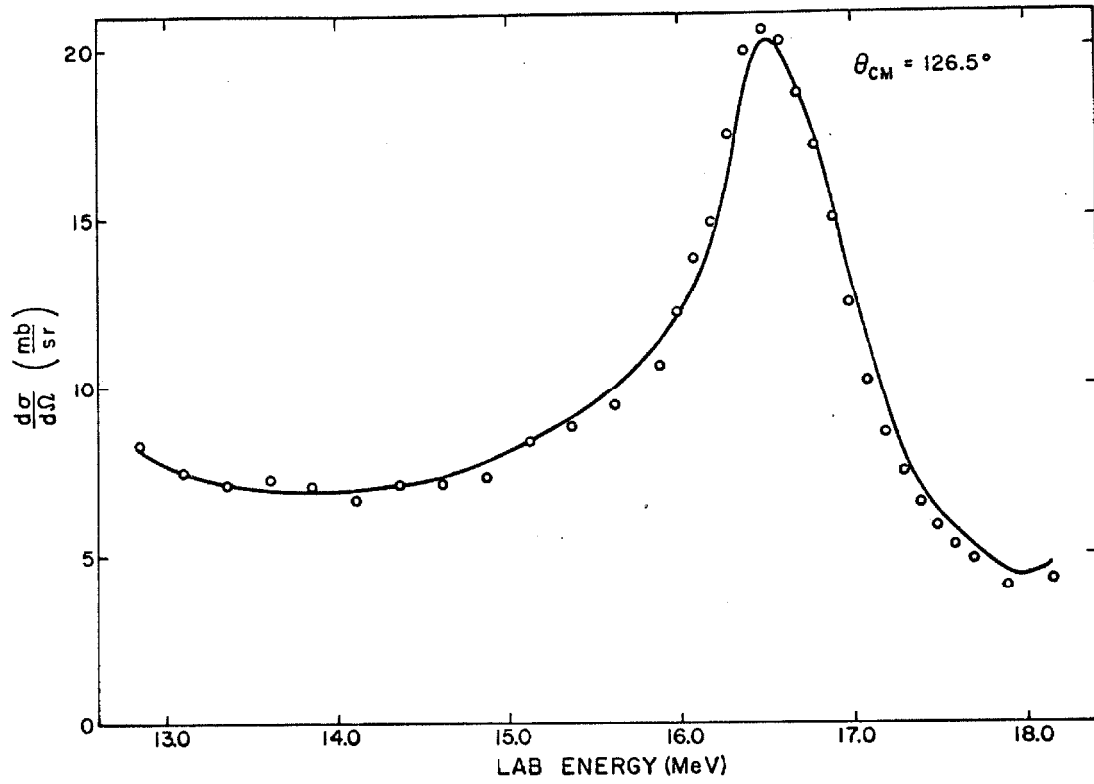
Figure 22

Angular Distributions for the ^{3}H(α, α)^{3}H Experiment

This figure shows the center-of-mass differential elastic scattering cross section as a function of center-of-mass angle. The open circles show the data points and the solid line shows the fit from the phase shift analysis. (Page 9)

Figure 23

Angular Distributions for the ^{3}H(α, α)^{3}H Experiment

This figure shows the center-of-mass differential elastic scattering cross section as a function of center-of-mass angle. The open circles show the data points and the solid line shows the fit from the phase shift analysis. (Page 9)

$E\alpha = 8.249$

$E\dot{\alpha} = 5.172$

Figure 24

Angular Distributions for the ^{3}H$(\alpha, \alpha)^3$H Experiment

This figure shows the center-of-mass differential elastic scattering cross section as a function of center-of-mass angle. The open circles show the data points and the solid line shows the fit from the phase shift analysis. (Page 9)
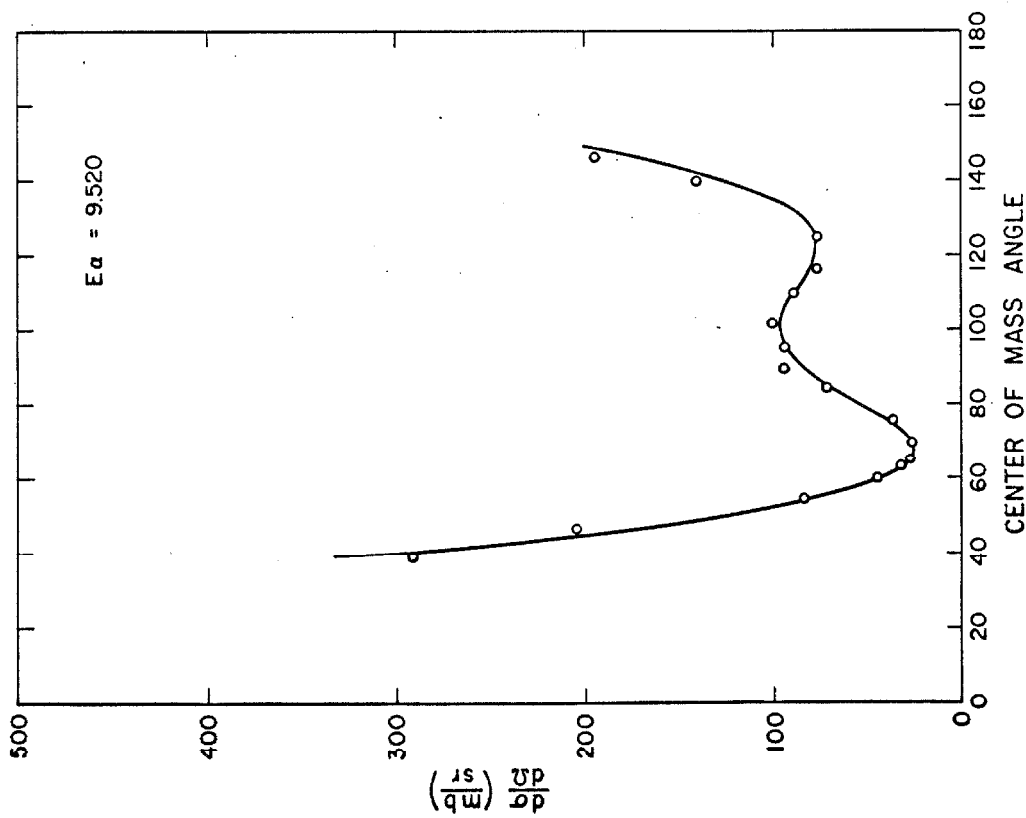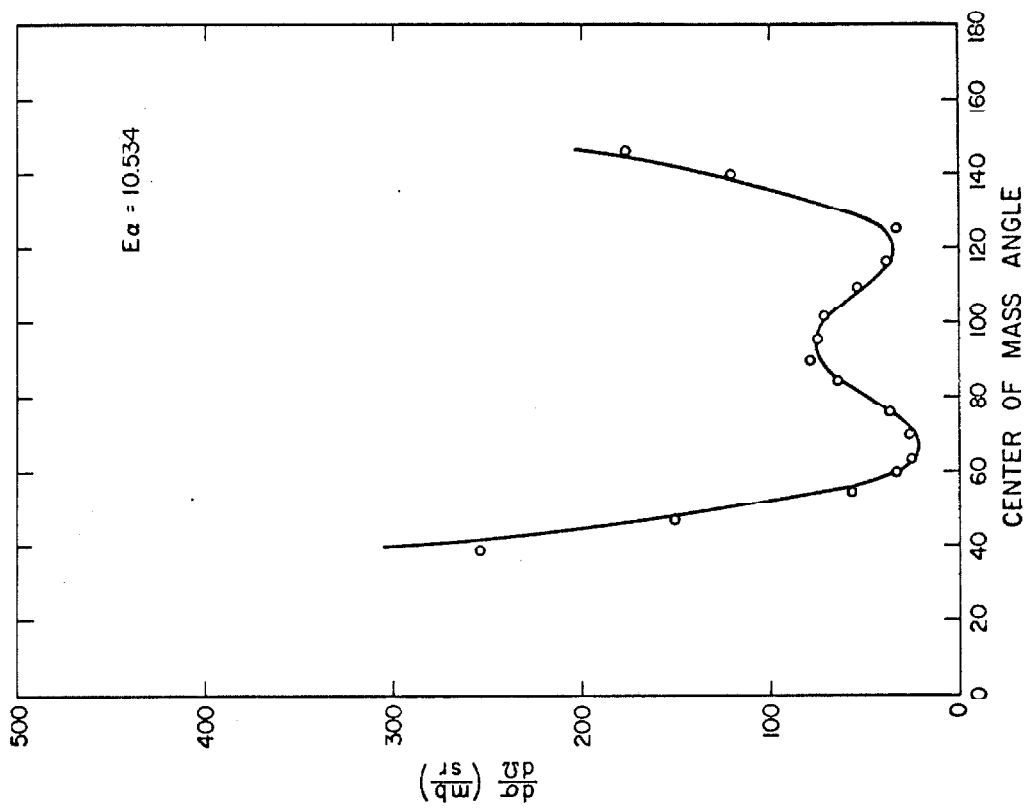
Figure 25

Angular Distributions for the ^{3}H(α, α)^{3}H Experiment

This figure shows the center-of-mass differential elastic scattering cross section as a function of center-of-mass angle. The open circles show the data points and the solid line shows the fit from the phase shift analysis. (Page 9)
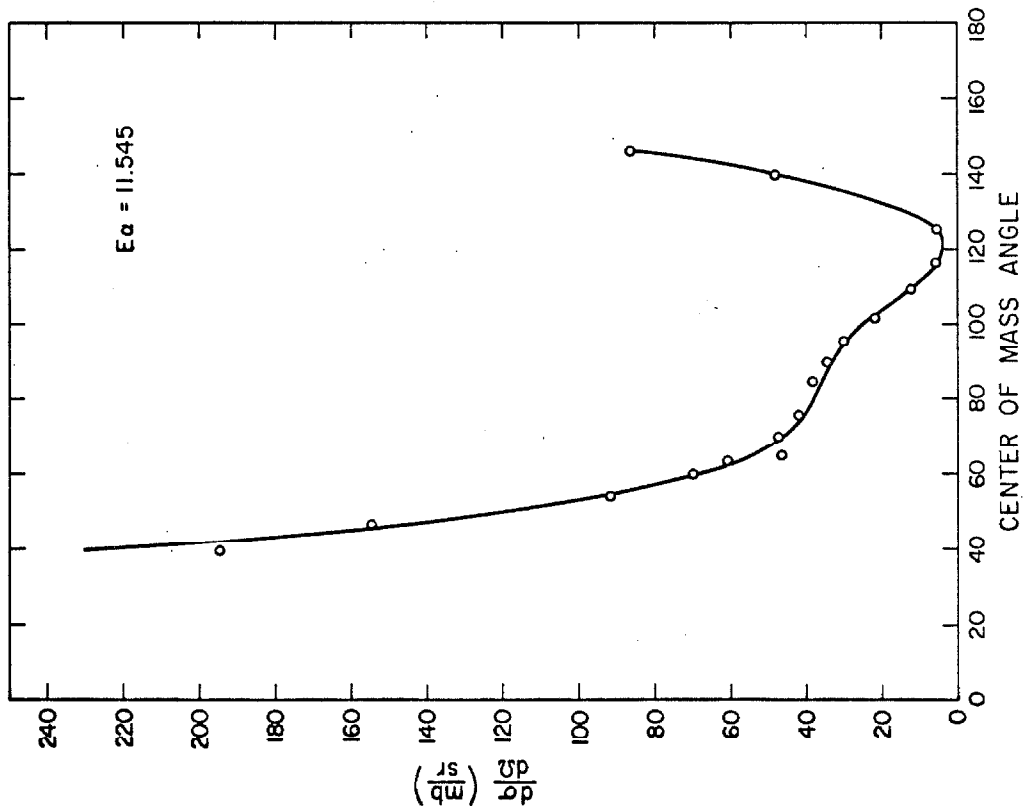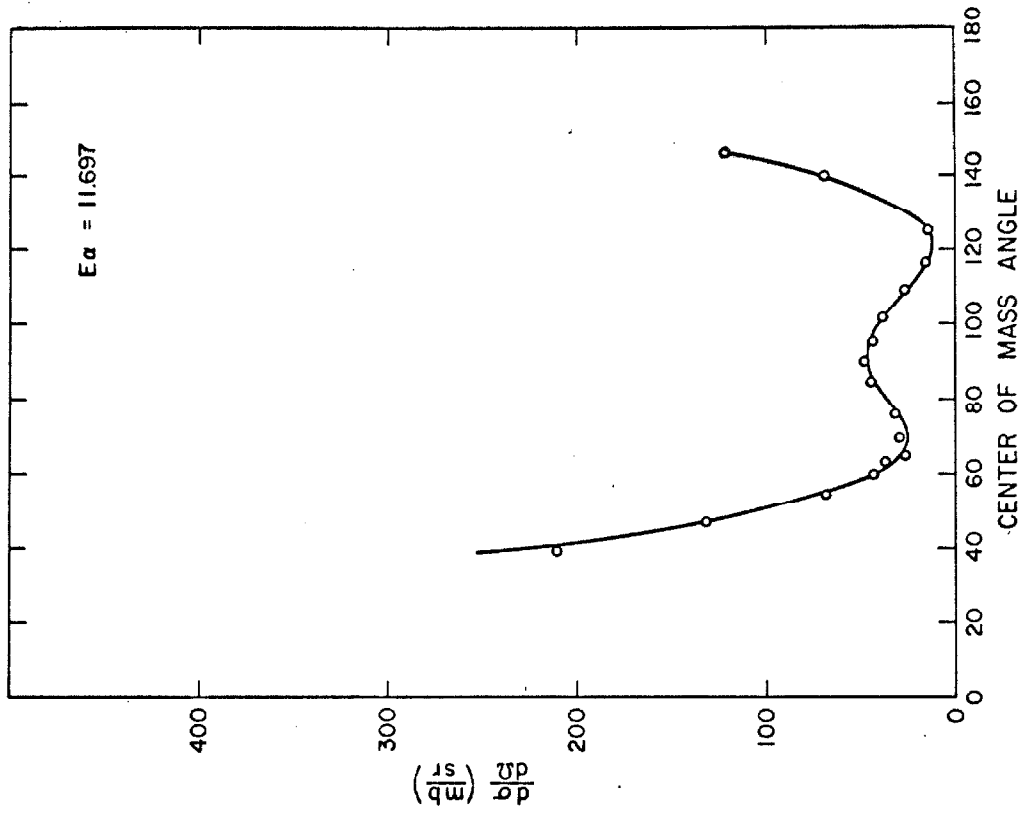
Figure 26

Angular Distributions for the ^{3}H(α, α)^{3}H Experiment

This figure shows the center-of-mass differential elastic scattering cross section as a function of center-of-mass angle. The open circles show the data points and the solid line shows the fit from the phase shift analysis. (Page 9)
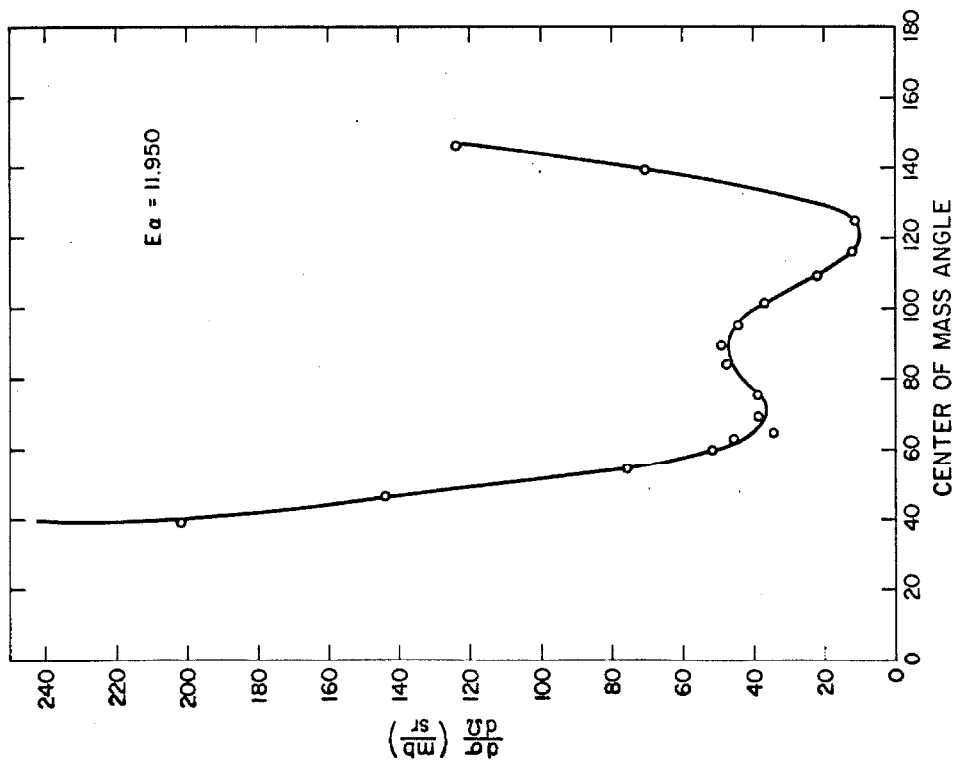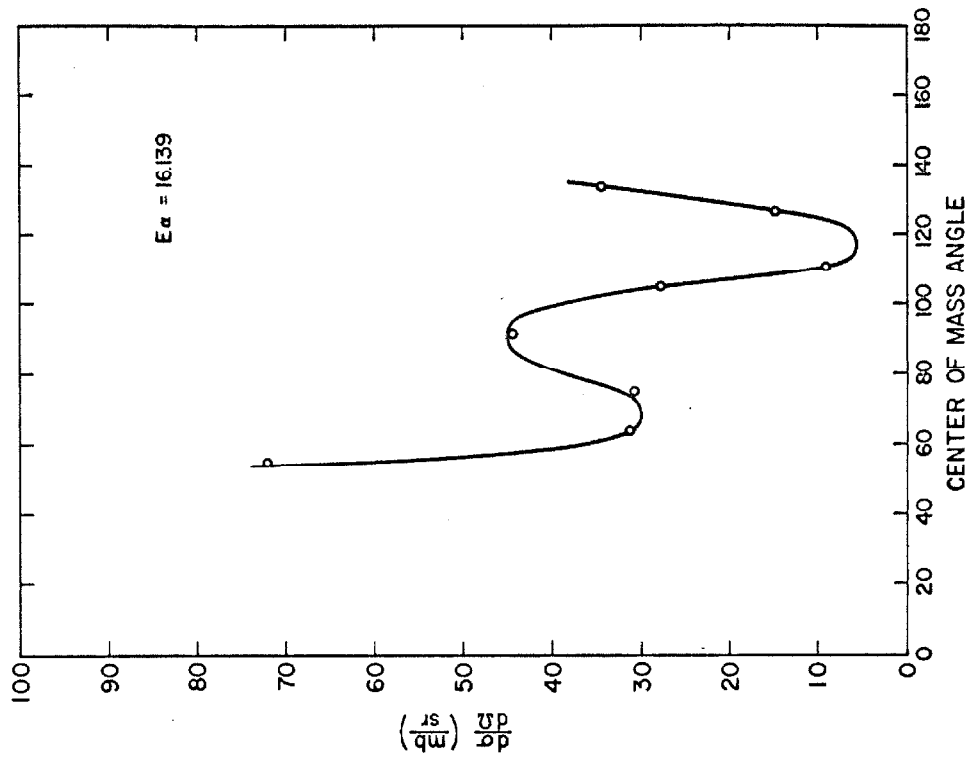
Figure 27

Angular Distributions for the ^{3}H(α, α)^{3}H Experiment

This figure shows the center-of-mass differential elastic scattering cross section as a function of center-of-mass angle. The open circles show the data points and the solid line shows the fit from the phase shift analysis. (Page 9)

Figure 28

Data for the Reaction ^{3}H(α, n)^{6}Li

This figure shows the data obtained with the zirconium tritide target. The number of counts are shown as a function of beam energy (E_α). The open circles represent the actual number of counts. The closed circles are the number of counts multiplied by 10 to show the threshold behavior. (Page 11)

$H^3(\alpha,n)Li^6$
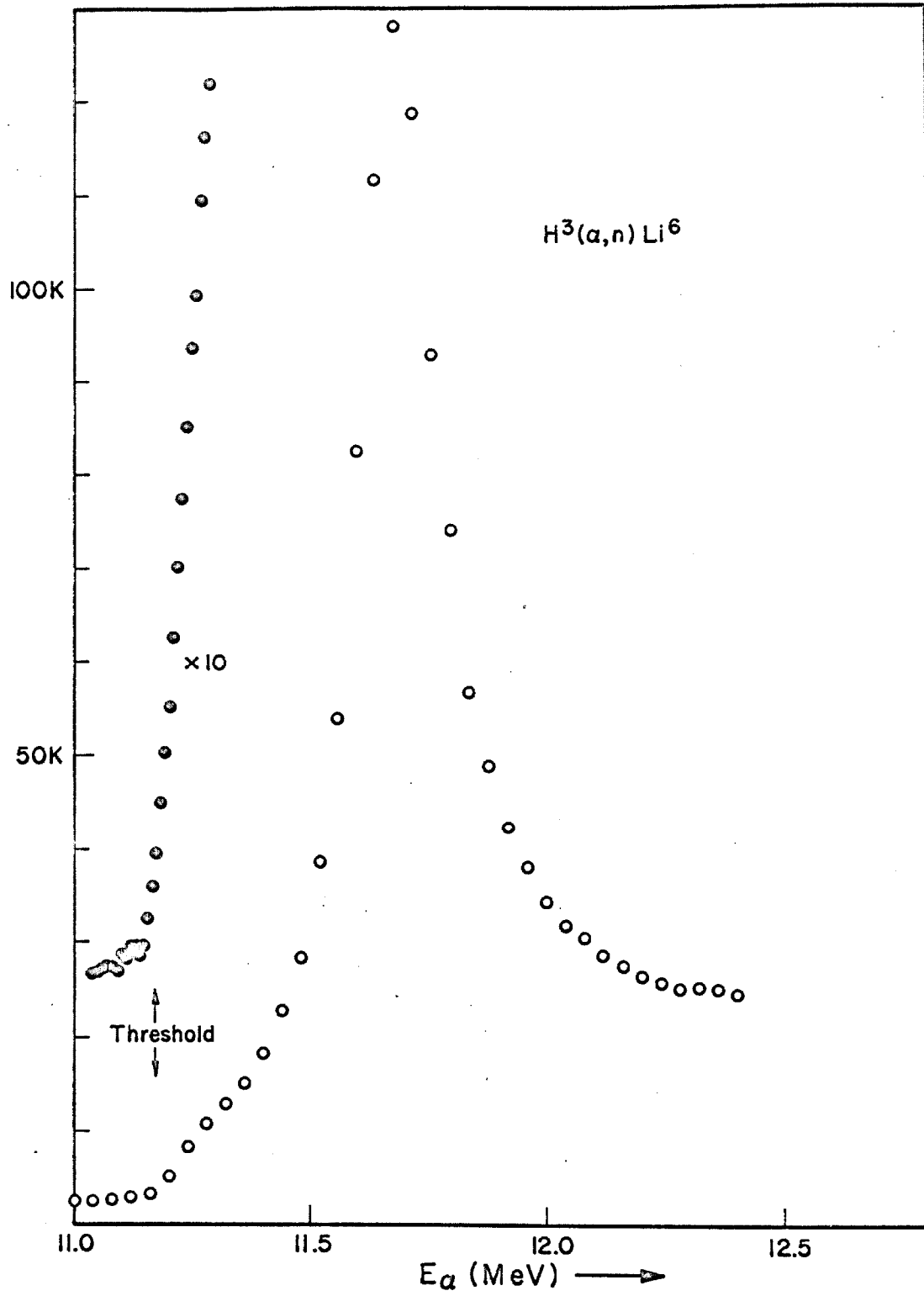
Figure 29

Data Obtained for the Reaction ^{3}H(α, n)^{6}Li from
the Inverse Reaction

This figure shows the total reaction cross section for
the reaction ^{3}H(α, n)^{6}Li as a function of laboratory energy. The
line serves only to connect the points. These data were obtained
by converting data on the reaction ^{6}Li(n, α)^{3}H to our system.
The data on the inverse reaction were obtained by Schwarz,
(1965). (Page 26)
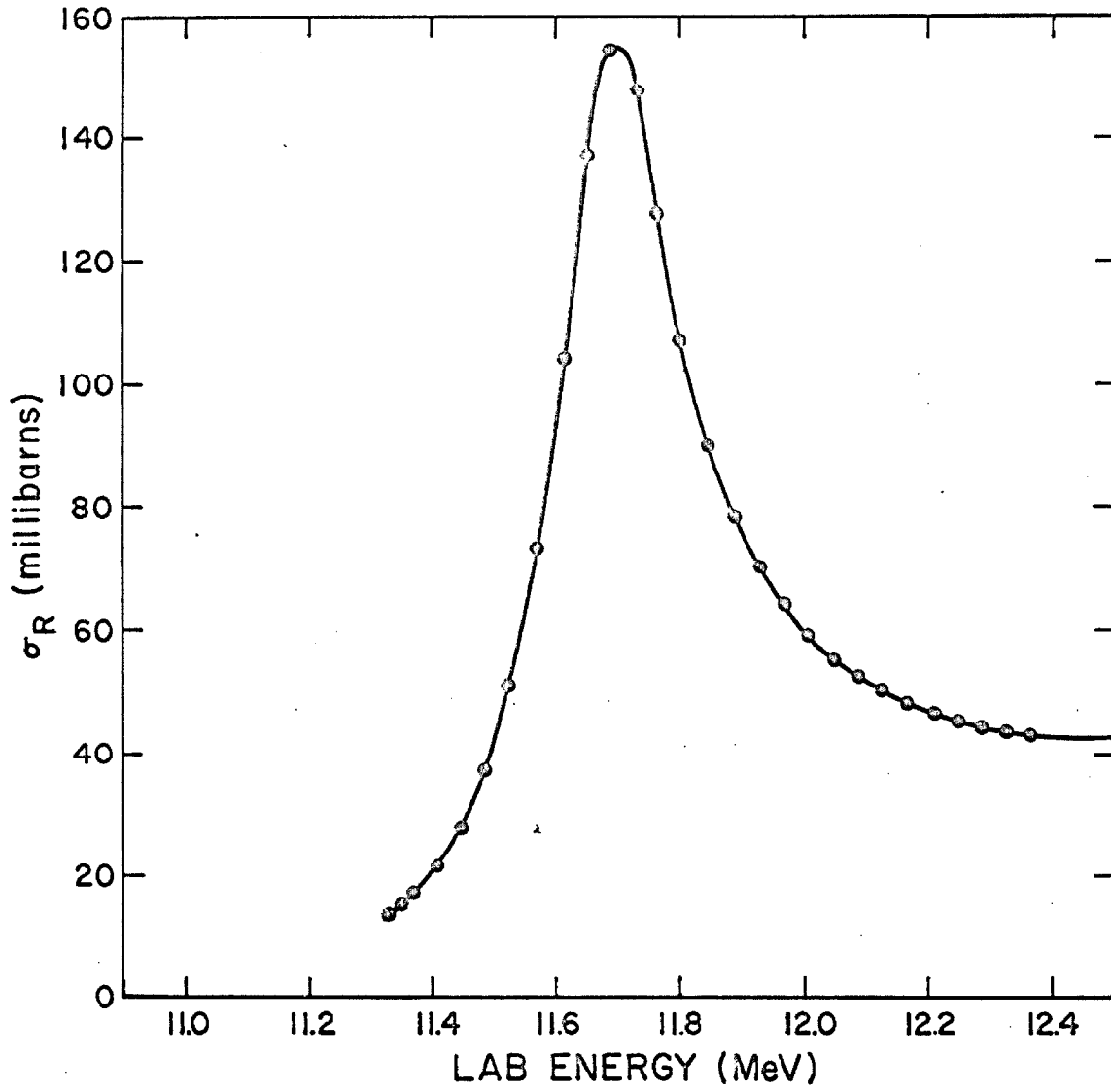
Figure 30

Schematic Diagram of the Detection Geometry
for the $^3H(\alpha, n^1)^6Li^*$ Reaction

This figure shows the geometry and apparatus used to
detect neutrons for the $^3H(\alpha, n^1)^6Li^*$ reaction. The paraffin
moderator is cast in the form of a cylinder with the target and
detector shown on axis. The diameter of the cylinder is 31 cm.
and its length is 33 cm. The distance from the target to the
detector is 19 cm. (Page 11)
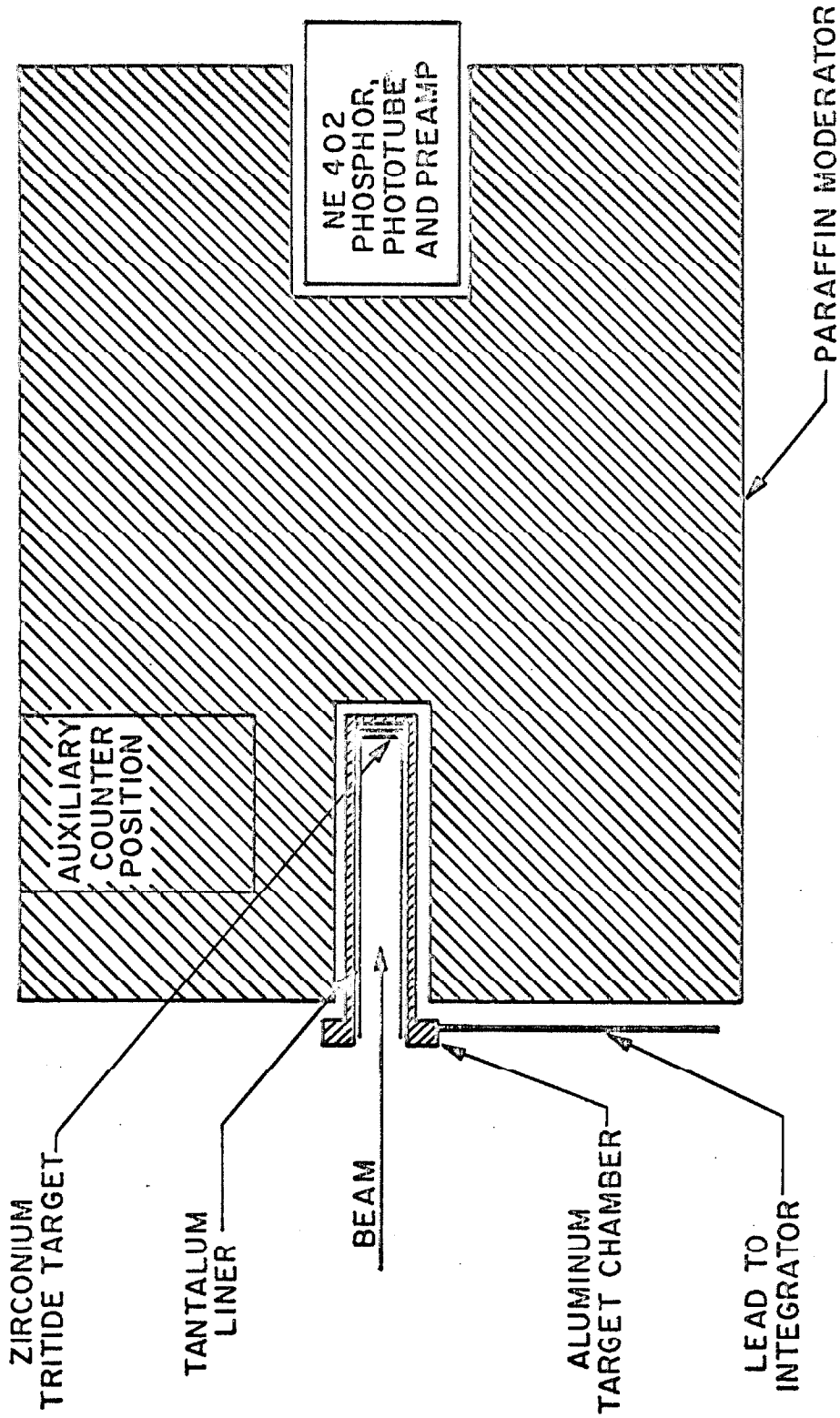
NEUTRON DETECTION GEOMETRY

Figure 31

Excitation Curve for the ^{3}H(α, n^1)^{6}Li* Reaction

      This figure shows the total reaction cross section for the ^{3}H(α, n)^{6}Li and ^{3}H(α, n^1)^{6}Li* reactions. The data on ^{3}H(α, n)^{6}Li below the ^{3}H(α, n^1)^{6}Li* threshold provides normalization and background subtraction data thus allowing the effect of the ^{3}H(α, n^1)^{6}Li* reaction to be separated. (Page 12)

261
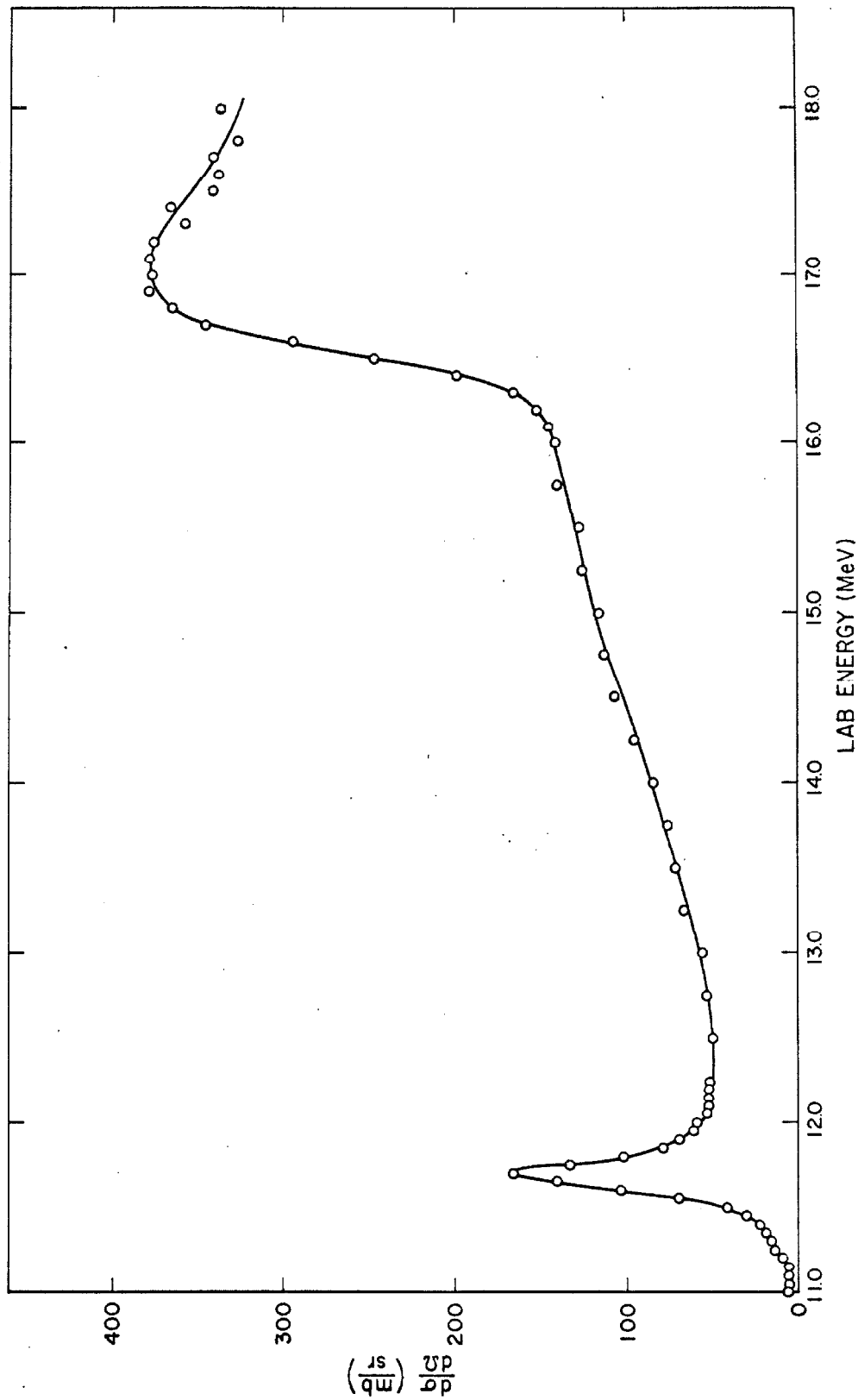
Figure 32

Diagram of the High Energy Gas Cell

This figure shows a diagram of the gas cell used to obtain the ^{4}He(^{3}He, ^{3}He)^{4}He data for energies above 14.7 MeV. (Page 15)

CLAMP
RING

O-RING
SEAL

LUCITE
CHAMBER TOP

BRASS BODY

FOIL WINDOWS
CENTER WINDOW
IS MYLAR
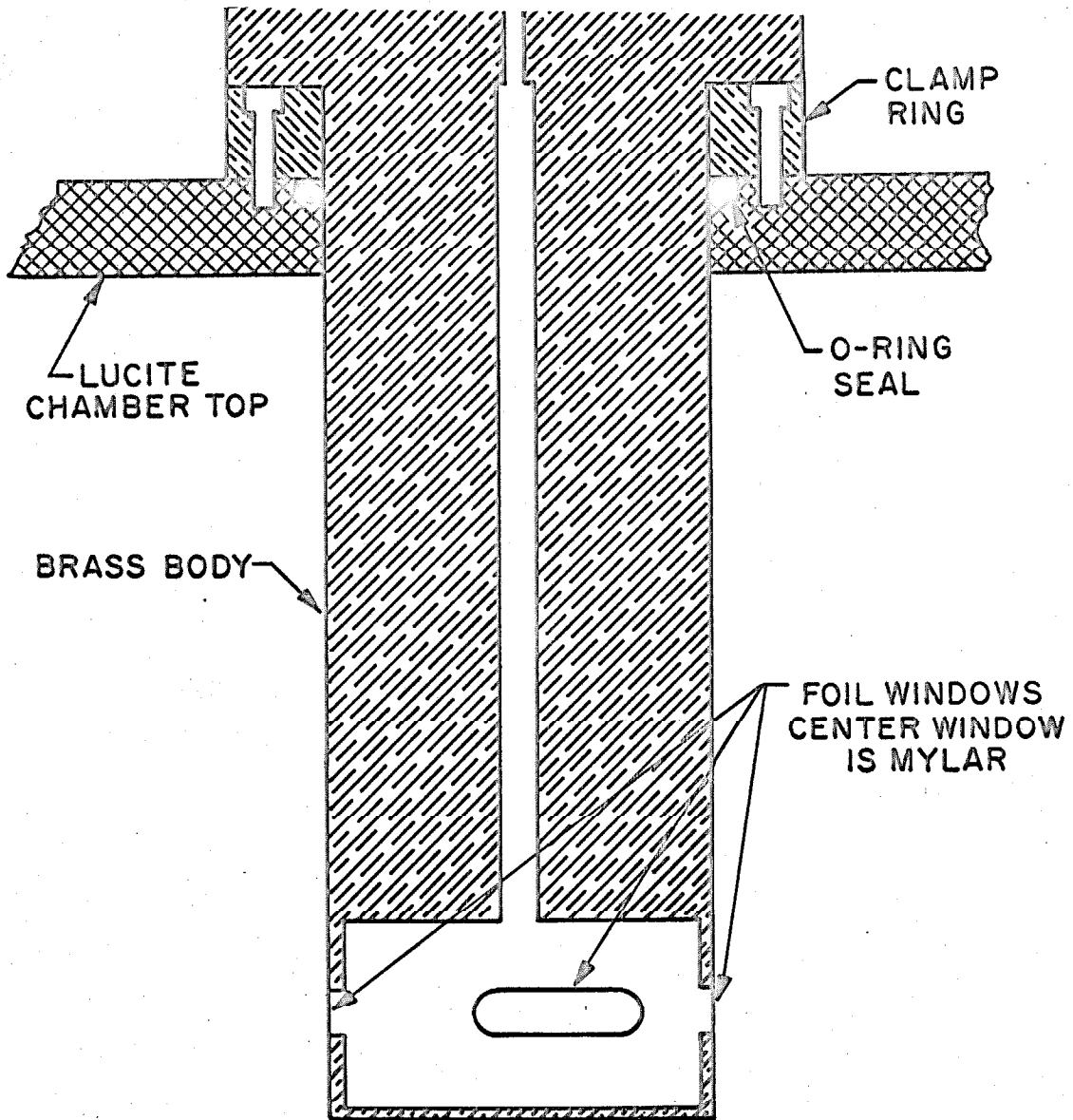
HIGH ENERGY GAS CELL

Figure 33

Typical Spectrum from the ^{4}He(^{3}He, ^{3}He)^{4}He Experiment

This figure shows a typical spectrum from the 400-channel analyzer. The first 200 channels show charge 1 particles. The second 200 show charge 2 particles. The highest group (in channel number) is the ^{3}He group. Just below it is the α group. The group near channel 80 is a proton group from the reaction ^{4}He(^{3}He, p)^{6}Li. The sharp group near channel 40 is a proton group from the reaction ^{4}He(^{3}He, p$_1$)^{6}Li*. The background under this group is due to deuterons from the breakup of ^{6}Li. (Page 16)

CHANNEL NUMBER

NUMBER OF COUNTS
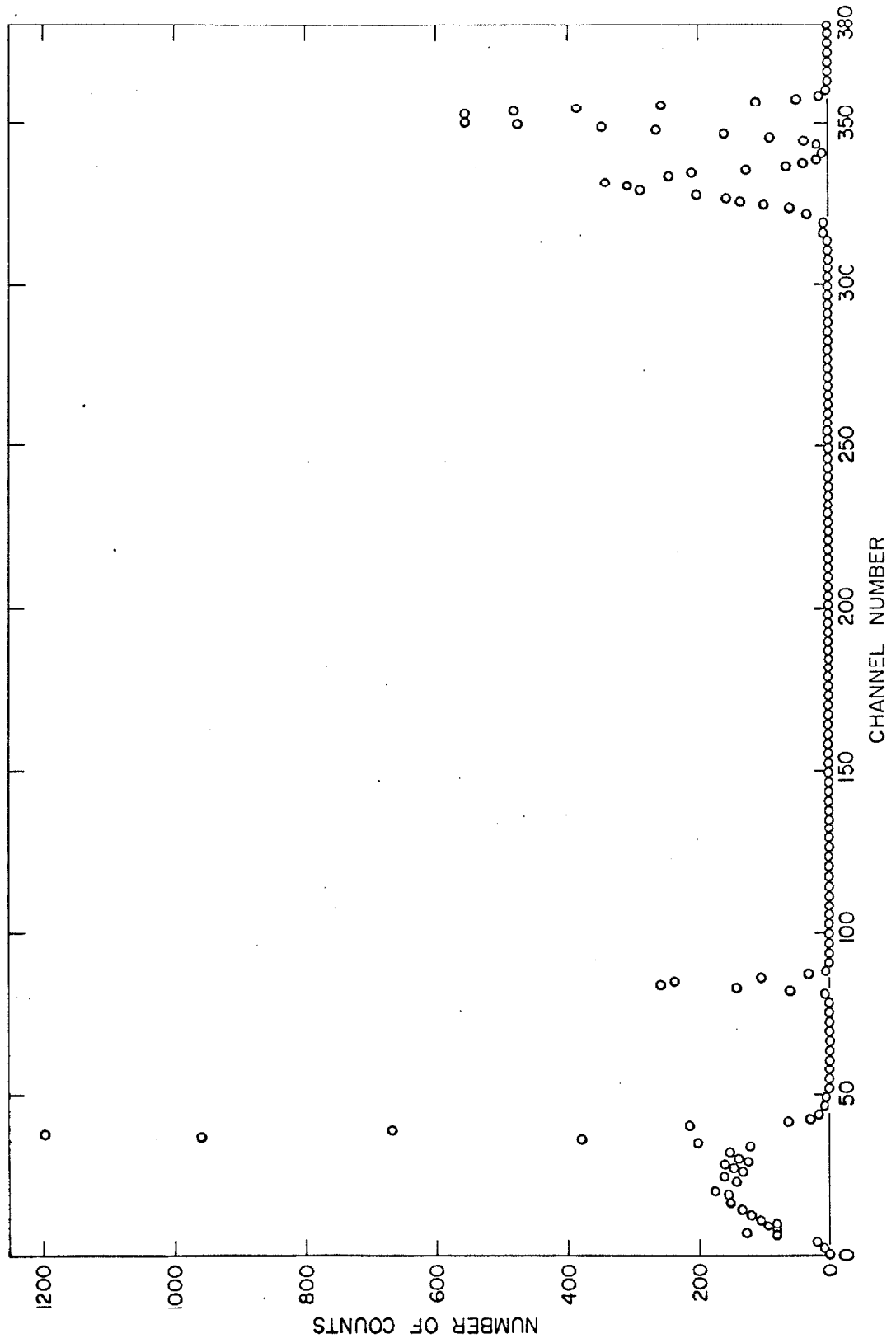
Figure 34

Excitation Curve for the ^{4}He(^{3}He, ^{3}He)^{4}He Experiment

This figure shows an excitation curve for the ^{4}He(^{3}He, ^{3}He)^{4}He experiment. The differential elastic scattering cross section (in the center-of-mass system) is plotted as a function of laboratory energy for the center-of-mass angle. The open circles are the data and the solid line is a fit from the phase shift analysis. (Page 17)
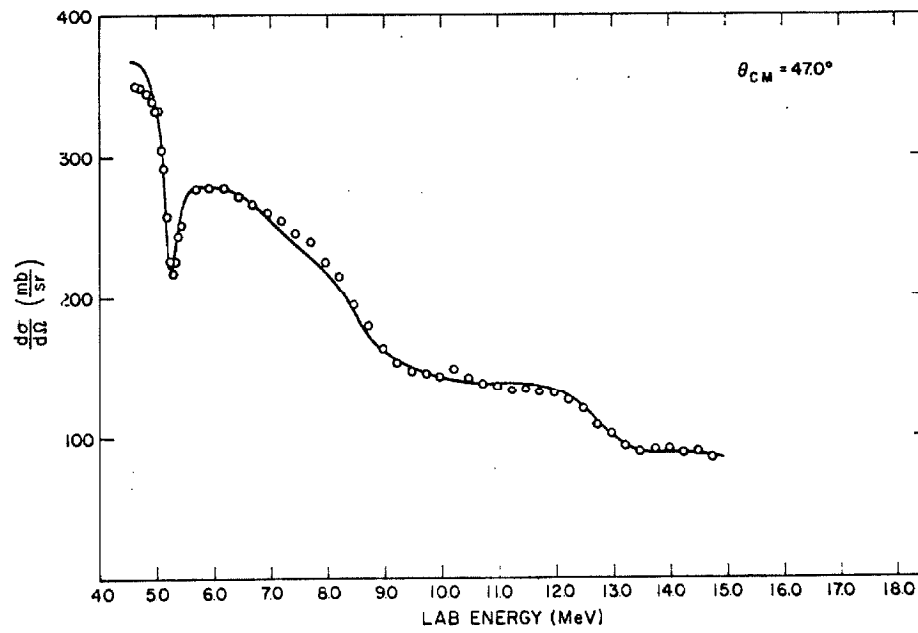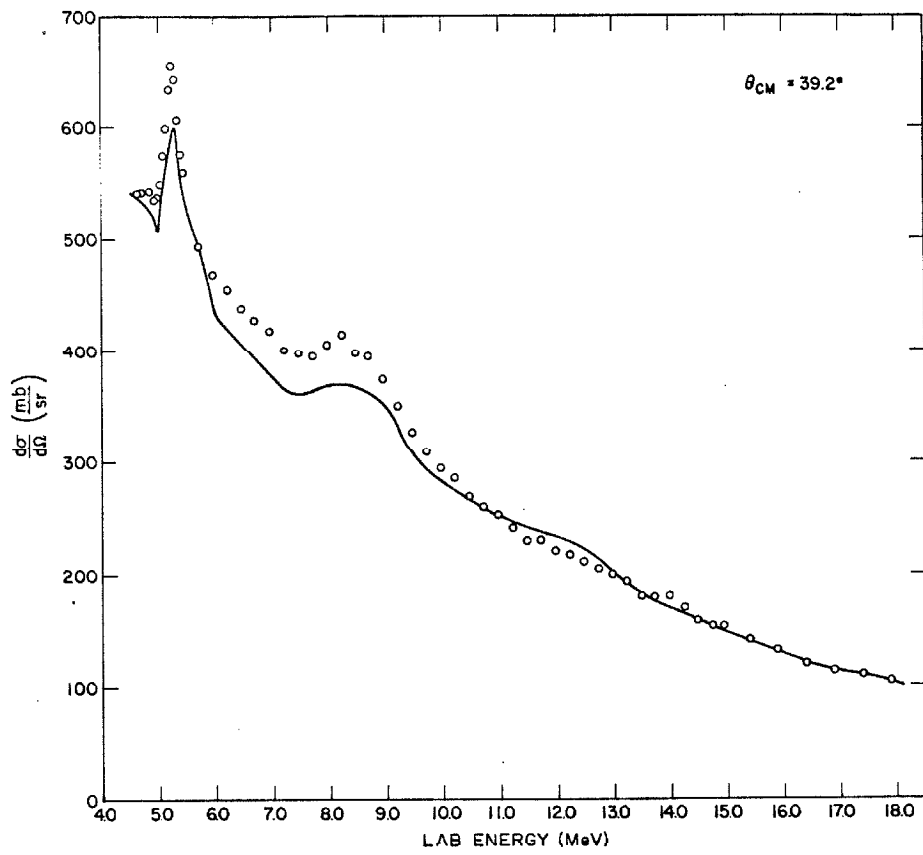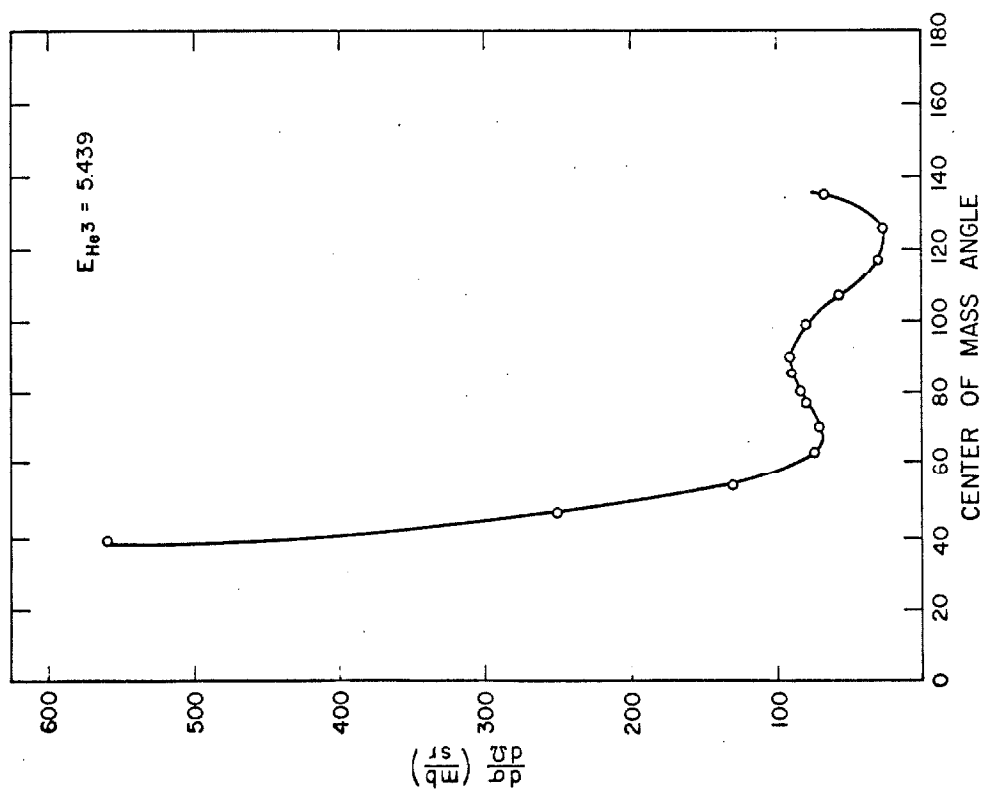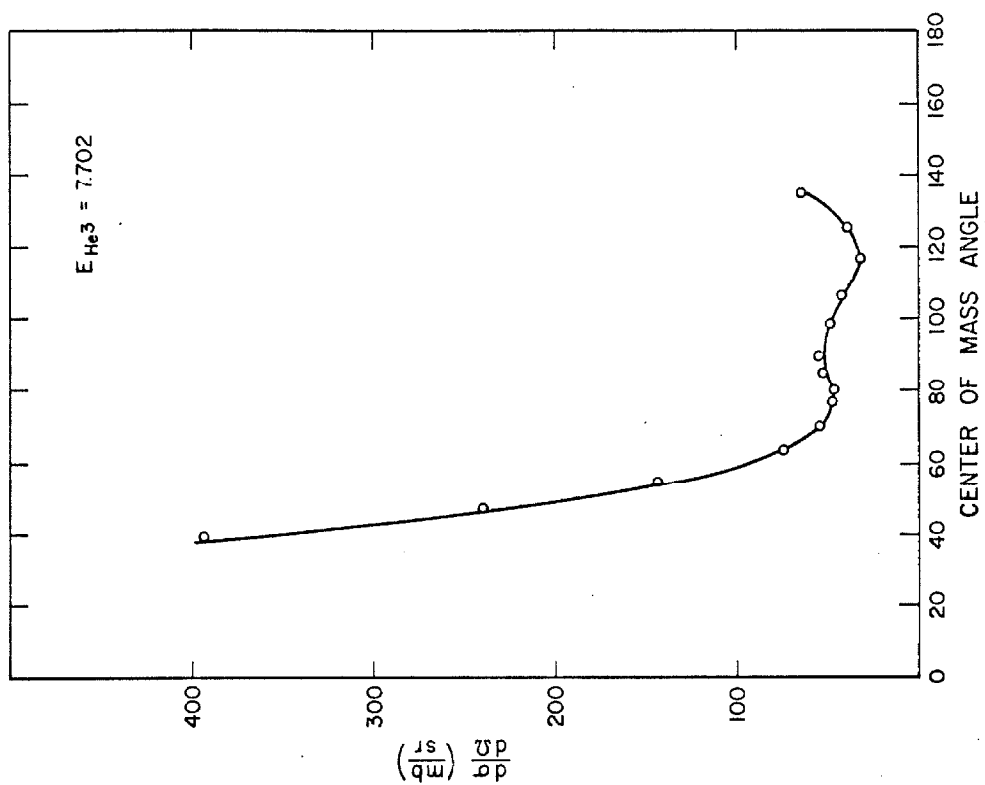
Figure 35

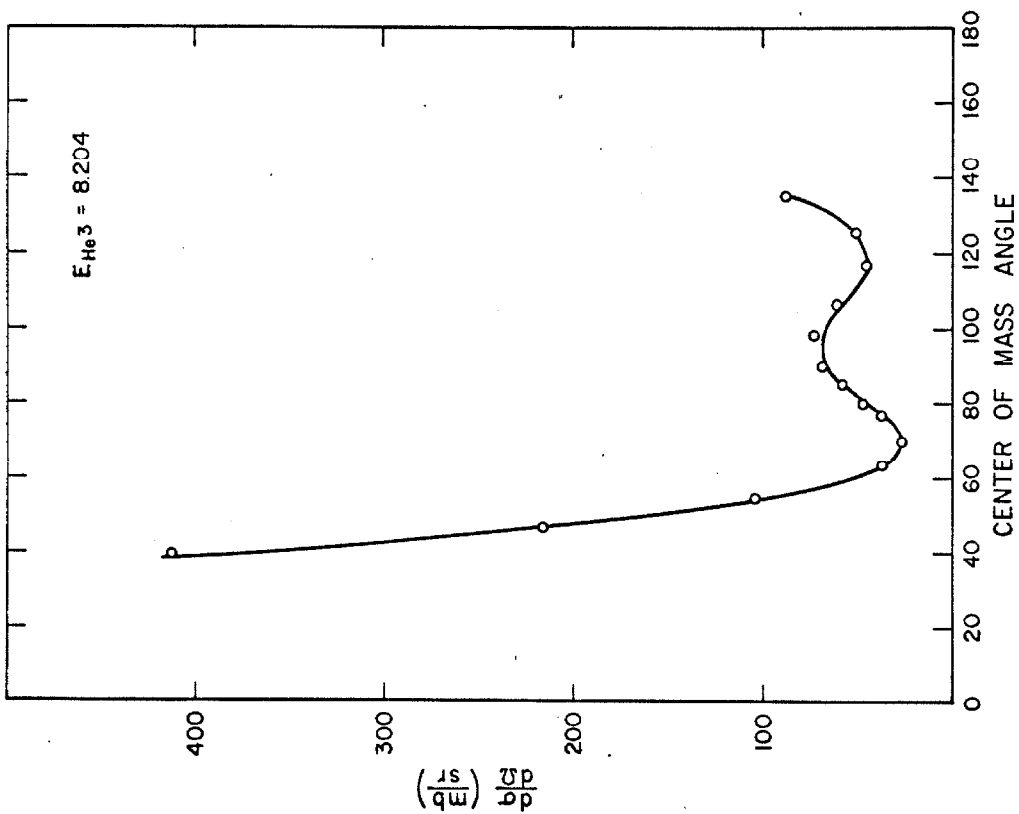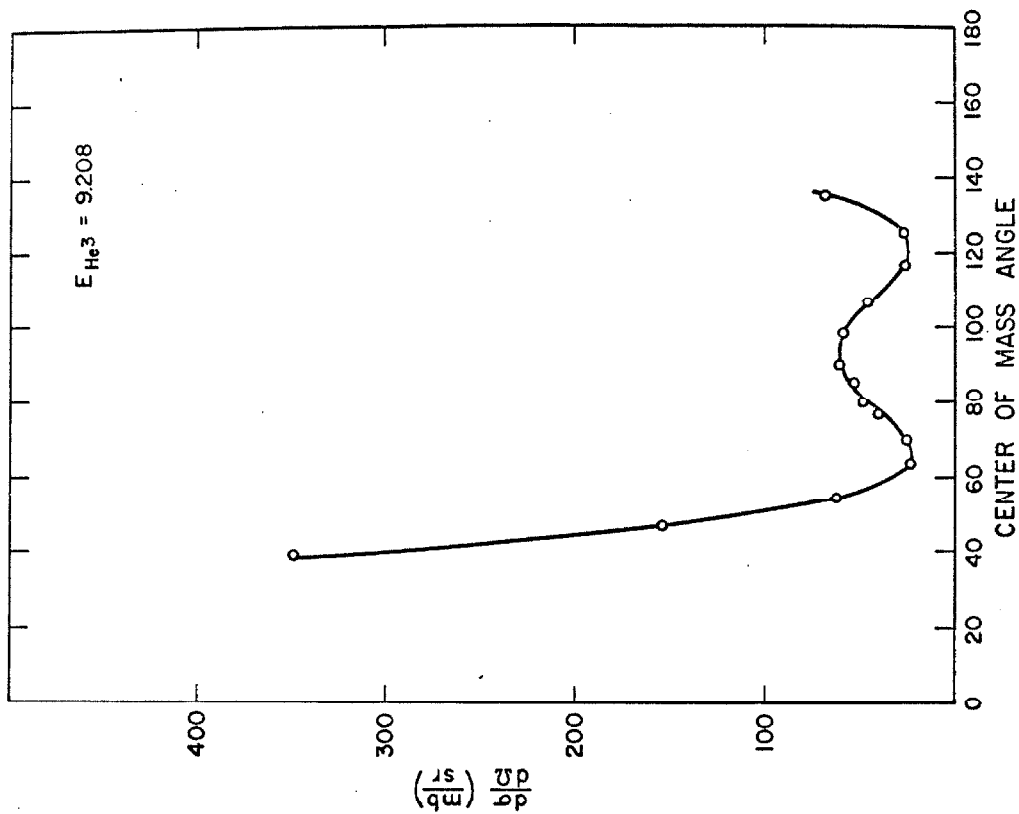Excitation Curve for the ^{4}He(^{3}He, ^{3}He)^{4}He Experiment

This figure shows an excitation curve for the ^{4}He(^{3}He, ^{3}He)^{4}He experiment. The differential elastic scattering cross section (in the center-of-mass system) is plotted as a function of laboratory energy for the center-of-mass angle. The open circles are the data and the solid line is a fit from the phase shift analysis. (Page 17)
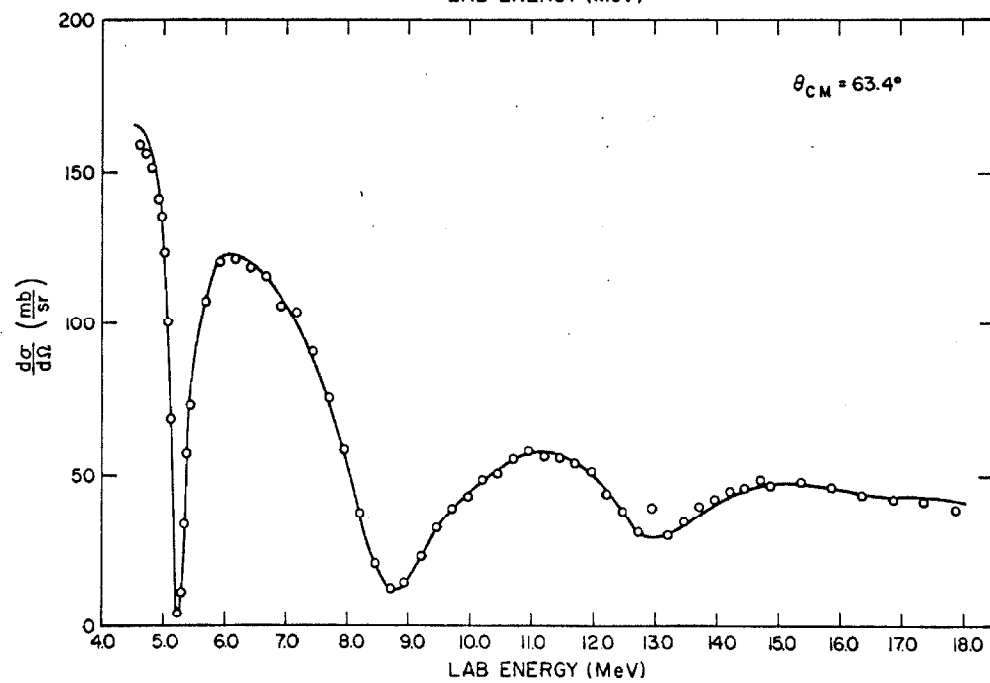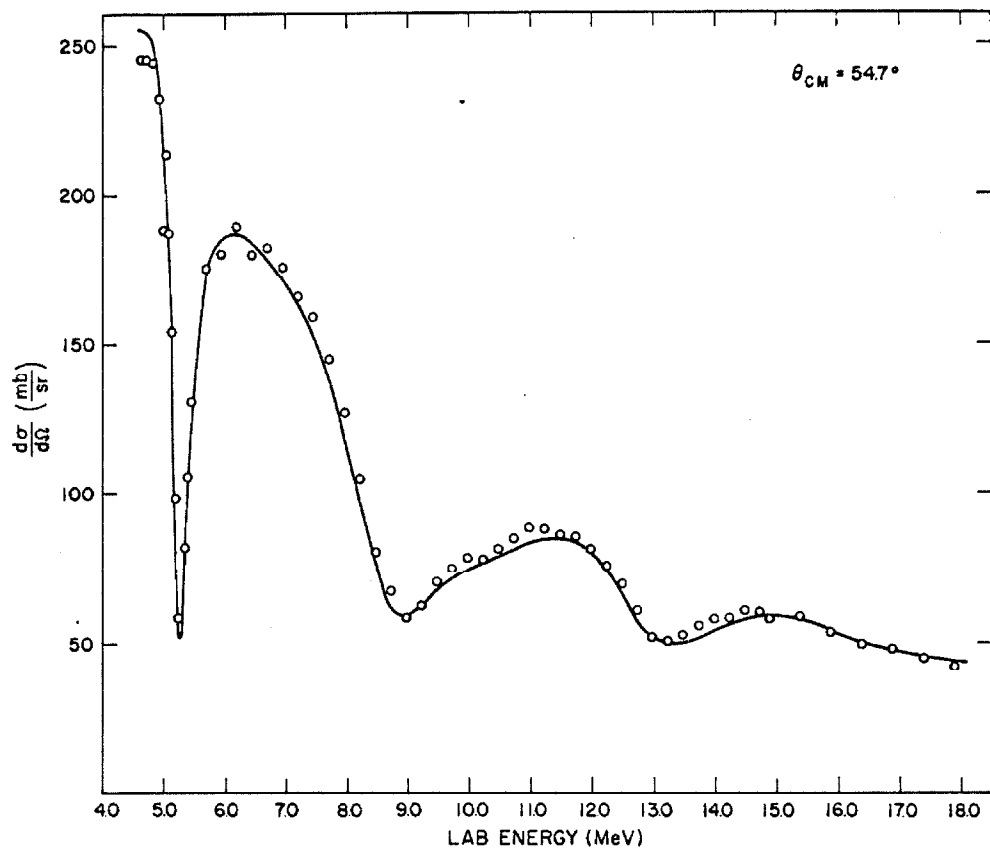
Figure 36

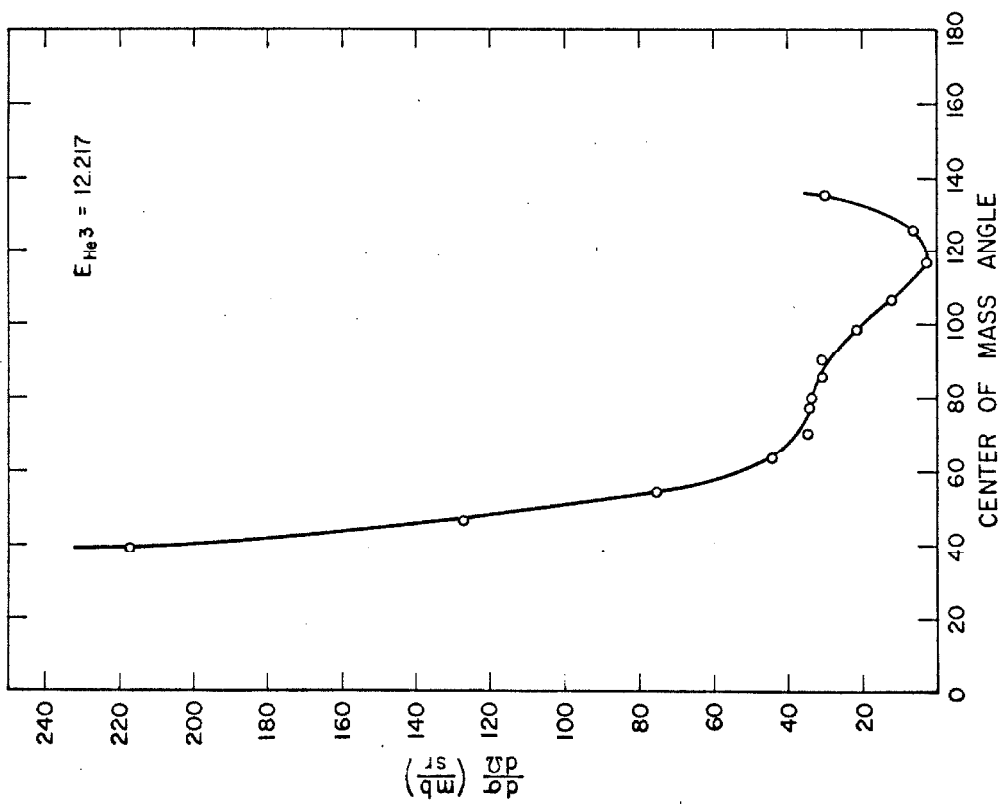Excitation Curve for the ^{4}He(^{3}He, ^{3}He)^{4}He Experiment

This figure shows an excitation curve for the ^{4}He(^{3}He, ^{3}He)^{4}He experiment. The differential elastic scattering cross section (in the center-of-mass system) is plotted as a function of laboratory energy for the center-of-mass angle. The open circles are the data and the solid line is a fit from the phase shift analysis. (Page 17)

$\theta_{CM} = 70.1°$
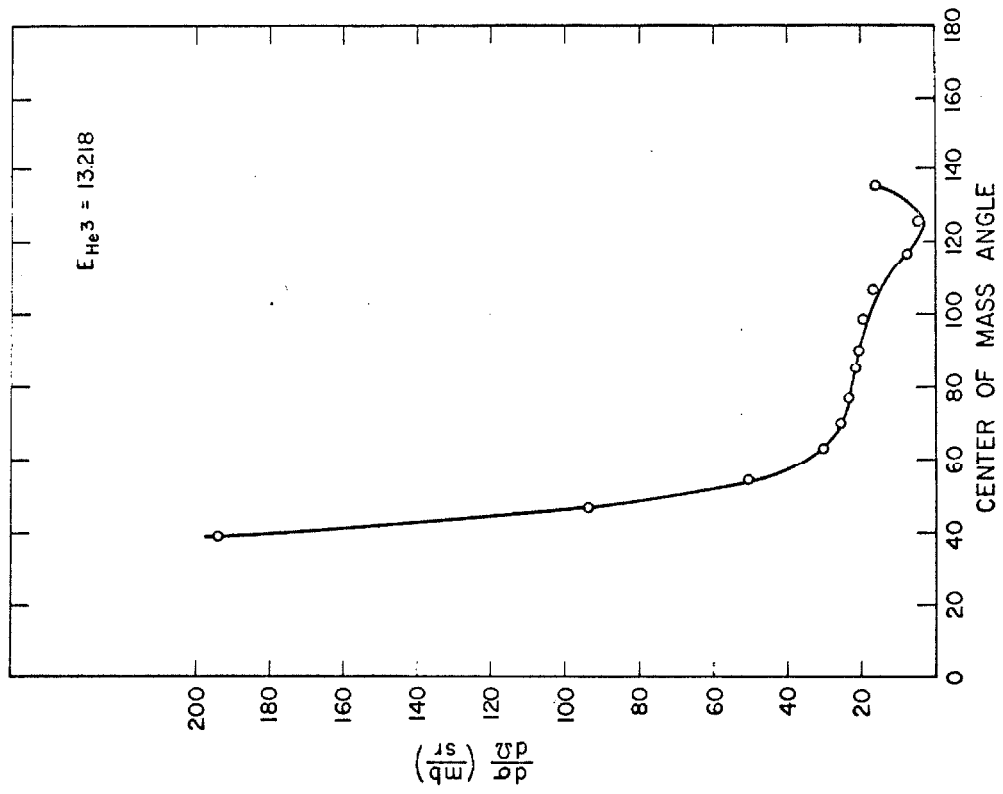
$\theta_{CM} = 77.0°$
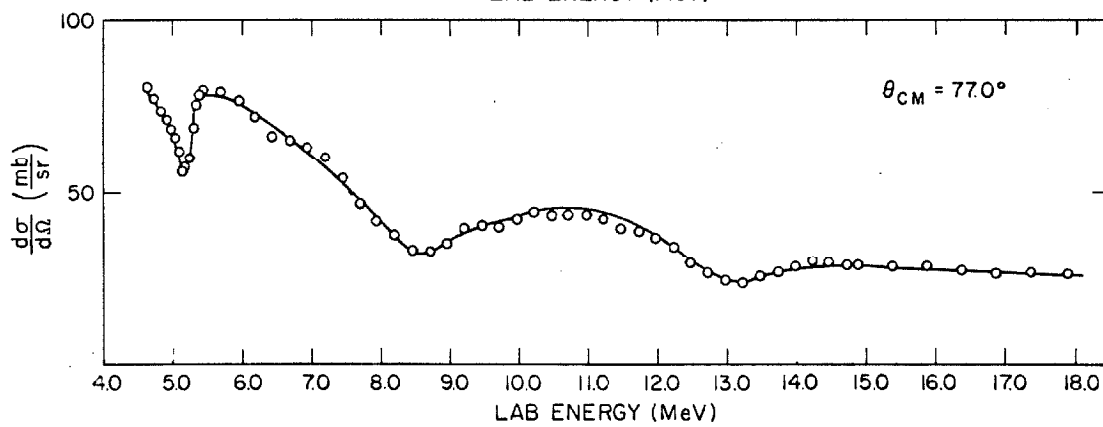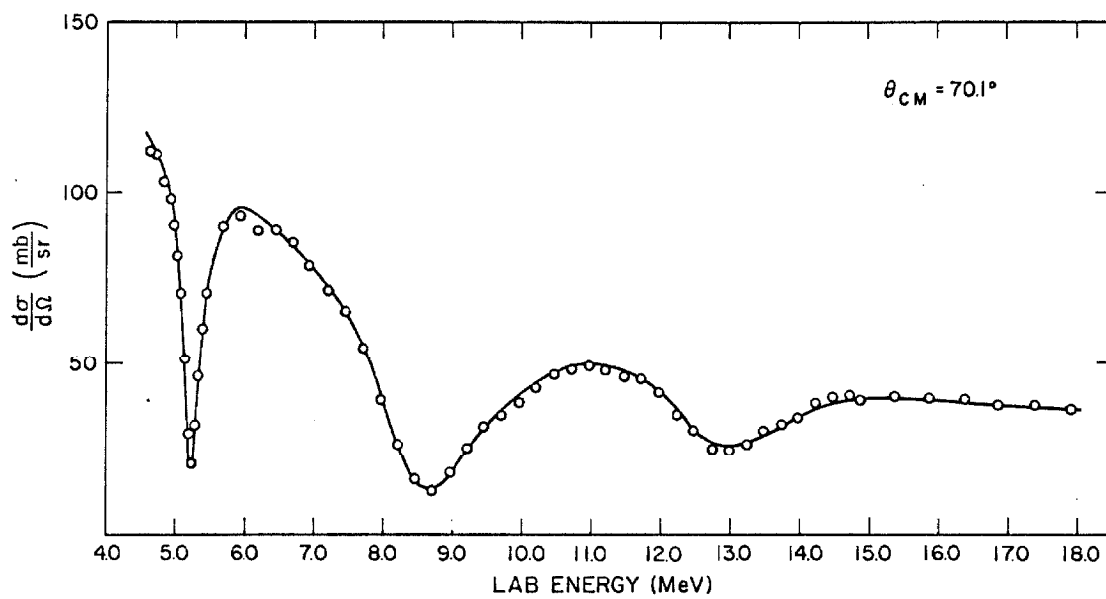
Figure 37

Excitation Curve for the ^{4}He(^{3}He, ^{3}He)^{4}He Experiment

This figure shows an excitation curve for the ^{4}He(^{3}He, ^{3}He)^{4}He experiment. The differential elastic scattering cross section (in the center-of-mass system) is plotted as a function of laboratory energy for the center-of-mass angle. The open circles are the data and the solid line is a fit from the phase shift analysis. (Page 17)
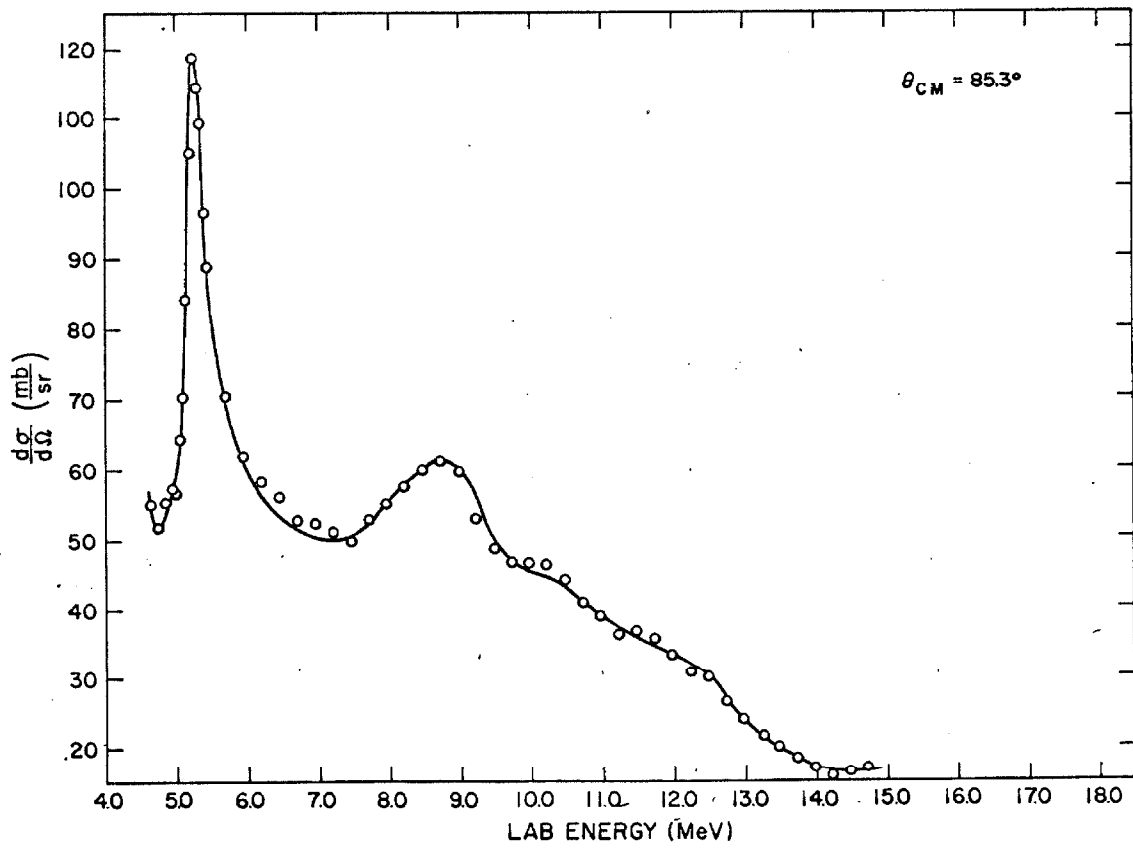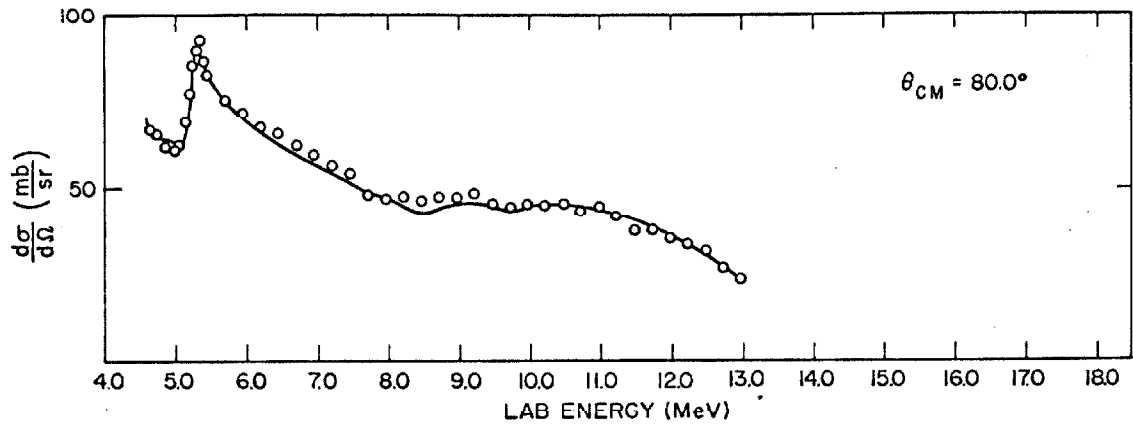
Figure 38

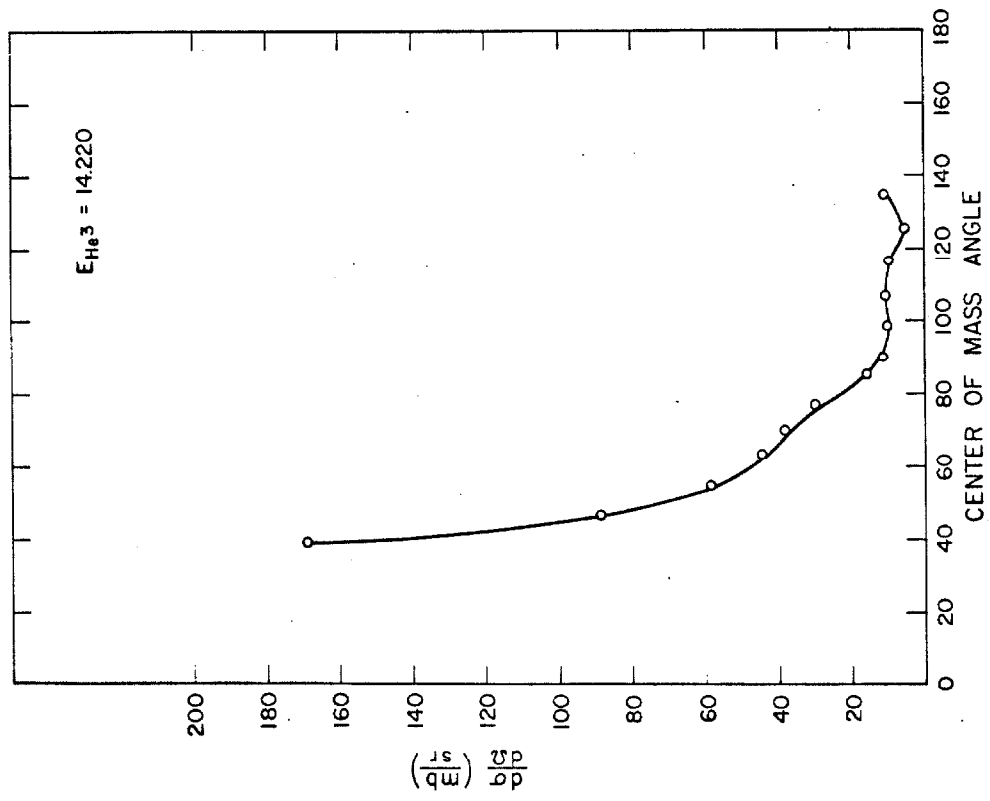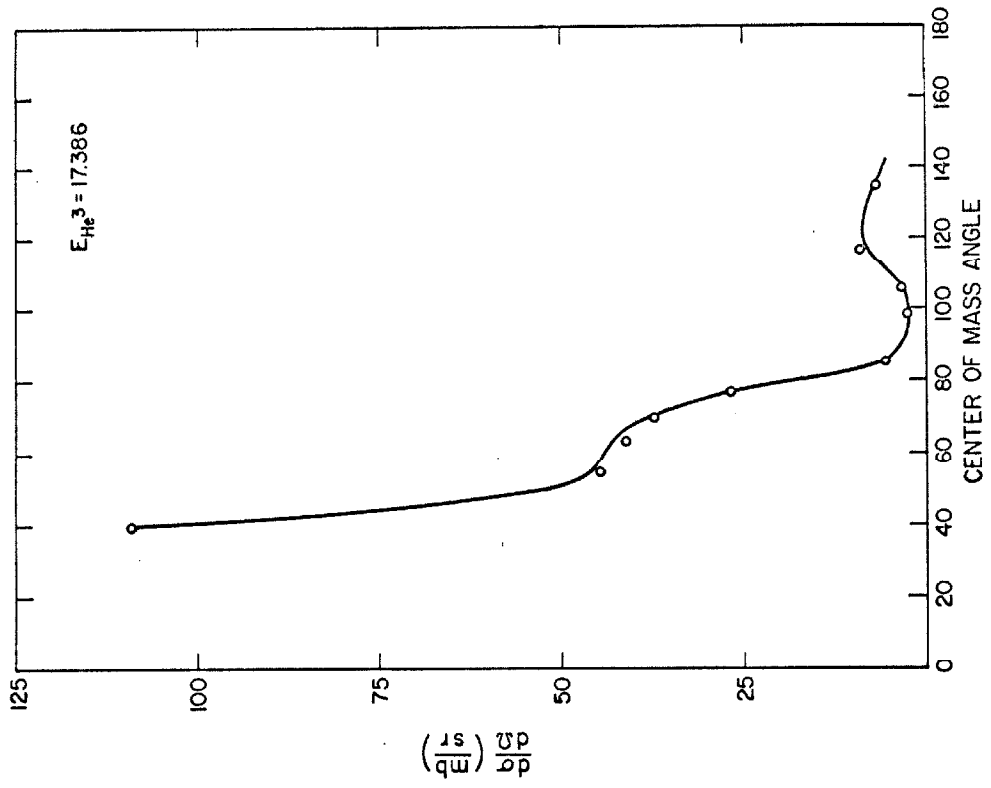Excitation Curve for the ^{4}He(^{3}He, ^{3}He)^{4}He Experiment

This figure shows an excitation curve for the ^{4}He(^{3}He, ^{3}He)^{4}He experiment. The differential elastic scattering cross section (in the center-of-mass system) is plotted as a function of laboratory energy for the center-of-mass angle. The open circles are the data and the solid line is a fit from the phase shift analysis. (Page 17)
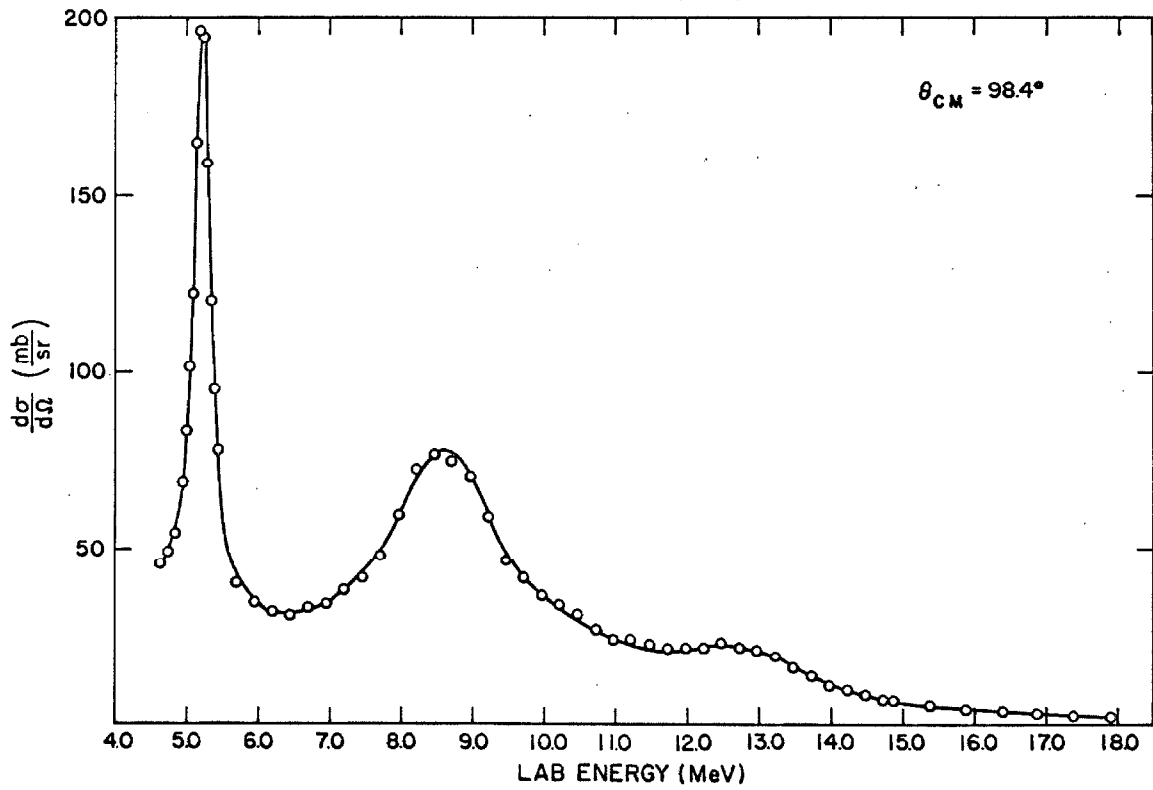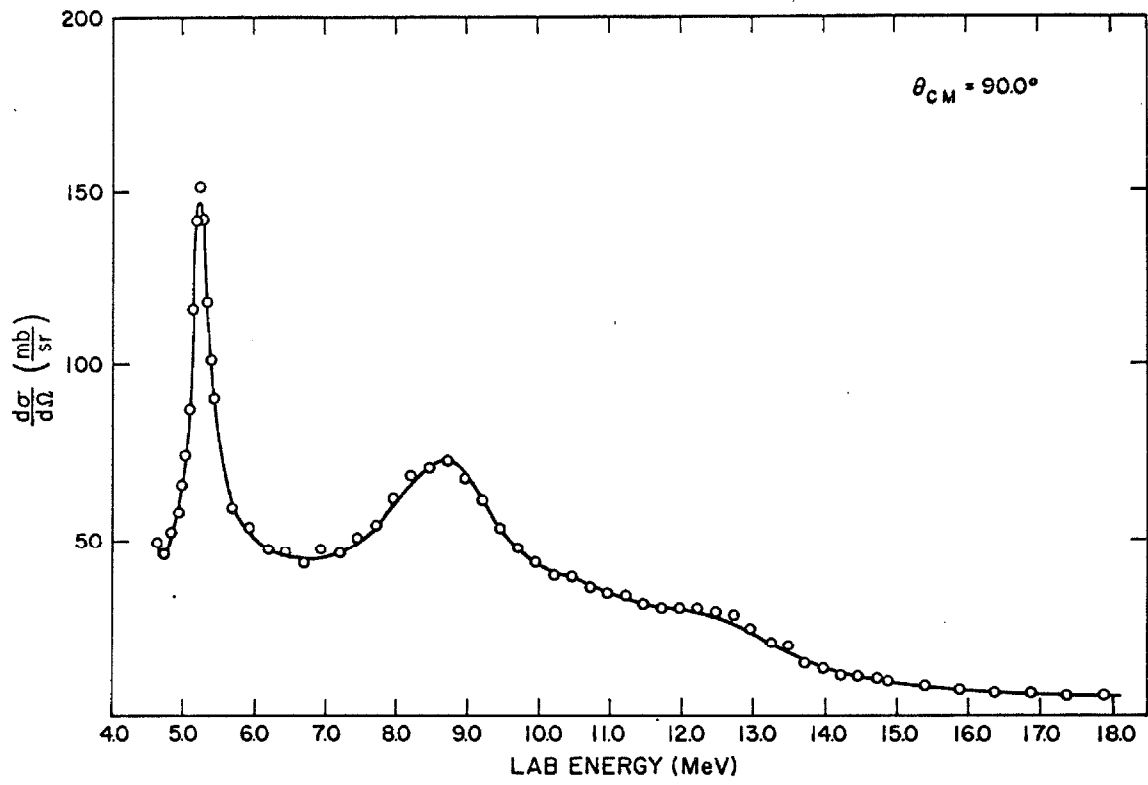
Figure 39

Excitation Curve for the ^{4}He(^{3}He, ^{3}He)^{4}He Experiment

This figure shows an excitation curve for the ^{4}He(^{3}He, ^{3}He)^{4}He experiment. The differential elastic scattering cross section (in the center-of-mass system) is plotted as a function of laboratory energy for the center-of-mass angle. The open circles are the data and the solid line is a fit from the phase shift analysis. (Page 17)
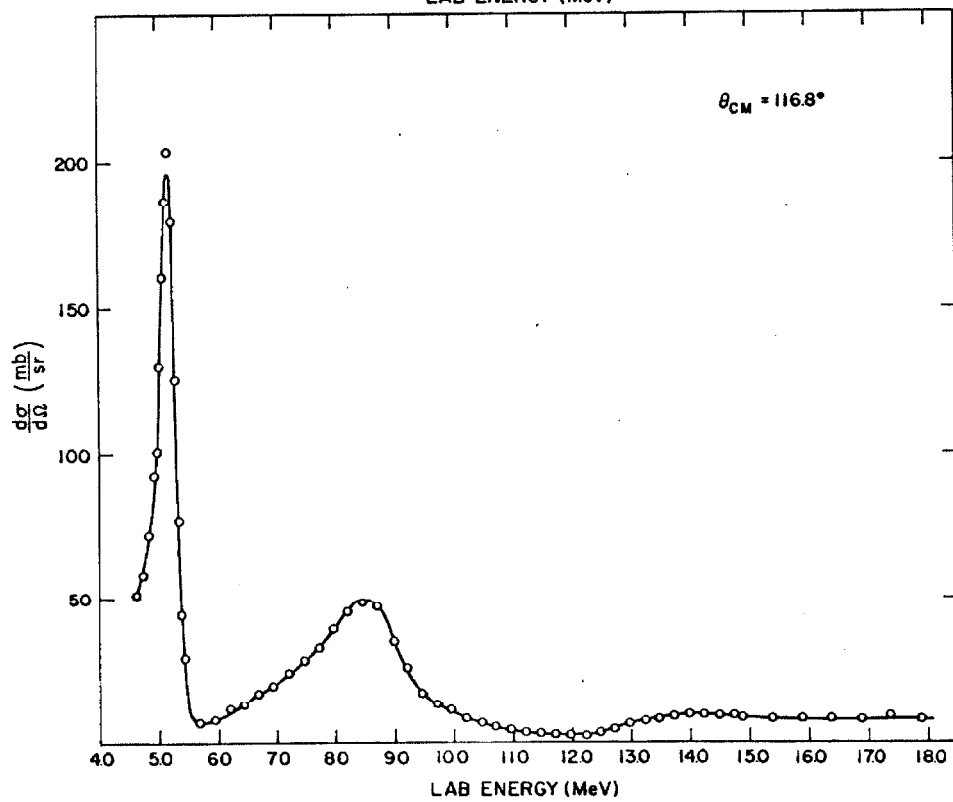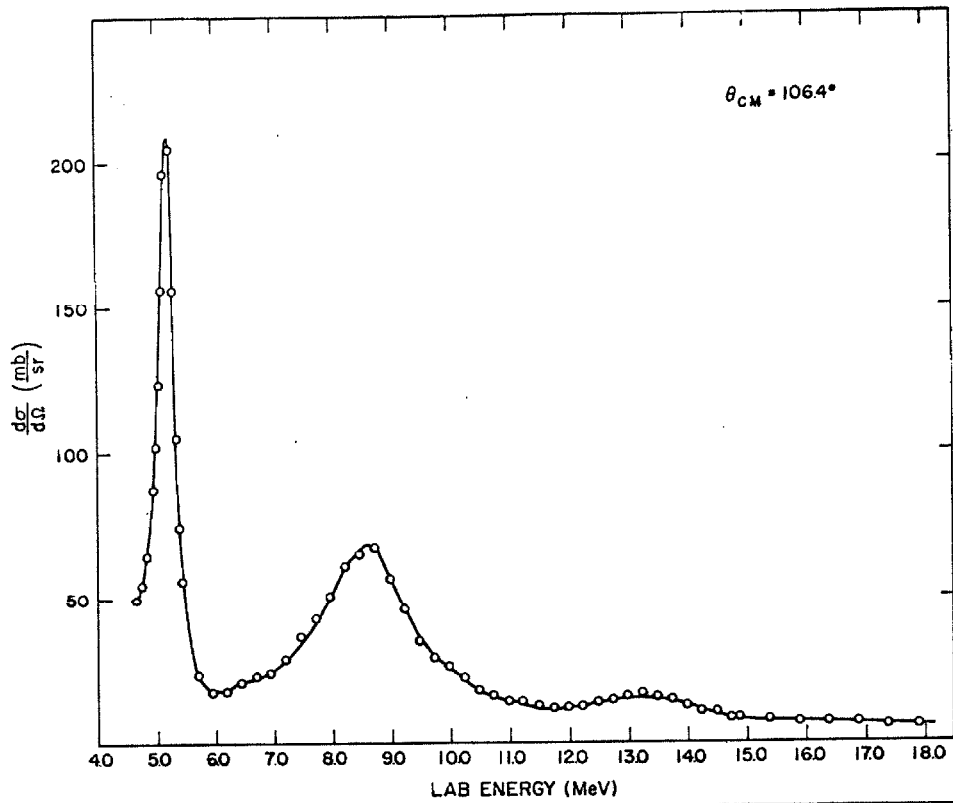
Figure 40

Excitation Curve for the ^{4}He(^{3}He, ^{3}He)^{4}He Experiment

    This figure shows an excitation curve for the ^{4}He(^{3}He, ^{3}He)^{4}He experiment. The differential elastic scattering cross section (in the center-of-mass system) is plotted as a function of laboratory energy for the center-of-mass angle. The open circles are the data and the solid line is a fit from the phase shift analysis. (Page 17)
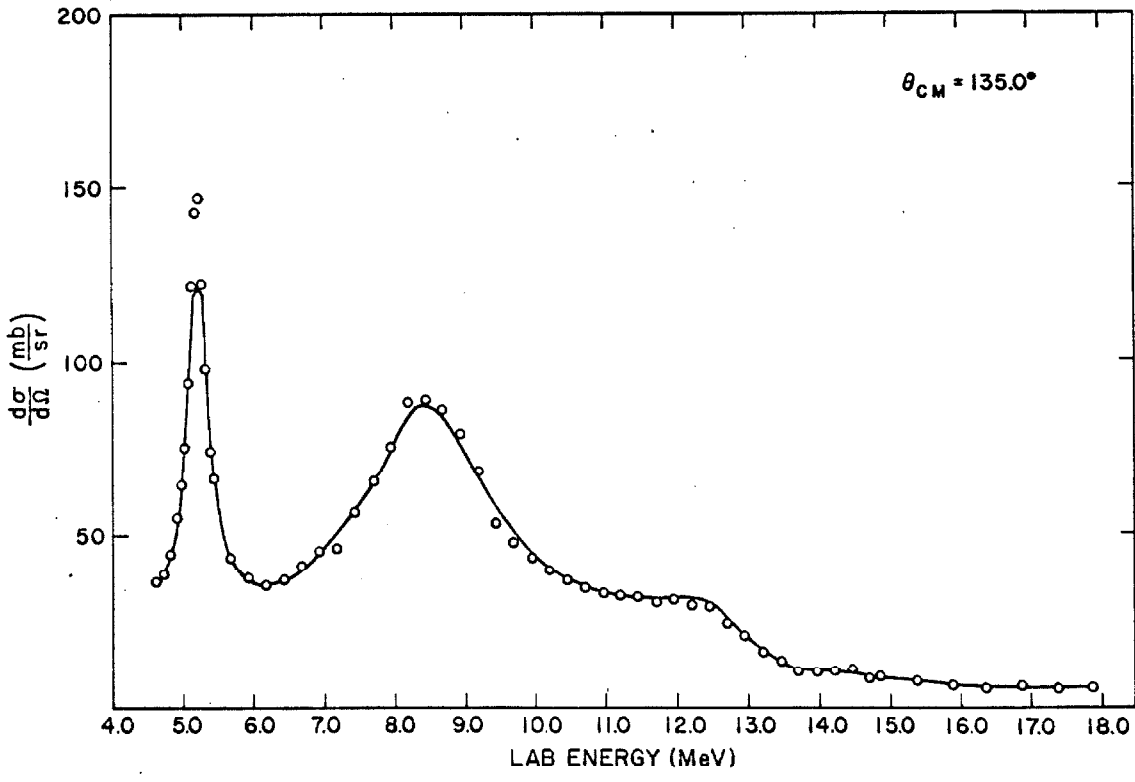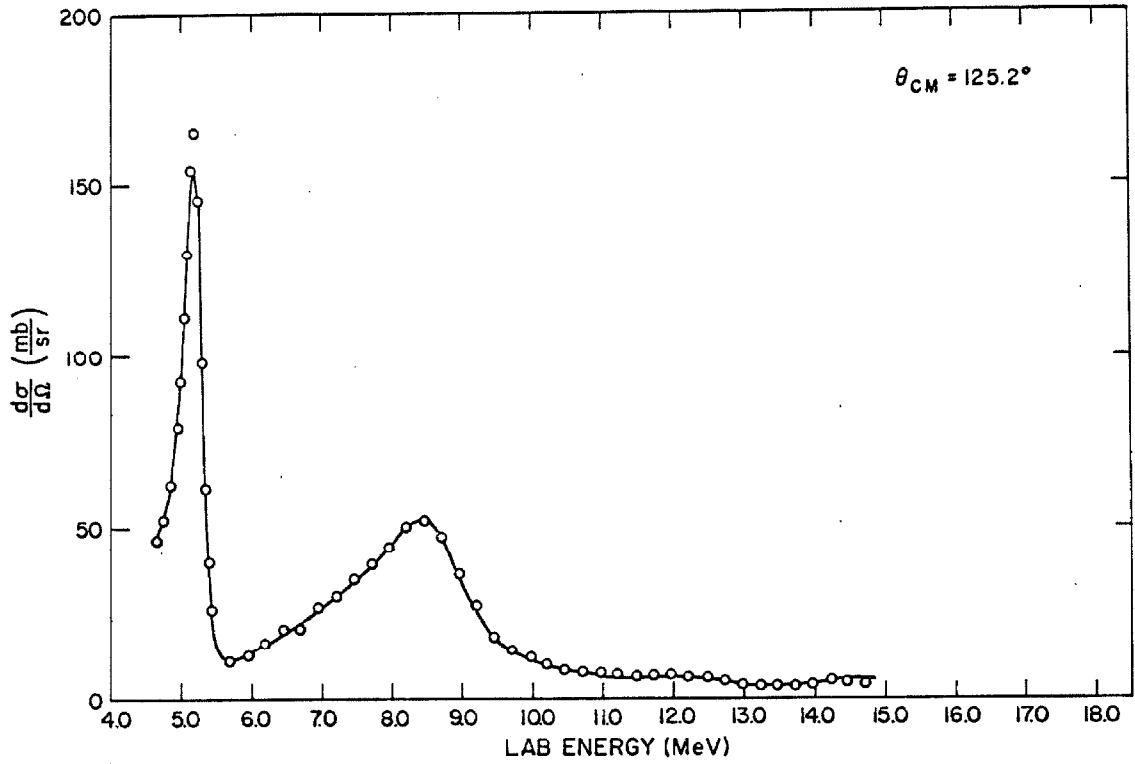
Figure 41

Angular Distribution for the ^{4}He(^{3}He, ^{3}He)^{4}He Experiment

This figure shows the differential elastic scattering cross section (in the center-of-mass system) as a function of center-of-mass angle. The open circles are data points and the solid line is a fit from the phase shift analysis. (Page 17)
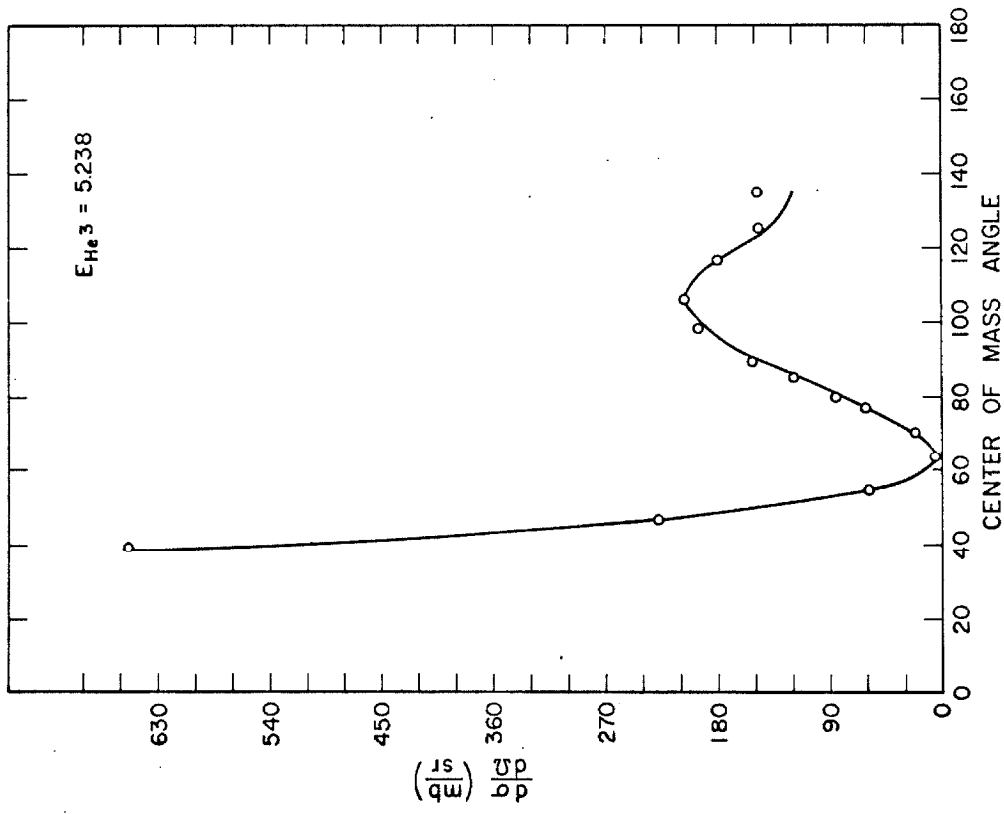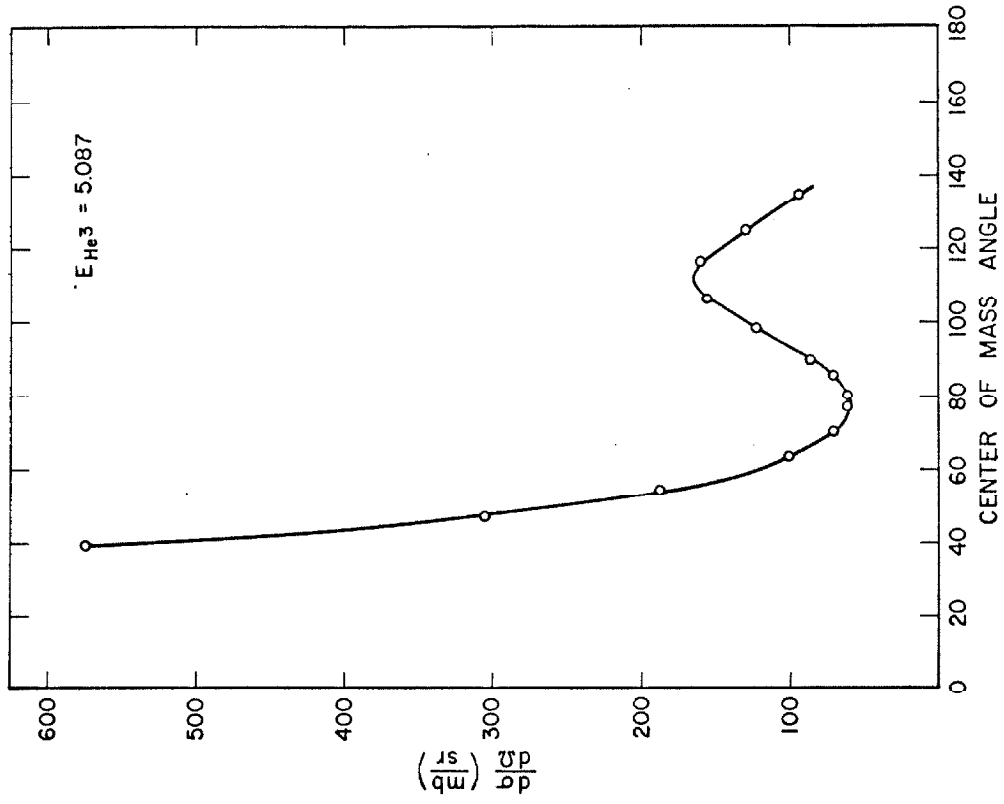
Figure 42

Angular Distribution for the ^{4}He(^{3}He, ^{3}He)^{4}He Experiment

This figure shows the differential elastic scattering cross section (in the center-of-mass system) as a function of center-of-mass angle. The open circles are data points and the solid line is a fit from the phase shift analysis. (Page 17)

$E_{He3} = 5.439$

$E_{He3} = 7.702$

CENTER OF MASS ANGLE

$\frac{d\sigma}{d\Omega} \left(\frac{mb}{sr} \right)$

Figure 43

Angular Distribution for the ^{4}He(^{3}He, ^{3}He)^{4}He Experiment

This figure shows the differential elastic scattering cross section (in the center-of-mass system) as a function of center-of-mass angle. The open circles are data points and the solid line is a fit from the phase shift analysis. (Page 17)

$E_{He3} = 8.204$

$E_{He3} = 9.208$

CENTER OF MASS ANGLE

$\frac{d\sigma}{d\Omega} \left(\frac{mb}{sr}\right)$

Figure 44

Angular Distribution for the ^{4}He(^{3}He, ^{3}He)^{4}He Experiment

This figure shows the differential elastic scattering cross section (in the center-of-mass system) as a function of center-of-mass angle. The open circles are data points and the solid line is a fit from the phase shift analysis. (Page 17)

$E_{He3} = 12.217$

CENTER OF MASS ANGLE

$\frac{d\sigma}{d\Omega} \left(\frac{mb}{sr} \right)$

$E_{He3} = 13.218$

CENTER OF MASS ANGLE

$\frac{d\sigma}{d\Omega} \left(\frac{mb}{sr} \right)$

Figure 45

Angular Distribution for the ^{4}He(^{3}He, ^{3}He)^{4}He Experiment

This figure shows the differential elastic scattering cross section (in the center-of-mass system) as a function of center-of-mass angle. The open circles are data points and the solid line is a fit from the phase shift analysis. (Page 17)

$E_{He^3} = 17.386$

$\frac{d\sigma}{d\Omega} \left(\frac{mb}{sr} \right)$

CENTER OF MASS ANGLE

$E_{He^3} = 14.220$

$\frac{d\sigma}{d\Omega} \left(\frac{mb}{sr} \right)$

CENTER OF MASS ANGLE

Figure 46

Excitation Curves for the ^{4}He(^{3}He, p)^{6}Li Experiment

This figure shows the differential reaction cross sections for the ^{4}He(^{3}He, p)^{6}Li reaction at 2 typical laboratory angles. The open dots are the data obtained using the gas cell. The closed dots are data obtained by filling the whole south 20° chamber with target gas. The lines serve only to connect the points. (Page 18)
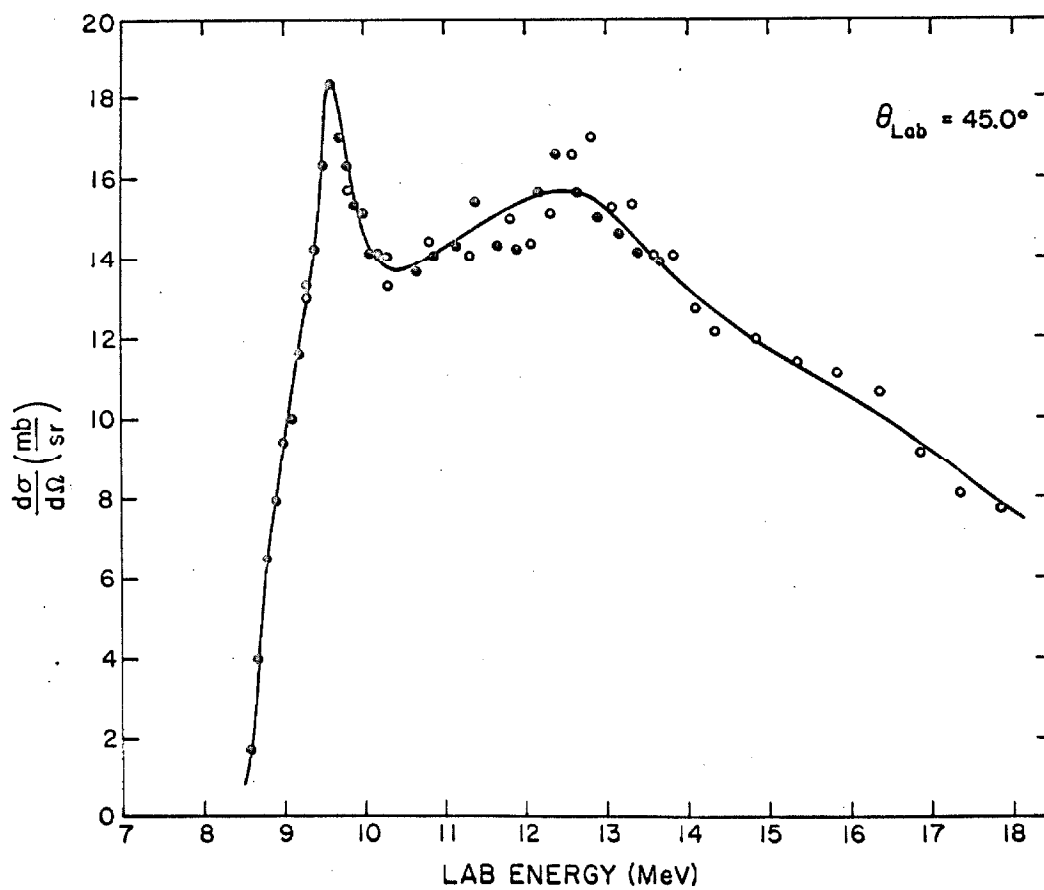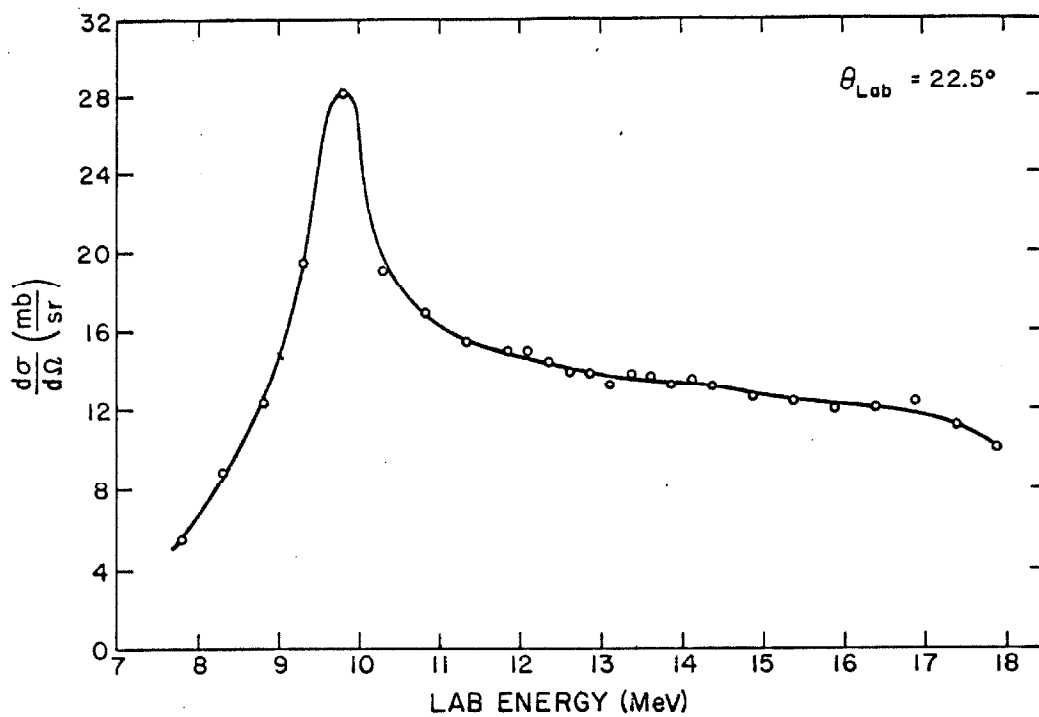
Figure 47

Angular Distributions for the ^{4}He(^{3}He, p)^{6}Li Reaction

This figure shows 2 angular distributions of the protons from the ^{4}He(^{3}He, p)^{6}Li reaction. Center-of-mass differential cross section is plotted against center-of-mass angle. The lines serve only to connect the open circle data points. (Page 18)

$E_{He^3} = 12.445$

GROUND STATE PROTONS

CENTER OF MASS ANGLE

$\frac{d\sigma}{d\Omega} \left(\frac{mb}{sr} \right)$

$E_{He^3} = 10.938$

GROUND STATE PROTONS

CENTER OF MASS ANGLE

$\frac{d\sigma}{d\Omega} \left(\frac{mb}{sr} \right)$
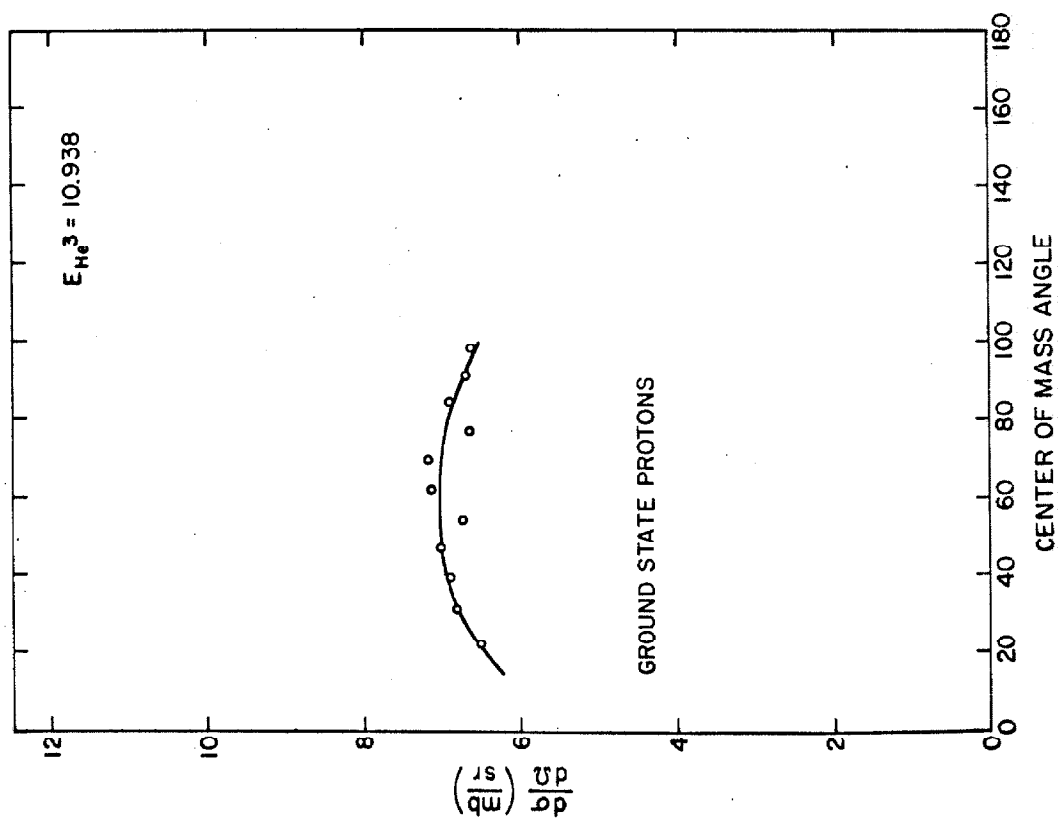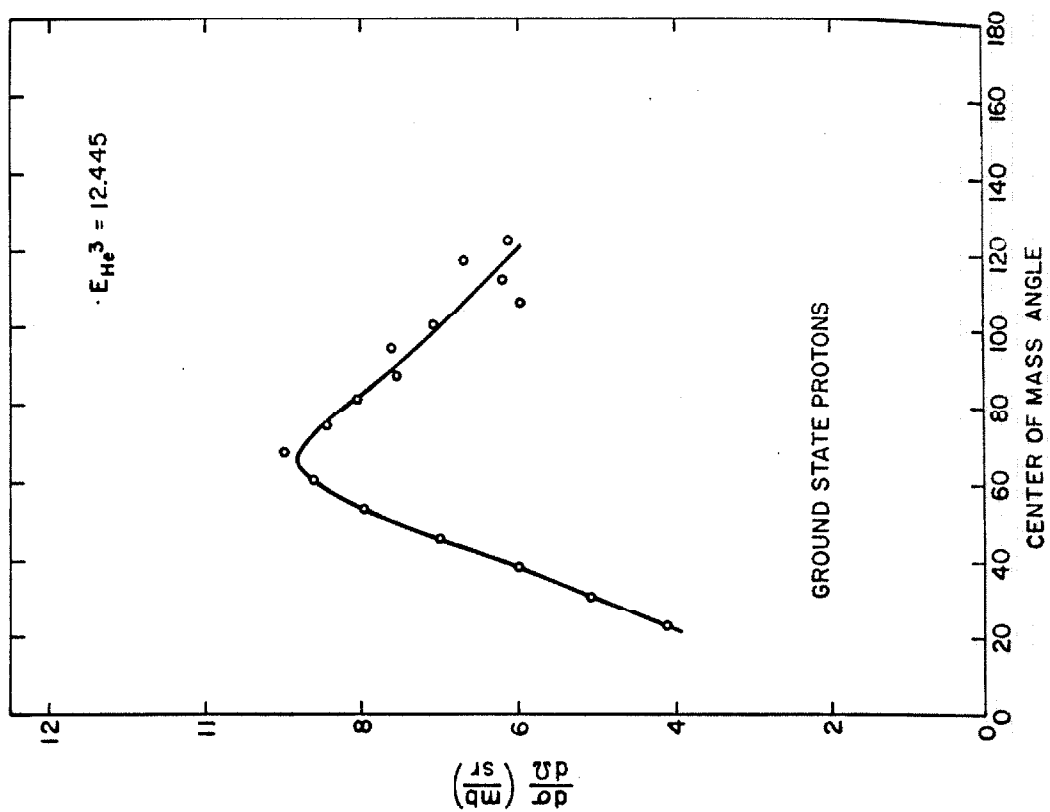
Figure 48

Angular Distributions for the $^4\text{He}(^3\text{He, p})^6\text{Li}$ and $^4\text{He}(^3\text{He,}$ $\text{p}^1)^6\text{Li*}$ Reactions

This figure shows another angular distribution for the ground state protons and also an angular distribution for the first excited state protons. The quantities plotted are the same as in Figure 47. Here too the line serves only to connect the data points. (Pages 18, 19)

$E_{He^3} = 12.445$

1st EXCITED STATE PROTONS

CENTER OF MASS ANGLE

$\frac{d\sigma}{d\Omega}\left(\frac{mb}{sr}\right)$

$E_{He^3} = 13.197$

GROUND STATE PROTONS

CENTER OF MASS ANGLE

$\frac{d\sigma}{d\Omega}\left(\frac{mb}{sr}\right)$
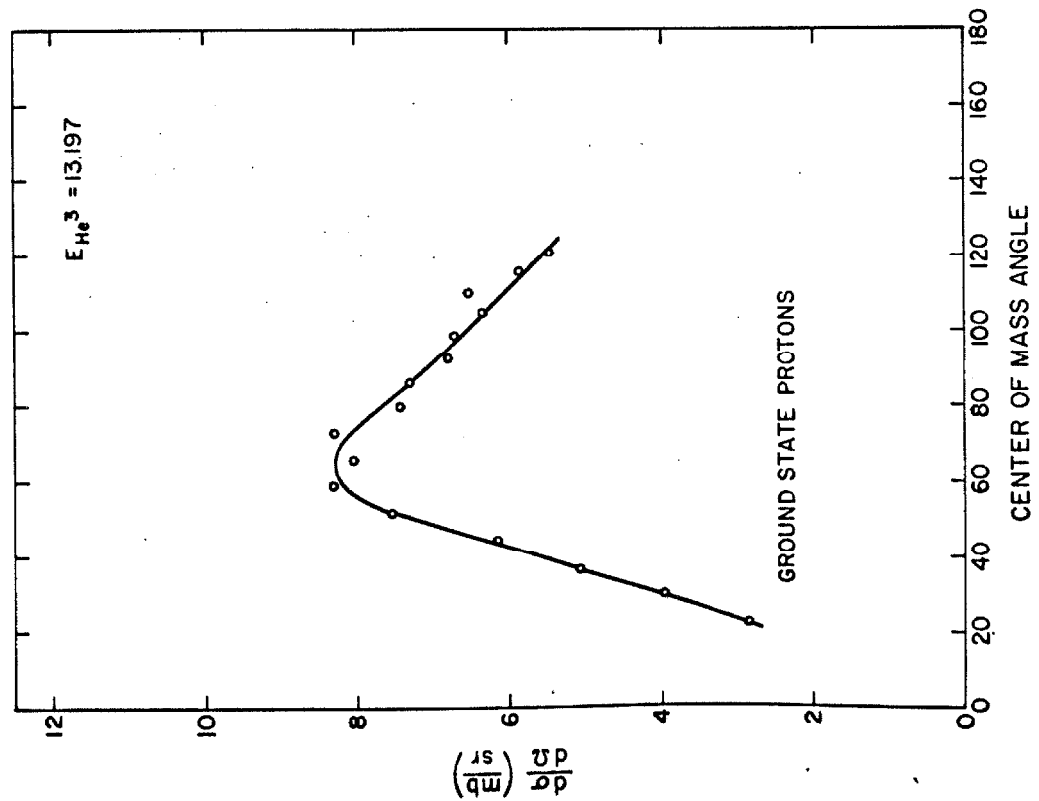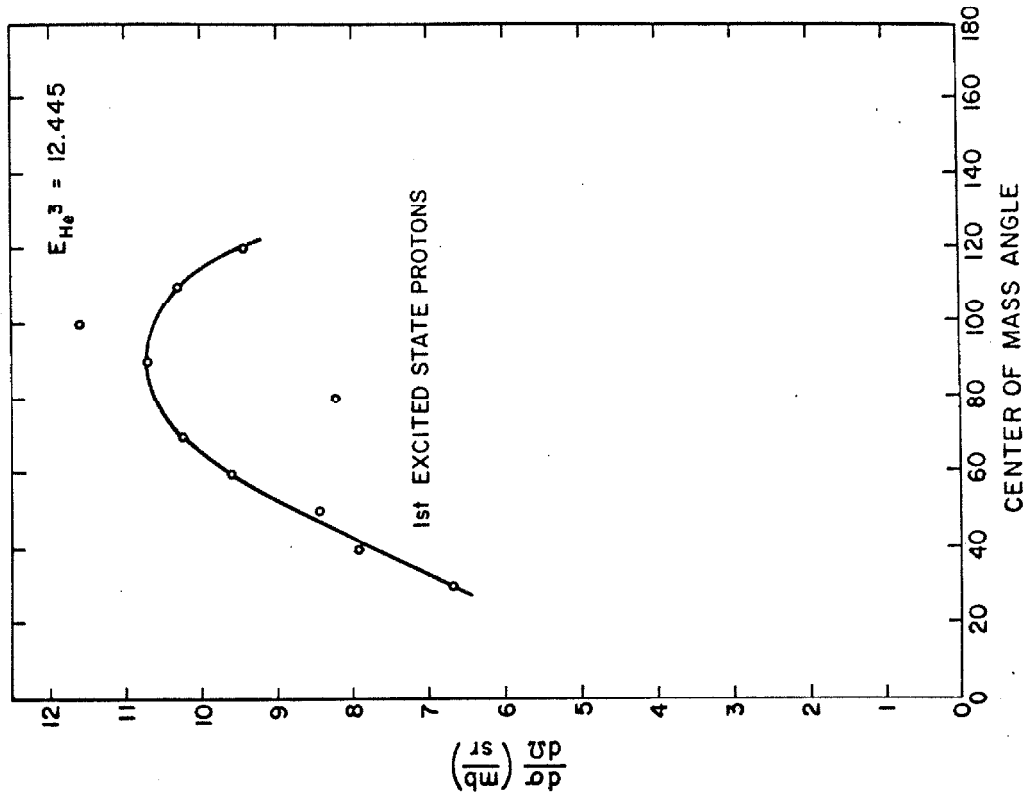
Figure 49

Angular Distributions from the ^{4}He(^{3}He, p^1)^{6}Li* Reaction

This figure shows two more angular distributions of the first excited state protons. The quantities plotted are the same as in Figure 47 and the lines serve only to connect the points. (Page 19)

$E_{He^3} = 14.872$

1st EXCITED STATE PROTONS

CENTER OF MASS ANGLE

$\frac{d\sigma}{d\Omega}\left(\frac{mb}{sr}\right)$

$E_{He^3} = 13.197$

1st EXCITED STATE PROTONS

CENTER OF MASS ANGLE

$\frac{d\sigma}{d\Omega}\left(\frac{mb}{sr}\right)$
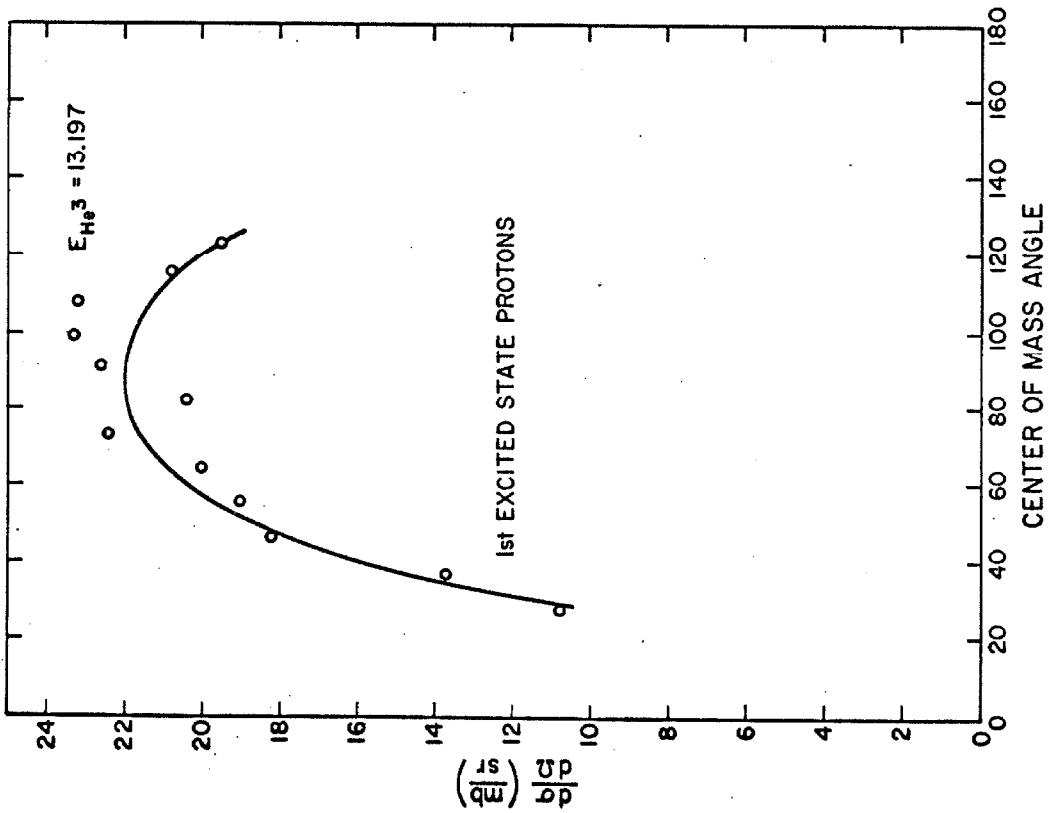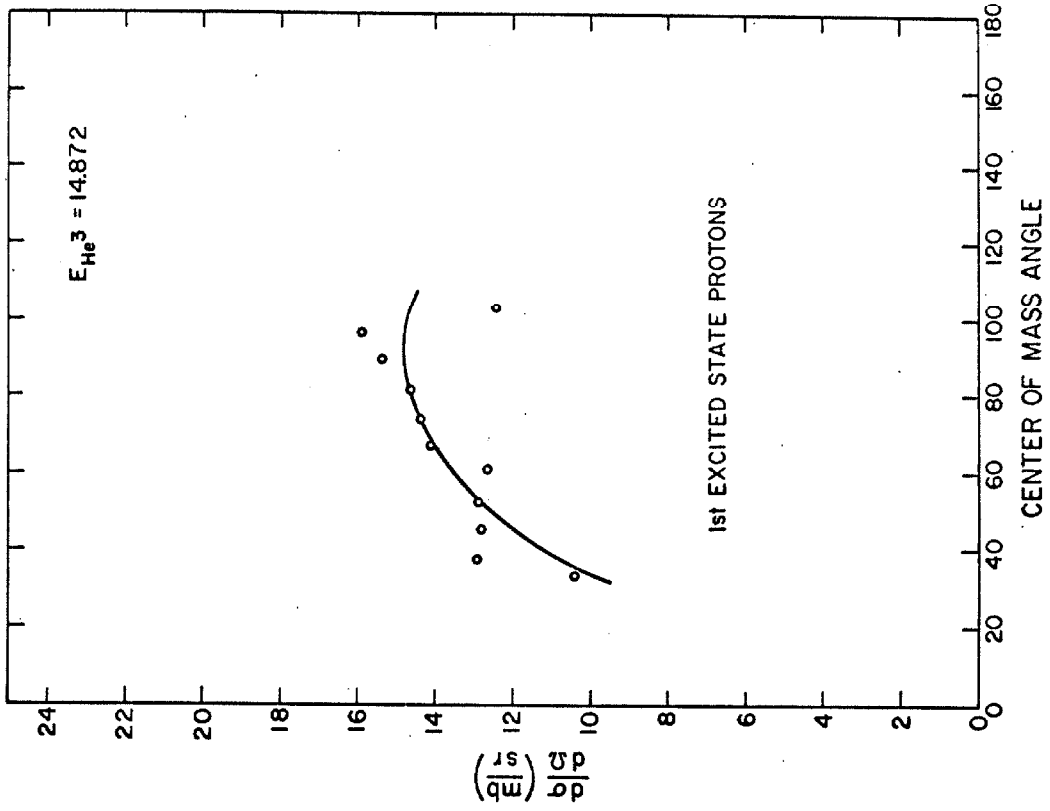
Figure 50

Excitation Curves for the $^4\text{He}(^3\text{He}, p^1)^6\text{Li*}$ Reaction

     This figure shows excitation curves of the first excited state protons for two laboratory angles. The shape is quite similar for other angles investigated. The laboratory differential cross section is plotted versus beam energy. The lines serve only to connect the points. (Page 19)
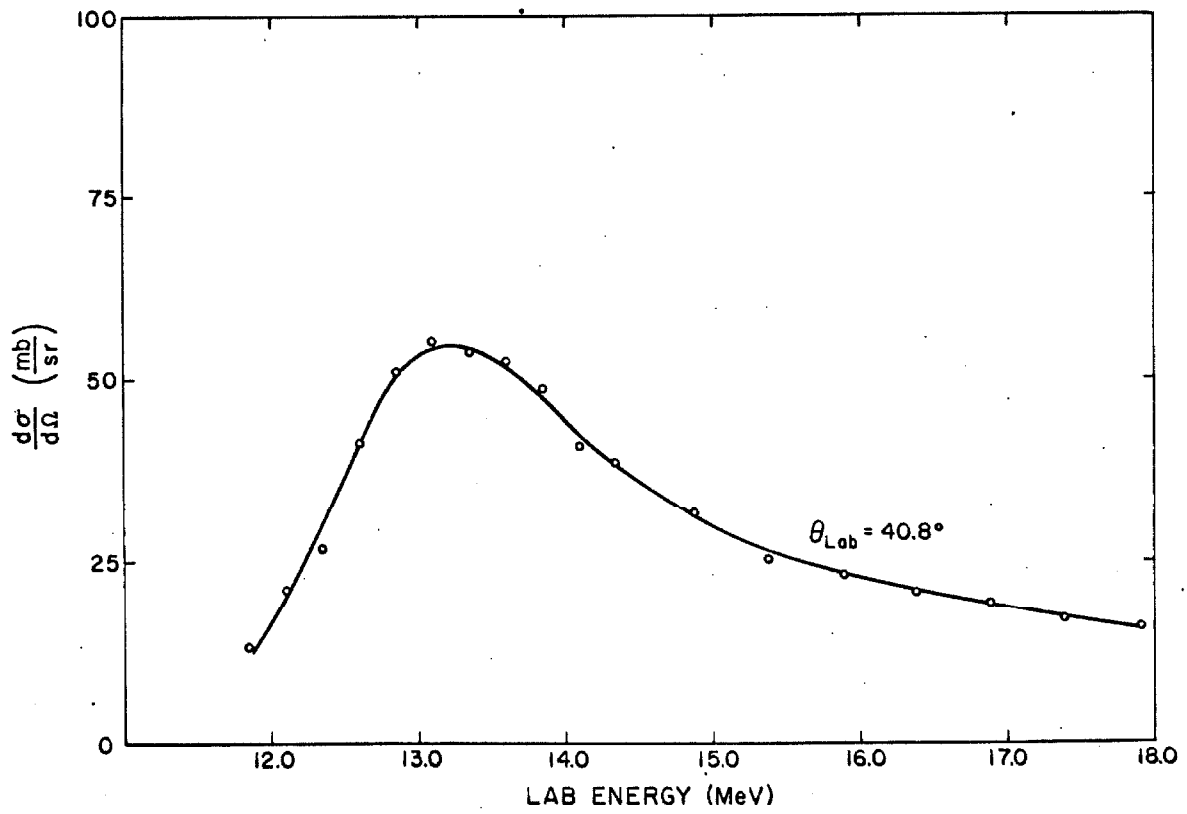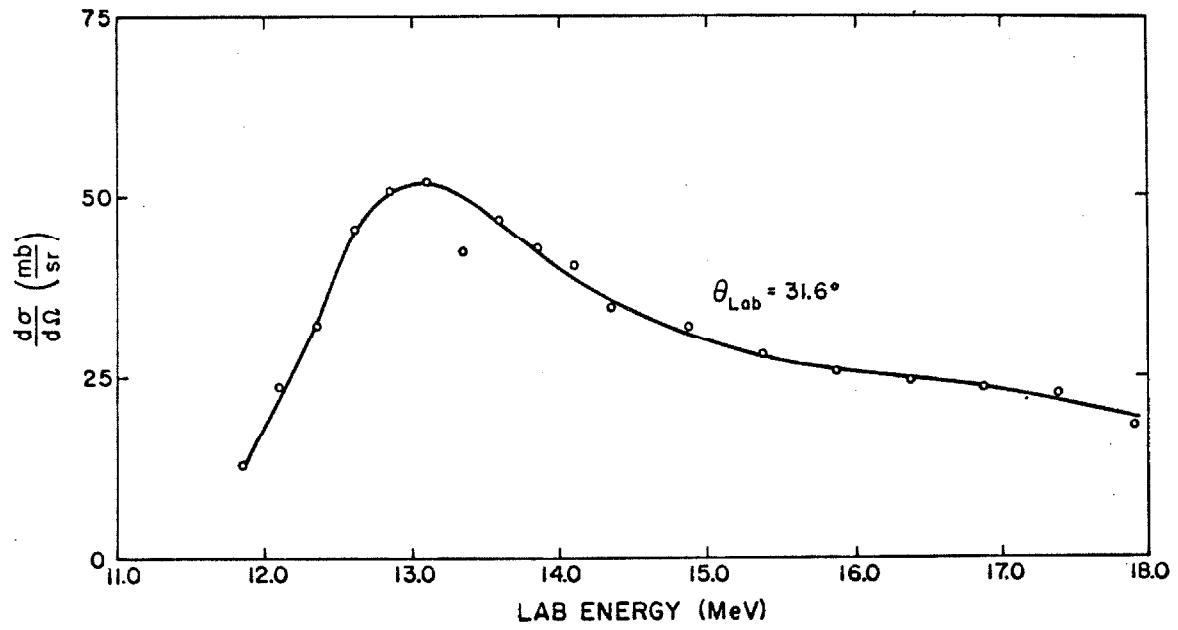
Figure 51

Energy Level Diagram

This figure shows the energy levels of ^{7}Li and ^{7}Be. The spins, parities and isospins of the levels are also shown.
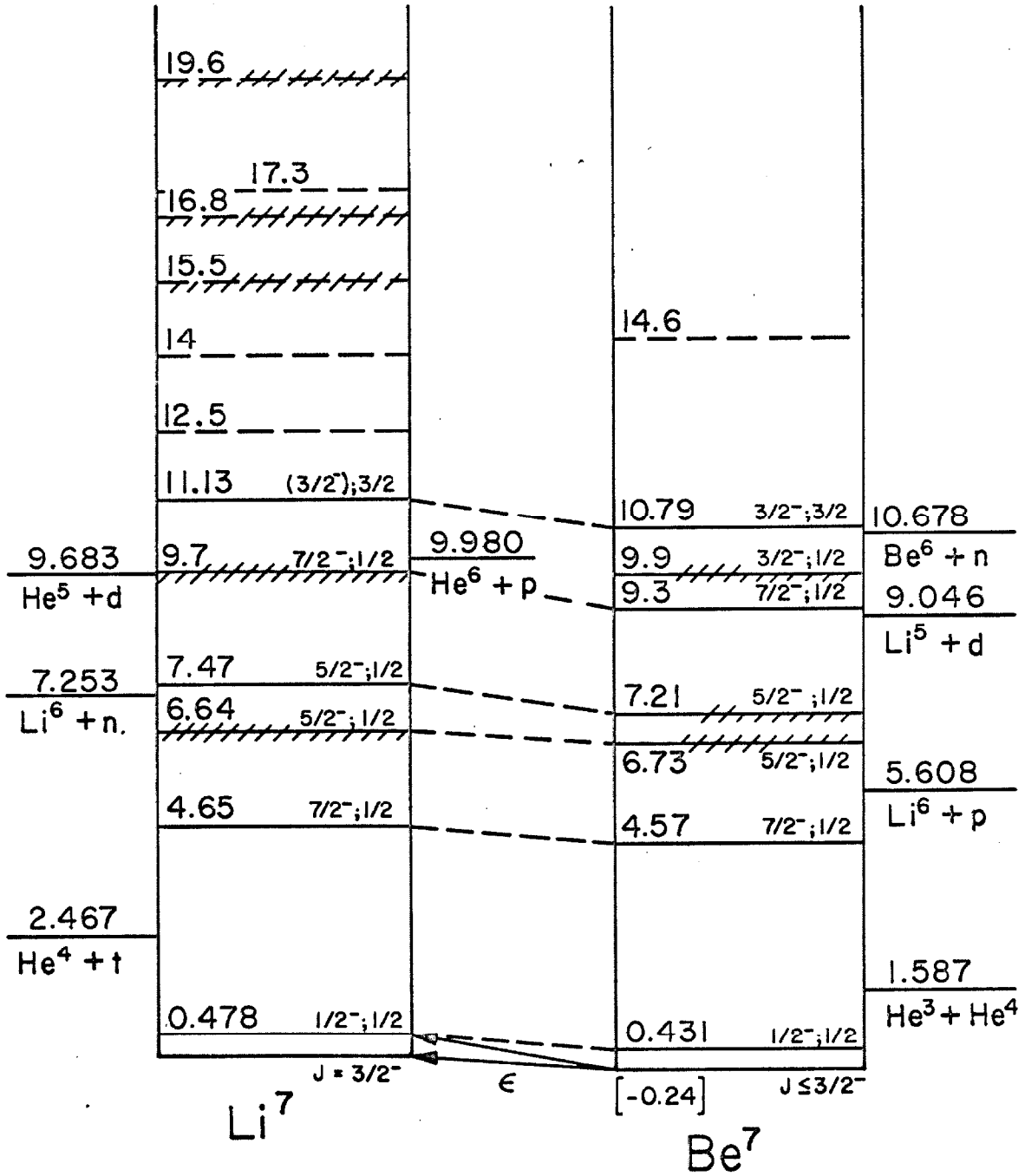
Figure 52

^{4}He(^{3}He, ^{3}He)^{4}He Phase Shifts in Degrees

This figure shows the phase shifts $\delta_{1/2}^+$, $\delta_{1/2}^-$ and $\delta_{3/2}^+$ as a function of energy. It also shows the parameters $X_{1/2}^+$ and $X_{3/2}^+$. The dashed line is a fit to the phase shift $\delta_{1/2}^+$ and corresponds to the s-wave scattering from a hard sphere of radius 2.8 Fermis. (Page 28)

$$S_{J\pi} = \cos^2 X_{J\pi} e^{2i\delta_{J\pi}}$$
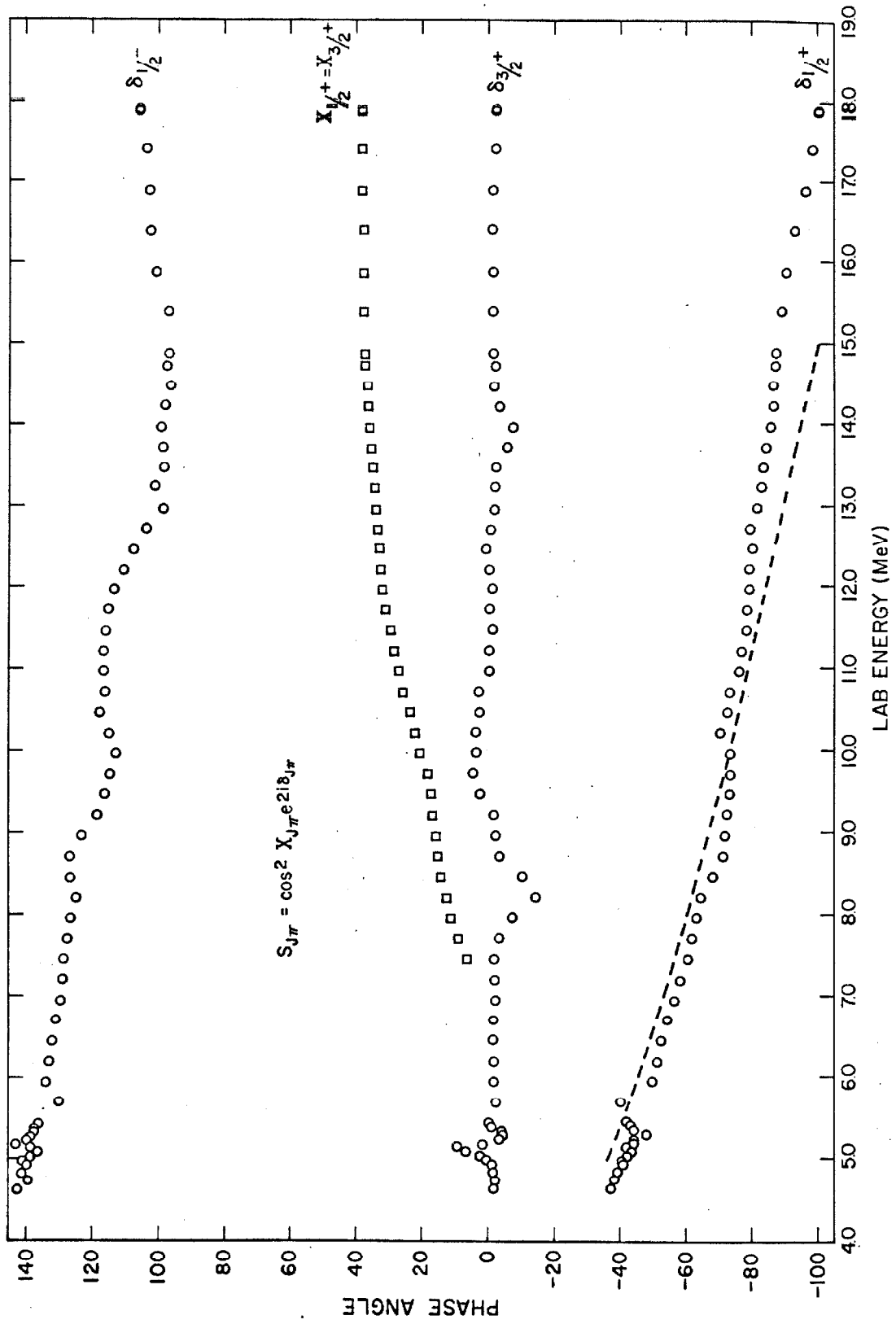
Figure 53

^{4}He(^{3}He, ^{3}He)^{4}He Phase Shifts in Degrees

This figure shows the phase shifts $\delta_{3/2}^{-}$ and $\delta_{5/2}^{+}$ as a function of energy. It also shows the parameters $X_{3/2}^{-}$ and $X_{5/2}^{+}$. (Page 28)
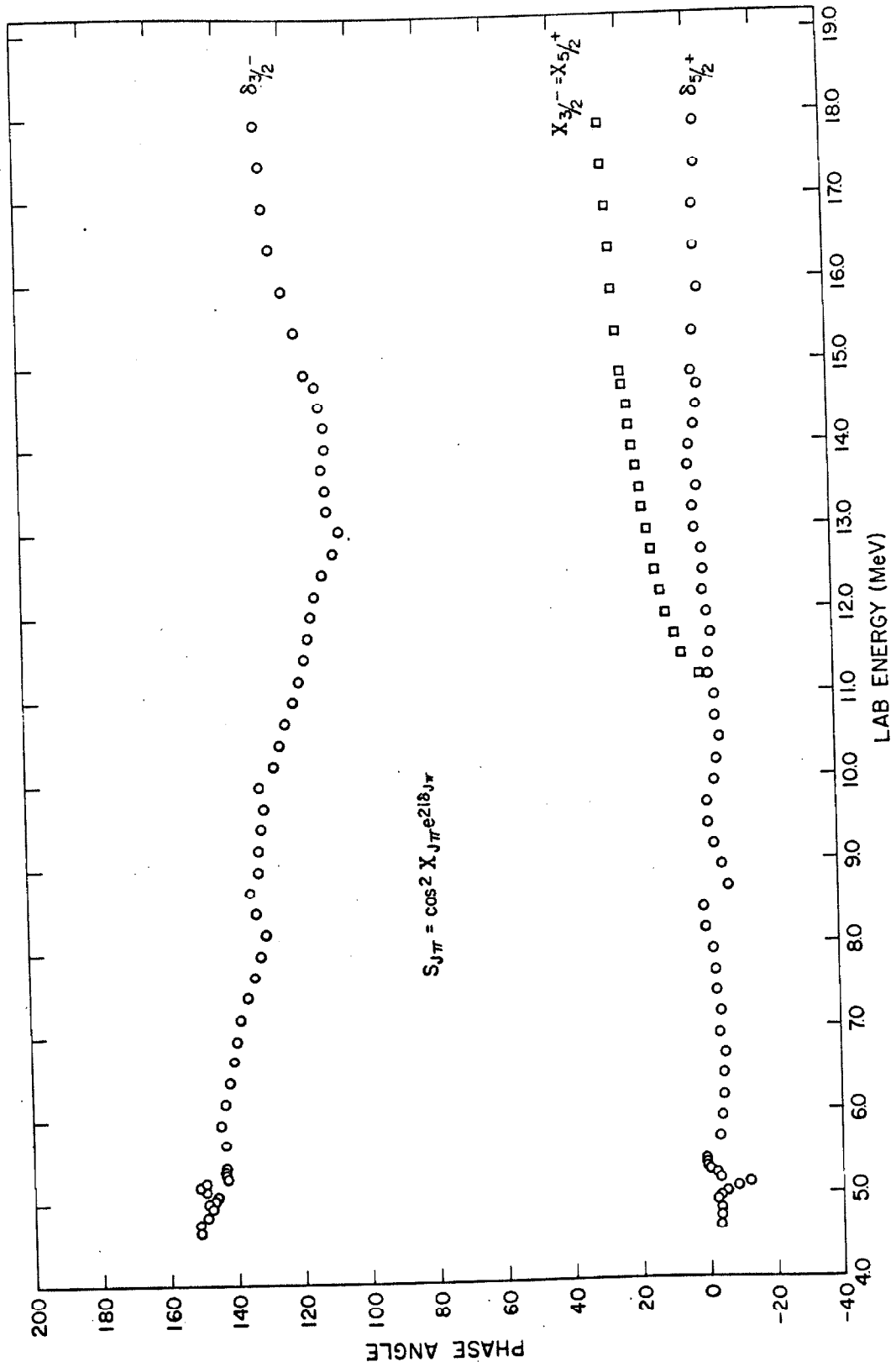
Figure 54

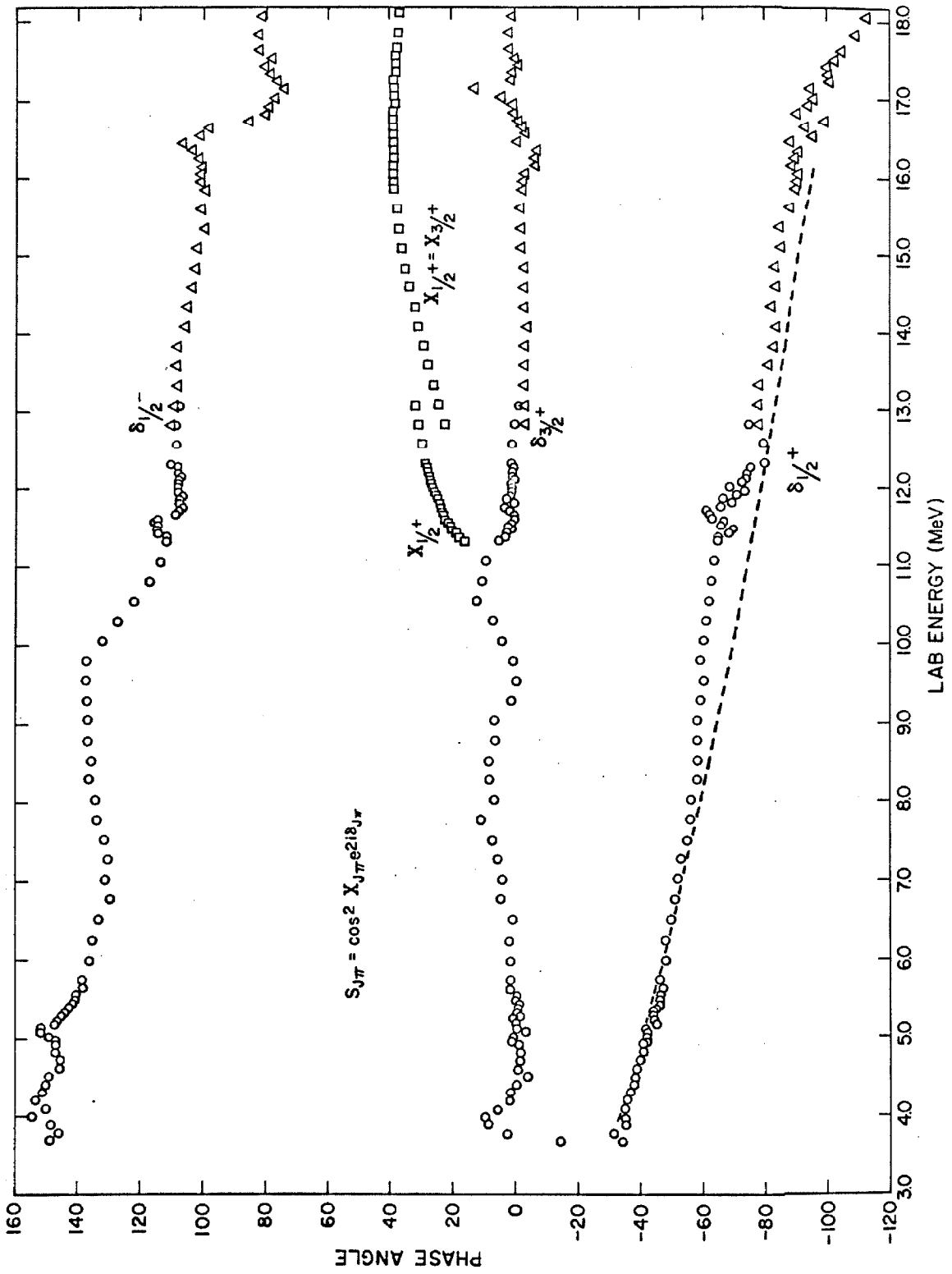$^4\text{He}(^3\text{He}, ^3\text{He})^4\text{He}$ Phase Shifts in Degrees

This figure shows the phase shifts $\delta_{7/2}^-$ and $\delta_{5/2}^-$. It also shows the parameters $X_{7/2}^-$ and $X_{5/2}^-$. The lines show the fits to the phase shifts from R-matrix theory. (Page 28)

$$S_{J\pi} = \cos^2 X_{J\pi} e^{2i\delta_{J\tau}}$$
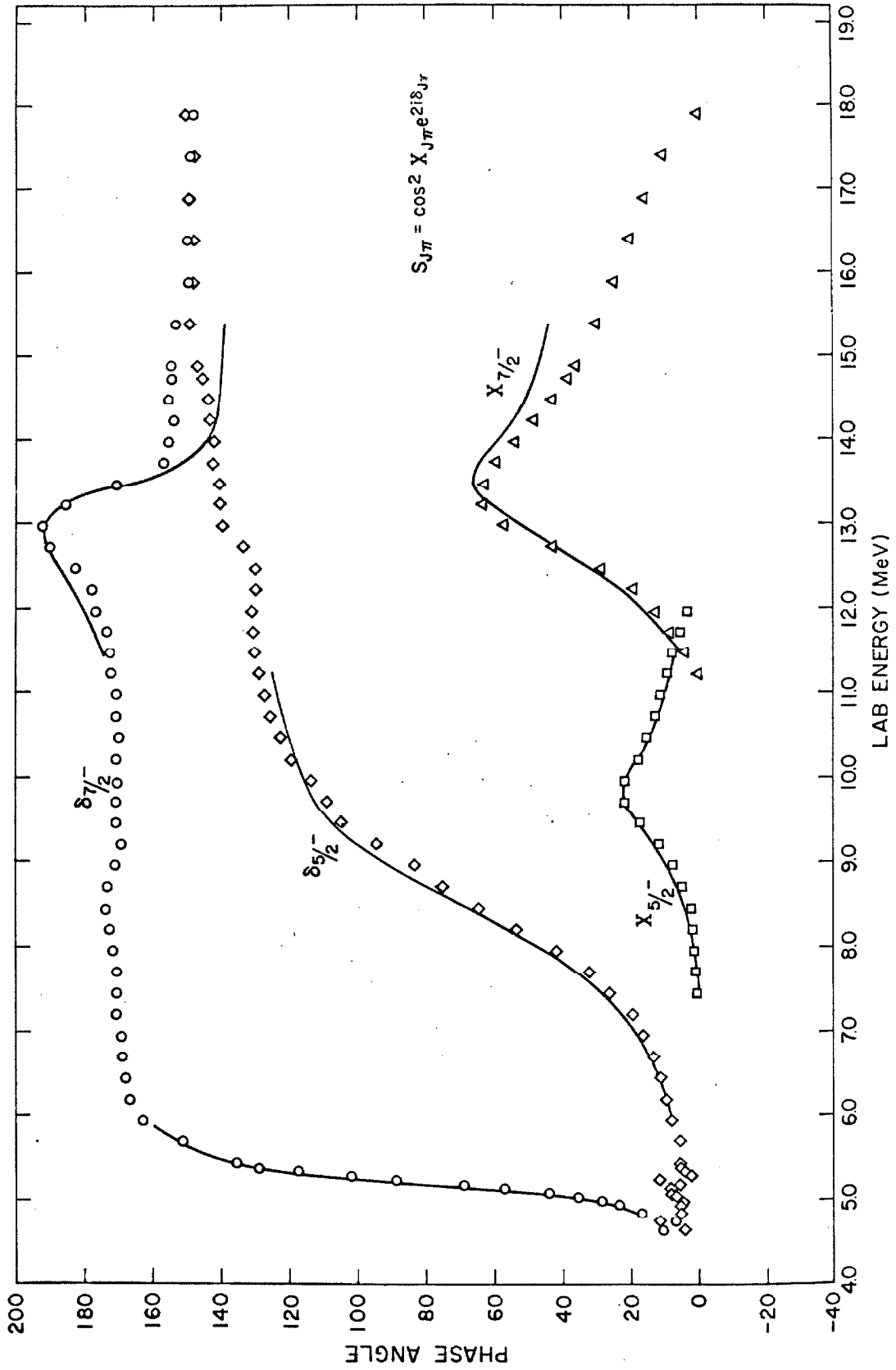
Figure 55

^{3}He Polarizations

This figure shows the spin polarizations of the scattered ^{3}He particles from the ^{4}He(^{3}He, ^{3}He)^{4}He experiment. The polarizations are calculated from the phase shifts obtained in the phase shift analysis. The Basel convention for the sign of the polarizations is used and the contour levels are plotted as a function of center-of-mass angle and laboratory energy. (Page 32)

LAB ENERGY (MeV)

CENTER OF MASS ANGLE
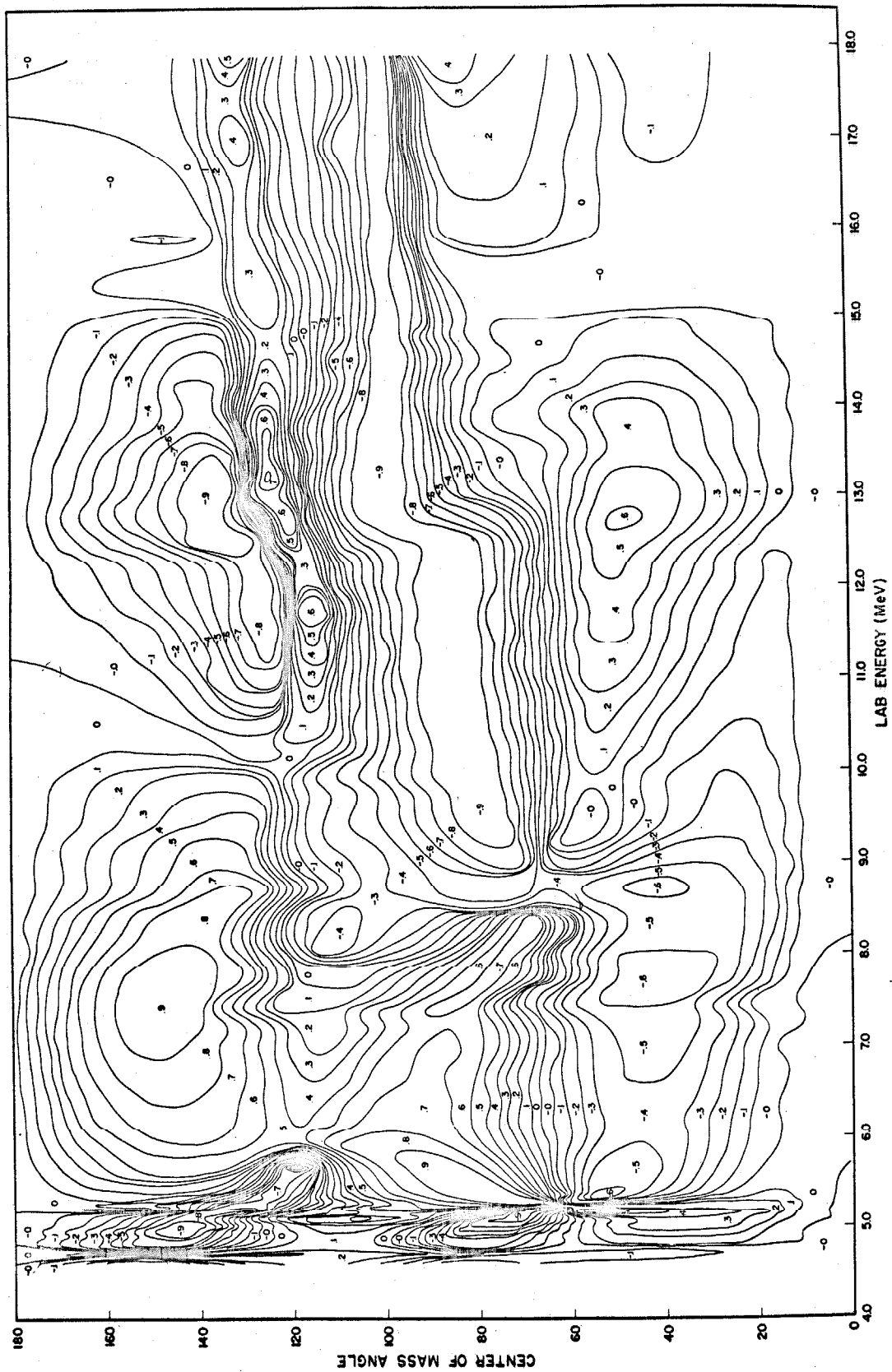
Figure 56

^{3}H$(\alpha, \alpha)^3$H Phase Shifts in Degrees

This figure shows the phase shifts $\delta_{1/2}^{+}$, $\delta_{1/2}^{-}$ and $\delta_{3/2}^{+}$ as a function of energy. It also shows the parameters $X_{1/2}^{+}$ and $X_{3/2}^{+}$. The dashed line is a fit to the phase shift $\delta_{1/2}^{+}$ and corresponds to the s-wave scattering from a hard sphere of radius 2.6 Fermis. The change of symbols near 13 MeV indicates that the phase shifts and $X_{J\pi}$'s obtained above this energy used the high energy beam data. Below this energy the low energy beam data were used. (Page 28)
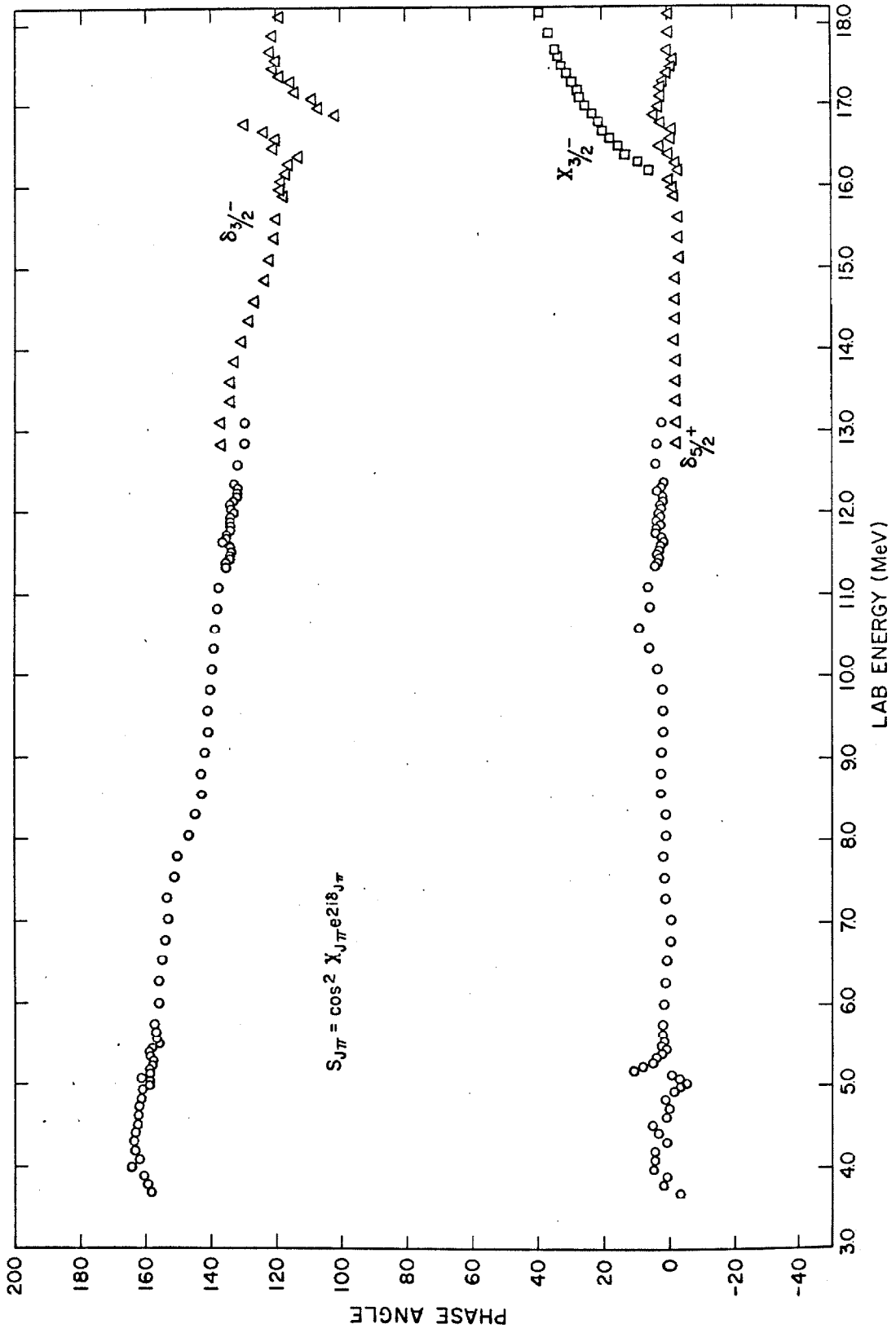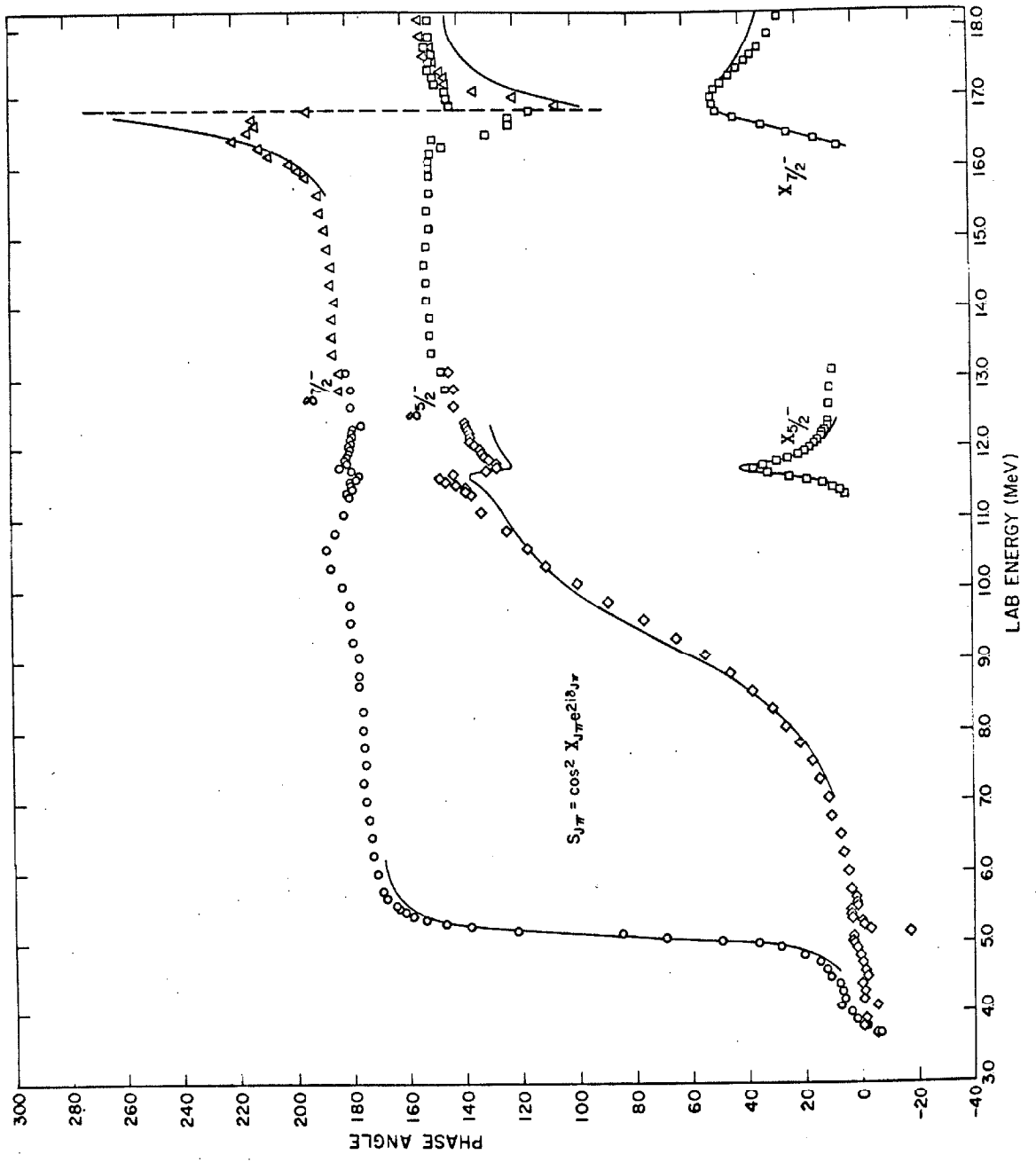
Figure 57

$^3\text{H}(\alpha, \alpha)^3\text{H}$ Phase Shifts in Degrees

This figure shows the phase shifts $\delta_{3/2}^-$ and $\delta_{5/2}^+$ as a function of energy. It also shows the parameter $X_{3/2}^-$. The change of symbols near 13 MeV indicates that the phase shifts and $X_{J\pi}$'s obtained above this energy used the high energy beam data. Below this energy the low energy beam data were used. (Page 28)

$S_{J\pi} = \cos^2 \chi_{J\pi} e^{2i\delta_{J\pi}}$

$\delta_{3/2}^-$

$\delta_{5/2}^+$

$X_{3/2}^-$

PHASE ANGLE

LAB ENERGY (MeV)

Figure 58

^{3}H$(\alpha, \alpha)^3$H Phase Shifts in Degrees

This figure shows the phase shifts $\delta_{7/2}^-$ and $\delta_{5/2}^-$ as a function of energy. Also shown are the parameters $X_{7/2}^-$ and $X_{5/2}^-$. The change of symbols near 13 MeV indicates that the phase shifts and $X_{J\pi}$'s obtained above this energy used the high energy beam data. Below this energy the low energy beam data were used. (Page 28)

$$S_{J\pi} = \cos^2 X_{J\pi} e^{2i\delta_{J\pi}}$$

Figure 59

Triton Polarizations

This figure shows the spin polarizations of the scattered tritons from the $^3H(\alpha, \alpha)^3H$ experiment. The polarizations are calculated from the phase shifts obtained in the phase shift analysis. The Basel convention for the sign of the polarizations is used and the contour levels are plotted as a function of center-of-mass angle and laboratory energy. (Page 32)
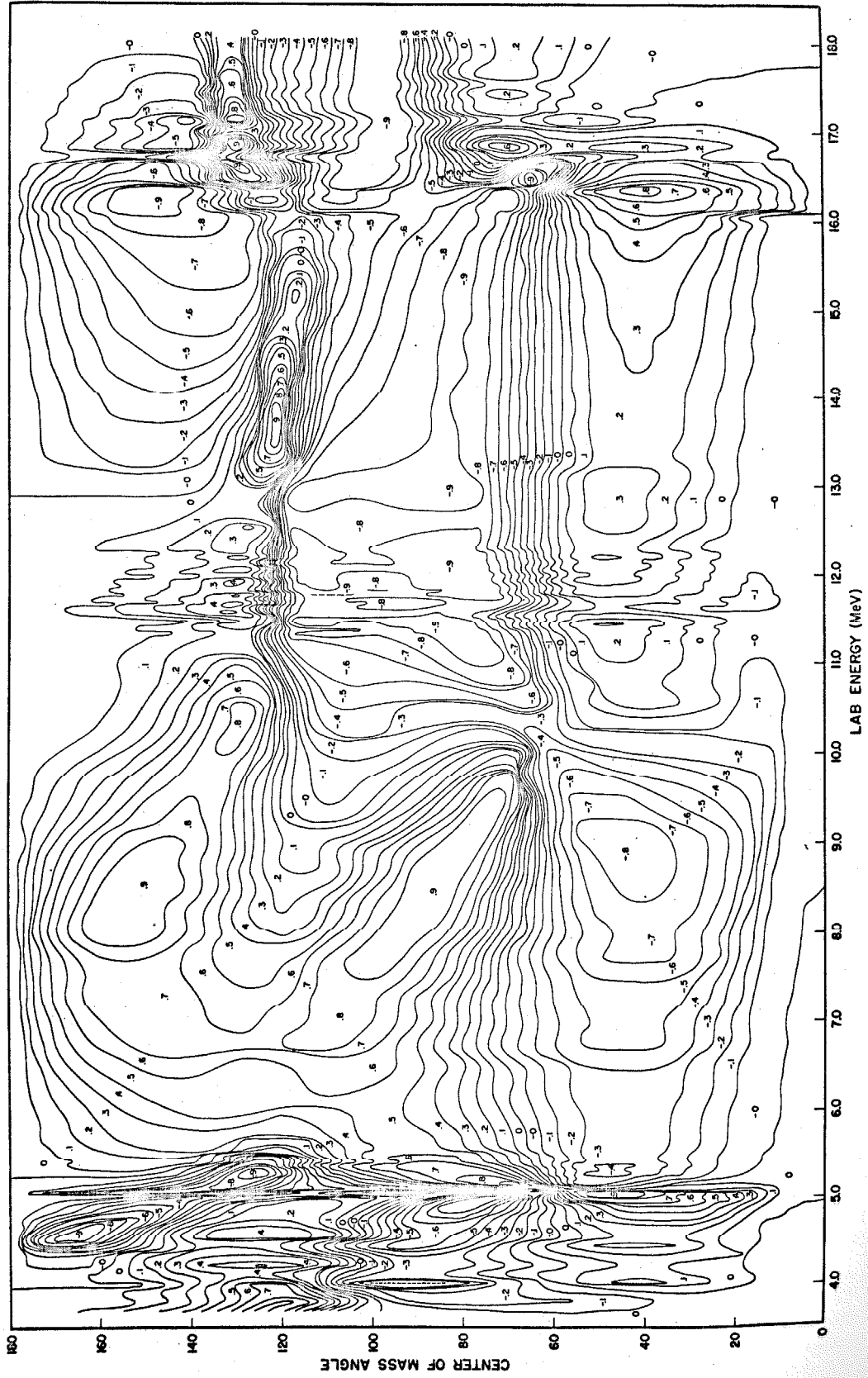
CENTER OF MASS ANGLE

LAB ENERGY (MeV)

Figure 60

^{7}Be Boundary Value Variations

This figure shows the value of the elastic reduced width amplitude for the $^{4}P_{5/2}$ state in ^{7}Be which gives the best fit for a given value of the boundary value B_e. The line is a smooth curve connecting the calculated points. (Page 45)
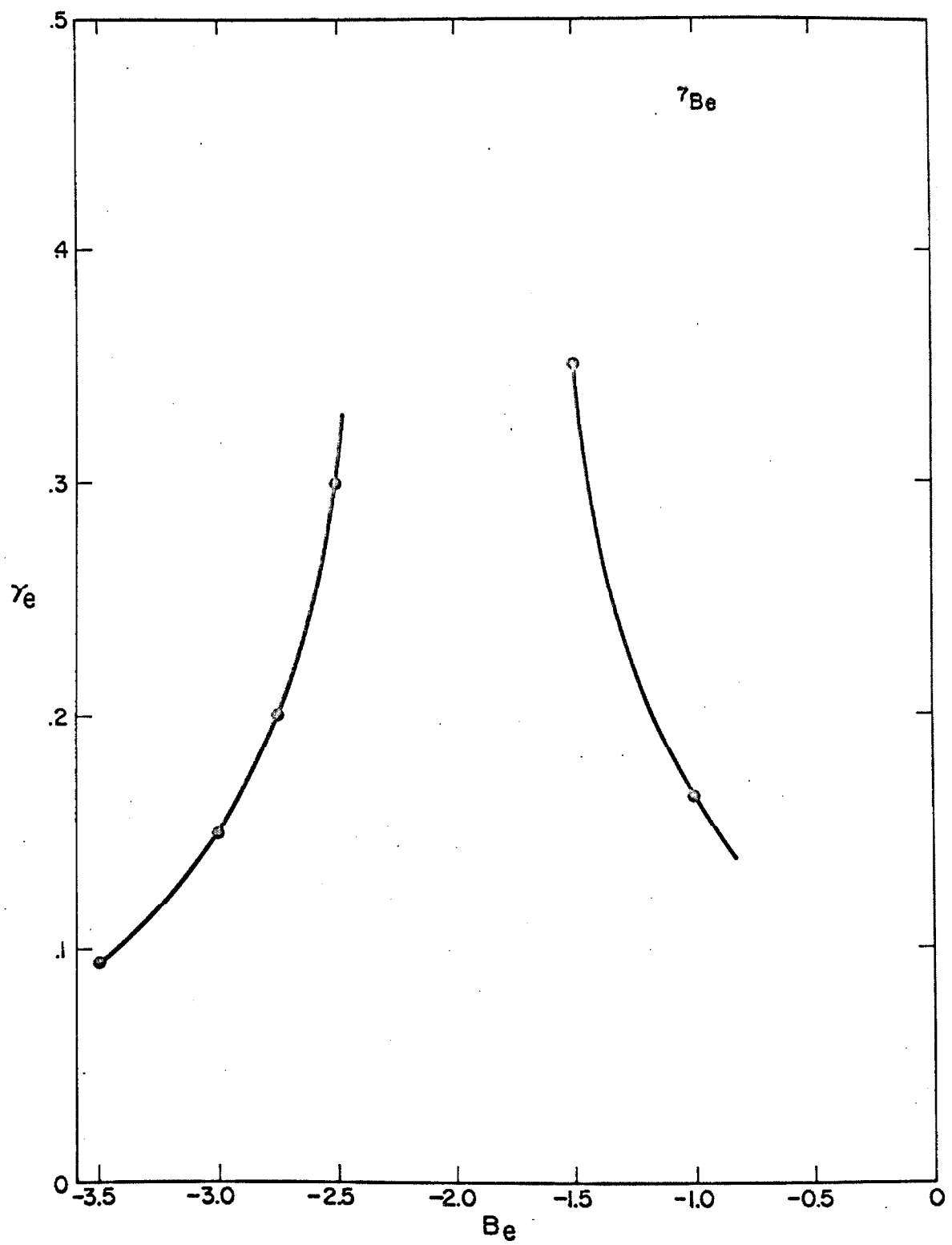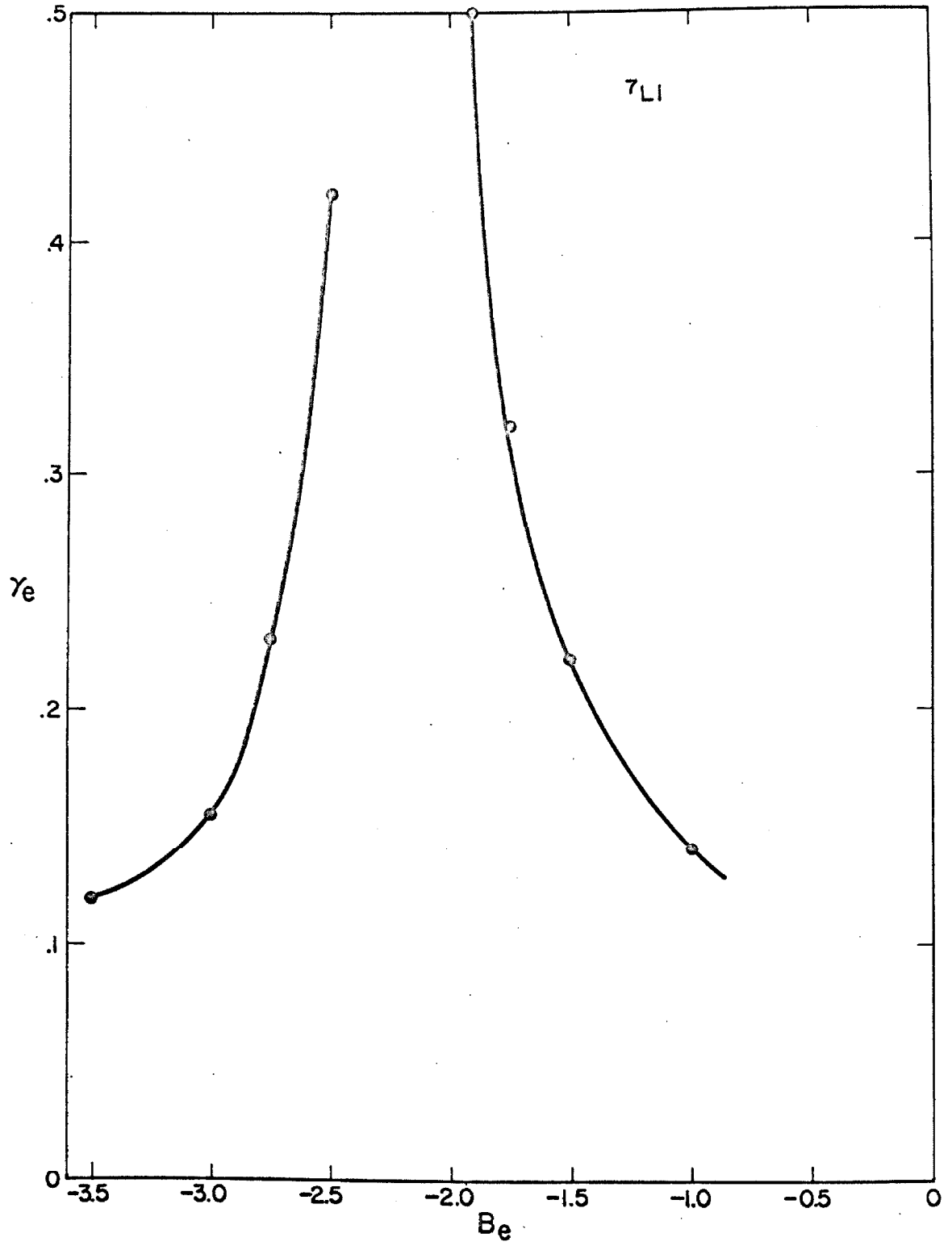
Figure 61

^{7}Li Boundary Value Variations

This figure shows the value of the elastic reduced width amplitude for the $^4P_{5/2}$ state in ^{7}Li which gives the best fit for a given value of the boundary value B_e. The line is a smooth curve connecting the calculated points. (Page 45)

Figure 62

Nuclear Model Predictions

This figure shows the energy levels for ^{7}Li or ^{7}Be with their spins, parities and isospins as predicted by the rotational model (Chesterfield, 1962) (b) and the shell model (Barker, 1966) (c). Parts (a) and (d) show ^{7}Li and ^{7}Be energy levels determined by experiment. The isospin is $\frac{1}{2}$ except for those levels listed as $T = \frac{3}{2}$. (Page 51)

11.13 3/2⁻;3/2			
10.60 3/2⁻		11.17 3/2⁻;3/2	
			10.79 3/2⁻;3/2
9.7 7/2⁻	9.80 7/2⁻	9.80 1/2⁻	9.9 3/2⁻
	9.43 1/2⁺	9.61 7/2⁻	
		9.17 3/2⁻	9.3 7/2⁻
7.47 5/2⁻	7.67 1/2⁻	7.48 5/2⁻	
	7.52 5/2⁻		7.21 5/2⁻
6.64 5/2⁻	6.27 5/2⁻	6.56 5/2⁻	6.73 5/2⁻
4.65 7/2⁻	4.91 7/2⁻	4.63 7/2⁻	4.57 7/2⁻
0.48 1/2⁻	0.48 1/2⁻	0.64 1/2⁻	0.43 1/2⁻
3/2⁻	-0.11 3/2⁻	3/2⁻	3/2⁻
⁷Li	ROTATIONAL MODEL	SHELL MODEL	⁷Be
(a)	(b)	(c)	(d)